NASA Conference Publication 2386

Transition in Turbines

Proceedings of a symposium sponsored by the
NASA Lewis Research Center and held at the
NASA Lewis Research Center
Cleveland, Ohio
May 15–16, 1984

NASA

NASA Conference Publication 2386

Transition in Turbines

Proceedings of a symposium held at
NASA Lewis Research Center
Cleveland, Ohio
May 15-16, 1984

NASA
National Aeronautics
and Space Administration

Scientific and Technical
Information Branch

1985

PREFACE

In October 1980 the Lewis Research Center sponsored a workshop on the problem of predicting local heat transfer in a gas turbine. The workshop strongly recommended further study of the transition mechanism in turbine airfoils. On the strength of that recommendation a program, involving both in-house and university grant research, was begun to deal with that issue. Brief progress reports on this research were presented at the beginning of this symposium. An invited lecture by Professor Mark Morkovin gave us a glimpse of the current understanding of transition initiation. He introduced the concept of a large-disturbance "bypass" mechanism for the initiation of transition. This mechanism, or some manifestation thereof, is suspected to be at work in the boundary layers present in a turbine flow passage.

With this background we formed small groups to focus on four relevant subtopics:

(1) The effect of upstream disturbances and wakes on transition
(2) Transition prediction models, code development, and verification
(3) Transition and turbulence measurement techniques
(4) The hydrodynamic condition of low-Reynolds-number boundary layers

Each group evaluated the current status of its topic and considered research that would advance knowledge in that topic. The collective progress advanced our understanding of the transition mechanism.

Robert W. Graham
Chairman

CONTENTS

IDENTIFICATION OF THE PROBLEM

Robert W. Graham
National Aeronautics and Space Administration
Lewis Research Center
Cleveland, Ohio 44135

Much of the research on transition in boundary layers has related to the fuselage, wings, or external control surfaces of aircraft. An interesting problem in external aerodynamics or fluid mechanics, it has attracted many researchers. Transition in boundary layers determines the lift, drag, and control characteristics of an aircraft. Much has been learned about the control of transition, and this has contributed to the design of low-drag airfoils for aircraft. The question of heat load on a supersonic aircraft or a reentry vehicle introduced another major concern related to transition. As is well known, there is a discontinuous jump in heat transfer between laminar and turbulent boundary layers at a given Reynolds number over a substantial Reynolds number range. The blunt reentry shape of crew capsules from Mercury to Apollo resulted from research that proved a laminar boundary layer with minimum heat transfer would exist over the blunt leading surface.

The fundamental research inspired by the boundary-layer transition problem has yielded significant information about the transition mechanism. Those who participated in this research are aware of the great challenge and difficulty involved. At least a decade of intensive research and study by many competent researchers was required before the initial analytical model of the mechanism was achieved. Small-disturbance theory has been employed as an analytical tool in predicting the onset of turbulent bursts that mark the beginning of transition in a boundary layer.

FLOW ENVIRONMENT

Bypass Transition

It is of particular significance to this symposium to understand how turbulence is initiated in boundary layers by large disturbances in the free stream. This type of transition mechanism has been called the bypass mode. Professor Morkovin summarized the status of transition theory and elaborated on the bypass mode. Several of the progress reports on current research presented at this symposium describe efforts to accrue more information about the nature of the bypass (or large disturbance) mode.

Upstream Disturbances

In addressing the specific problem of transition in a gas turbine, it can be assumed that the hot gases entering the turbine are in a highly disturbed state and that the bypass mode is the likely transition mechanism. This assumption is justified by considering the flow history of the gases before they enter the turbine. In either a flight or stationary gas turbine the gases

are compressed shortly after being ingested, by either an axial or a centrifugal compressor. The staged blading and struts introduce unsteadiness and wake disturbances into the flow. Some early results of a Lewis study to simulate wake condition effects on heat transfer were presented at this symposium.

Most of the high-pressure gas then enters the combustor, where fuel injection, heat addition, and induced mixing contribute to flow unsteadiness. Modeling the complex interaction of fluid mechanics and chemical reaction during combustion is receiving considerable attention at Lewis, and some results were reported at this symposium.

By the time the gas has been compressed and burned, it is difficult to describe its condition in conventional fluid mechanics terminology relating to turbulence. Certainly the gas flow is not steady and the eddy structure is far from being homogeneous turbulence. In fact, the term "turbulence" may be completely inappropriate in describing the condition of the gas. The usual sources of turbulence in a classical experiment may be relatively unimportant in a turbine. Such terms as turbulence intensity can have meanings in the turbine flow regime that are entirely different from those associated with external flow aerodynamics.

In a paper published in 1975, R.L. Evans proposed three definitions of flow disturbance with regard to turbomachinery. The categories included an overall disturbance level, in which the total fluctuation in velocity V' was normalized with respect to an average flow velocity $\overline{U}$; a free-stream turbulence level, in which the turbulence fluctuation v' was normalized with respect to $\overline{U}$; and an unsteadiness level, which related the difference between the instantaneous velocity and an average velocity at that instant normalized with respect to a time-averaged velocity. Although such definitions do not eliminate all of the problems in describing or quantifying the disturbances, they suggest that the conventional definitions of turbulence are not proper or adequate.

More consequential than the definition are how the disturbances and unsteadiness affect the local heat transfer rates on the turbine surfaces. An axial-flow turbine has approximately 100 airfoil-shaped blades. Because each blade develops its own boundary layer, transition occurs on each blade. The unsteadiness and disturbances in the flow field ahead of the turbine influence the development of the boundary layers and the transition process itself. Since heat transfer occurs across the boundary layer, anomalous heat transfer conditions can occur anywhere on the blade. Generally the heat transfer over the leading edge of the blade exceeds that predicted by stagnation flow theory. Designers resort to augmentation coefficients to account for these higher levels of heat transfer. Depending on the practice and judgment of the designer, the augmentation factor can vary from 20 to 80 percent above the reference level of heat transfer associated with quiescent flow. NASA studies of this particular heat transfer problem are reported in this proceedings.

Horseshoe Vortices

Upstream of the intersection of the blades (or vanes) with the hub or casing wall, an unusual vortex flow pattern develops that has a marked effect on local heat transfer. The vortex bends into a bow wave, or horseshoe, shape.

The scrubbing action of the vortex augments local heat transfer, and the trailing edges become a part of the secondary flow pattern that moves from the pressure surface of one blade to the suction surface of an adjacent blade. The role of this vortex pattern in determining the nature of the boundary layers on the wall or hub and on the blade surface is not well understood. It can be considered as one of many flow disturbances that influence the laminar or turbulent characteristics of the boundary layers. Heat transfer near the horseshoe vortex has been measured recently at Rensselaer Polytechnic Institute, as summarized in this proceedings.

Curvature Effects

Another flow phenomenon in the turbine blade rows is the rapid turning of the flow over a broad angle. Depending on which surface of the turbine blade is being examined, the curvature is convex or concave. As has been observed in research on curved channels, a convex surface attenuates the eddy structure of the boundary layer. In contrast, a concave surface enhances turbulence. Obviously curvature has a significant influence on the transition process in turbine boundary layers.

Acceleration-Deceleration

In addition to curvature effects the blade boundary layers are subject to severe velocity gradients (accelerations and decelerations). It is well known that the turbulent structure in a boundary layer is affected by velocity gradients. Acceleration is a stabilizing influence that attenuates the intensity by stretching or straining the eddies. Deceleration tends to be destabilizing and thus promotes turbulence.

TRANSITION MODELS

In a turbine all of the aforementioned effects operate simultaneously. Two (or more) effects may reinforce or cancel each other. It is difficult to make predictions that comprehend all of these effects and their interactions. Attempts have been made to use boundary-layer codes to prescribe transition criteria that enable the codes to shift from laminar to turbulent calculations. Some of these attempts, reported herein, were not satisfactory. While being careful to distinguish turbine flow unsteadiness and stochastic effects from classical turbulence, we cannot dismiss the significant efforts in the modeling of classical turbulence. Computational methods and modern computer systems have enabled modeling efforts once thought beyond possibility. Turbulence modeling is being pursued at Lewis in the acknowledged transition domain.

CONCLUDING REMARKS

I have attempted to identify some of the physical effects of turbulence and to portray the complexity of the transition mechanism. There are more variables and more physical effects than one cares to deal with for any problem. Our task is to select the highest order effects and to determine what must be learned in order to increase our understanding.

COMBUSTOR TURBULENCE

C. John Marek
National Aeronautics and Space Administration
Lewis Research Center
Cleveland, Ohio 44135

The turbulence entering the turbine is produced in the combustor. High turbulence levels from the combustor can alter the location of the transition point on the turbine vane. The dynamics of turbulence and the progress being made in computing the flow are discussed.

The contraction between a combustor (fig. 1) and a turbine inlet can be anywhere from 50 percent on advanced engines to 75 percent (25-percent open area) on older engines. Effective blockages of the combustor are about 75 percent. Combustors operate at reference velocities of 30 m/sec with incoming dilution jet velocities of 120 m/sec.

Only a few measurements have been made of combustor turbulence, and these have usually been at the combustor exit. In 1979 turbulence was measured at the exit of a T-63 combustor (ref. 1) with 75-percent contraction (fig. 2). With combustion and at isothermal conditions, typical turbulence levels were 6 to 10 percent. These data were taken with a laser Doppler velocimetry (LDV) system, and the velocity probability distribution was fitted to a Gaussian (fig. 3). The turbulence intensity is the standard deviation of the sample. At flight idle conditions the turbulence level was 7 percent. The probability distribution tended to be Gaussian over a wide range of velocity. Therefore the probability of an event or of a given velocity being different from the mean could be determined.

Data presented at a recent meeting on hot-section technology (HOST) (fig. 4) show LDV measurements taken at the exit of a combustor in a free jet (fig. 5). Again, the combustor had 75-percent contraction (or 25-percent open area). The nozzle was 50 mm in diameter, and the measurements were taken 60 mm, or 1.2 jet diameters, downstream. In cold flow the turbulence intensity was 8 percent on the centerline and 50 percent at the edge. The higher values show the influence of the mixing wake on turbulence. In hot flow the turbulence intensity was 9 percent in the core region, so it did not increase much with combustion. The exhaust velocity, of course, went from 60 m/sec in cold flow to 220 m/sec with combustion.

For a simple round jet the turbulence intensity was normalized with the centerline velocity, with peak values of 20 percent and dropping off toward the edge (fig. 6(a)). The axial distribution of the maximum turbulence intensity (fig. 6(b)) showed lower values below Z/D = 10, representing the potential core.

The turbulence intensities for a combustor exhaust are about 10 percent for 75-percent contraction. Future engines will probably be designed with close to 50-percent contraction. Turbulence increases with decreasing contraction. For 10-percent turbulence in the exhaust the combustor turbulence would

be 40 percent; so engines with 50-percent contraction would have a turbine inlet turbulence of 20 percent.

A motion picture of the dynamics of combustor turbulence was taken at the University of California, Berkeley. The motion picture (C-315) is available on loan from the NASA Lewis Research Center by sending in the request card at the end of this document. Some still photographs from the motion picture (fig. 7) show large-scale structures. The premixed propane-air flowed at 20 m/sec through a two-dimensional nozzle over a rearward-facing step. The step was 2.5 cm high and 17.8 cm deep. As the fuel-air ratio of the mixture was increased, the flame speed increased. Instability occurred and the flame flashed over the lip. The boundary layer on the nozzle lip went through transition, probably caused by the flow instability arising from the dynamics of the combustion process. The dynamics of the flow is evident in the motion picture. In the next sequence (fig. 7(b)) an additional step was placed in the exhaust to determine the effect of contraction on the turbulence leaving the combustor. The step produced a 50-percent contraction. Amazingly, the turbulence unwound and went straight into the contraction. The size of the turbulence structures was tailored by the duct to the size of the available duct height. Flashback occurred at a different fuel-air ratio than it did without the downstream step. The structure of the flame front and this particular wave were quite different from the flow without the downstream step. The term "wave" is used because of the influence of the downstream step on the flow, which was at the same velocity as in the sequence with the single step. Color schlieren photography at 6000 frames/sec was used, and frame duplication was used to slow down an event. The schlieren system is sensitive to small temperature gradients. In the motion picture the combustion zone is the black region and the regions of unburned gas and the reacted gas underneath the step appear blue.

The final sequences of the motion picture present random vortexes calculated by the method of Chorin. The turbulence is quite dynamic. It is hard to predict the flashback condition. By using the Chorin technique turbulent flow can be computed with and without combustion.

Without combustion large-scale turbulence structures as well as much finer turbulence scales were present (fig. 8). As the Reynolds number increased, the scale of turbulence became finer. Turbulence would be expected to increase with combustion. However, as the temperature rose from 600 to 1600 K the viscosity went up by a factor of 10, so the Reynolds number actually went down. You might then expect that turbulence would decrease.

In a frequency spectrum taken with a high-response pressure transducer just downstream of a typical swirl can combustor, most of the frequencies were below 2000 Hz (fig. 9). Few intense peaks occurred. As the pressure was increased from 700 to 1420 kPa (7 to 14 atm), the Reynolds number and the energy in the higher frequencies increased. In an engine the combustor velocity remains nearly constant and the mass flow increases with pressure. However, with all of the dynamics the turbulence did not change significantly.

The progress being made toward computing turbulence is discussed in detail in references 3 and 4. Reference 3 gives the theoretical background and reference 4 presents the computer program MIMOC used to compute the two-dimensional unsteady flow.

In the MIMOC method two types of finite vortex elements are introduced (fig. 10). A vortex sheet is a line vortex. Sheets are introduced at the wall to satisfy the no-slip boundary condition and to simulate the generation of turbulence at the wall. When a sheet moves out of a boundary layer of thickness δ_s, it becomes a vortex blob and its image. The vortices are moved with a particular variance. The variance of the Gaussian distribution is proportional to the time step and inversely proportional to the Reynolds number. The vortices move a distance ΔZ, which is the sum of the convected distance and the random motion. A reduced-time coordinate system is used. The reduced time τ is the time t multiplied by the inlet channel velocity U_0 and divided by the duct height H. The Reynolds number is also defined in terms of H. The motion of each vortex blob (fig. 11) is computed from the local velocity created by all of the other elements plus the Gaussian random walk.

Comparing the experimental data and the random vortex method shows good agreement for the mean velocities (fig. 12) but poorer agreement for the turbulence intensities normalized by the inlet velocity (fig. 13). Remember that these computations include no turbulence constants but only the turbulence generated by the fundamental equations. Intensity peaks at about 20 to 30 percent in the shear layer for both the nonreacting and reacting flows. The Reynolds number in this comparison is 22 000. For reacting flow the peak in intensity shifted down into the recirculation region and the recirculation region shortened with reaction.

The time history of the calculated velocity at a point in the flow (fig. 14) looks realistic, like the signal from a hot wire. A histogram was made of these points (fig. 15); the distribution looks Gaussian.

When the results were analyzed with a fast Fourier transform (FFT), the frequency spectrum could be plotted (fig. 16). The results are presented in reduced frequency, which is the duct height divided by the inlet velocity. The power is high below 200 Hz, with peaks. Some of the peaks may be caused by the lack of resolution in the calculation. The frequency spectrum rolls off as the experimental data. A power spectral distribution (fig. 17) shows most of the power (75 percent) below a reduced frequency of 1.

The turbulent characteristics of the flow need to be quantified in order to be able to predict transition in turbines. Chorin's method is useful for understanding and predicting vortex flows.

REFERENCES

1. Zimmerman, D.R.: Laser Anemometer Measurements at the Exit of a T63-C20 Combustor. (DDA-RN-79-4, Detroit Diesel Allison; NASA Contract NAS3-21267.) NASA CR-159623, 1979.

2. Seasholtz, Richard G.; Oberle, Lawrence G.; and Weikle, Donald H.: Laser Anemometry for Hot Section Applications. Turbine Engine Hot Section Technology, NASA CP-2289, 1983, pp. 57-67.

3. Ghoniem, A.F.; Chorin, A.J.; and Oppenheim, A.K.: Numerical Modelling of Turbulent Flow in a Combustion Tunnel. Philos. Trans. R. Soc. London, Ser. A, vol. 304, no. 1484, Mar. 9, 1982, pp. 303-325.

4. Ghoniem, Ahmed F.; Marek, Cecil J.; and Oppenheim, Antoni K.: Modeling Interface Motion of Combustion (MIMOC). NASA TP-2132, 1983.

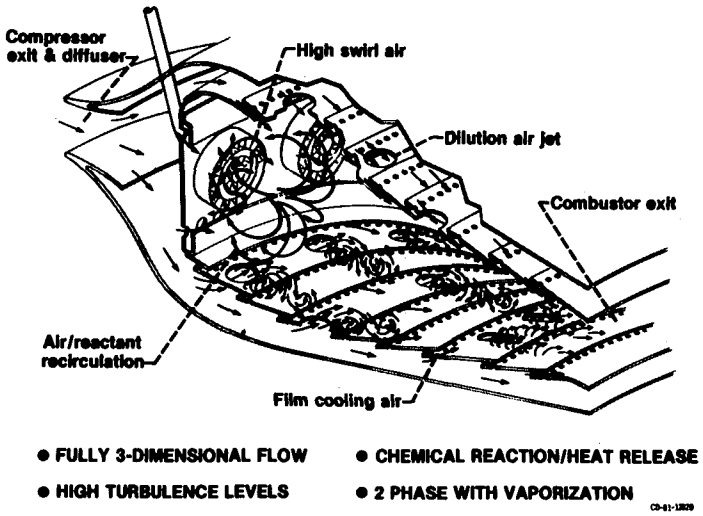

Figure 1. - Combustion flow phenomena.

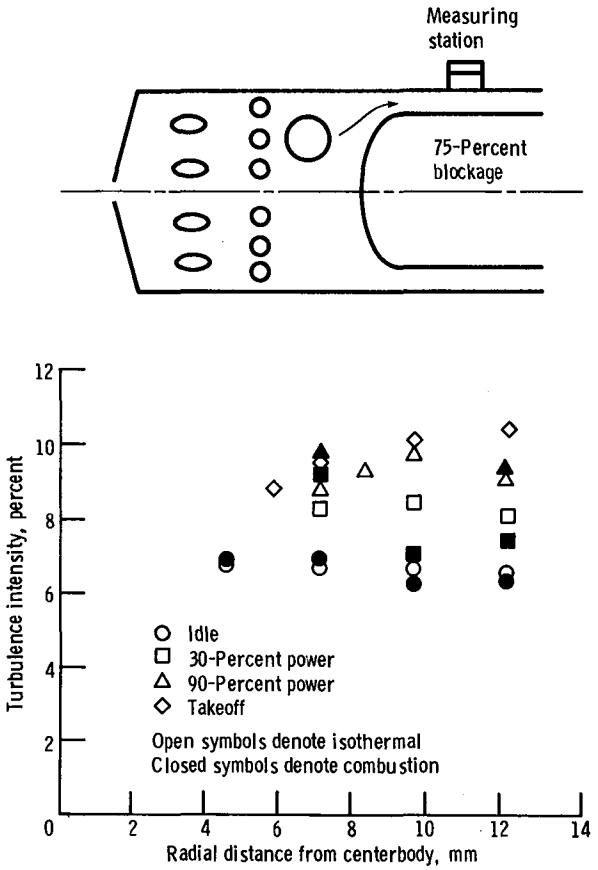

Figure 2. - LDV measurements of turbulence intensity. (From ref. 1.)

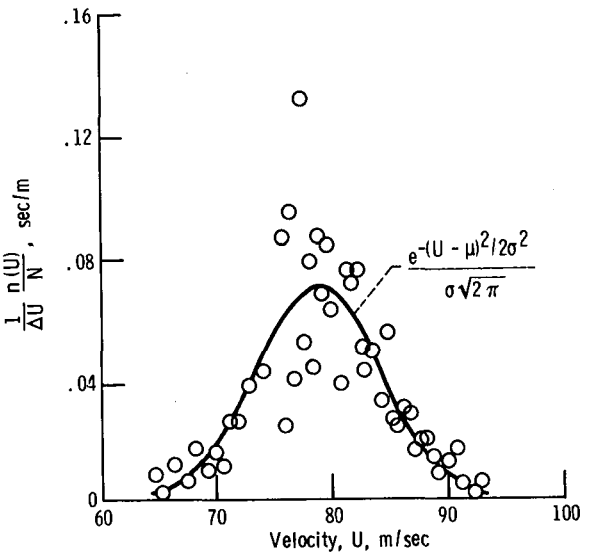

Figure 3. - Determination of turbulence intensity from probability distribution. Flight-idle burning, $r = 7.10$ mm; $\mu = 79.0$ m/s; $\sigma = 5.50$ m/s; $\sigma/\mu = 6.96$ percent; $U_{upper} = 94.0$ m/s; $U_{lower} = 64.0$ m/s; $\langle U \rangle = 79.0$ m/s; $s = 5.61$ m/s; $s/\langle U \rangle = 7.10$ percent; $N = 820$. (From ref. 1.)

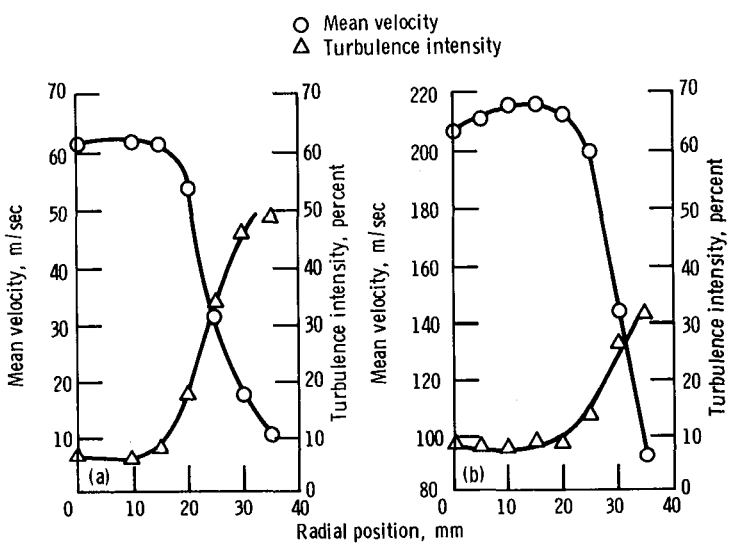

(a) Isothermal. Temperature, 25 °C.
(b) With combustion. Temperature, 780 °C.

Figure 4. - Combustor exhaust measurements. Axial position downstream, 60 mm. (From ref. 2.)

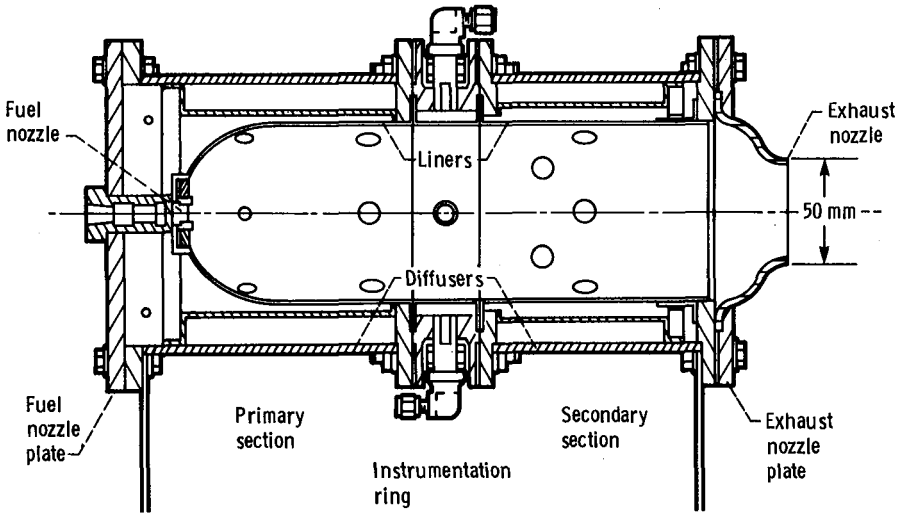

Figure 5. - Laboratory combustor.

CD-85-15972

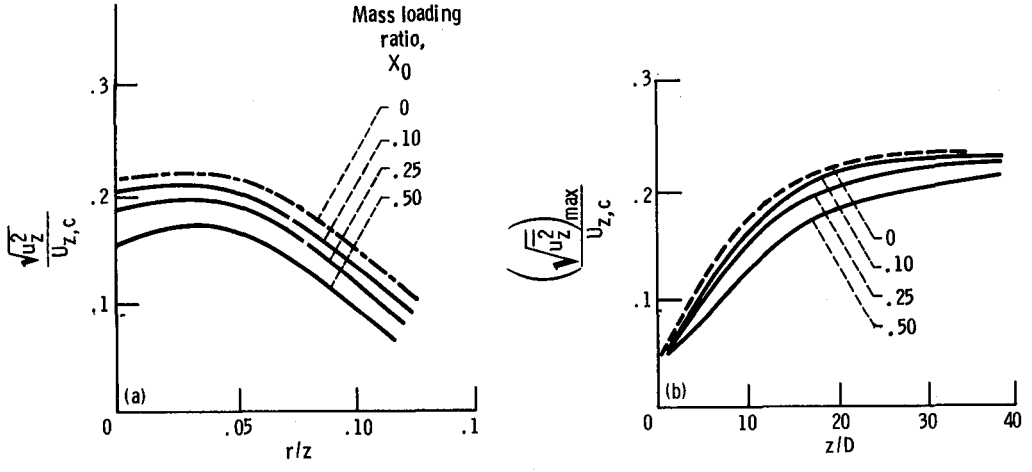

(a) Turbulence intensity distribution at z/D = 20.
(b) Axial distribution of maximum turbulence intensity.

Figure 6. - Turbulence intensity distributions.

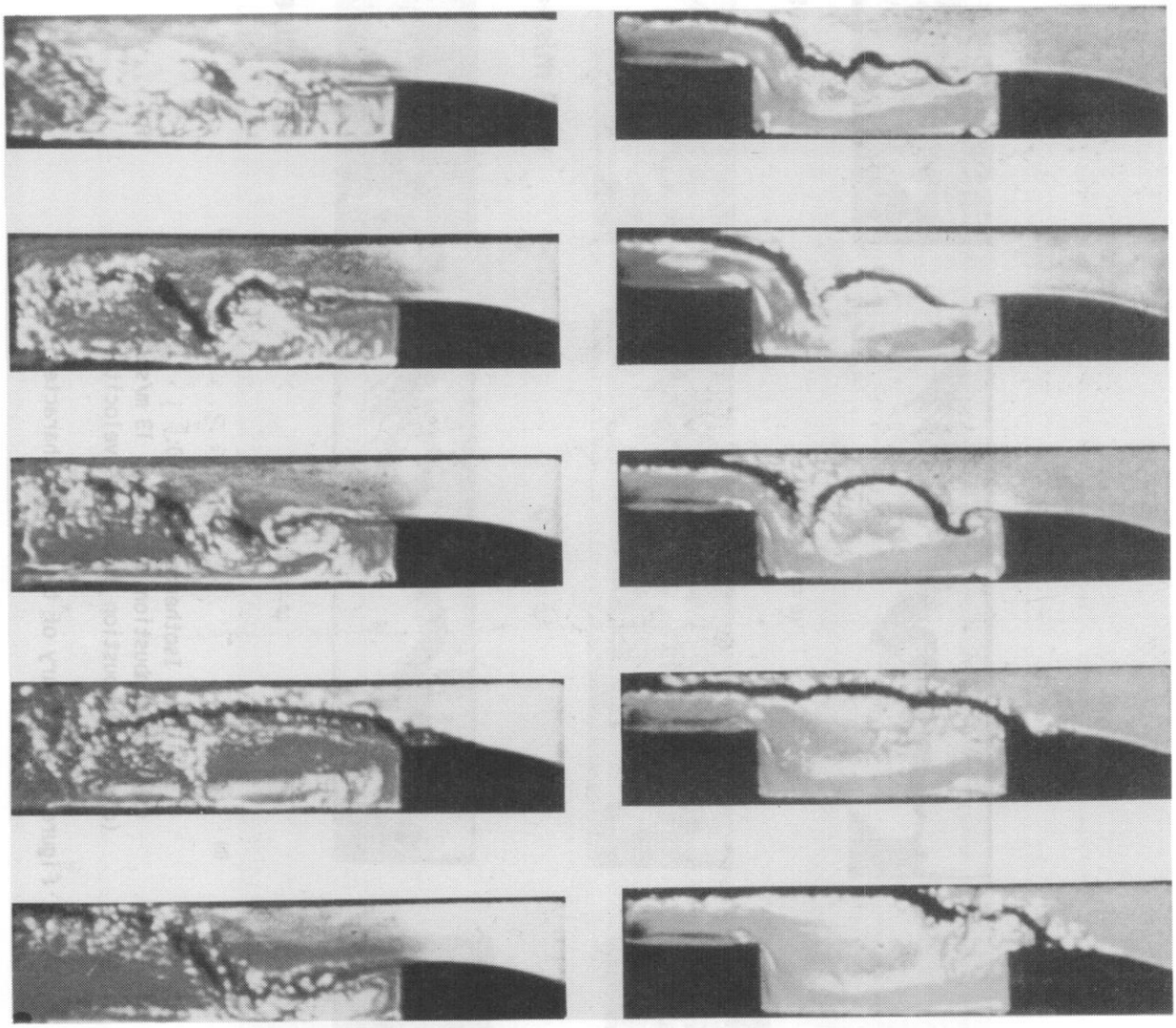

(a) (b)

(a) Sequence 1.
(b) Sequence 2.

Figure 7. - Still photographs of color schlieren motion pictures. (Flow from right to left.)

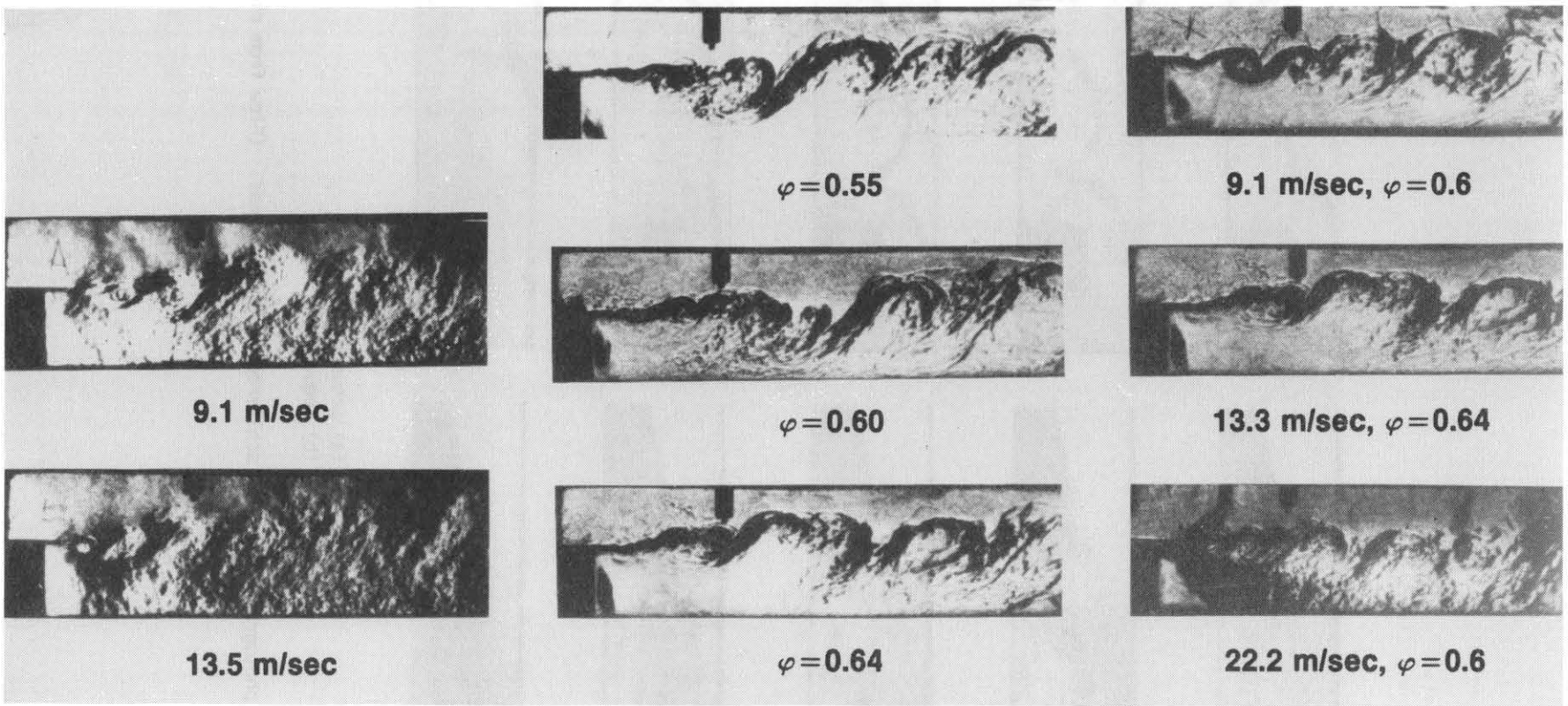

(a) Isothermal; $\varphi = 0$.
(b) With combustion; velocity, 13 m/sec.
(c) With combustion at various velocities.

Figure 8. - Summary of turbulence characteristics.

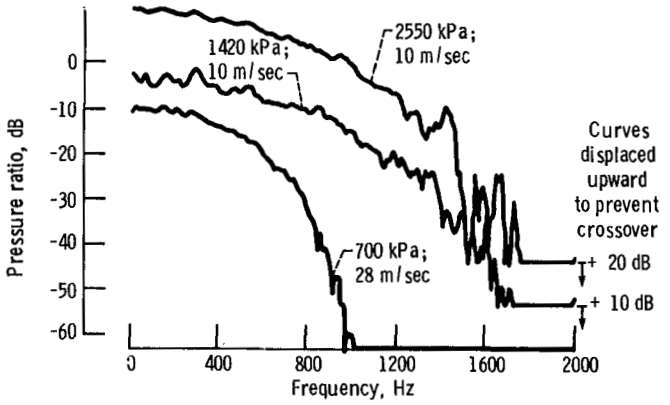

Figure 9. - Frequency spectrum downstream of swirl can combustor. Temperature, 550 K.

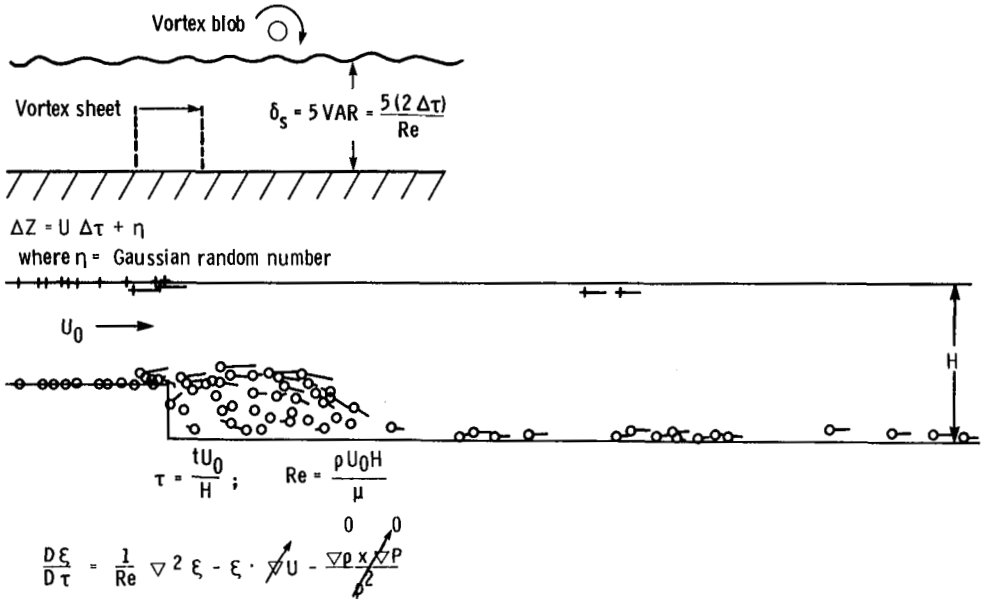

Figure 10. - Modeling interface motion of combustion by Chorin's random vortex method.

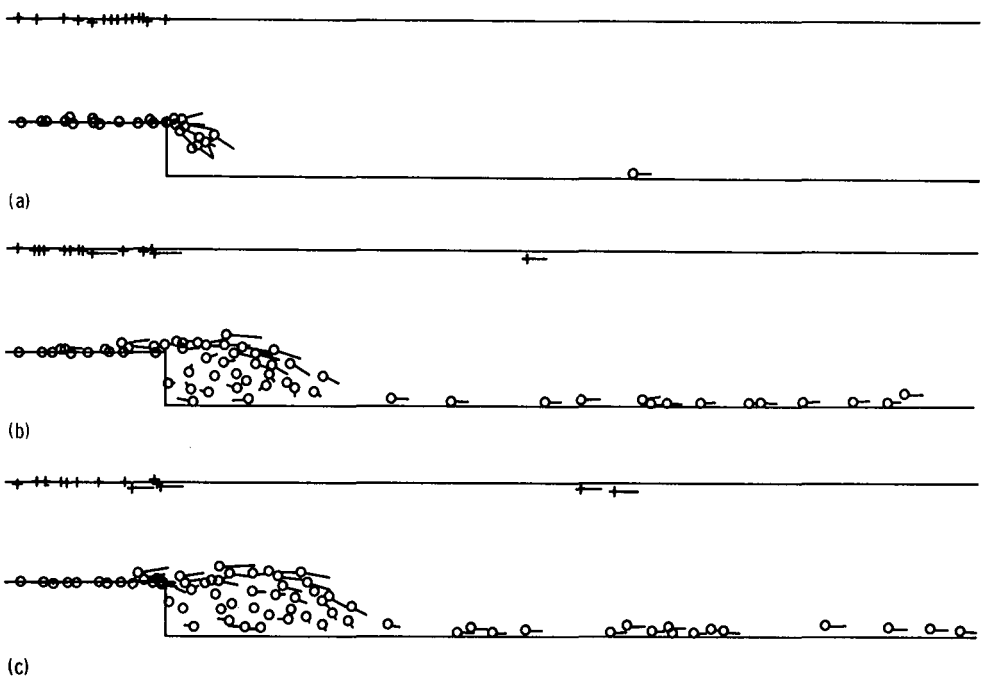

Figure 11. - Motion of vortex blobs computed by Chorin's method. Reynolds number, 10 000.

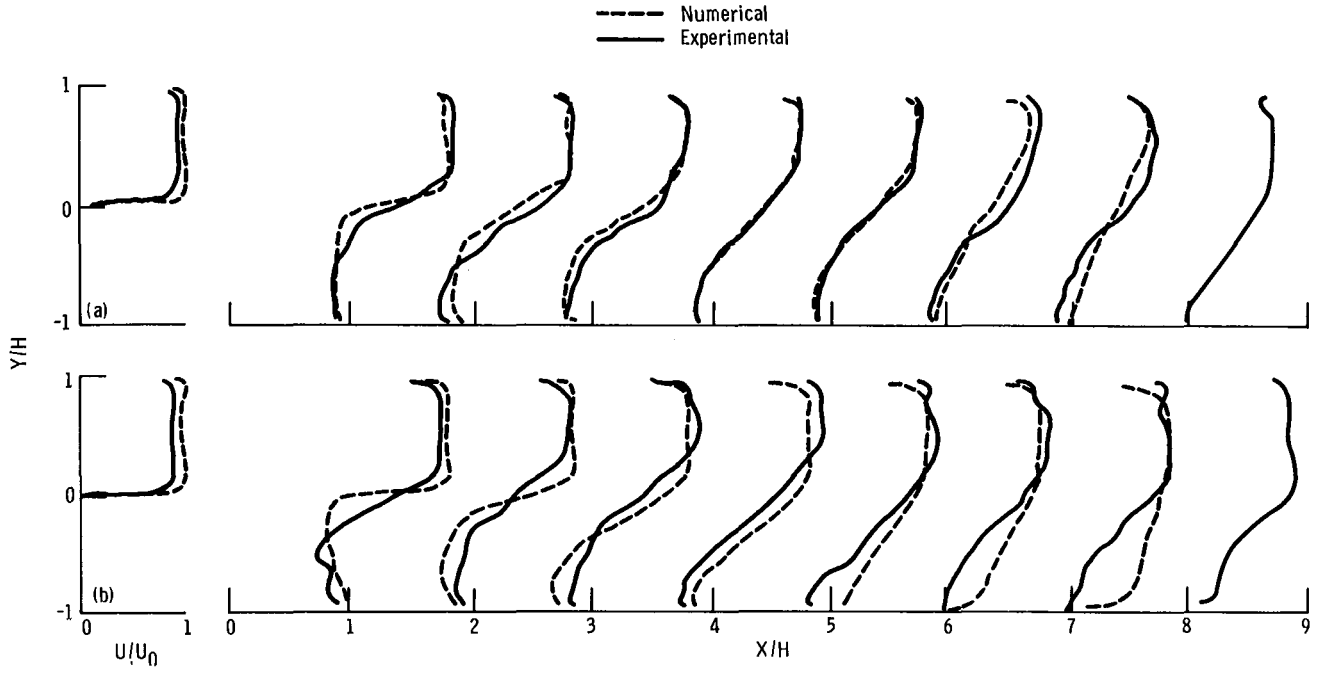

Figure 12. - Comparison of experimental and numerical data for mean velocity.

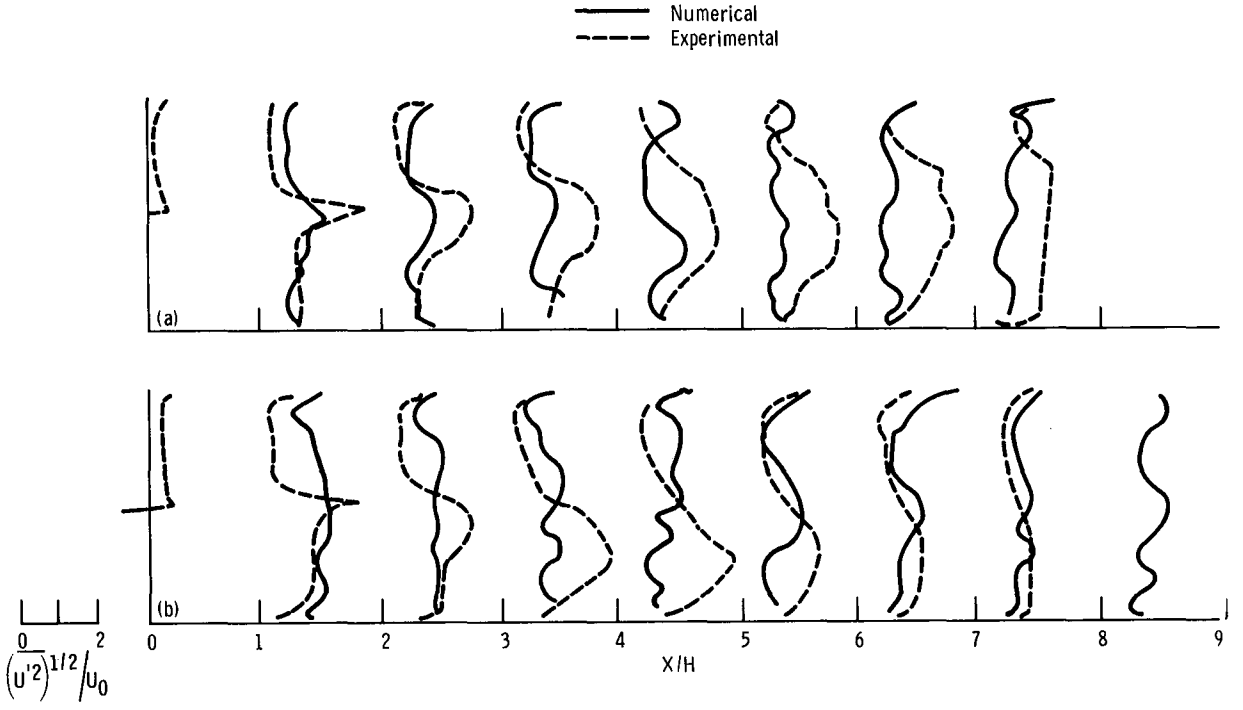

Figure 13. - Comparison of experimental and numerical data for turbulence intensity. (Same configuration as fig. 12.)

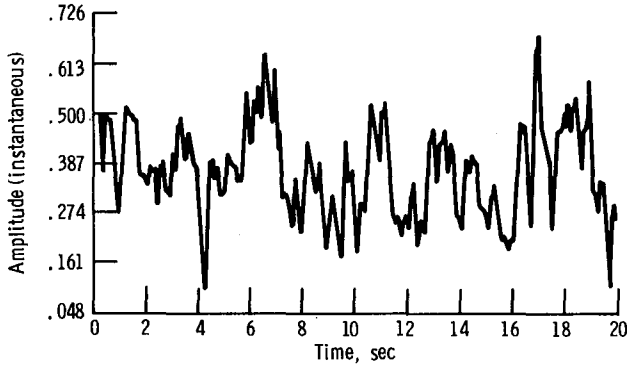

Figure 14. - Instantaneous time history of calculated velocity. x/H = 1.8; Reynolds number, 10 000.

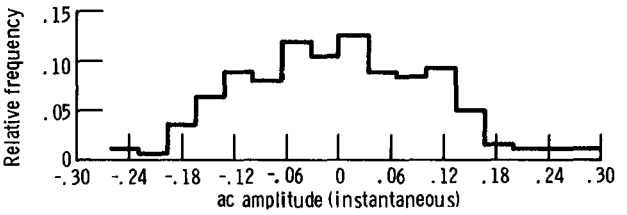

Figure 15. - Computed probability distribution. x/H = 1.8.

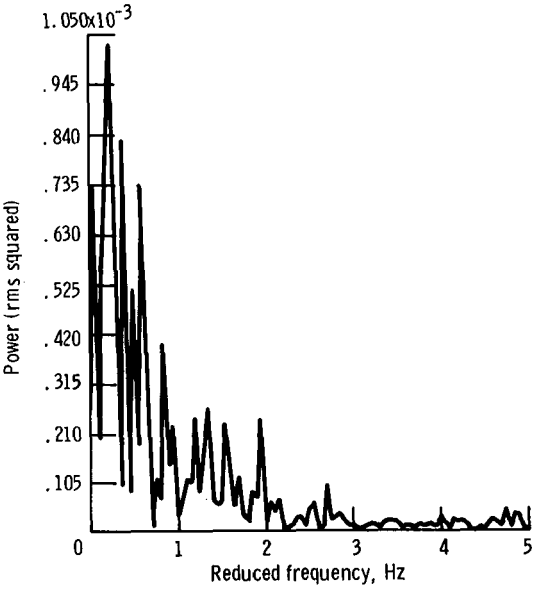

Figure 16. - Computed power spectrum. x/H = 1.8.

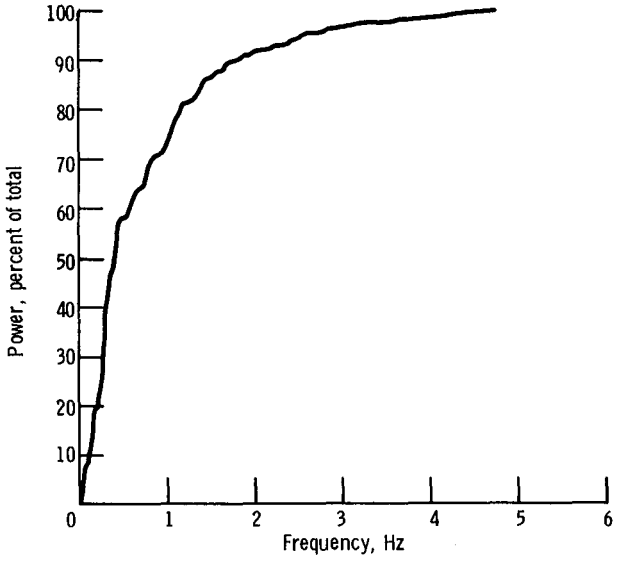

Figure 17. - Power spectral distribution. x/H = 3.6.

PRELIMINARY RESULTS OF A STUDY OF THE RELATIONSHIP BETWEEN FREE-STREAM TURBULENCE AND STAGNATION REGION HEAT TRANSFER*

G. James VanFossen, Jr., and Robert J. Simoneau
National Aeronautics and Space Administration
Lewis Research Center
Cleveland, Ohio 44135

A study is being conducted at the NASA Lewis Research Center to investigate the mechanism that causes free-stream turbulence to increase heat transfer in the stagnation region of turbine vanes and blades. The work is being conducted in a wind tunnel at atmospheric conditions to facilitate measurements of turbulence and heat transfer. The model size is scaled up to simulate Reynolds numbers (based on the leading-edge diameter) that are to be expected on a turbine blade leading edge. Reynolds numbers from 13 000 to 177 000 were run in the present tests.

Spanwise-averaged heat transfer measurements with high and low turbulence have been made with "rough" and smooth surface stagnation regions. For smooth surfaces the boundary layer remained laminar even in the presence of free-stream turbulence. If roughness was added, the boundary layer became transitional as evidenced by the heat transfer increase with increasing distance from the stagnation line.

Hot-wire measurements near the stagnation region downstream of an array of parallel wires showed that vorticity in the form of mean velocity gradients was amplified as the flow approached the stagnation region. Circumferential traverses of a hot-wire probe near the surface of the cylinder showed that the fluctuating component of velocity changed in character depending on free-stream turbulence and Reynolds number.

Finally smoke-wire flow visualization and liquid-crystal surface heat transfer visualization were combined to show that, in the wake of an array of parallel wires, heat transfer was lowest where the fluctuating component of velocity (local turbulence) was highest. Heat transfer was the highest between pairs of vortices where the induced velocity was toward the cylinder surface.

SYMBOLS

D cylinder diameter, cm

d rod diameter, cm

e height of roughness element, cm

h heat transfer coefficient, W/m^2 °C

---

*Also published as NASA Technical Memorandum 86884.

q" heat flux, W/m^2

Re Reynolds number

T temperature, K

X distance measured upstream from forward stagnation line, cm

z spanwise coordinate, cm

θ circumferential coordinate, deg

INTRODUCTION

In gas turbine blade design, predicting heat transfer in the stagnation region is critical because the heat flux is usually highest in this region. The heat transfer in the stagnation region can be predicted if the free-stream flow is laminar (ref. 1). In a gas turbine, flows are highly turbulent, with intensities of 8 to 15 percent. If the turbulence intensity in the free stream is higher than 1 percent, heat transfer in the stagnation region is augmented.

Flow in the stagnation region of a turbine blade can be simulated by a cylinder in crossflow. There have been many experimental investigations of the effect of turbulence intensity on heat transfer to a cylinder in crossflow (e.g., refs. 2 to 6). Most of these investigations have measured an increase in heat transfer in the stagnation region for some increased level of free-stream turbulence and then tried to correlate the heat transfer increase to some parameter involving the turbulence intensity. This approach has had limited success. Trends are clearly present, but there is great scatter in the data, particularly between the data of different researchers.

The mathematical modeling of stagnation region flow has been divided into several areas. One set of modelers has attempted to develop a turbulence model that can be used to solve the two-dimensional boundary-layer equations and predict the level of heat transfer (refs. 2, 7, and 8). The results are a correlation of the mixing length or turbulent viscosity and the Prandtl number with other flow parameters.

A more plausible model of heat transfer augmentation by free-stream turbulence is the vortex stretching model. It is hypothesized that, as vortical filaments with components of their axes normal to the stagnation line and normal to the free-stream flow are convected into the stagnation region, they are stretched and tilted by the divergence of streamlines and acceleration around the body. Through conservation of angular momentum this stretching intensifies the vorticity. The increased vorticity is hypothesized to be the cause of the augmented heat transfer in the stagnation region. Some examples of the work on this theory are given in references 9 to 14, and the work is reviewed in reference 15. It was deduced (refs. 9 and 10) that the mathematical model allowed only turbulent eddies above a certain neutral scale to enter the Hiemenz flow (ref. 16) boundary layer. Once inside the boundary layer, however, the eddies can be broken down into smaller eddies by the action of viscosity. The three-dimensional vorticity transport equations were

solved for a free-stream velocity that was periodic in the spanwise coordinate. This boundary condition supplied the vorticity to the stagnation region in an orientation that allowed it to be stretched by the mean flow. A few special cases where the period in velocity was near the neutral scale have been solved. It was found that the thermal boundary layer is much more sensitive to external vorticity than the hydrodynamic boundary layer.

In reference 11 measurements of grid turbulence that contained eddies of all orientations near the stagnation point of a circular cylinder show that eddies with scales much larger than the cylinder diameter are not amplified as they approach the stagnation point but smaller scale eddies are amplified as they approach the cylinder. These measurements are external to the boundary layer. In references 12 and 13 a hot wire was used to measure the amplification of turbulence near the stagnation point of both a cylinder and an airfoil. The turbulence was produced by an upstream array of parallel rods. Spectral measurements were then used to deduce a so-called most-amplified scale. Flow visualization with smoke also shows a regular array of vortex pairs near the stagnation point. The array of vortex pairs is clearly outside the theoretical laminar boundary layer.

Reference 14 describes a threshold for vortex formation near the stagnation region of a bluff body from the wakes of an array of parallel wires placed upstream. If the wires are too far upstream or the Reynolds number is too small, no vortices are formed on a bluff body. Heat transfer augmentation in the stagnation region increases sharply when vortices are formed. The size of the vortices scales with the width of the upstream disturbance wake and not with boundary-layer thickness.

Calculations and measurements made in reference 5 show the boundary-layer velocity profiles to be essentially laminar even in the presence of free-stream turbulence. The temperature field, however, is more sensitive to free-stream turbulence. This implies that heat transfer will be increased more than skin friction by free-stream turbulence.

A collection of experimental observations has been assembled here to construct a picture of this complex phenomenon. Spanwise-averaged heat transfer data are presented to show the effect of free-stream turbulence and surface roughness on the condition (laminar or turbulent) of the thermal boundary layer. Hot-wire measurements are used to show how vorticity from mean velocity gradients is amplified as it approaches the stagnation region. Finally a combination of flow visualization using the smoke-wire technique and thermal visualization using liquid crystals is used to show the relationship between vortex pairs produced by mean velocity gradients and the spanwise heat transfer distribution.

APPARATUS

Wind Tunnel

All tests were conducted in the wind tunnel shown schematically in figure 1. Room air first flowed through a turbulence damping screen with an 18x18 mesh of 0.24-mm (0.0095-in) diameter wire. Large-scale turbulence from the room air was then broken up by flowing it through a honeycomb of approximately 12 000 plastic "soda straws," which were 0.64 cm (0.25 in) in

diameter by 19.69 cm (7.75 in) long. The air then passed through a final damping screen identical to the first. A 4.85:1 contraction (contraction in spanwise direction only) then accelerated the air entering the test section. The maximum velocity attainable in the test section was about 46 m/sec (150 ft/sec), and the clear-tunnel turbulence level was less than 0.5 percent at all flow rates.

The test section was 15.2 cm (6.0 in) wide by 68.6 cm (27.0 in) high. The models were mounted horizontally in the tunnel. Hot-wire surveys and smoke-wire flow visualization indicated that the center 7.6 cm (3.0 in) of the tunnel was free from turbulence generated by the side-wall boundary layer. All measurements were confined to this center region of the tunnel test section.

After leaving the test section the flow passed through a transition section into a 25-cm (10-in) pipe, through two long-radius elbows, into a flow straightener, and into an orifice run. The orifice plate had a diameter of 19.1 cm (7.5 in). The flow rates used in these tests were measured with this orifice. Air then passed through a 25-cm (10-in) butterfly valve, which was used to control the flow rate, and then to the building altitude exhaust system.

The temperature of the air entering the wind tunnel was measured by four exposed ball Chromel-Alumel thermocouples around the perimeter of the inlet. These four temperatures were averaged to give the total (or stagnation) temperature.

Turbulence Generators

For some of the high-turbulence cases a turbulence-generating biplane grid of 0.318-cm (0.125-in) diameter rods spaced 10 rod diameters apart was installed 79.6 rod diameters upstream of the model leading edge. For the flow visualization tests and some of the heat transfer tests an array of parallel 0.051-cm (0.020-in) diameter wires spaced 12.5 wire diameters apart was installed 547.5 wire diameters (4.21 cylinder diameters) upstream of the model leading edge. For the spanwise hot-wire traverses the same parallel-wire array was used, but the wires were spaced 37.5 wire diameters apart.

Hot Wire

Turbulence was measured with a constant-temperature, hot-wire anemometer. Signals were linearized, and the mean component of velocity was read on an integrating digital voltmeter with an adjustable time constant. The fluctuating component was read on a true rms voltmeter that also had an adjustable time constant. The hot-wire probe was a 4-μm (1.65-μin) diameter, tungsten, single-wire probe. The hot wire was calibrated before each use in a free jet of air at nearly the same temperature ($\pm$1 deg C) as the wind tunnel flow. The frequency response of the hot-wire system was determined to be around 30 kHz by the standard square-wave test.

Turbulence scale was estimated by using an autocorrelation of the hot-wire signal. The autocorrelation was obtained on a dual-channel, fast Fourier transform (FFT) spectrum analyzer. The area under the autocorrelation

function gave an integral time scale. This time scale was then multiplied by the mean velocity to obtain the integral length scale.

Smoke Wire

Flow visualization was accomplished by using the smoke-wire technique described in reference 17. A 0.008-cm (0.003-in) diameter wire was stretched across the tunnel parallel to the cylinder axis slightly below the stagnation plane. The wire was coated with oil, as recommended in reference 17, by using a cotton swab. A timing circuit was then used to start current flow to heat the wire and vaporize the oil and, after an adjustable delay, to fire a strobe light to expose the film. A 35-mm camera with telephoto lens and closeup attachments was then used to make high-quality images of the flow and heat transfer patterns in the stagnation region. Two strobe lights were used, one from each side of the tunnel. The best lighting angle for smoke visualization was 90° from the viewing angle. This angle was not an optimum angle for the viewing of the liquid-crystal models. As explained in reference 18, if the lighting angle and the viewing angle are not the same, there is a color shift in the liquid crystal. Thus simultaneous smoke and liquid-crystal thermal visualization photographs can only be used to obtain qualitative heat transfer results.

TEST SPECIMENS

Spanwise-Averaged Heat Transfer

Spanwise-averaged heat transfer coefficients were measured on a 6.6-cm (2.6-in) diameter cylinder (fig. 2). The cylinder was 15.2 cm (6 in) long and was made of wood. Heat transfer coefficients around the circumference of the cylinder were measured with electrically heated copper strips (fig. 3). Each strip was 6.6 cm (2.6 in) long by 0.51 cm (0.21 in) wide and 0.318 cm (0.125 in) deep. A Kapton-encapsulated electric heater was fastened to the back of each copper strip with pressure-sensitive adhesive. A stainless steel sheathed, closed, grounded-ball, Chromel-Alumel thermocouple was soft soldered into a groove in each copper strip. The copper heat flux gauges were embedded in the surface of the cylinder at 10° intervals around the circumference. The average gap between copper strips was 0.10 cm (0.04 in) and was filled with epoxy. Although there were eight copper strips, only the inner six strips were used as measuring gauges; the outer two served as guard heaters to minimize heat loss by conduction. Guard heaters were also used on the ends of the copper strip gauges (fig. 2). A guard heater was also used behind the measuring gauges to stop radial heat conduction to the rear of the cylinder. A thin coat of lacquer was sprayed on the surface of the cylinder and the copper gauges to keep the copper from oxidizing and changing emissivity. In operation the copper strips were maintained at a constant temperature by a controller described in reference 19. The data reduction technique used for the spanwise-averaged model is also described in reference 19.

For some of the tests, the spanwise-averaged heat transfer model was used to investigate the effect of surface roughness. A coat of clear lacquer was sprayed onto the model, and sand was then sprinkled on the wet surface from an ordinary salt shaker. Another thin coat of lacquer then held the sand in place. Since the roughness elements were too large to be measured with a

profilometer, an optical comparator was used to estimate roughness. The maximum height of any one roughness element was 0.0572 cm (0.0225 in). The average height of the roughness elements above the surface was 0.033 cm (0.013 in), which gave a relative roughness e/D of 0.005.

An afterbody was used with the cylinder for some tests to eliminate the alternate vortex shedding from the rear of the cylinder. The afterbody consisted of a 5.08-cm (2.0-in) long straight segment that was tangent to the cylinder surface 90° from the stagnation line. A 10° wedge then extended downstream and ended in a cylindrical trailing edge 0.3175 cm (0.125 in) in diameter.

Liquid-Crystal Models

Spanwise variations in heat transfer coefficient were mapped with three models (fig. 4). One was a cylinder with the same dimensions as the spanwise-averaged heat transfer model. The second had the same dimensions as the spanwise-averaged model plus the afterbody. The third was scaled to one-half the size of the spanwise-averaged model plus the afterbody.

All of the liquid-crystal models were constructed by using the techniques in reference 18. Briefly, a heater element consisting of polyester sheet with a vapor-deposited gold layer was fastened to the model surface with double-sided tape. Bus bars of copper foil were fastened to the heater edges, which were parallel to the cylinder axis and located at the rear of the cylinder. Silver conductive paint was used to improve electrical conductance between the copper foil and the gold. A commercially available plastic sheet containing cholesteric liquid crystals was fastened over the heater with double-sided tape.

The gold heater was checked for uniformity in still air by using the liquid-crystal sheets to monitor temperature gradients. The liquid crystal was calibrated in a water bath to determine the temperature that corresponded to color. Yellow indicated a temperature of 54.8 $\pm$ 0.2 °C (130.6 $\pm$ 0.4 °F).

In operation, the cylinder was heated by passing an electric current through the gold film. This supplied a uniform heat flux at the surface of the cylinder. Electric power to the model was adjusted so that the area of interest on the surface turned yellow. Neglecting radiation and conduction losses, which are small, the heat transfer coefficient can be computed as

$$h = \frac{q''}{T_{yellow} - T_{air}}$$

Thus yellow traces an iso-heat-transfer coefficient contour on the model.

Traversing Cylinder

Turbulence measurements near the surface of the cylinder were made with a traversing cylinder (fig. 5). This cylinder was made of wood and had a hole drilled along a diameter. A hot-wire probe could be inserted through this hole and positioned close to the surface. The area around the hot-wire probe

was filled in with modeling clay to match the contour of the cylinder. The traversing cylinder extended through holes in the tunnel walls; felt was used as a seal between the cylinder and the walls. The cylinder could thus be traversed axially across the tunnel span or rotated about its axis, carrying the hot wire with it.

ERROR ANALYSIS

An error analysis was performed for each of the spanwise-averaged heat transfer data points by the method of Kline and McClintock (ref. 20). The average error for all of the data points was 5.7 percent, and the maximum error for any one data point was 7.8 percent. Error estimates were not made for the hot-wire and liquid-crystal data.

RESULTS AND DISCUSSION

In this section spanwise-averaged heat transfer distributions around a circular cylinder in cross flow, are presented for high and low free-stream turbulence as well as the effect of surface roughness. Hot-wire measurements are presented to demonstrate amplification of vorticity in the free stream as the flow approaches the stagnation region. Finally, flow visualization and thermal visualization are combined to show the relationship between vortex pairs formed in the stagnation region and spanwise variations in surface heat transfer.

Spanwise-Averaged Heat Transfer

Nusselt number as a function of angle from the stagnation point was determined for the four cases (fig. 6). All of the data were taken at a Reynolds number of 177 000 (based on free-stream conditions and cylinder diameter). Low-turbulence data were taken with a clear tunnel and high-turbulence data were taken with a biplane grid. The grid produced turbulence of about 2.4 percent with a scale of 0.50 cm (0.20 in). Also plotted on the figure is an exact solution of the laminar boundary-layer equations due to reference 1. The data shown on figure 6 were for the cylinder without the afterbody; data taken with the afterbody in place were identical within experimental error.

Smooth surface - low turbulence. - The agreement between the exact solution and the smooth-cylinder, low-turbulence data is well within the experimental error and thus confirms the accuracy of the experimental method (fig. 6).

Smooth surface - high turbulence. - For the cylinder placed downstream of the biplane grid (fig. 6) turbulence increased the heat transfer virtually uniformly around the circumference (measurements were only made up to 50° from stagnation) by about 30 percent. This agrees well with the data of other observers: for example, the theory of reference 2 predicts an increase in Nusselt number at the stagnation point of 27.8 percent for these conditions.

Rough surface - low turbulence. - Adding sand roughness to the cylinder surface with 0.5-percent free-stream turbulence did not change the heat

transfer rate at the stagnation point from the smooth-surface case (fig. 6). As the angle from stagnation increased, however, the heat transfer rate also increased, most likely because boundary-layer transition was triggered by the roughness elements.

Rough surface - high turbulence. - For the sand-roughened surface with 2.4-percent free-stream turbulence the effect of free-stream turbulence was greatest nearest the stagnation point, where the heat transfer rate was again about 30 percent higher than in the low-turbulence case. As the angle from stagnation became larger, the high- and low-turbulence data (rough surface) merged as the boundary layer became more turbulent.

Surface roughness had no effect on heat transfer at the stagnation line but changed the character of the boundary layer in the downstream direction. It seems that the boundary layer on the smooth surface remains laminar at the Reynolds numbers tested (i.e., no turbulence is produced within the boundary layer). Free-stream turbulence somehow acts on a laminar boundary layer to augment heat transfer.

Hot-Wire Measurements

Streamwise traverse. - A streamwise traverse of a single hot wire was performed with the wire oriented parallel to the 6.6-cm (2.6-in) diameter cylinder axis and as close as possible to the plane of the stagnation streamline. An array of 0.05-cm (0.02-in) parallel wires spaced 12.5 wire diameters apart was located 4.21 cylinder diameters (547.5 wire diameters) upstream of the stagnation point. This wire array produced vorticity (gradients in the mean velocity) in an orientation that could be stretched and amplified. The traverse was made 0.044 to 3.06 cylinder diameters upstream of the stagnation point at a Reynolds number of 177 000 (based on cylinder diameter). It is typical of all traverses made over the Reynolds number range (31 000 to 177 000). The mean velocity (fig. 7) fell monotonically as the stagnation region was approached. The fluctuating velocity (rms, fig. 7), however, first decayed with distance downstream of the grid (decreasing X/D) and then sharply increased and peaked at about 0.085 cylinder diameter upstream from the stagnation point. This peak was far outside the predicted laminar boundary-layer thickness of 0.003 cylinder diameter (ref. 16). These results are very similar to those of reference 12.

Spanwise traverse. - Two spanwise traverses of a hot wire oriented perpendicular to the cylinder axis and centered in the plane of the stagnation streamline were made. The cylinder leading edge was located 4.21 cylinder diameters downstream of an array of 0.05-cm (0.02-in) diameter parallel wires spaced 37.5 wire diameters apart. Both traverses were made at a Reynolds number of 31 000 (based on cylinder diameter) and are typical of those for the complete Reynolds number range. Both traverses are presented at the same scale in figure 8. For the traverse taken at 1.06 cylinder diameters upstream from the stagnation line, the wire wakes are clearly visible in the mean velocity trace. The turbulent fluctuations are high in the wire wakes and low in the relatively undisturbed flow between wires. At 0.095 cylinder diameter upstream the mean velocity greatly decreased, but the depth of the wake increased, an indication of increasing vorticity as the stagnation region was approached. The fluctuating component of velocity also increased in the wire wakes as the stagnation region was approached.

Circumferential traverses. - A hot wire oriented parallel to the cylinder axis and located 0.012 cylinder diameter from the cylinder surface was traversed in the circumferential direction $\pm 21°$ at a Reynolds number of 125 000 (based on cylinder diameter). For the clear tunnel (fig. 9(a); i.e., free-stream turbulence intensity less than 0.5 percent), the mean velocity increased with angle from stagnation as the flow accelerated around the body, and the fluctuating component of velocity was lowest at the stagnation point. This functional form of the fluctuating velocity with angle was independent of Reynolds number for all flows tested with the clear tunnel. For an array of parallel 0.05-cm (0.02-in) diameter wires spaced 12.5 wire diameters apart and located 547.5 wire diameters upstream of the stagnation line (fig. 9(b)), the mean velocity trace was identical to that for the clear tunnel, but the fluctuating velocity had completely changed. The minimum at the stagnation line in the clear tunnel changed to a maximum, and the level away from the stagnation region decreased. The large variations in fluctuating velocity with angle in the clear tunnel were damped. This change in character was Reynold-number dependent: below a Reynolds number of 95 000 (based on cylinder diameter; 730 based on wire diameter), the fluctuating velocity was at a minimum at the stagnation point with or without a wire array (fig. 9(a)). Above a Reynolds number of 95 000 the fluctuating velocity looked like figure 9(b). We have no explanation for this phenomenon.

Simultaneous Flow - Thermal Visualization

The smoke-wire flow visualization and liquid-crystal thermal visualization techniques were combined to show the relationship between spanwise variations in heat transfer and vortices in the stagnation region. These vortices were formed from the wakes of wires placed upstream of the cylindrical leading edge and arranged as shown in figure 5. The leading-edge region for the 6.6-cm (2.6-in) diameter cylindrical-leading-edge model with afterbody taken at a Reynolds number of 13 000 is shown in figure 10. The Reynolds number for the wires was about 100; for wire Reynolds numbers less than 120 the wakes were laminar (i.e., no Karman trails were formed). The dark lines on the surface of the model were drawn in a 1.27-cm (0.5-in) square grid pattern for visual scaling. The model and relative camera position are shown in figure 11.

The smoke shows that a vortex pair formed from the wake of each wire. The vortices were well outside the theoretical laminar boundary layer. The dark, vertical stripes in the liquid crystal were regions of low temperature and thus high heat transfer. Thus, contrary to expectations, the regions of highest heat transfer were not under the vortices but between vortex pairs, where the free-stream turbulence was lowest. In this region the induced velocity from neighboring vortex pairs was directed toward the cylinder surface. Conversely, the region of minimum heat transfer was directly under the vortex pair. This was the region of highest free-stream turbulence as measured by a hot wire outside the boundary layer. Figure 12 shows schematically the spatial relationship of the wires, wakes, vortex pairs, and the peaks in heat transfer.

The heat transfer - vortex pattern was the same for all three models used (fig. 4). It was the same for the cylinder without the afterbody as for cylinder with the afterbody. The half-scale model with the afterbody also had the same heat transfer pattern, but the vortices appeared smaller in diameter

at the same free-stream velocity. The spanwise spacing of vortex pairs remained equal to the wire spacing. The Reynolds number for the half-scale model was one-half that for the large cylinder with the afterbody.

For the half-scale model the spanwise heat transfer coefficient varied along the stagnation line (i.e., (maximum h - minimum h)/0.5 (maximum h + minimum h)) from 7 percent at a Reynolds number of 16 000 to 16 percent at a Reynolds number of 89 000. This is the magnitude found for spanwise variations in mass transfer caused by periodic irregularities in a screen (ref. 21). Such measurements were not made for the other models.

High-speed motion pictures of smoke near the stagnation point of the cylinder without the afterbody were taken at a Reynolds number of 13 000. Vortices still were formed in the stagnation region, but the stagnation point oscillated because of alternate vortex shedding from the rear of the cylinder.

Vortices were only visible for Reynolds numbers less than about 120 (based on wire diameter). At higher Reynolds numbers the wire wakes became unstable and finally fully turbulent, making it impossible to see the vortices. The heat transfer pattern, however, remained unchanged at all Reynolds numbers, indicating that the vortices must still be there although they could not be seen. A time-exposure photograph was taken in the hope that the random fluctuations from the wire wakes would be averaged out and the relatively steady vortex pattern would thus be made visible. The random fluctuations were indeed averaged out, but no steady vortices could be seen.

SUMMARY OF RESULTS

This report has presented preliminary results of a study to investigate the relationship between free-stream turbulence and heat transfer augmentation in the stagnation region. The effects of free-stream turbulence and surface roughness on spanwise-averaged heat transfer were investigated. Turbulence was measured upstream of a cylinder placed in the wake of an array of parallel wires that were perpendicular to the cylinder axis. Finally, flow visualization and thermal visualization techniques were combined to show the relationship between vortices in the stagnation region and spanwise variations in heat transfer.

The major conclusions were as follows:

1. Surface roughness has no effect on heat transfer at the stagnation point.

2. Free-stream turbulence has the same effect on heat transfer at the stagnation point for smooth and rough cylinders.

3. The boundary layer downstream of the stagnation point remains laminar in the presence of free-stream turbulence and is forced into transition by surface roughness for the range of Reynolds numbers and turbulence levels tested.

4. Vorticity in the form of mean velocity gradients is amplified as it approaches the stagnation region.

5. Turbulent fluctuating velocity is amplified as it approaches the stagnation region, reaches a peak, and then is damped as it approaches the boundary layer.

6. Heat transfer in the stagnation region is highest where the turbulent fluctuations are lowest. This occurs between the wakes formed by parallel wires upstream and perpendicular to the axis of the cylinder. This corresponds to the region between vortex pairs, where the velocity induced by the vortices is toward the cylinder surface. Conversely, the lowest heat transfer occurs where the induced velocity is away from the cylinder surface.

7. Vortices formed in the stagnation region from mean velocity gradients are well outside the theoretical laminar boundary layer.

REFERENCES

1. Frossling, N., "Evaporation, Heat Transfer, and Velocity Distribution in Two-Dimensional and Rotationally Symmetrical Laminar Boundary-Layer Flow," NACA TM-1432, 1958.

2. Smith, M.C., and Kuethe, A.M., "Effects of Turbulence on Laminar Skin Friction and Heat Transfer," Physics of Fluids, Vol. 9, No. 12, Dec. 1966, pp. 2337-2344.

3. Kestin, J., and Wood, R.T., "The Influence of Turbulence on Mass Transfer from Cylinders," Journal of Heat Transfer, Vol. 93, No. 11, Nov. 1971, pp. 321-327.

4. Giedt, W.H., "Effect of Turbulence Level of Incident Air Stream on Local Heat Transfer and Skin Friction on a Cylinder," Journal of the Aeronautical Sciences," Vol. 18, No. 11, Nov. 1951, pp. 725-730, 766.

5. Hanarp, L.R., and Sunden, B.A., "Structure of the Boundary Layers on a Circular Cylinder in the Presence of Free Stream Turbulence," Letters in Heat and Mass Transfer, Vol. 9, May-June 1982, pp. 169-177.

6. Lowery, G.W., and Vachon, R.I., "Effect of Turbulence on Heat Transfer from Heated Cylinders," International Journal of Heat and Mass Transfer, Vol. 18, No. 11, Nov. pp. 1229-1242.

7. Wang, C.R., "Turbulence and Surface Heat Transfer Near the Stagnation Point of a Circular Cylinder in Turbulent Flow," NASA TM-83732, 1984.

8. Gorla, R.S.R., and Nemeth, N., "Effects of Free Stream Turbulence Intensity and Integral Length Scale on Heat Transfer From a Circular Cylinder in Crossflow," U. Grigull, et al., eds., Heat Transfer 1982, Vol. 3, Hemisphere Publishing Corp., Washington, D.C., 1982, pp. 153-158.

9. Sutera, S.P., Maeder, P.F., and Kestin, J., "On the Sensitivity of Heat Transfer in the Stagnation-Point Boundary Layer to Free-Stream Vorticity," Journal of Fluid Mechanics, Vol. 16, Part 4, Aug. 1963, pp. 497-520.

10. Sutera, S.P., "Vorticity Amplication in Stagnation-Point Flow and Its Effect on Heat Transfer, Journal of Fluid Mechanics, Vol. 21, Part 3, Mar. 1965, pp. 513-534.

11. Britter, R.E., Hunt, J.C.R., and Mumford, J. C., "The Distortion of Turbulence by a Circular Cylinder," Journal of Fluid Mechanics, Vol. 92, Part 2, May 28, 1979, pp. 269-301.

12. Sadeh, W.Z., and Brauer, H.J., "Coherent Substructure of Turbulence Near the Stagnation Zone of a Bluff Body," Journal of Wind Engineering and Industrial Aerodynamics, Vol. 8, No. 1-2, July 1981, pp. 59-72.

13. Sadeh, W.Z., and Sullivan, P.P., "Turbulence Amplification in Flow About an Airfoil," ASME Paper 80-GT-111, Mar. 1980.

14. Hodson, P.R., and Nagib, H.M., "Vortices Induced in a Stagnation Region by Wakes-Their Incipient Formation and Effects on Heat Transfer from Cylinders," AIAA Paper 77-790, June 1977.

15. Morkovin, M.V., "On the Question of Instabilities Upstream of Cylindrical Bodies," NASA CR-3231, 1979.

16. Schlichting, H., "Boundary Layer Theory," 4th ed., McGraw Hill, p. 78.

17. Jansen, B.J. Jr., "Flow Visualization Through the Use of the Smoke Wire Technique," AIAA Paper 81-0412, Jan. 1981.

18. Hippensteele, S.A., Russell, L.M., and Stepka, F.S., "Evaluation of a Method for Heat Transfer Measurements and Thermal Visualization Using a Composite of a Heater Element and Liquid Crystals," Journal of Heat Transfer, Vol. 105, No. 1, Feb 1983, pp. 184-189.

19. VanFossen, G.J., et al., "Heat Transfer Distributions Around Nominal Ice Accretion Shapes Formed on a Cylinder in the NASA Lewis Icing Research Tunnel," AIAA Paper 84-0017, Jan. 1984.

20. Kline, S.J., and McClintock, F.A., "Describing Uncertainties in Single-Sample Experiments," Mechanical Engineering, Vol. 75, No. 1, Jan. 1953, pp. 3-8.

21. Marziale, M.L., and Mayle, R.E., "Mass Transfer From a Circular Cylinder-Effects of Flow Unsteadiness and 'Slight Nonuniformities'," Rensselaer Polytechnic Institute, Troy, New York, Sept. 1984. (NASA CR-174759).

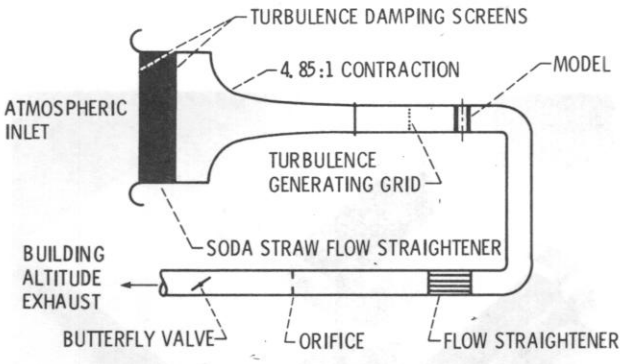

Figure 1. - Schematic of wind tunnel.

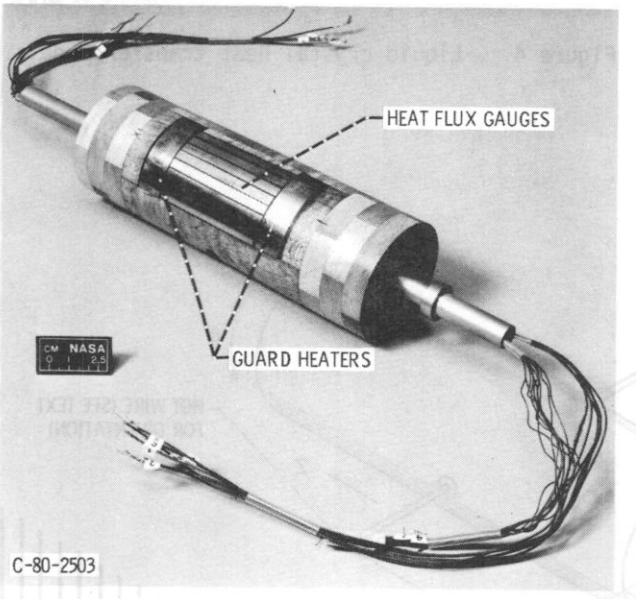

Figure 2. - Spanwise-averaged heat transfer model.

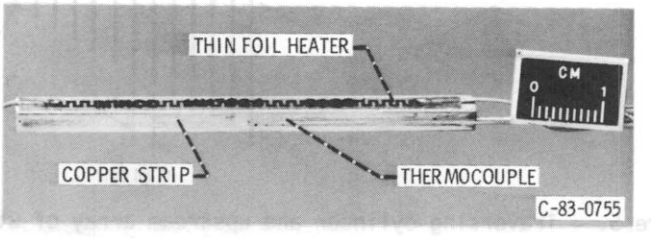

Figure 3. - Heat flux gauge.

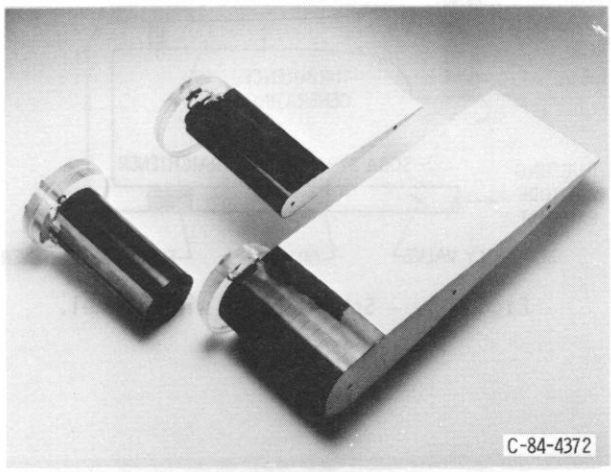

Figure 4. - Liquid-crystal heat transfer models.

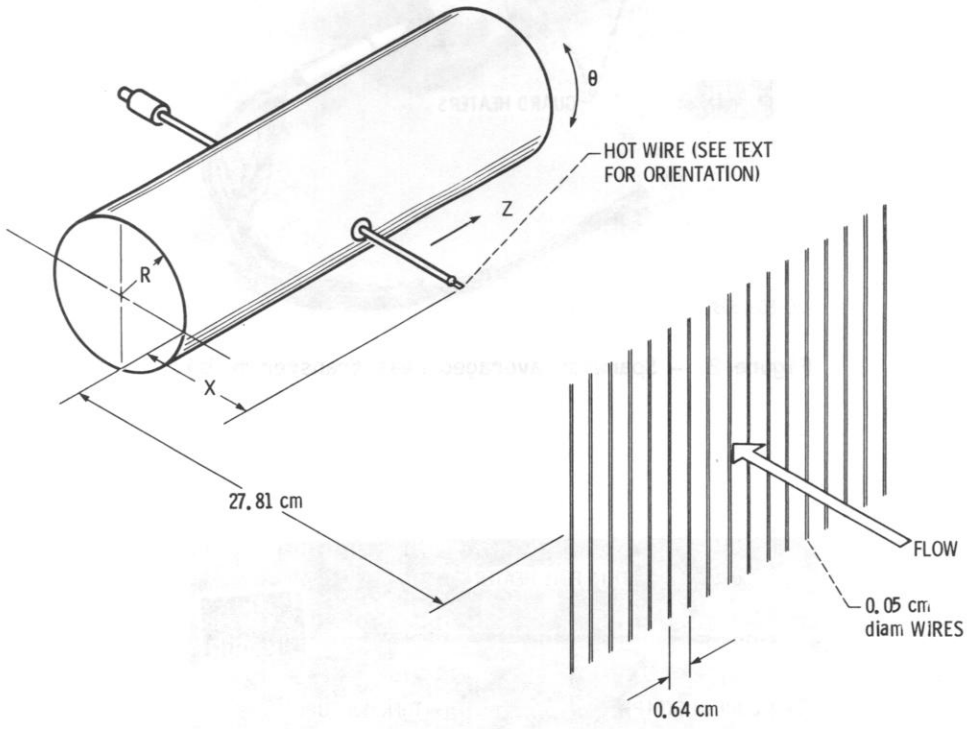

Figure 5. - Traversing cylinder and upstream array of wires.

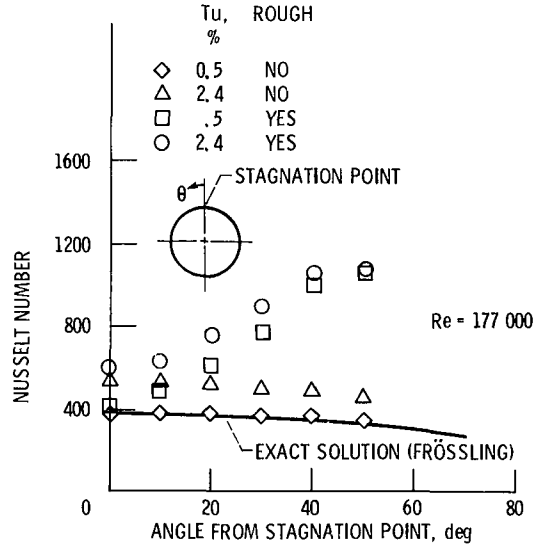

Figure 6. - Effect of free-stream turbulence and surface roughness on spanwise-averaged heat transfer for cylinder in crossflow. Re = 177 000.

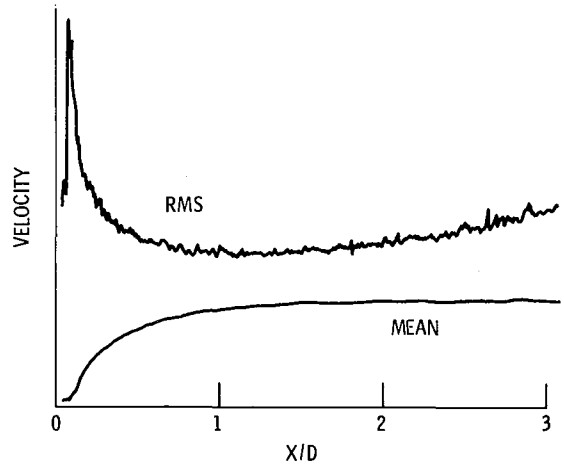

Figure 7. - Streamwise traverse of hot wire close to stagnation streamline.

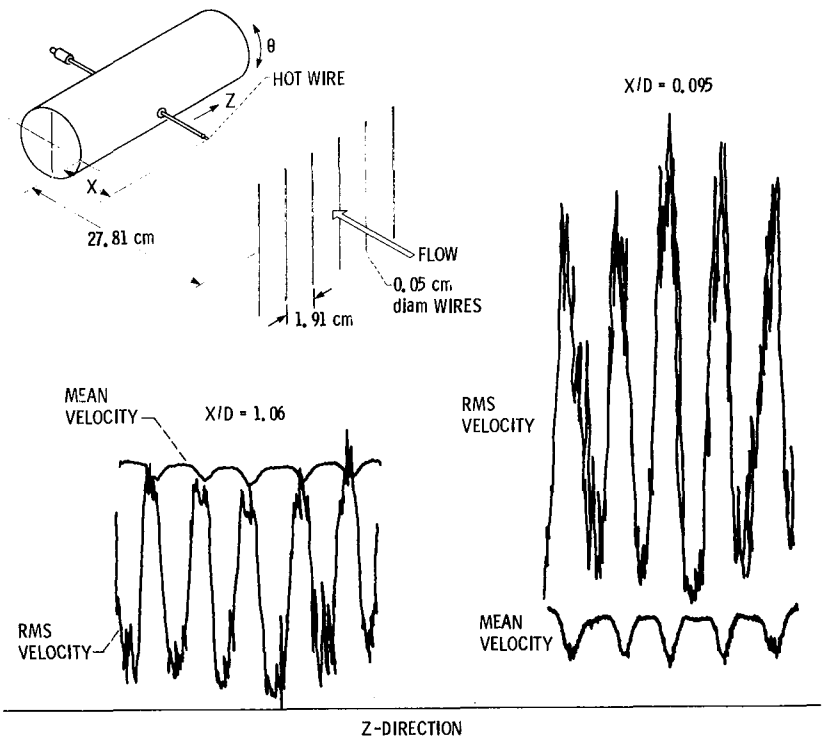

Figure 8. - Spanwise traverses of hot wire near cylinder stagnation point. (Abscissa of rms and mean velocity plots is offset slightly because of pen offset on x-yy' recorder.)

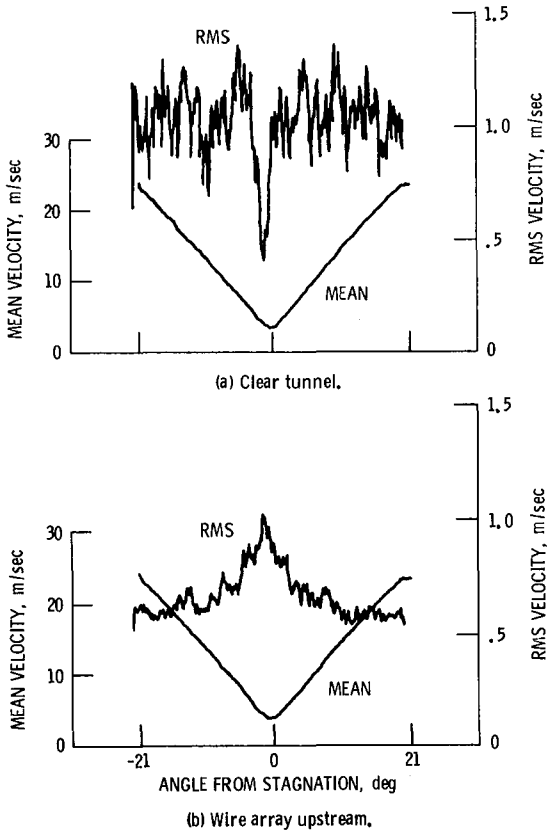

Figure 9. - θ-direction hot-wire traverse. Re_D = 125 000.

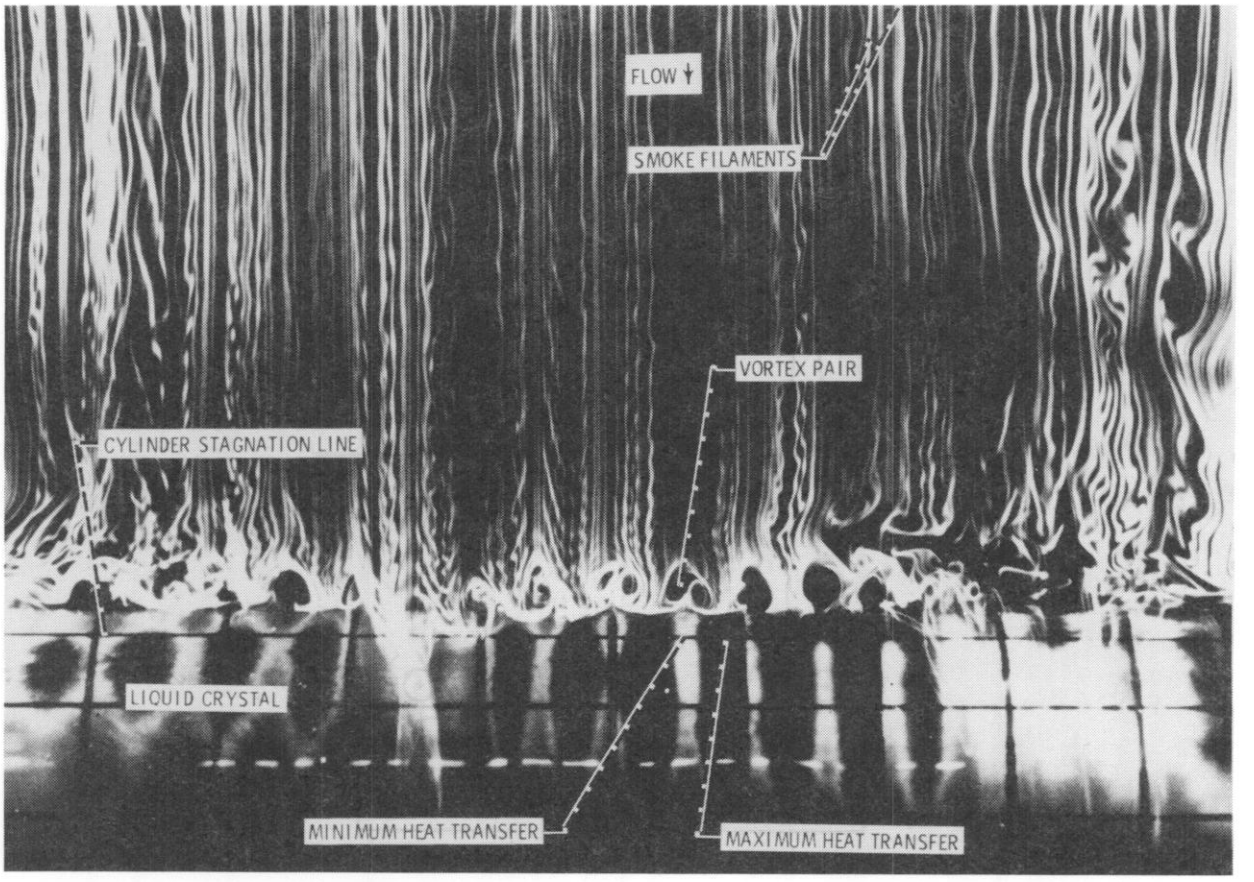

Figure 10. - Combined thermal and flow visualization of cylinder in crossflow.

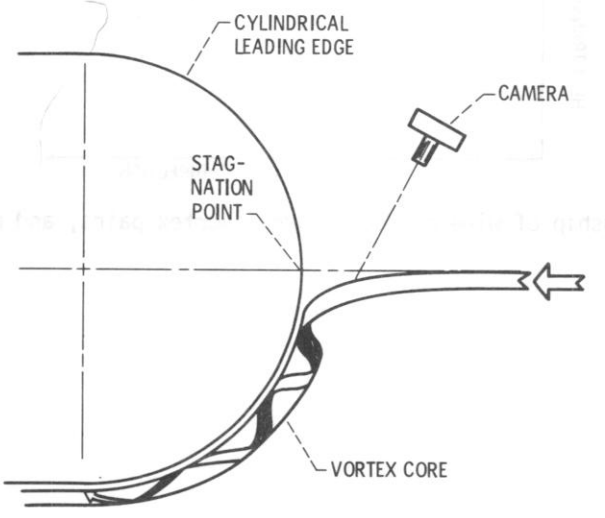

Figure 11. - Liquid-crystal model and relative camera position.

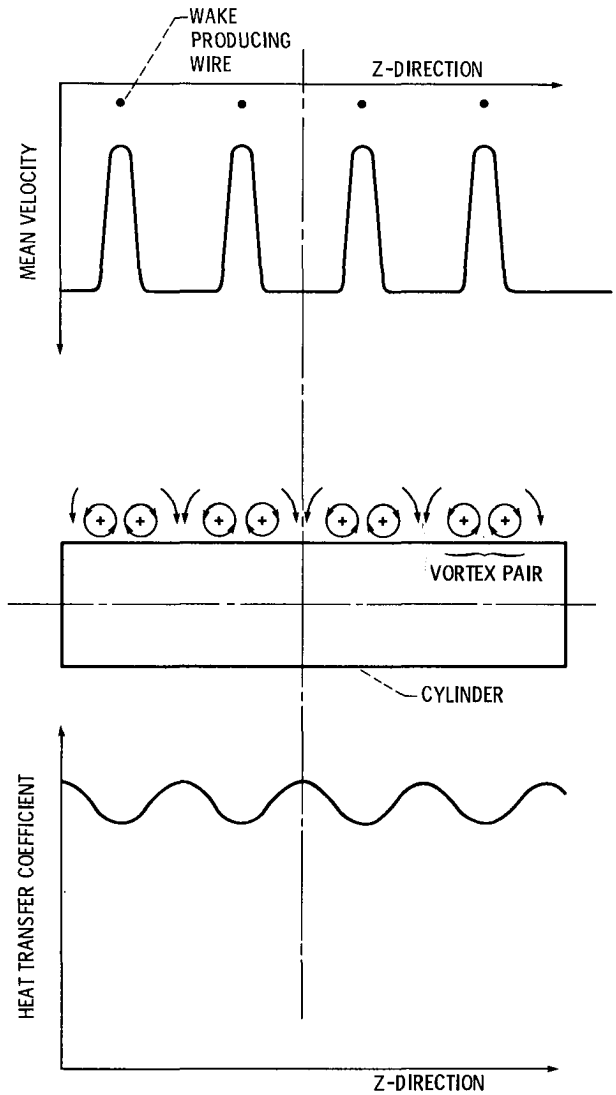

Figure 12. - Relationship of wire-produced wakes, vortex pairs, and peaks in heat transfer.

TRANSITION IN A DISTURBED ENVIRONMENT

E. Reshotko and D.K. Paik
Case Western Reserve University
Cleveland, Ohio 44106

The title of this presentation is the title of our research grant. While transition study is the objective of the work, the results to date are principally on the properties of turbulent boundary layers at low Reynolds numbers.

EXPERIMENTAL EQUIPMENT

The work was done in a small open-return wind tunnel of poor flow quality. Furthermore its flow quality could easily be made worse. The tunnel (fig. 1) is 19.7 cm (7-3/4 in) high. The test section is about 66 cm (26 in) long. The flow velocity is of the order of 6 m/sec (20 ft/sec) so that unit Reynolds numbers are about 366 000/m (120 000/ft). The test plate spans the tunnel and fills the length of the test section. The plate leading edge is elliptical, and a small flap is attached to the downstream end of the plate to set the attachment line on the working side of the leading edge of the plate. Measurements were made over the first 18 cm (0.6 ft) downstream of the leading edge by using a translating hot-wire probe in the spanwise centerplane. No spanwise variations are measured. Length Reynolds numbers for all of the data recorded were under 75 000. Test section turbulence levels were altered by placing grids at the location ahead of the contraction indicated in figure 1. The grids used and the corresponding test-section turbulence levels are shown in figure 2.

MEAN BOUNDARY-LAYER RESULTS

The mean boundary-layer development is shown in figure 3. In the absence of a grid the growth of Re_θ (fig. 3(a)) seems to be laminar, but the values are at about twice the Blasius level for the same distance from the leading edge. With grid 1 the boundary layer starts growing at a more rapid rate (shaded points) beyond 9 cm from the leading edge. For grid 2 the more rapid growth begins at about 6 cm from the leading edge. The corresponding shape factors are shown in figure 3(b). In the absence of a grid the shape factors decrease continuously from about 2.6 to 1.9 over the range of measurement. The no-grid data are believed to be transitional for reasons to be elaborated later. With grids 1 and 2 the shaded points corresponding to the more rapid growth in momentum thickness in figure 3(a) have shape factors below 1.7 and are believed to be turbulent. For these points a shear velocity u_τ could be obtained by fitting the profiles to a law of the wall.

An example of the determination of u_τ is shown in figure 4 for the grid 2 profile at $x = 9$ cm. The law-of-the-wall expression used is the algebraic form developed by Musker (ref. 1) that includes the laminar sublayer and the buffer layer and in the log-linear region displays Coles' constants (ref. 2). By comparing the experimental points made dimensionless with different values of u_τ with the Musker curve, a value of u_τ of 0.34 m/sec (1.12 ft/sec) was chosen based primarily on the points in the near log-linear

region. A more impressive fit is shown in figure 5. To be noted in both figures 4 and 5 is the absence of a wake component to the velocity profile. This is true of all the points obtained with grids 1 and 2 that are identified as turbulent.

For the no-grid case (fig. 6) a shear velocity determination could not be made in this way as the profiles did not display law-of-the-wall similarity. Hence what is plotted is u/u_e versus y/δ. The boundary-layer thickness δ is not a measured thickness. Rather it is computed from the displacement thickness and shape factor by using the relation $\delta/\delta^* = (H + 1)/(H - 1)$. With this normalization the location where $y/\delta = 1$ corresponds to a 0.95 velocity ratio. The profiles are collapsed for $y > \delta$, while for $y < \delta$ the velocity profiles fill out with distance downstream. This supports the identification of the no-grid data as transitional.

Next, we consider the skin friction behavior of the turbulent points obtained with grids 1 and 2. Shown in figure 7 is a semilog plot of u_e/u_τ versus Re_θ. The present data are the shaded points in the lower left of the figure, which correspond to the shaded points in figure 3. The other points come from prior investigations of flat-plate turbulent boundary layers at low turbulence levels and include the Wieghardt data as reduced by Coles (ref. 3), the data of Purtell, Klebanoff, and Buckley (ref. 4), and the data of Murlis, Tsai, and Bradshaw (ref. 5). All these data at low turbulence level seem consistent with each other and with Coles' (ref. 2) model based on a diminishing wake strength as Re_θ reduces toward a value just below 500. The present data display both the level and slope for u_e/u_τ versus Re_θ of a boundary layer that has no wake strength. This is seen by comparison with the calculated curve from the Musker profile for $\pi = 0$.

In 1962, Coles (ref. 2) did allude to the reduction in wake strength and elevated skin friction to be expected with an increase in turbulence level. A more plausible physical hypothesis has been advanced by Huffman and Bradshaw (ref. 6) through their comparison of turbulent boundary layers developing under a quiescent irrotational free stream with the turbulent flow in pipes, where the turbulent core is neither quiescent nor irrotational. In the latter flow there is no observable wake; in the former there is definitely a wake component to the velocity profiles. For the turbulent boundary layer at low Reynolds numbers in quiescent environments, Huffman and Bradshaw attribute the erosion of the wake component to the increased importance of the viscous superlayer - the interface between the boundary layer and the irrotational external flow - in eroding the wake component. For external flows at elevated free-stream turbulence - by analogy to the situation in pipes - the wake component is eroded more severely if not entirely as in the present results. An attempt will be made in our future work to develop this argument further in conjunction with other data sets for turbulent boundary layers developing in disturbed streams.

DISTURBANCE FLOW RESULTS

Figures 8 and 9 show the longitudinal turbulence intensity distribution at various values of Re_θ for the grid 1 and grid 2 data, respectively. The peak value of u'/u_τ is about 2.35 to 2.4 at $y^+ = 13$. The approximate similarity shown in the figures is in good agreement with the results of Purtell et al. (ref. 4). Beyond the peak, the data points fall until they

eventually level at u_e'/u_τ corresponding to the free-stream disturbance level. Taken together with the u_e/u_τ values for these profiles, they give a measure of the free-stream disturbance level, which turns out to be about 5.5 percent for grid 1 and 6.7 percent for grid 2. The Purtell et al. (ref. 4) data shown in figure 9 indicate significantly lower free-stream disturbance levels and also some spreading with Reynolds number beyond the peak. One can perhaps surmise the Reynolds number dependence of viscous superlayer effects in the Purtell data that are absent in the present results for high free-stream disturbance levels.

For the no-grid case (fig. 10), we do not have u_τ as a reference quantity. Plotted in figure 10 therefore is u'/u_e versus y/δ^*. The profiles fill out with distance downstream, but the peak values occur consistently at y/δ^* of about 1.2, very close to the location of $y/\delta^* = 1.33$ for which the low-frequency u' peak was observed in laminar flows at low free-stream turbulence levels by Klebanoff (ref. 7) and others. It would be of interest to see if the Klebanoff argument when applied to law-of-the-wall turbulent profiles explains the observed peak at $y^+ = 13$.

It is of interest at this point to look at disturbance spectra. Figure 11 shows spectra taken in the free stream 6 cm downstream of the leading edge of the plate for the three free-stream disturbance levels. Note the increase in intensity at the low frequencies with increase in turbulence level due to the grids. Inside the boundary layer, the spectra for grids 1 and 2 (figs. 12 and 13, respectively) are essentially unchanged with downstream distance at these high disturbance levels. For the no-grid case, however, there are progressive changes in the shape and intensity of the spectra (fig. 14). Although the intensities there are small, the largest growth rates occur in the frequency range 50 to 100 Hz (fig. 15), corresponding to $\beta\nu/u_e^2$ between 120×10^{-6} and 250×10^{-6}. It is premature to ascribe any linear instability connotations to this result.

SUMMARY

The foregoing is an interim report of our investigation. It is apparent that there is much yet to be done. One thing that is fairly clear is that no standard laminar flow was observed. Furthermore the turbulent mean flow data seem reasonable for the elevated disturbance levels of our tests in the sense that there is no discernible wake component to any of the profiles and that the variation of skin friction with Re_θ is consistent with zero wake strength. The no-grid data are in all likelihood transitional. This case requires additional concentrated study in order to obtain more definite information regarding the transition process in a disturbed environment.

REFERENCES

1. Musker, A.J.: Explicit Expression for the Smooth Wall Velocity Distribution in a Turbulent Boundary Layer. AIAA J., vol. 17, no. 6, June 1979, pp. 655-657.

2. Coles, D.E.: The Turbulent Boundary Layer in a Compressible Fluid, Rand Corp., Rep. R-403-PR, 1962.

3. Coles, D.E.: The Young Person's Guide to the Data. In Proceedings of 1968 AFOSR-IFP-Stanford Conf. (Vol. II), Stanford Univ., 1969, pp. 1-45.

4. Purtell, L.P.; Klebanoff, P.S.; and Buckley, F.T.: Turbulent Boundary Layer at Low Reynolds Number. Phys. Fluids, vol. 24, no. 5, May 1981, pp. 802-811.

5. Murlis, J.; Tsai, H.M.; and Bradshaw, P.: The Structure of Turbulent Boundary Layers at Low Reynolds Numbers. J. Fluid Mech., vol. 122, 1982, pp. 13-56.

6. Huffman, G.D.; and Bradshaw, P., A Note on von Karman's Constant in Low Reynolds Number Turbulent Flows. J. Fluid Mech., vol. 53, 1972, pp. 54-60.

7. Klebanoff, P.S.: Private communication.

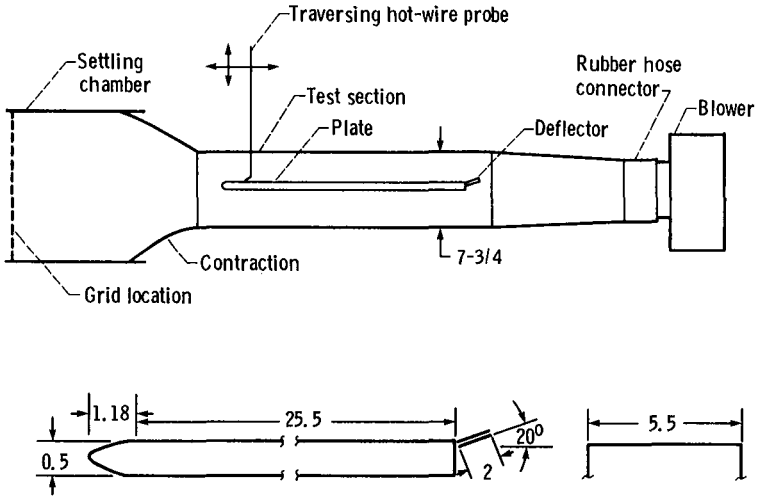

Figure 1. - Schematic diagrams of wind tunnel and test plate. (Dimensions are in inches.)

Grid	Dimensions, in				Open area, percent	u'_e/u_e, percent
	a	b	c	d		
1	1.75	1.50	2.25	1.75	33	5-6
2	1.38	1.75	1.25	2.00	24	6-7

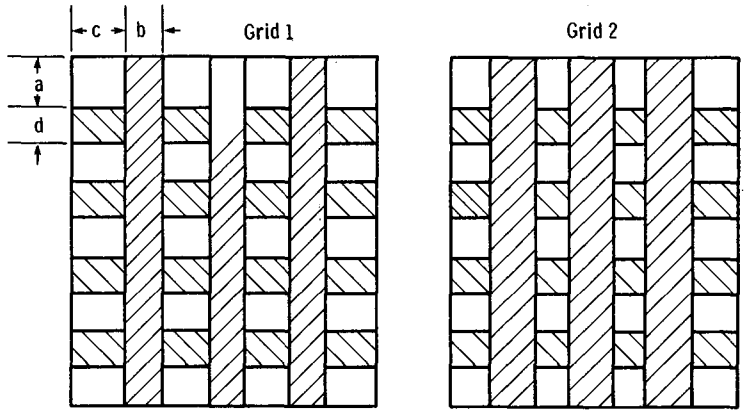

Figure 2. - Shapes and dimensions of grids.

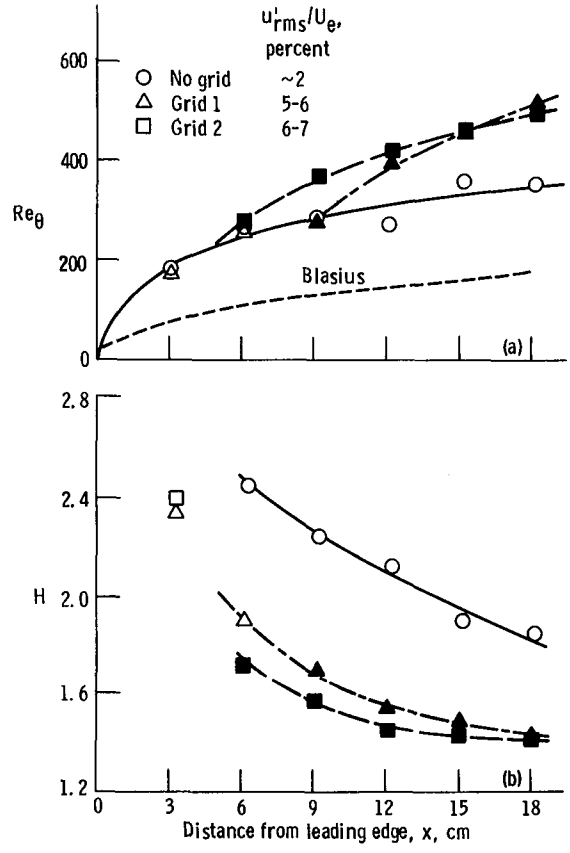

(a) Boundary-layer growth.
(b) Shape factor variation.

Figure 3. - Mean boundary-layer development.

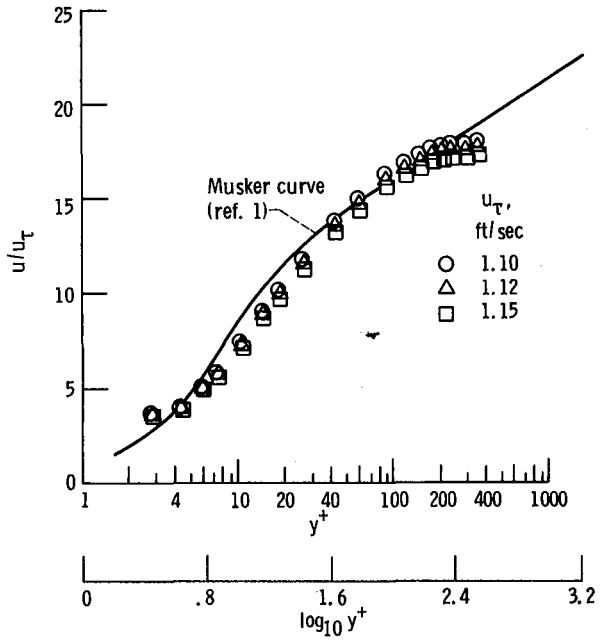

Figure 4. - Mean-velocity profile at 9 cm - grid 2. u_τ = 1.12 ft/sec.

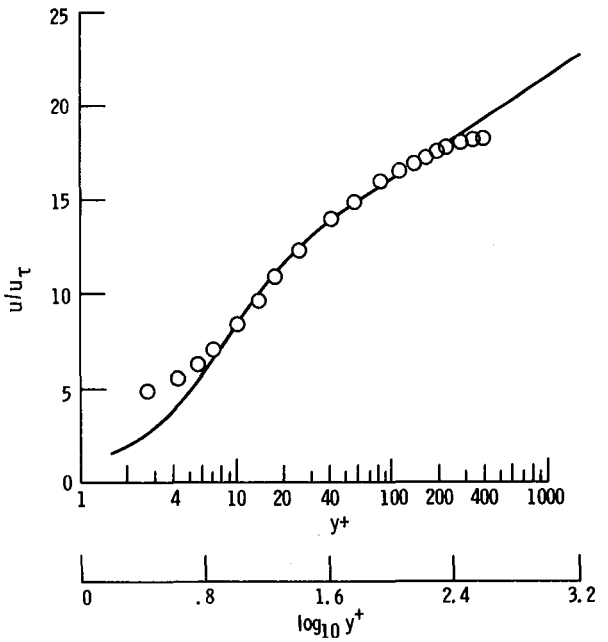

Figure 5. - Mean-velocity profile at 15 cm - grid 2. u_τ = 1.09 ft/sec.

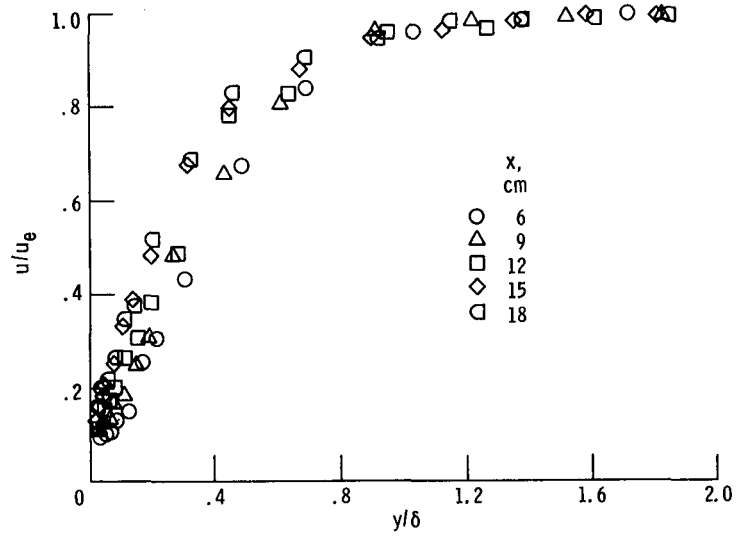

Figure 6. - Development of boundary layer - no grid.

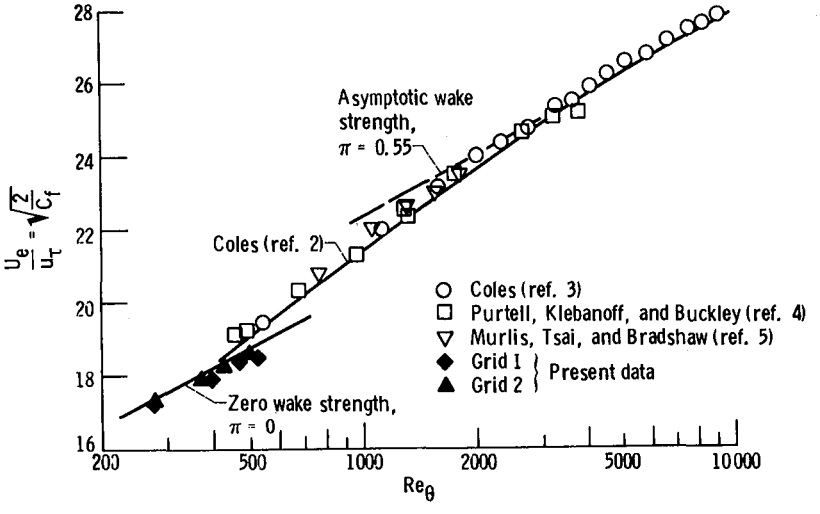

Figure 7. - Skin friction of turbulent boundary layers at low Reynolds numbers.

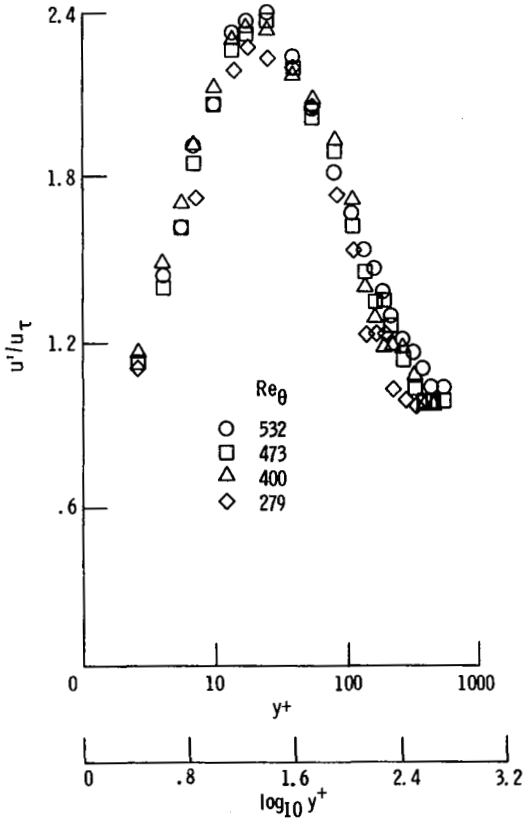

Figure 8. - Distribution of longitudinal fluctuating velocity - grid 1.

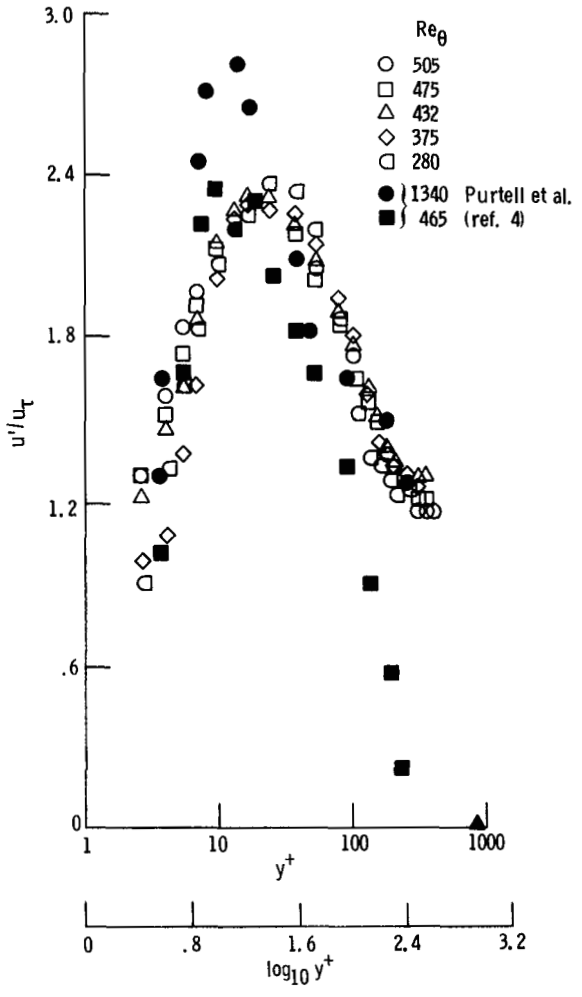

Figure 9. - Distribution of longitudinal fluctuating velocity - grid 2.

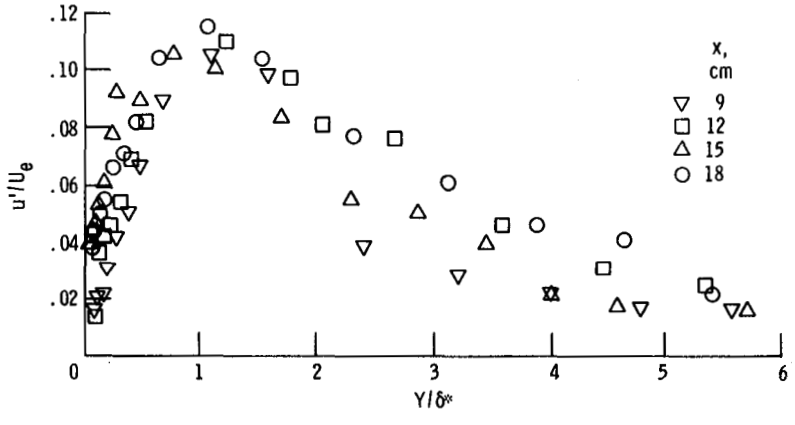

Figure 10. - Disturbance profiles for no-grid case.

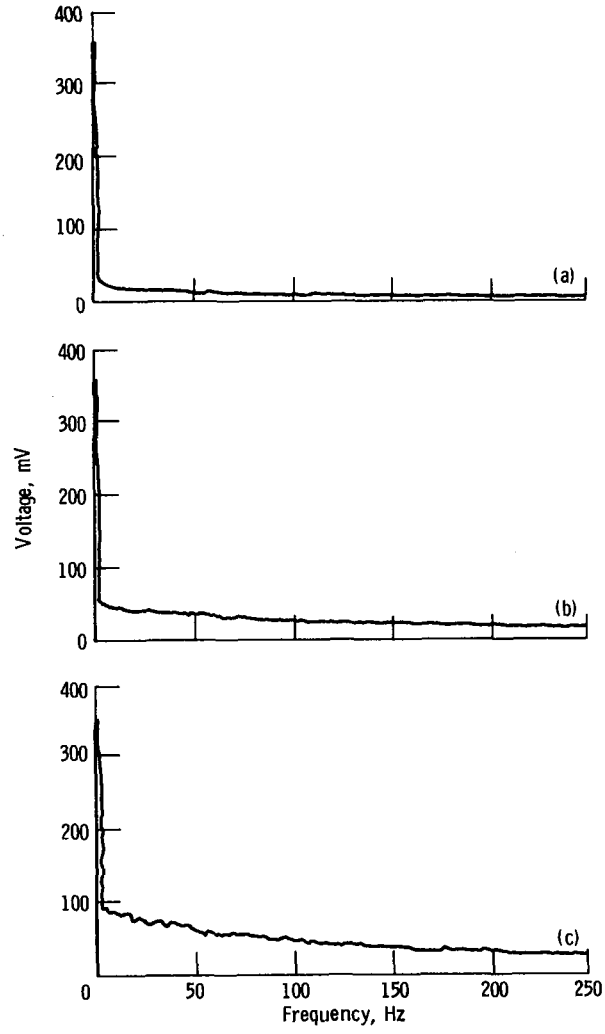

(a) No grid. (b) Grid 1. (c) Grid 2.

Figure 11. - Free-stream turbulence spectra, 0-250 Hz.

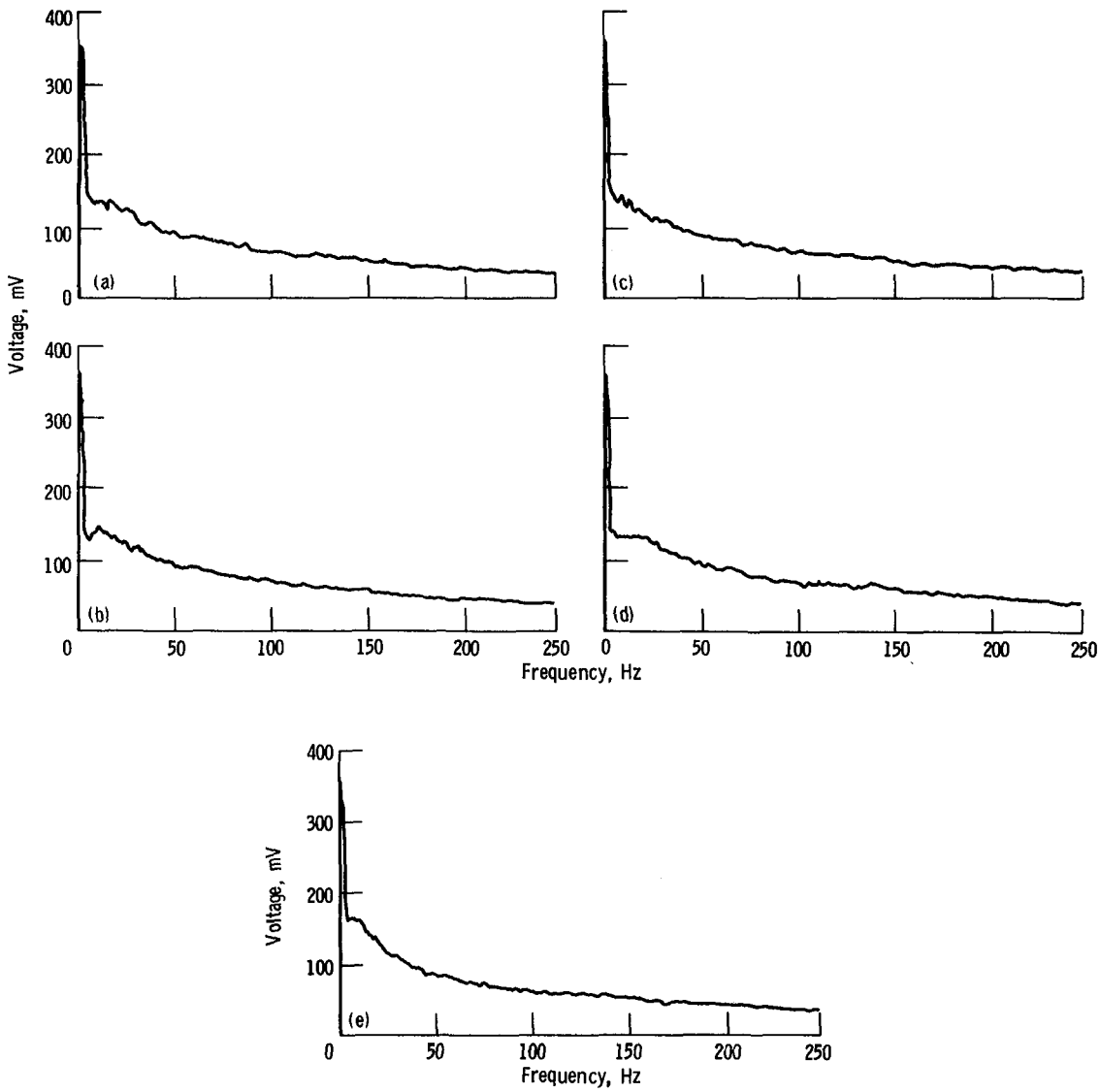

(a) x = 18 cm. (c) x = 12 cm.
(b) x = 15 cm. (d) x = 9 cm.
(e) x = 6 cm.

Figure 12. - Spectra of u' with increasing distance from leading edge - grid 1.

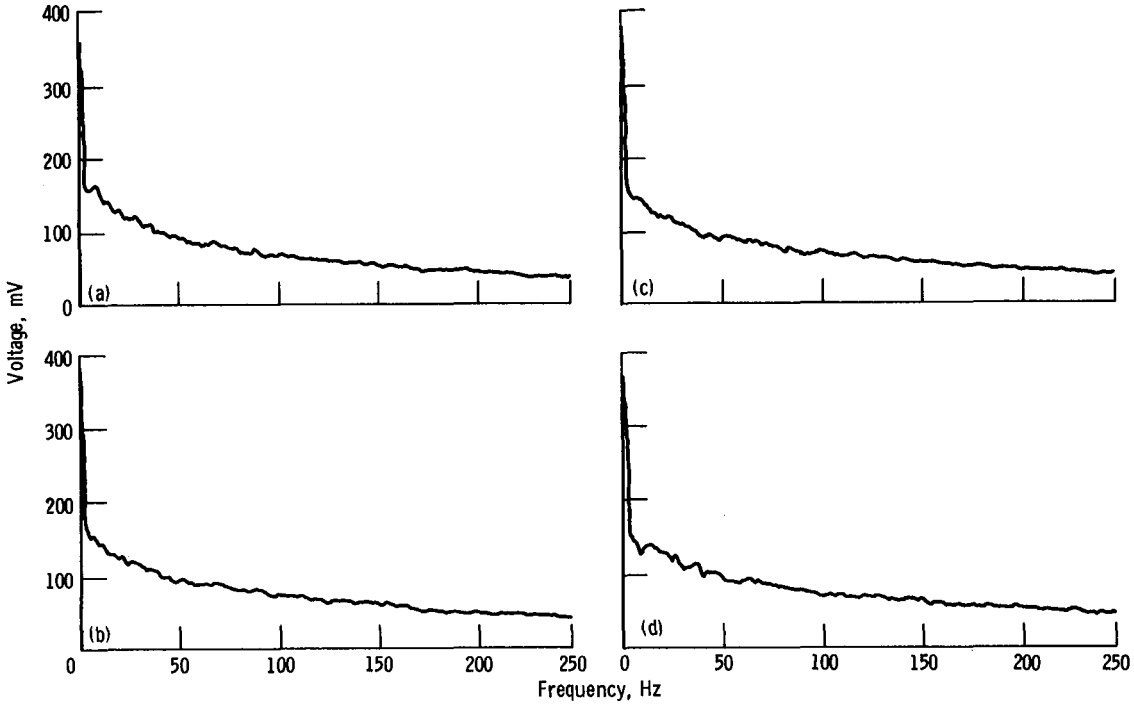

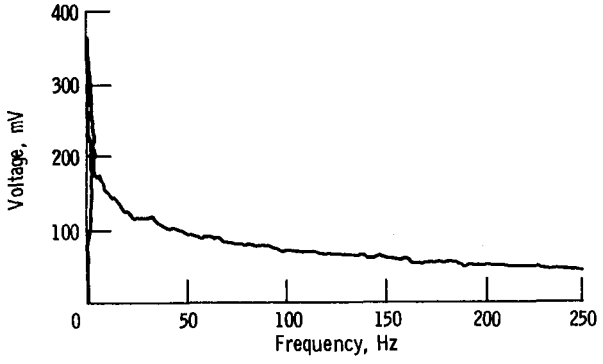

(a) x = 18 cm. (c) x = 12 cm.
(b) x = 15 cm. (d) x = 9 cm.
(e) x = 6 cm.

Figure 13. - Spectra of u' with increasing distance from leading edge - grid 2.

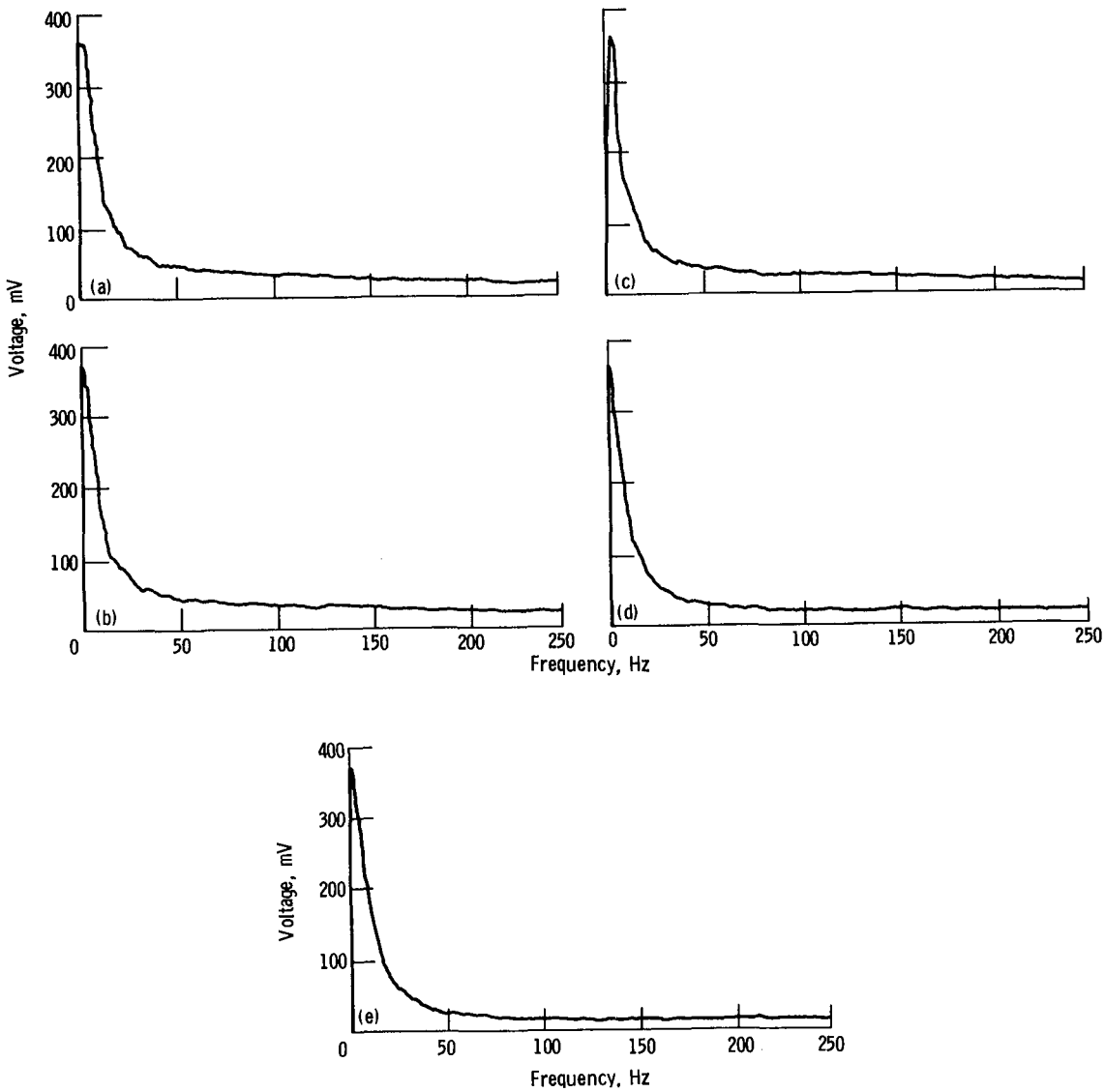

(a) x = 18 cm. (c) x = 12 cm.
(b) x = 15 cm. (d) x = 9 cm.
(e) x = 6 cm.

Figure 14. - Disturbance spectral data inside boundary layer - no grid.

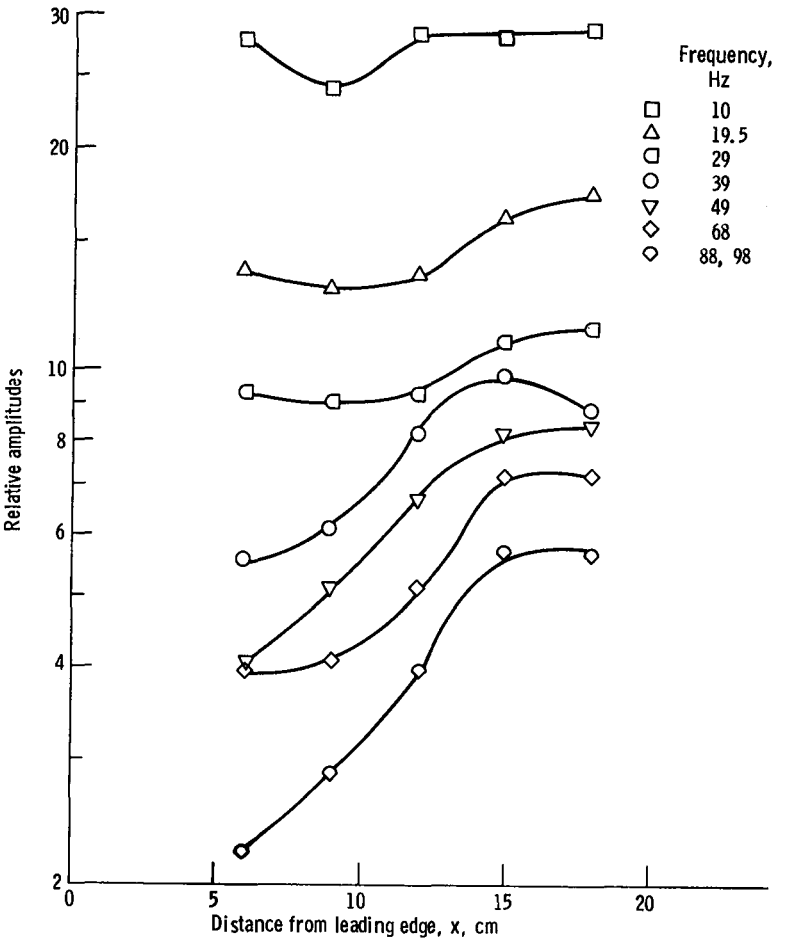

Figure 15. - Relative amplitudes of selected frequencies - no grid.

EXPERIMENTAL OBSERVATION OF TRANSITION BEHAVIOR ON A FLAT PLATE

Henry T. Nagamatsu
Rensselaer Polytechnic Institute
Troy, New York 12181

INTRODUCTION

In studying transition behavior a shock tube and tunnel were used to produce high temperatures, and thin-film platinum heat gauges were used to measure local heat flux as well as to detect the transition of the laminar boundary layer over a flat plate and a cone. Initial investigations were conducted in the hypersonic shock tunnel to obtain high-temperature information for the development of an ICBM nose cone. Shock Mach numbers as large as 50 with a temperature of 15 000 K after the incident wave were produced in the driven tube (ref. 1). And now we are using shock tubes to investigate the heat transfer over various surfaces to 2500 K for the development of future gas turbines.

The shock tube is an ideal method of producing high-temperature gas for which the equilibrium properties are fairly well known. Thin-film platinum heat gauges are either sputtered (ref. 2) or painted (ref. 3). These gauges, with a response time of 1 μsec are effective in detecting the transition of the laminar boundary layer (refs. 3 to 6) as well as in measuring the local heat flux.

I will describe the shock tubes that were constructed at Rensselaer Polytechnic Institute, under the sponsorship of Dr. R. Graham of the NASA Lewis Research Center and Dr. W. Aung of the National Science Foundation, to obtain heat transfer information over a temperature range 360 to 2500 K for the design of advanced jet engines. I will describe the thin-film heat gauges that were developed and some of the experimental heat transfer results for laminar, transition, and turbulent boundary layers. The transition phenomenon has been investigated with heat gauges since 1960 in shock tubes and tunnels; some of the results are presented in references 2 to 8.

DESCRIPTION OF SHOCK TUBES AND HEAT GAUGES

RPI Low- and High-Pressure Shock Tubes

RPI low- and high-pressure shock tubes (refs. 3 and 7) are shown in figure 1. Both of these shock tubes are 21 m (70 ft) long with a diameter of 10.2 cm (4 in), and the drivers are 3 m (10 ft) long with 18.3 (60-ft) long driven tubes. The low-pressure tube is copper tubing with a maximum pressure of 690 kPa (100 psi); the maximum pressure for the stainless steel tube is 12 400 kPa (1800 psi). In the high-pressure shock tube it is possible to obtain heat transfer data at a pressure of 4150 kPa (600 psi) and temperatures to 2500 K for future water-cooled gas turbines for generating power. At the end of the high-pressure shock tube a nozzle with an exit diameter of 60 cm (24 in) can be attached. With this hypersonic nozzle a flow Mach number of 25 in air has been achieved (ref. 1).

At present we are using both shock tubes to obtain heat transfer over flat plates with and without pressure gradients, stagnation point heat transfer for circular cylinders, and heat transfer in gas turbine vanes. The results obtained in the low-pressure shock tube on the laminar boundary-layer transition and heat transfer for laminar, transition, and turbulent boundary layers will be discussed.

To orient people who are not familiar with the shock tube technique, the operation of the shock tube is briefly described. A shock tube (x-t) diagram is presented in figure 2. The pressures in the driver and driven tubes are selected to produce the desired heated air in the test section (ref. 9). The locations of the shock wave, the contact surface, and the head of the rarefaction wave in the driver after the diaphragm separating the driver and the driven tube is broken and at time $t = t_1$ are shown in figure 2. Across the incident shock wave the gas is heated to temperature T_2, compressed to pressure P_2, and imparted flow velocity V_2. The incident shock wave is reflected from the end of the tube (as shown in fig. 2 for time $t = t_2$). After the reflected shock wave the gas is further heated to temperature T_5 and compressed to pressure P_5. For a solid end wall the flow velocity after the reflected shock wave is zero and is a function of the ratio of the open area in the end wall to the shock tube cross-sectional area. By selecting this area ratio it is possible to produce the desired flow Mach numbers of 0.15 and 0.45 after the reflected shock wave to simulate the inlet flow Mach numbers for gas turbine vanes and blades, respectively.

Heat transfer distribution over bodies can be determined in region 2 after the incident shock wave or in region 5 after the reflected shock wave from the reflection plate (refs. 3, 7, and 8). The duration of the test time in the test section is limited by the arrival of the expansion wave from the driver end (fig. 2). The shock tube is a very effective method for producing high-temperature and high-pressure gas for which the thermodynamic properties are well defined for the equilibrium condition.

A test section with a square cross section with area equal to that of the 10.2-cm (4-in) diameter driven tube was constructed and attached to the end of the low-pressure shock tube. This section was constructed with adjustable top and bottom walls to permit testing with a pressure gradient over the flat plate (fig. 3) for simulating the accelerating flow over vanes and blades. Windows are mounted to side walls for taking schlieren photographs of the boundary layer over the flat plate.

Piezoelectric pressure transducers (e.g., fig. 4) are located in the test section to measure the pressure after the incident and reflected shock waves. The response time of the quartz pressure gauges is approximately 10 μsec.

Thin-film platinum heat gauges were constructed by painting the platinum on the Pyrex substrate, which was placed in an oven to evaporate the solvent and to cause the platinum to adhere to the Pyrex. The platinum is approximately 104 Å thick and has a resistance of about 15 Ω. At the General Electric Research and Development Center the heat gauges were fabricated by sputtering platinum to the glass to a thickness of approximately 300 Å (refs. 2 and 4 to 6). These platinum heat gauges have a response time of a few microseconds and a current of approximately 30 mA. The heat gauge power supply schematic is shown in figure 5. A change in the surface temperature due to the heat transfer increases the resistance of the platinum and causes a voltage

change that is recorded on the oscilloscope. A computer is used to calculate the heat flux from the voltage trace (refs. 2, 3, and 7).

A flat plate with a span of 9 cm (3.55 in) and with thin-film platinum heat gauges is shown in figure 6. The platinum film is about 0.305 cm (0.12 in) long and 0.15 cm (0.06 in) wide and the diameter of the glass disk is 0.13 cm (0.05 in). With these heat gauges it is possible to measure the local heat flux as well as to detect the transition of the laminar boundary layer.

EXPERIMENTAL RESULTS AND DISCUSSION

For evaluating the local heat transfer rate it is necessary to determine the heat gauge constant β, which is defined as

$$\beta = \frac{(\rho C_p k)_b}{\alpha} \tag{1}$$

where ρ, C_p, and k are the density, specific heat, and thermal conductivity of the backing material and α is the thermal resistivity of platinum. The gauge constants β are used in calculating the heat transfer for each gauge. The gauge constant was obtained by accurately evaluating the initial voltage jump that is displaced on an oscilloscope trace when the incident shock wave passes over the heat gauge. The expression for the heat gauge constant is

$$\beta = \frac{I_0 R_0}{\Delta E} k_w [T_w - T_{wi}] S'(0) \left[\frac{\pi}{2} \frac{1}{\nu_w} \frac{U_2}{U_1} \right]^{\frac{1}{2}} \tag{2}$$

where I_0 and R_0 are initial gauge current and resistance, ΔE the step change in voltage, k_w the thermal conductivity at the wall, T_w the wall temperature, T_{wi} the insulated wall temperature, ν_w the kinematic viscosity at the wall, U_2 the velocity behind the normal stationary shock, U_1 the free-stream velocity, and $S'(0)$ a coefficient tabulated in reference 10.

The heat gauge traces for laminar, transition, and turbulent boundary layers are presented in figure 7 for the flow over a flat plate (fig. 3), with a flow Mach number after a reflected shock wave of 0.12 and a gas temperature of 405 K. The laminar trace for a low Reynolds number (fig. 7(a)) is smooth after the passage of the reflected shock wave. As the Reynolds number increases, the transition trace (fig. 7(b)) shows oscillations associated with the passage of turbulent bursts over the heat gauge. For high Reynolds number with a turbulent boundary layer the heat gauge trace (fig. 7(c)) has a relatively smooth parabolic shape with a superimposed high-frequency oscillation caused by the presence of turbulent eddies. Similar heat gauge traces were observed for laminar, transition, and turbulent boundary layers over a 10° cone of 1.2-m (4-ft) length at Mach 10 (refs. 4 and 5) and of 2.4-m (8-ft) length for Mach 16 (ref. 6) and on the shock tube wall (ref. 3). The turbulent trace indicates the decrease in voltage output from the initiation of the flow over the flat plate. This decrease is due to the expansion wave from the shock tube driver arriving in the test section (fig. 2).

The experimental heat transfer rate was reduced from the voltage-time oscilloscope traces presented in figure 7. The voltage traces were then digitized by using a Talos digitizer to evaluate the corresponding local heat flux as a function of time and the following equation derived by Vidal (ref. 11) was used:

$$q(t) = \frac{\beta\sqrt{\pi}}{2I_0R_0}\left\{\frac{E(t)}{\sqrt{t}} + \frac{1}{\pi\sqrt{t}}\int_0^t \frac{\left[\sqrt{t}\cdot E(t)\right] - \left[\sqrt{t}\cdot E(\tau)\right]}{(t-\tau)^{3/2}}\, d\tau\right\} \qquad (3)$$

This equation is solved by numerical integration through a computer program on the IBM 3033 and by using the digitized voltage data to obtain the experimental value for the local heat transfer rate, Stanton, and Nusselt numbers as functions of time.

The experimental results for the laminar boundary-layer heat transfer to the shock tube wall (ref. 3) and flat plate (refs. 7 and 8) agreed well with Mirels' (ref. 10) prediction for the variation with time of the heat flux after the passage of the incident shock wave (as shown in fig. 8 for the shock tube wall). Similar laminar heat transfer variation with time after the incident shock wave was observed for the flat plate (refs. 7 and 8) at low Reynolds numbers.

The digitized voltage trace and the corresponding local heat flux for laminar, transition, and turbulent boundary layers for the heat gauge located 7.95 cm (5.16 in) from the leading edge of the flat plate are presented in figures 9(a) to (c), respectively, for a gas temperature of 416 K, Mach 0.12, and a wall-to-gas temperature 0.71 (ref. 12). A laminar boundary layer was observed for a Reynolds number of 9.96×10^3, and the digitized voltage trace and the heat flux are presented in figure 9(a). The laminar boundary layer over the plate after the passage of a reflected shock wave is established in approximately 1 msec. There is a scatter in the heat flux result due to the digitizing of the heat gauge voltage trace. For a Reynolds number of 4.72×10^4 the boundary layer over the plate is in the transition regime with large variations in the local heat flux (fig. 9(b)). These large fluctuations for the transition boundary layer are caused by the passage of turbulent bursts over the heat gauge (as observed previously in refs. 3 to 8). The fast response time of the thin-film platinum heat gauge detects the variation in the heat flux to the surface. A fully developed turbulent boundary layer was observed for a Reynolds number of 1.32×10^6 (fig. 9(c)). The digitized voltage trace is relatively smooth and decreases after 12 msec when the expansion wave arrives from the driver section (fig. 2). The corresponding heat flux is nearly constant for the duration of the test gas over the heat gauge. Once the boundary layer is fully turbulent over the plate, a sublayer exists near the surface of the plate, and consequently the voltage trace is smooth with small-amplitude, high-frequency fluctuations (refs. 3 to 8).

CONCLUSIONS

A shock tube is a useful device to produce shock-heated air over a temperature range of 350 to 2500 K. By using a reflected shock wave technique it is possible to produce flow Mach numbers of 0.12 and 0.45 to simulate the flow

Mach numbers for future gas turbine vanes and blades, respectively. And it is possible to produce pressures as high as 40 atm after the reflected shock wave.

Going from a circular driven tube to a square test section and deflecting the top and bottom walls permitted the investigation of the effects of pressure gradient on the heat transfer to a flat plate. This method simulates the accelerating flow through vanes and blades.

Thin-film platinum heat gauges with a response time of approximately 1 μsec can be used to detect the transition phenomena for the laminar boundary layer in subsonic to hypersonic flows. A computer is used to calculate from the heat gauge voltage output the local heat flux for laminar, transition, and turbulent boundary layers for gas temperatures as high as 2500 K.

REFERENCES

1. Nagamatsu, H.T.; Geiger, R.E.; and Sheer, R.E., Jr.: Hypersonic Shock Tunnel. ARS J., vol. 29, no. 5, May 1959, pp. 332-340.

2. Nagamatsu, H.T.; Weil, J.A.; and Sheer, R.E., Jr.: Heat Transfer to Flat Plate in High Temperature Rarefied Ultra-High Mach Number Flow. ARS J., vol. 32, no. 4, Apr. 1962, pp. 533-541.

3. Dillon, R.E., Jr.; and Nagamatsu, H.T.: Heat Transfer Rate for Laminar, Transition, and Turbulent Boundary and Transition Phenomenon on Shock Tube Wall. AIAA Paper 82-0032, Jan. 1982.

4. Nagamatsu, H.T.; Graber, B.C.; and Sheer, R.E., Jr.: Transition of Hypersonic Boundary Layer. Phys. Fluids, vol. 8, no. 2, Feb. 1965, pp. 211-221.

5. Nagamatsu, H.T.; Graber, B.C.; and Sheer, R.E., Jr.: Roughness, Bluntness, and Angle of Attack Effects on Hypersonic Boundary Layer Transition. J. Fluid Mech., vol. 24, Part 1, Jan. 1966, pp. 1-31.

6. Nagamatsu, H.T.; Graber, B.C.; and Sheer, R.E., Jr.: Hypersonic Laminar Boundary Layer Transition on 8-Foot-Long, 10° Cone, M_1 = 9.1-16. AIAA J., vol. 5, no. 7, July 1967, pp. 1245-1252.

7. Pedrosa, A.C.F.; and Nagamatsu, H.T.: Convective Heat Transfer on Flat Plate at Very High Temperature and Pressure Gradient. ASME Paper 83-GT-113, Mar. 1983.

8. Brostmeyer, J.D.; and Nagamatsu, H.T.: Flat Plate Heat Transfer for Laminar Transition and Turbulent Boundary Layers Using a Shock Tube. AIAA Paper 84-1726, June 1984.

9. Ferri, A.: Fundamental Data Obtained from Shock-Tube Experiments. Pergamon Press, New York, 1961, pp. 86-133.

10. Mirels, Harold: Laminar Boundary Layer Behind Shock Advancing into Stationary Fluid. NACA TN-3401, 1955.

11. Vidal, R.J.: Model Instrumentation Techniques for Heat Transfer and Force Measurements in a Hypersonic Shock Tunnel. Cornell Aeronautical Laboratory, Report AD-917-A-1, Feb. 1956.

12. Nagamatsu, H.T.; and Hinckel, J.N.: Heat Transfer Investigation in the Junction Region of Circular Cylinder to a Flat Plate at 90° Location. ASME Paper 84-WA/HT-70, Dec. 1984.

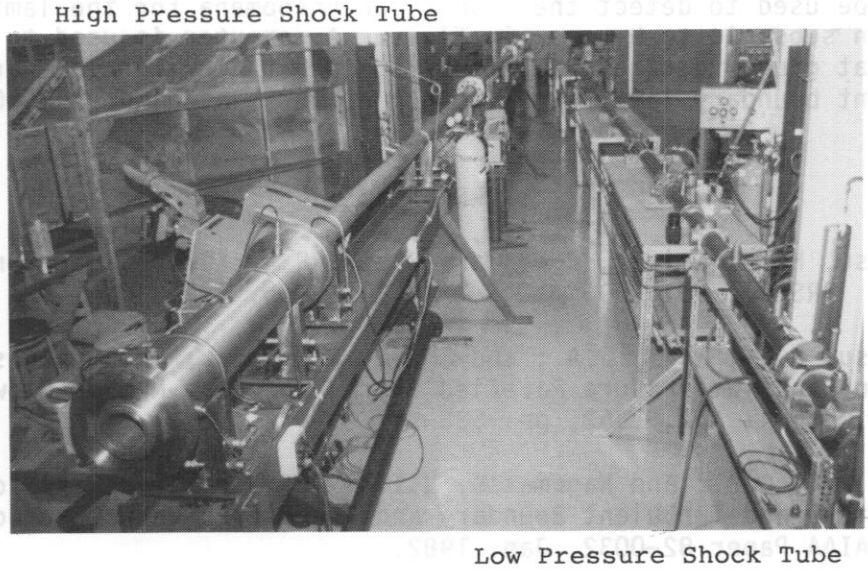

Figure 1. - RPI shock tube.

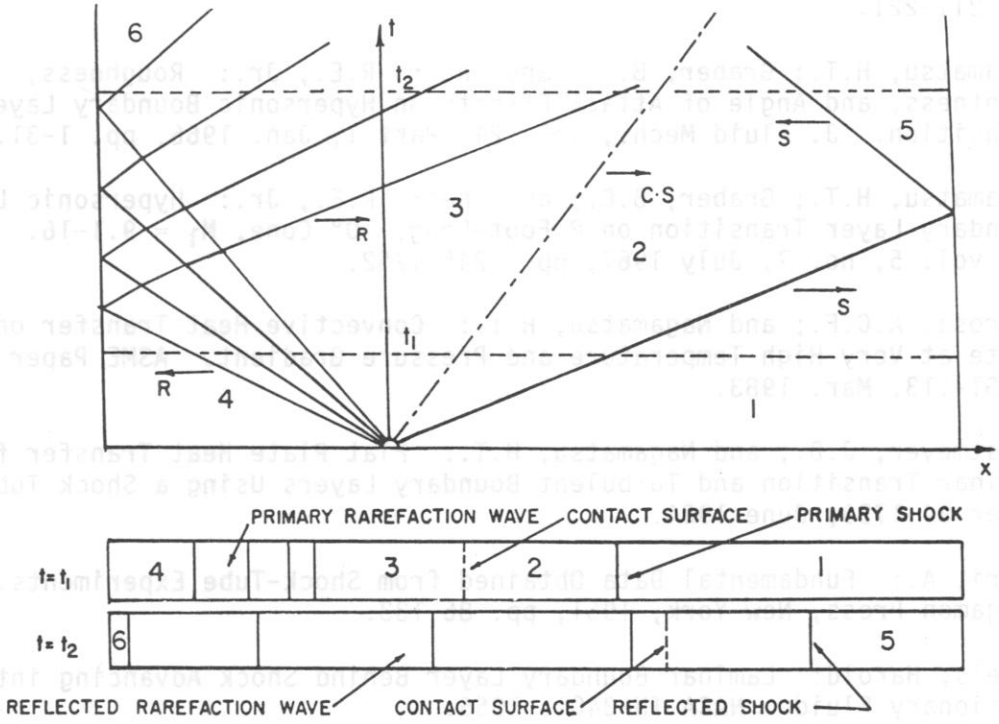

Figure 2. - Ideal wave system in a shock tube.

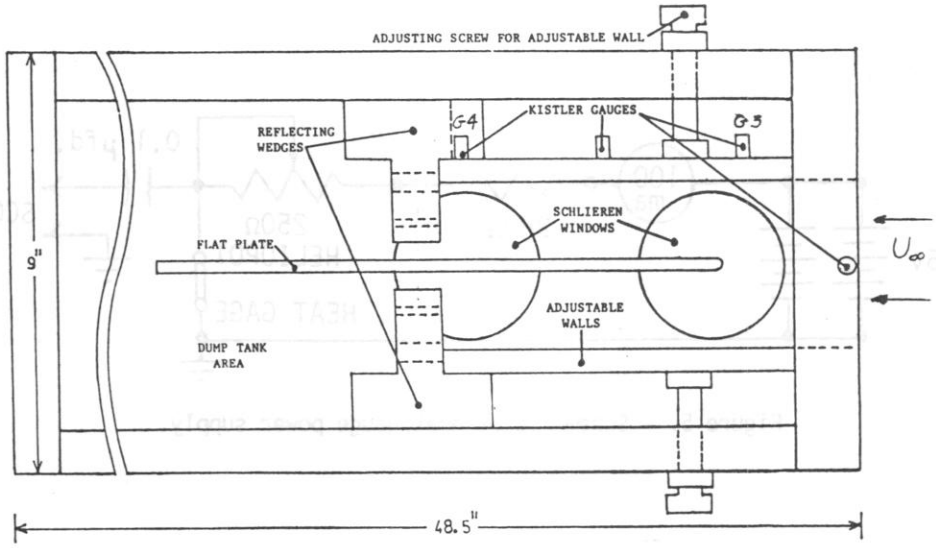

Figure 3. - Schematic of square test section.

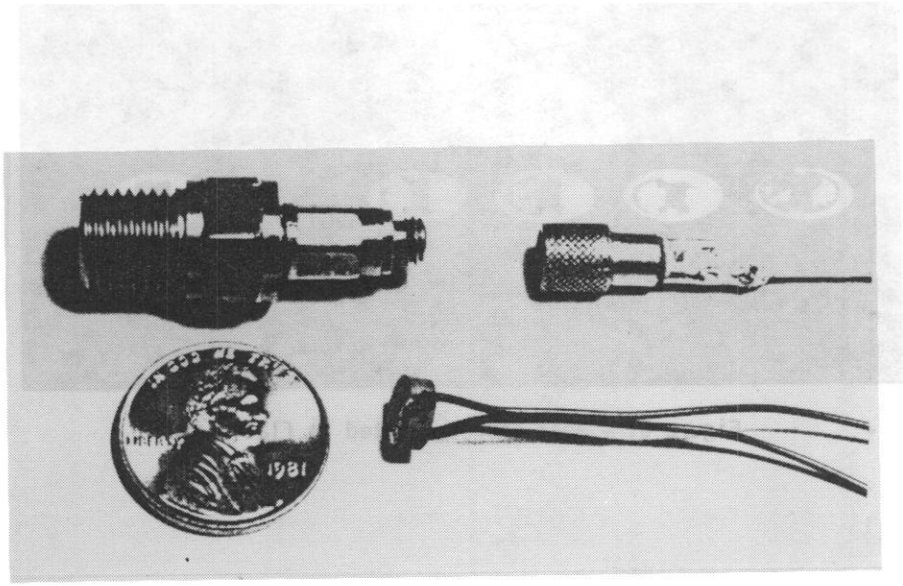

Figure 4. - Kistler type-603 quartz pressure gauge and lead-zirconate-titanate piezoelectric crystal.

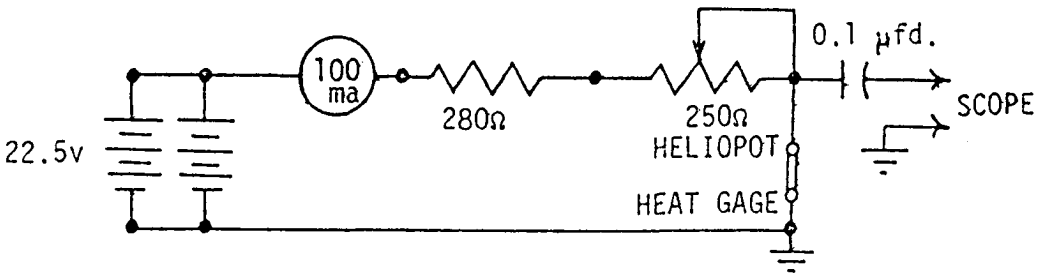

Figure 5. - Schematic of heat gauge power supply.

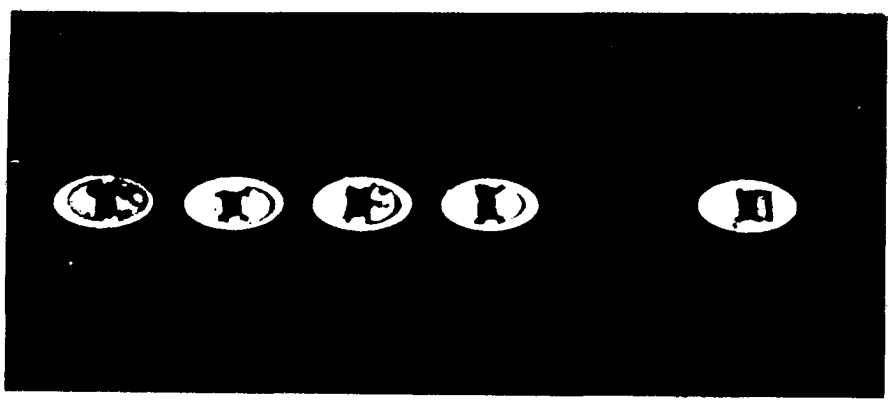

Figure 6. - Heat gauges mounted in flat plate.

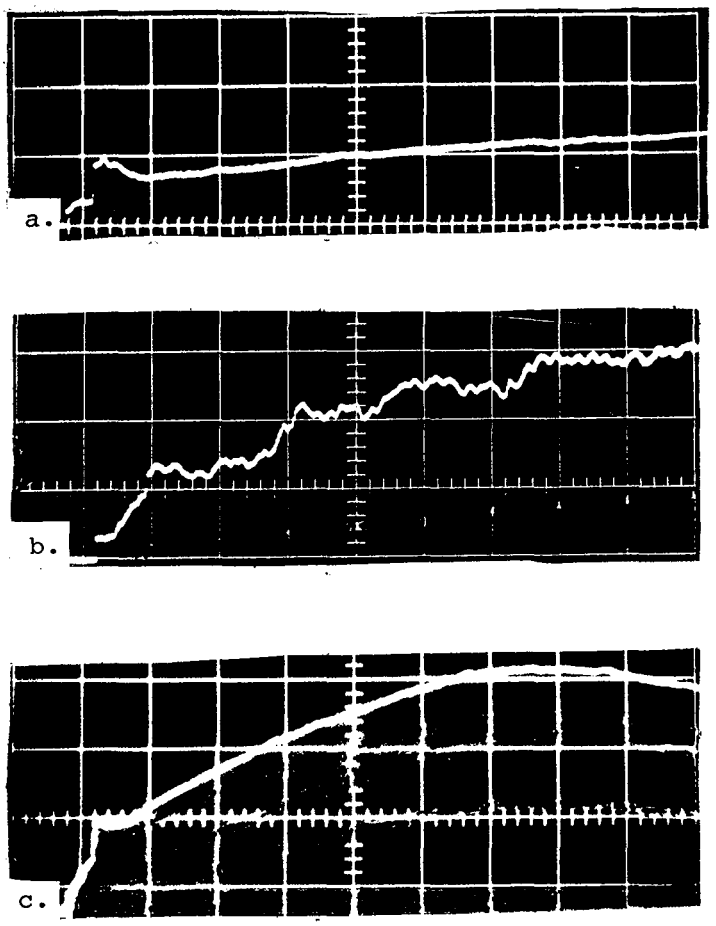

(a) Laminar, Re/cm = 698.
(b) Transition, Re/cm = 3000.
(c) Turbulent, Re/cm = 93 200.

Figure 7. - Heat gauge traces for laminar, transition, and turbulent boundary layers. M = 0.12; T_g = 405 K.

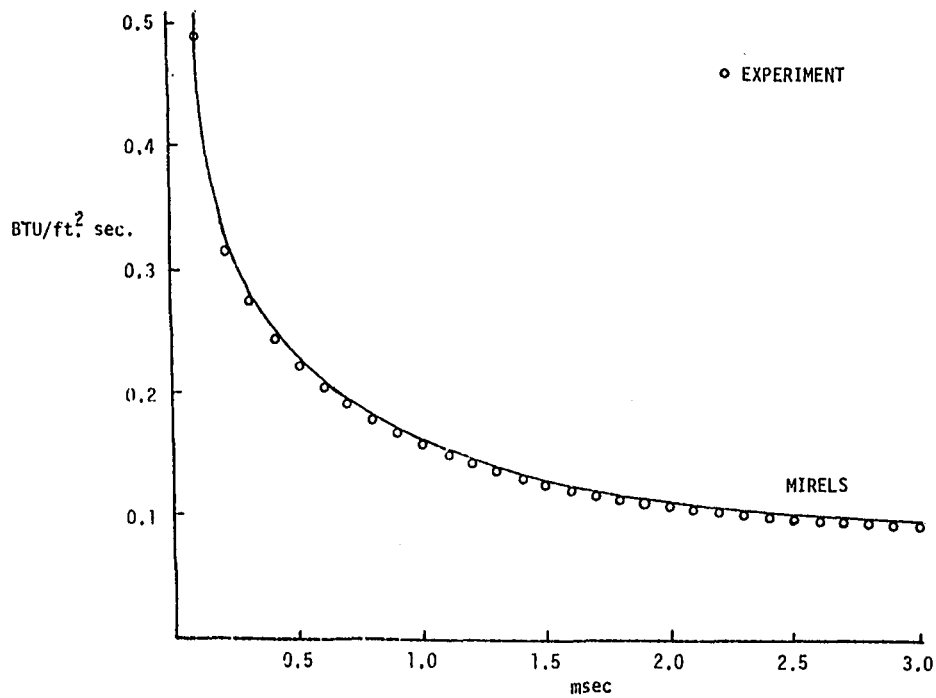

Figure 8. - Local heat transfer rate for laminar boundary layer. $M_2 = 0.697$; $T_2 = 409$ K; Re/cm = 2.48×10^3.

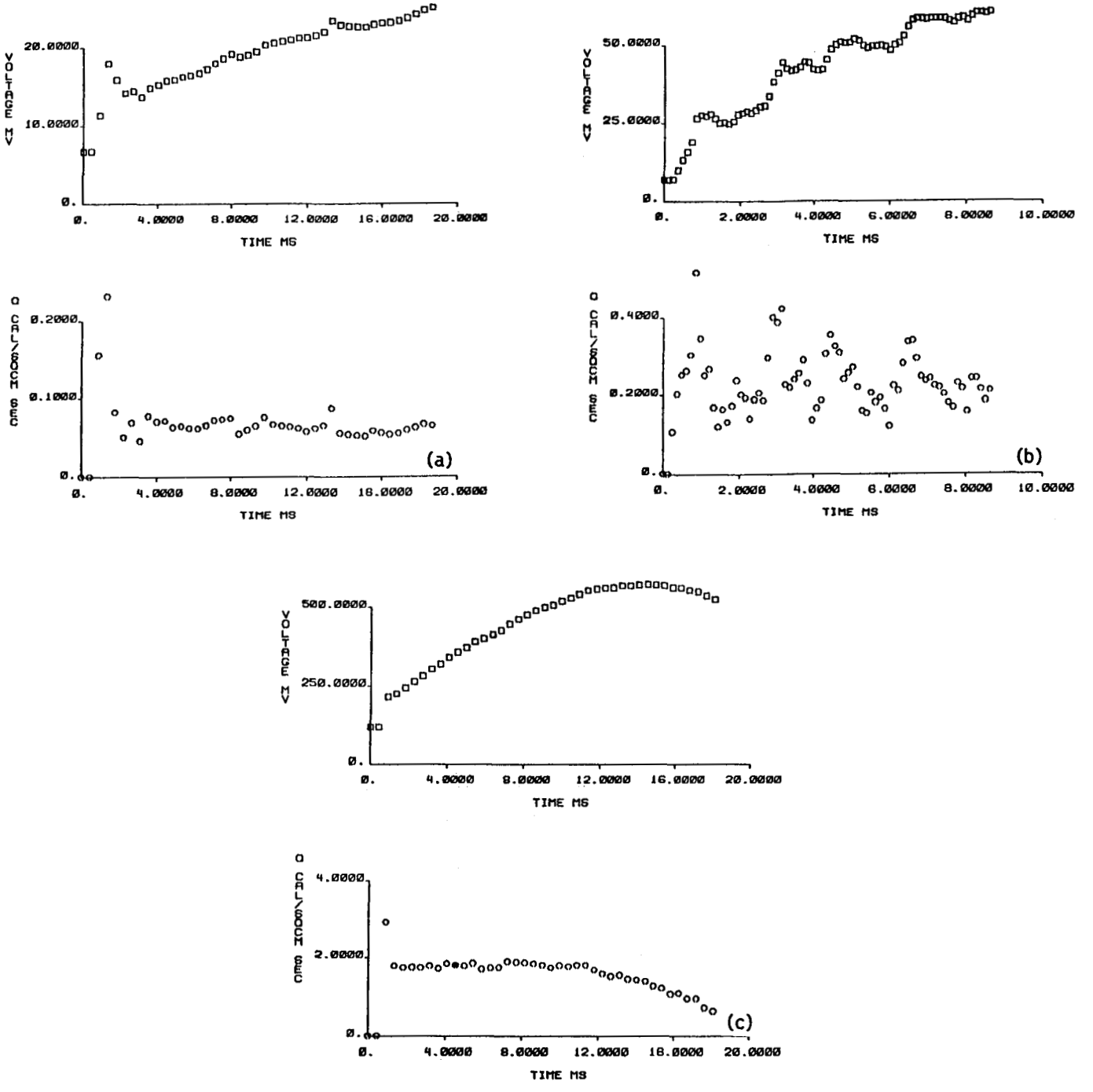

(a) T_g = 416 K; Re = 9.96×10^6.
(b) T_g = 405 K; Re = 4.72×10^4.
(c) T_g = 405 K; Re = 1.32×10^6.

Figure 9. - Digitized voltage traces and heat transfer for laminar boundary layer. M = 0.12.

FLAT-PLATE TRANSITION

Barbara A. Ercegovic
National Aeronautics and Space Administration
Lewis Research Center
Cleveland, Ohio 44135

A heat transfer workshop held at Lewis in 1980 highlighted the need for more transition research. Therefore in 1981 we began a new research effort to build a boundary-layer transition tunnel. This facility only recently became operational. The data obtained so far are merely qualitative. The main goal is to predict heat transfer given any combination of factors such as pressure gradient, turbulence level, Reynolds number, or intermittency factor.

The boundary-layer transition tunnel (fig. 1) is a closed-loop tunnel that controls the turbulence level, velocity, and temperature of the air within it. We may add the ability to control the unsteadiness. The lid of the test section is hinged and can be raised or lowered to set the test-section pressure gradient. The initial test surface is adiabatic, but we anticipate use of a heated or cooled test surface for investigating the effects of roughness or even curvature. The circuit (fig. 2) consists of a blower, a flow-conditioning box, a test section, a diffuser section, a damper valve, and an air heater. The return leg consists of an air filter box and a heat exchanger. The tunnel is essentially at atmospheric pressure, since the blower has a capacity of only about 3 kPa (12 in of H_2O). We can vary the air temperature within the tunnel from about 15 to 65 °C (60 to 150 °F), but any given run is done at isothermal conditions. We will be testing over the velocity range 3.5 to 35 m/sec (10 to 100 ft/sec). The pressure gradient can be adjusted anywhere from adverse to favorable. The test section has a cross section 15.5 cm high by 69 cm wide by 1.53 m long (6 in by 27 in by 5 ft). The static pressure distribution can be measured across the entire test surface. Thirty taps are located along the centerline 20 cm (8 in) on either side of center, with a slight concentration at the leading edge of the plate (fig. 3). The test surface is also instrumented with flush-mounted hot-film sensors, which are used to detect the transition. The hot-film sensors are concentrated along the centerline, with a few 15.5 cm (6 in) off center (fig. 4). Most centerline sensors are spaced 5.1 cm (2 in) apart.

A major problem with this facility has been the flow distribution along the tunnel cross section. Because of the blower exit geometry there is a high degree of nonuniformity in the flow field. Figure 5 shows contour lines at the exit of the blower, before the flow-conditioning box. Each line is a line of constant velocity. The goal was a variation from the mean velocity of no more than ± 2 percent. As shown, the pattern is very nonuniform at this location. The flow-conditioning box uses perforated plates, screens, baffles, and "soda straws" to straighten out the flow. At the exit to the flow-conditioning box (fig. 6), going into the contraction, the flow distribution is greatly improved. To achieve various levels of turbulence, four sets of grids (table I) can be inserted into the flow-conditioning box, one at a time. The grids go from fine (1) to coarse (4). The percentage of open area ranges from 61 to 65 percent. Turbulence intensities range from 0.46 percent with no grid

to 5.46 percent with the coarsest grid. This is for a free-stream velocity of about 16.8 m/sec (55 ft/sec).

A continuous oscilloscope trace of one sensor located on the centerline about 45 cm (18 in) from the leading edge (fig. 7) shows Tollmien-Schlichting waves. The free-stream velocity in this case was 17.7 m/sec (58 ft/sec). The frequency of these disturbances was about 225 Hz, which is in the range of the Tollmien-Schlichting disturbance. Upstream sensors showed purely laminar flow with lower amplitudes in the disturbance. Downstream sensors showed higher amplitudes and occasional turbulent bursts. Figure 8 shows traces of sensors 1, 2, 5, and 6, which are consecutive along the centerline of the test section. A turbulent burst is just entering upon sensor 1. It moves downstream and is picked up by the other sensors. The burst enlarges as it moves downstream. Figure 9 shows an oscilloscope trace of sensor 1, which is the first sensor on the centerline. The other three traces are for sensors 26, 27, and 28, which are the first three to the left of the centerline. A turbulent burst approaches sensor 26, moves on to sensors 27 and 28, and breaks down into turbulence. Since the turbulence does not appear on sensor 1, whatever is on sensor 1 does not necessarily show up on sensor 26.

The remainder of the information contained herein is only qualitative and gives an idea of the type of data we will be able to obtain. Figure 10 shows the intermittency factor as a function of X, where intermittency is defined as the fraction of time that the flow is turbulent at any given location. For an intermittency factor of 1 the flow is fully turbulent. At the lowest Reynolds number and $X = 56$ cm (21 in), the intermittency factor is just beginning to increase above the zero (laminar) level. As the Reynolds number increases, this initial increase in intermittency factor moves upstream. Therefore as the Reynolds number increases, the onset of transition occurs earlier. Figure 11 is a plot of the rms fluctuating output divided by the relative dc output as a function of X. The y-axis variable is a qualitative representation of the level of the fluctuation; it gives the starting location and shows the length of the transition zone. The voltage peaks within the transition region. At the lowest Reynolds number, about 300 000, the voltage begins to increase at $X = 56$ cm (21 in) but has not yet peaked. At a Reynolds number of 428 000, the voltage has begun to pick up, has peaked, and is dropping again at $X = 56$ cm (21 in). At the highest Reynolds number, 500 000, at $X = 10$ cm (4 in), the fluctuating voltage starts at a higher level, peaks, and then drops off and remains fairly constant at a level higher than that before the transition. Figure 12 is a plot of intermittency factor as a function of X for a unit Reynolds number of 1 500 000/m (490 000/ft). The pressure gradient K was varied within the test section by changing the position of the lid. For $K = 0$ the intermittency is about 0.22 (i.e., transition has already started). At $X = 31$ cm (12 in), the flow is fully turbulent. For accelerated flow (i.e., positive values of K), transition is delayed downstream (e.g., for $K = 13.8 \times 10^{-8}$). For decelerated flow (i.e., negative values of K), the starting point of the transition moves upstream, and the flow becomes fully turbulent at successively earlier locations on the flat plate. Figure 13 is a plot of the same data with the rms voltage over the dc output as a function of X. Again, for $K = 0$ the flow has already started into transition at $X = 15.5$ cm (6 in) since it has peaked and dropped off. As K becomes positive, transition is delayed. As K becomes negative, the start of transition is pushed much farther upstream. The initial increase in the fluctuating voltage occurs at successively smaller values of X as K becomes increasingly negative.

TABLE I. - TURBULENCE LEVELS DOWNSTREAM OF CONTRACTION

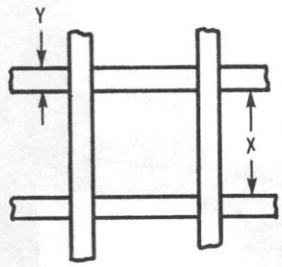

Grid	Ratio of space to width of bar, X/Y	Open area, percent of total area	Turbulence, percent
0	(a)	100	0.46
1	0.69/0.19	62	.98
2	2.06/0.50	65	2.06
3	5.50/1.50	62	4.58
4	7.00/2.00	61	5.46

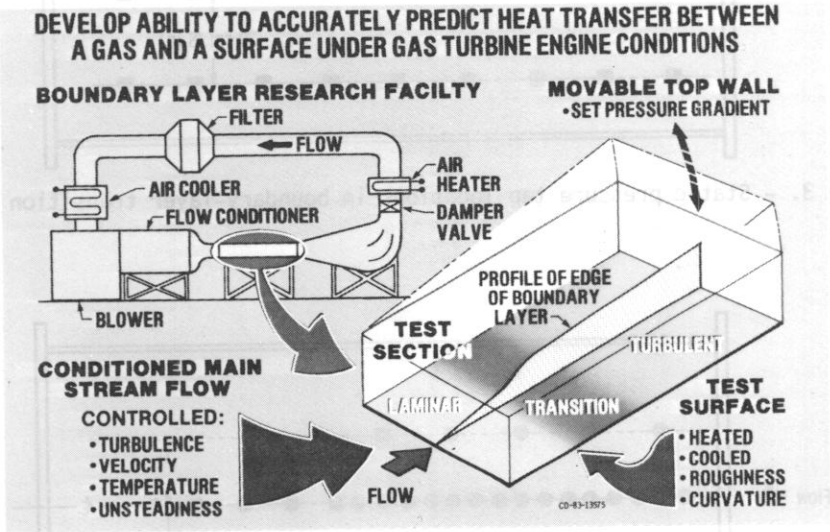

Figure 1. - Boundary-layer research.

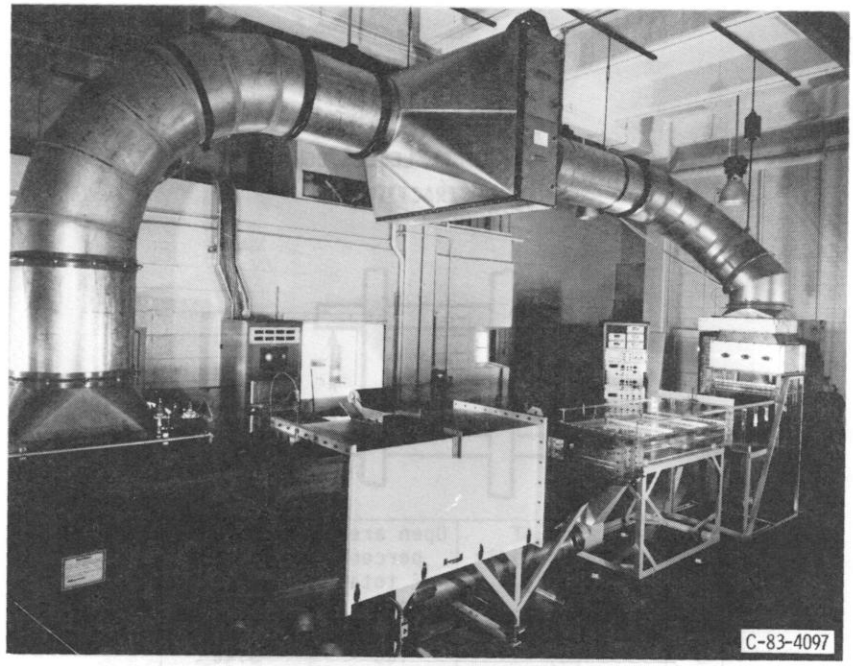

Figure 2. - Test facility.

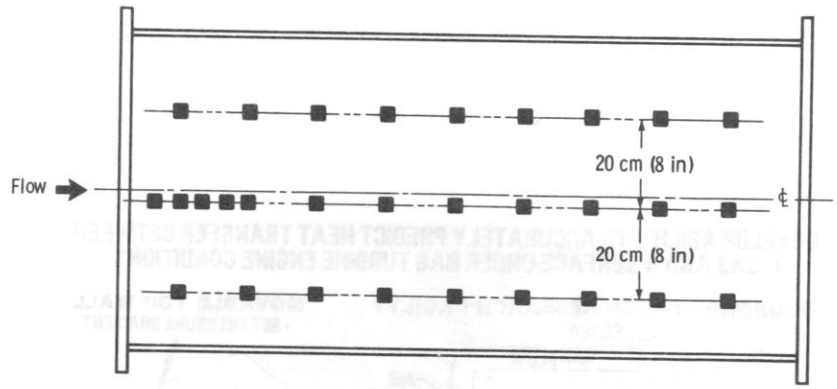

Figure 3. - Static pressure tap locations in boundary-layer transition tunnel.

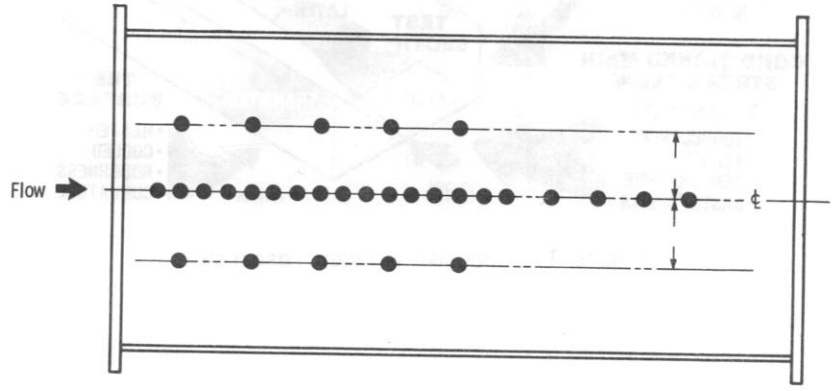

Figure 4. - Thin-film sensor locations in boundary-layer transition tunnel.

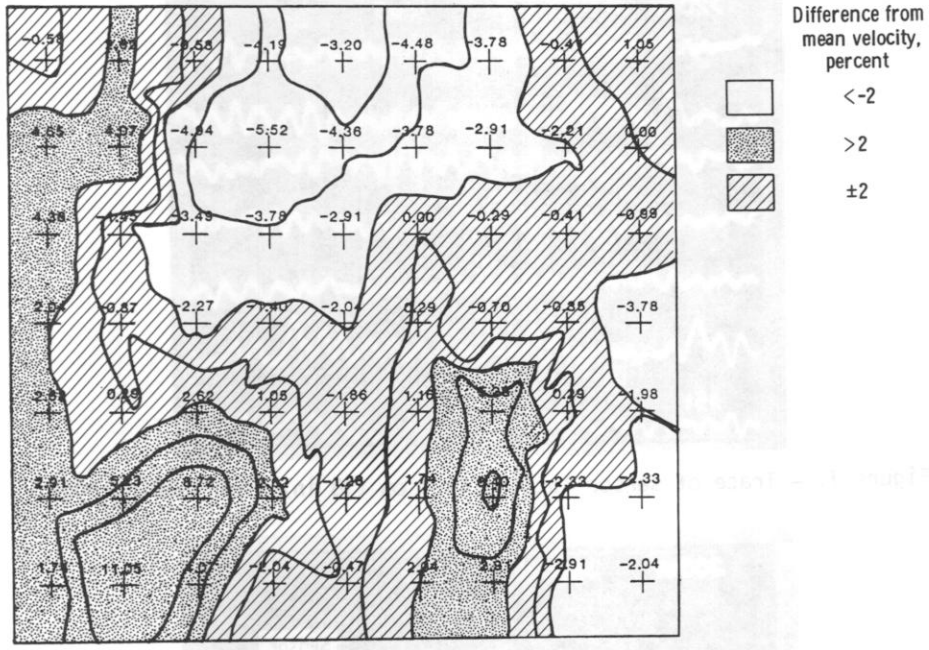

Figure 5. - Contour lines at blower exit.

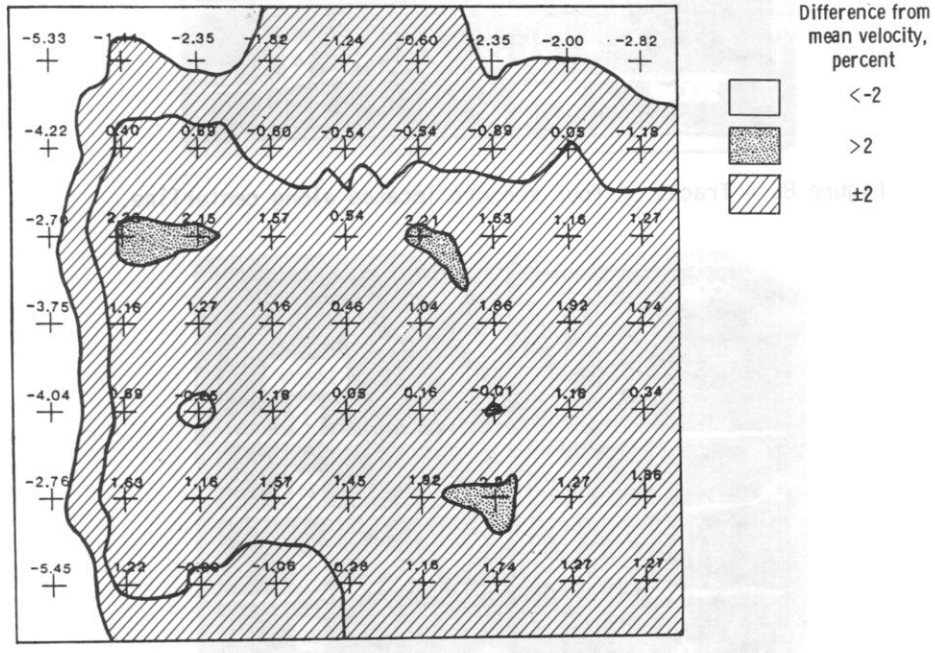

Figure 6. - Contour lines at exit of flow-conditioning box.

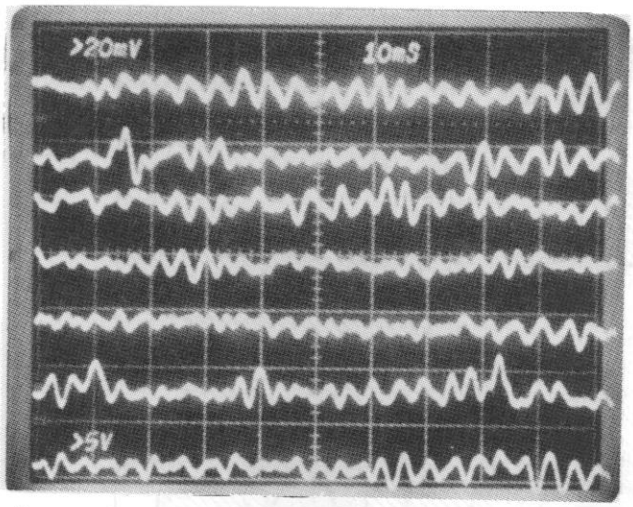

Figure 7. - Trace of sensor located 45.7 cm (18 in) from leading edge.

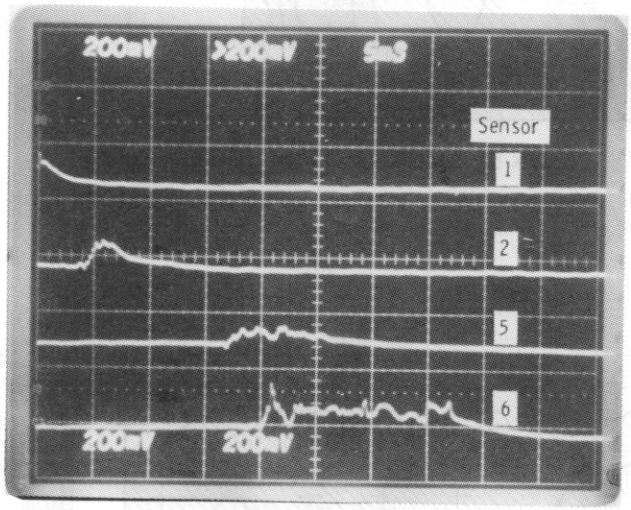

Figure 8. - Traces of four sensors located along centerline.

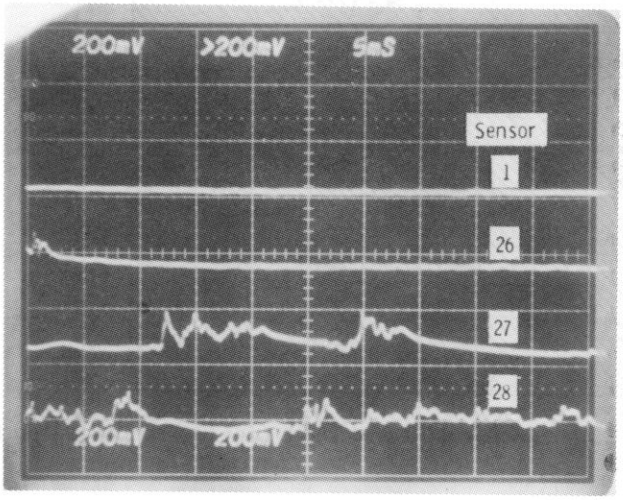

Figure 9. - Traces of four sensors on and to left of centerline.

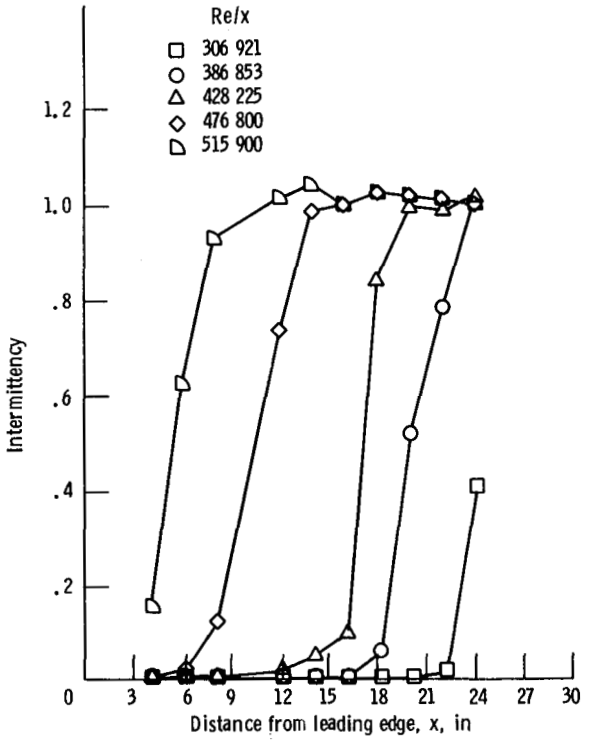

Figure 10. - Intermittency as function of distance from leading edge.

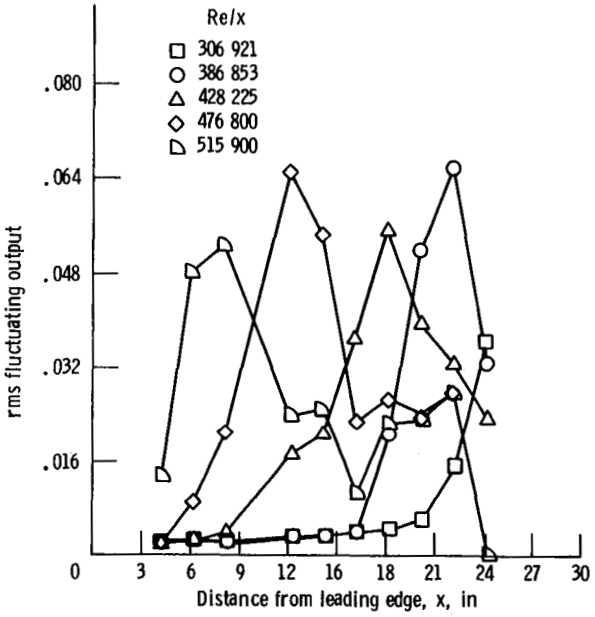

Figure 11. - rms fluctuating output as function of distance from leading edge.

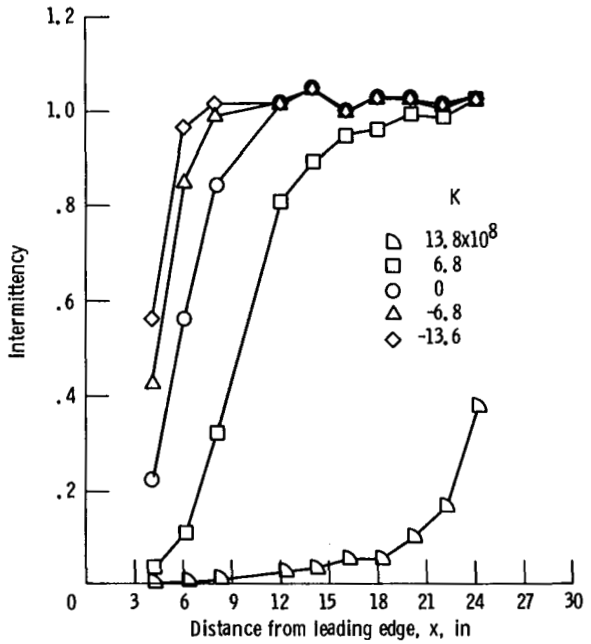

Figure 12. - Intermittency as function of distance from leading edge for Re/x = 490 000.

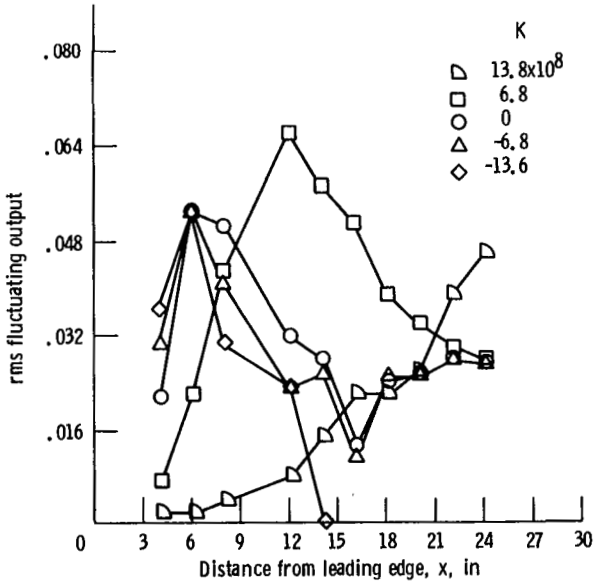

Figure 13. - rms fluctuating output as function of distance from leading edge for Re/x = 490 000.

HEAT TRANSFER AND FLUID MECHANICS MEASUREMENTS IN TRANSITIONAL BOUNDARY LAYER FLOWS

T. Wang
Clemson University
Clemson, South Carolina 29631

T.W. Simon
University of Minnesota
Minneapolis, Minnesota 55455

J. Buddhavarapu
TSI Inc.
St. Paul, Minnesota

ABSTRACT

Experimental results are presented to document hydrodynamic and thermal development of flat-plate boundary layers undergoing natural transition. Local heat transfer coefficients, skin friction coefficients, and profiles of velocity, temperature, and Reynolds normal and shear stresses are presented. A case with no transition and transitional cases with 0.68% and 2.0% free-stream disturbance intensities were investigated. The locations of transition are consistent with earlier data. A late-laminar state with significant levels of turbulence is documented. In late-transitional and early-turbulent flows, turbulent Prandtl number and conduction layer thickness values exceed, and the Reynolds analogy factor is less than, values previously measured in fully turbulent flows.

NOMENCLATURE

c_p	Specific heat
$C_f/2$	Skin friction coefficient
Pr	Prandtl number
Pr_t	Turbulent Prandtl number
$\dot{q}''$	Heat flux
Re_x	x-Reynolds number
$Re_{\delta*}$	Displacement thickness Reynolds number
Re_θ	Momentum thickness Reynolds number
St	Stanton number
TI	Turbulence intensity
T^+	$\dfrac{(T_w - T)\sqrt{\tau_w/\rho}}{\dot{q}''/(\rho c_p)}$
u, v	Streamwise and cross-stream velocity
u', v'	Streamwise and cross-stream velocity fluctuations
$\overline{u}$	Streamwise mean velocity
U_τ	Friction velocity ($\equiv\sqrt{\tau_w/\rho}$)
U^+	$\equiv \overline{u}/U_\tau$
x	Streamwise distance
y	Cross-stream distance from the wall
Y^+	Inner coordinate, $\equiv \dfrac{y\,U_\tau}{\nu}$
$Y^+_{c\ell}$	Conduction layer thickness in inner coordinates
z	Spanwise distance from center-span

Greek

ρ	Density
τ	Shear stress
ν	Kinematic viscosity
δ_{99}	Boundary layer thickness based on 99% of the free-stream velocity
δ^*	Displacement thickness
θ	Momentum thickness
Λ_θ	Acceleration parameter, $\dfrac{\theta^2}{\nu}\dfrac{dU_\infty}{dx}$

Subscripts

∞	at free stream
w	at wall

INTRODUCTION

Transition from laminar to turbulent boundary layer flow effects significant increases in local wall shear stresses and convective heat transfer rates. These increases must be appropriately factored into the design of many types of equipment, e.g. compressor and gas turbine blades. Presently, the poor predictability of the location and streamwise coverage of transition on gas turbine blades results in either reduced longevity of the blade or reduced performance of the engine below design objectives. This inability to predict transition is partially due to a lack of experimental data, both heat transfer and hydrodynamic, which isolate the separate effects on transition. This, in turn, has retarded the endeavor to understand the transition process and to develop general prediction models. Some effects which are known to influence boundary layer transition are free-stream turbulence, acoustic disturbances, surface vibration, surface roughness, streamwise acceleration, cross-stream straining, film cooling injection,

separation, compressibility effects, and streamwise curvature. Some characteristics of boundary layer transition which tend to exacerbate the difficulty in understanding the fundamentals are three-dimensionality; unsteadiness; interaction of several influences; and sensitivity to small influences which are not under the control of the experimenter or known to the designer. As much as 50-80% of a typical turbine blade surface is covered by flow undergoing transition (1). It is therefore important that a program of systematic, well-controlled experimental studies be initiated to provide the data base necessary for developing improved transition prediction models.

The present experiment focuses on the effect of free-stream turbulence intensity and includes measurements of surface heat transfer rates as well as profiles of mean and turbulence quantities in the laminar, transitional, and turbulent flows. This test is the beginning of a series of tests which isolate the effects of free-stream turbulence intensity, streamwise acceleration, and streamwise curvature on transition. It is part of an ongoing series of experimental investigations on gas turbine heat transfer at the Heat Transfer Laboratory of the University of Minnesota.

As early as 1936. G. I. Taylor (2) analyzed free-stream turbulence effects on transition for flow past a sphere. His work is believed to be the first where the effects of free-stream disturbances on transition were discussed. Early experiments of boundary layer transition on a flat plate were made by Hall and Hislop (3). Van Driest and Blumer (4) developed an early prediction model by assuming that the breakdown of laminar flow occurs whenever the maximum of the local cross-span vorticity in the boundary layer becomes sufficiently distant from the wall. Their model, which accounts for free-stream turbulence and streamwise acceleration effects, is still considered one of the better predictors of transition (5). Several constants in their model were determined from existing experimental data. Later, as more data became available, these constants were adjusted somewhat, e.g. (6). A forced-oscillation method for investigating boundary layer transition was introduced by Schubauer and Skramstad (7) to demonstrate the growth and evolution of disturbances in laminar flows. They concluded that when the free-stream turbulence intensity exceeds 0.1%, transition is caused directly by random disturbances and is not precluded by selective amplification of sinusoidal oscillations (as with lower-disturbance flows). Klebanoff, Tidstrom, and Sargent (8) observed that, in low-disturbance flows, an initially two-dimensional wave, the growth of which is predictable by linear theory of instability, develops three-dimensionalities--a feature of strong nonlinear development. The termination of this development is indicated by a sudden increase in the wave amplitude. Spangler and Wells (9) studied the importance of the frequency spectra and the origin of the disturbance (e. g. acoustic) on transition in low free-stream turbulence intensity flows (<0.10%). They determined the disturbance intensity, versus disturbance frequency, required to initiate transition. A review of the understanding and prediction of transition, current to 1969, was presented by Tani (10).

An empirical model for predicting the onset and end of transition was proposed by Hall and Gibbings (11). It included the effects of free-stream turbulence and streamwise pressure gradient. Recently Abu-Ghannam and Shaw (12) developed an empirical relationship for the prediction of the start of transition, the end of transition and the development of momentum thickness, shape factor, intermittency factor, and skin friction coefficient during transition. The sole parameters in their model are the free-stream turbulence intensity and the free-stream acceleration.

In the gas turbine environment, free-stream turbulence intensities are in the range 5-20%. To the authors' knowledge, few detailed transition studies have been conducted in such highly turbulent flows. Dyban, Epik, and Suprun (13) investigated the structure of laminar boundary layers developing under elevated free-stream turbulence intensities from 0.3% to 25.2%. They found a peak in oscillation magnitude within the boundary layer, believed to be caused by the penetration of free-stream fluctuations. This peak amplitude reached a maximum in the 4.5% free-stream turbulence intensity case. The waveform of this oscillation was not sinusoidal but more turbulent-like with energy distributed across a wide range of frequencies. They called the late-laminar boundary layers which show this behavior "pseudo-laminar" to separate them from the laminar and transitional boundary layers which are considered to be fundamentally different. The authors know of few other experiments where the turbulence (oscillation) development for natural transition through the laminar, "pseudo-laminar", transitional, and turbulent stages was documented (14, 15). More on transition can be found in Refs. (16-19).

The above studies are for isothermal flows. The following are studies of heat transfer in transitional flows: Junkhan and Serovy (20) conducted experiments on a constant-temperature flat plate to investigate the effect of free-stream turbulence intensity on heat transfer through transitional boundary layers. They found no effects of free-stream turbulence intensity within the laminar flow--only the well-documented effect on the location of transition. Simon and Moffat (21) measured heat transfer rates in a boundary layer which was undergoing transition on a convex-curved surface. They concluded that the onset of transition was delayed and that the evolution of transition was retarded by convex curvature. Recently, Blair (22, 23) conducted several tests on a uniformly heated flat wall where free-stream turbulence intensities were varied over the range 0.7% to 6.0%. He concluded that fully turbulent mean velocity profiles were established faster than fully turbulent mean temperature profiles. This indicates a breakdown of the Reynolds analogy and a larger effective turbulent Prandtl number in the very early turbulent flow than in a mature turbulent flow. He also showed that the transition Reynolds number is insensitive to streamwise acceleration for $\Lambda_\theta < 0.08$ over this turbulence intensity range. This is consistent with the van Driest and Blumer model.

In the present study, Reynolds streamwise-normal stresses were measured in addition to surface heat transfer coefficients and mean velocity and temperature profiles to show the evolution of the turbulence structure inside laminar, transitional, and turbulent boundary layers during natural transition. Reynolds shear stresses were measured in the early-turbulent boundary layer. Two free-stream turbulence intensity levels, 0.68% and 2%, were investigated. The streamwise pressure gradients in the three tests were small, and believed to be insignificant, with $\Lambda_\theta < 0.02$. Values in excess of 0.05 are needed to have a perceptible effect on the location of transition for these free-stream turbulence intensity values (4).

EXPERIMENTAL FACILITY

The test program employed the open-circuit, boundary layer heat transfer facility shown in Fig. 1. Air is first drawn through 5 μm filter material to a large centrifugal blower, then forced through a finned-tube heat exchanger and screen pack assembly to enter the test region. Free-stream nominal velocities were

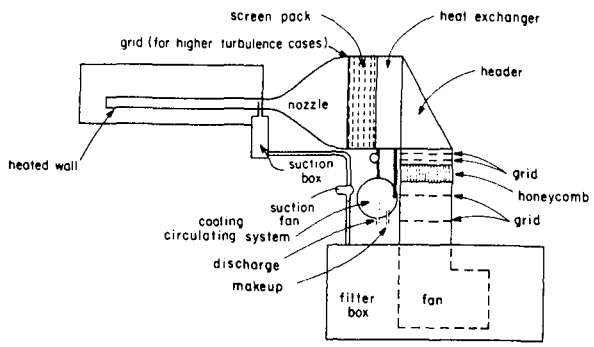

FIG. 1 PLAN VIEW OF TEST FACILITY

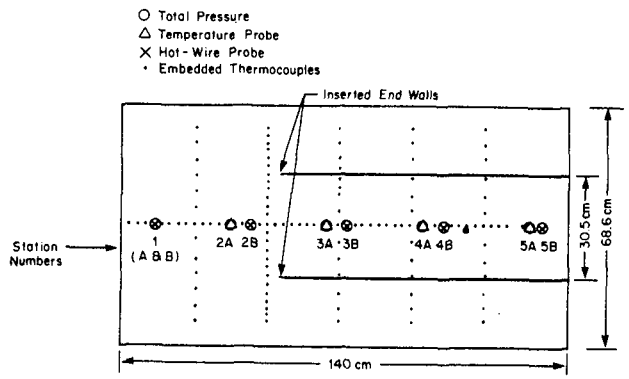

FIG. 2 MEASUREMENT LOCATIONS - HEATED BOUNDARY LAYER FLOW DATA TAKEN AT "A" STATIONS AND ISOTHERMAL FLOW DATA TAKEN AT "B" STATIONS

12 m/s and 35 m/s, uniform to ± 0.2% across the tunnel cross-section, for the present experiment, and the free-stream temperature was nominally 25°C, uniform to ± 0.05°C and constant to within ± 0.2°C. The room temperature was held constant to within ± 0.5°C. The test region is rectangular, 11.4 cm x 68.6 cm (4.5 inches x 27 inches) in cross-section, and 1.4 m (55 inches) long. The test section was designed and constructed so that transition data with streamwise wall curvature could eventually be taken. For this straight-wall study, it was necessary to insert end-walls beginning with sharp leading edges after 50 cm of the streamwise length and continuing throughout the remainder of the test region. These inserted end-walls reduced the effective span from 68.6 cm to 30.5 cm as shown in Fig. 2. One side wall of the tunnel, 68.6 cm x 1.4 m, was heated to nominally 10°C above the oncoming air temperature with a heat flux of 240 W/m^2, uniform to ± 1.0%.

This is the heated, flat wall upon which data for the present study was taken. Strong suction was applied at the leading edge of this wall to remove the boundary layer which grows inside the nozzle. Therefore, the initial flow on the test wall simulated the classical sharp-leading-edge configuration. The heated test wall is flexible so that transition studies with

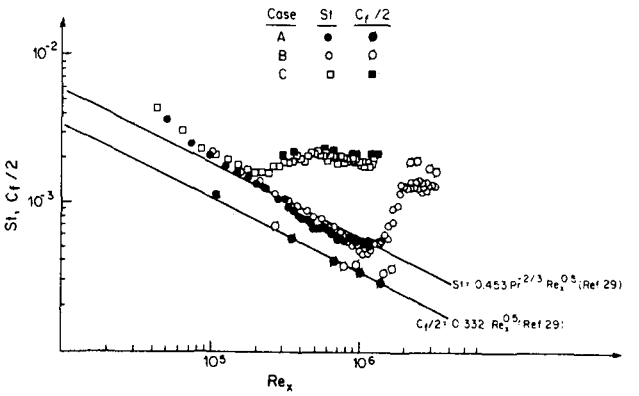

FIG. 3 STANTON NUMBERS AND SKIN FRICTION COEFFICIENTS VS. x-REYNOLDS NUMBER

varying degrees of streamwise curvature could later be taken. The description of this heated wall follows. It begins with the surface adjacent to the room (the outside) and proceeds to the test surface (the inside). A 15.2 cm (6 inch) thick fiberglass insulation pad was installed on the outside of a 5 mm (3/16 inch) thick polycarbonate plastic (Lexan) support wall to minimize heat transfer to the room. Attached to the inside of the support wall is a 1 mm (0.045 inch) thick heating pad constructed of heater foil sandwiched between glass cloth and silicon rubber sheets. The foil provides Joule heating when energized with 60-cycle AC current using variable transformer voltage control. Bonded to the heater is a 0.25 mm (10 mil) thick rubber spacer within which 120, 3-mil, chromel-constantan thermocouple wires were embedded. These thermocouples are distributed along the wall center-span, with a 2.54 cm (1 inch) spacing, and were uniformly distributed across the span at five streamwise locations (see Fig. 2). Covering the thermocouples, in contact with their junctions, and bonded to the spacer, is a 0.1 mm (4 mil) thick sheet of stainless steel. Bonded to the stainless steel and providing the test surface is a 0.025 mm (1 mil) thick sheet of reflective film. This film, type P-19 manufactured by the 3M Company, was added to reduce the uncertainty attributable to radiation exchange with the test wall.

The free-stream and boundary layer mean temperatures were measured with 3-mil thermocouples constructed of wire from the same manufacturing run as that of the embedded thermocouples. The thermocouples were calibrated in the tunnel against a calibrated, precision thermister known to be stable by continued comparison against a platinum resistance thermometer in the calibration laboratory. Mean velocity profiles were measured using 0.7 mm (28 mil) O.D. boundary layer total pressure tubes, 0.063 mm (2.5 mil) wall static ports, and a ± 9 cm H_2O maximum pressure, reluctance-type, diaphragm differential pressure transducer (Validyne DP-45). Mean velocity measurements were taken in both heated and isothermal flows. Small variations in properties were included in the data reduction; the mean of the wall and free-stream temperature was used for property evaluation. Reynolds normal stresses were obtained in the isothermal flow with a horizontal hot-wire (TSI Model 1218, T1-5) maintained at a constant temperature. Reynolds shear stresses were taken in isothermal flows using a boundary layer X-wire (TSI Model 1243, T 1.5) with constant-tempera-

ture operation. The anemometer bridges were TSI Models 1050 and IFA-100. The pressure transducer and anemometer signals were digitized with an H-P Model 3437A, 3-1/2 digit voltmeter. Because only one digitizer was available, the shear stress measurements were taken one-wire-at-a-time. This is essentially the rotating slant-wire technique (24). Thermocouple EMF values were recorded with a Fluke Model 2205A multi-channel scanner. The total power supplied to the heater was computed as the product of a power factor, the measured voltage across the heater, and the current through the heater computed from the measured voltage across a precision resistor. The power factor, measured prior to the test, was within 0.1% of 1.0. Data was reduced in a HP Series 200 Model 16 laboratory computer.

Corrections were made within the data reduction program for heat transfer through the fiberglass insulation, radiation exchange with the test wall, and streamwise conduction within the heated wall. A complete uncertainty analysis of the wall heat transfer data was also made within the data reduction program. This analysis employed the Kline and McClintock (25) methodology for computing the propagation of uncertainties and the Moffat (26) methodology for incorporating known contributors to bias error. Nominal values of wall heat flux uncertainty are presented along with other relevant uncertainties in Table 1. Details of the heater design, data reduction techniques, and wall heat flux uncertainty analysis can be found in Refs. (27, 28).

EXPERIMENTAL RESULTS AND DISCUSSION

The results of the following three cases are presented herein:

A. The Laminar Baseline Case (Turbulence Intensity, TI = 0.3%) - The laminar boundary layer extends over the entire test length. Transition correlations and the unsteadiness of the data indicate that transition is about to begin at the channel exit.

B. The Lower Free-Stream Turbulence Intensity Case (TI = 0.68%) - The velocity is increased from that of Case A and the onset of transition is moved to about one-third of the test length.

C. The Higher Free-Stream Turbulence Intensity Case (TI = 2.0%) - A coarse grid is inserted upstream of the nozzle and the free-stream velocity is reduced to move the onset of transition into the first one-third of the test length.

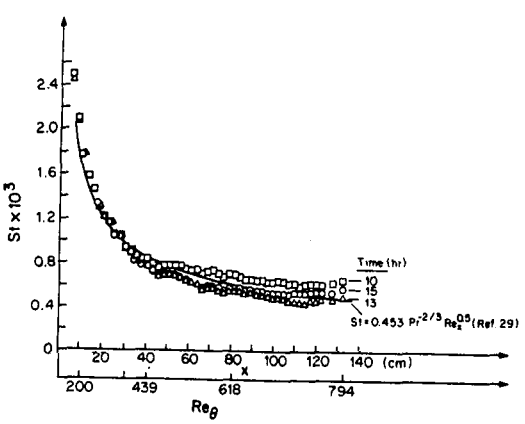

FIG. 4 LONG-PERIOD UNSTEADINESS OF STANTON NUMBER DATA FOR CASE A

Variables	Range	Uncertainty
St in the laminar & turbulent region	$0.2 \sim 5.x10^{-3}$	± 2%
St in the transition region	$0.2 \sim 2.x10^{3}$	± 3%
Mean Velocity	0 ~ 35 m/s	± 2%
Mean Temperature	20 ~ 40 C	± 0.1°C
$\sqrt{\overline{u'^2}}/U_\infty$	0.1 ~ 11%	± 5%
$\overline{u'v'}/U_\tau^2$	0 ~ 1	± 10%
C_f (other than in transition)	$0.2 \sim 2.0x10^{-3}$	± 5%

TABLE 1 MEASUREMENT UNCERTAINTIES

A. The Laminar Baseline Case - Case A

The test facility was first qualified by conducting an all-laminar boundary layer test. A comparison of the results to laminar boundary layer theory (29), Fig. 3, shows that the Stanton numbers and skin friction coefficient values for this case follow the laminar correlation well, except at the very end of the test where it appears that transition is near. Stanton numbers for this and the subsequent cases were calculated directly from the measured (and corrected) wall heat flux and the measured local free-stream velocity, free-stream temperature, and wall temperature. The wall temperature was taken as an average of five readings over a period of fifteen minutes. Skin friction coefficients were computed from the wall shear stress; which, in turn, is calculated from the local near-wall velocity gradient, $\tau_w = \mu(du/dy)_w$; and the local free-stream velocity. One unanticipated result in this experiment was the long-period unsteadiness shown in Fig. 4. Three sets of data were taken in one fifteen-hour run. The first was taken after a ten-hour stabilization period as was also required for case B and case C. As shown, the data fluctuated ± 10% about the laminar line. The mean data of the 5-hour data-taking period follow the laminar correlation well. The curve labeled "15-hour" is the data shown on Fig. 3. The theoretical stability limit for laminar boundary layer flow for a flat plate is $Re_\theta = 200$ (30) which, for this case, corresponds to 10 cm of development length and an x-Reynolds number of 0.97×10^5. Note that the Stanton number data remains repeatable for the first 30 cm ($Re_\theta = 400$) within the 5-hour data-taking period. The unsteadiness of this flow is presumed to be due to the sensitivity of this boundary layer to small disturbances to the flow in the face of a low free-stream turbulence intensity of 0.3%. Possibilities would include the small variations in free-stream and wall temperatures (within the stated uncertainties) or small uncontrolled variations in tunnel vibration. Subsequent runs taken under these conditions over a period of one month showed that this long-period unsteadiness is repeatable. Long-period unsteadiness was not observable in cases B and C of this study, which have turbulence intensities of 0.68% and 2.0% respectively.

Spanwise variations of Stanton number for five streamwise positions are shown on Fig. 5. At the first two positions, the heat transfer coefficient is very spanwise-uniform; the stable laminar boundary layer is two-dimensional. Transition appears to begin as streaks off center-span. It symmetrically migrates toward the center-span. Transition is believed to be triggered in the three-dimensional corner flow region near the end-wall. It then is believed to propagate by acoustic disturbance toward the center as discussed in Ref. (31). No spanwise data is shown for the region beyond the inserted end-walls (see Fig. 2).

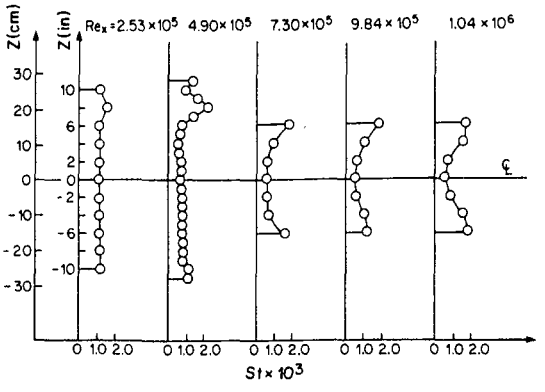

FIG. 5 SPANWISE DISTRIBUTIONS OF LOCAL STANTON NUMBER FOR CASE A (BASELINE CASE)

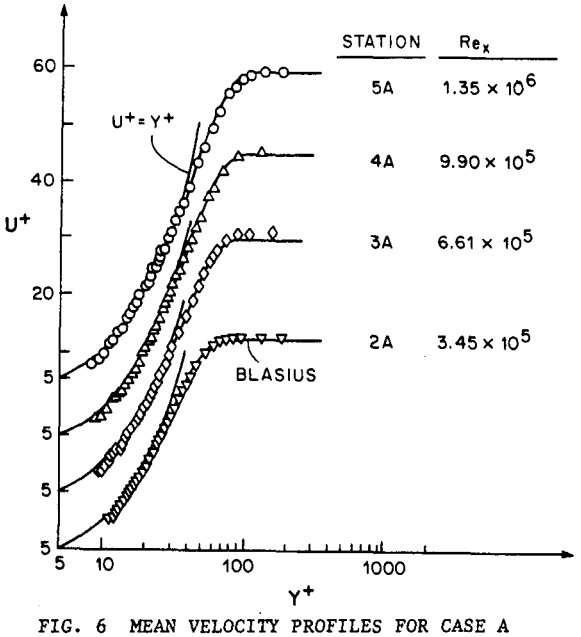

FIG. 6 MEAN VELOCITY PROFILES FOR CASE A

At the end of the test section, the momentum thickness Reynolds number is approximately 800. According to the transition model of van Driest and Blumer (4), transition should begin about $Re_\theta = 890$ for a case having a free-stream turbulence intensity of 0.3%; the flow is very near transition.

Mean velocity and mean temperature profiles plotted in inner coordinates, U^+ v.s. Y^+ and T^+ v.s. Y^+, are shown on Figs. 6 and 7, respectively. They appear to be typical laminar boundary layer profiles. Blasius velocity profiles are shown for comparison on Fig. 6. Mean velocity and temperature data were taken for this run and subsequent runs as time-averages over 30-40 second periods.

A thermal energy balance applied over the entire test length using the time-average Stanton numbers on the centerline assuming two-dimensional flow achieved closure to within 3%. This closure, the nearness of the Stanton number data to the laminar correlation, and the lack of premature transition in this case suggest that the facility is free of significant, uncontrolled disturbances and that the measurements are free of significant bias error. A momentum balance was also attempted; the lack of closure was 30%.

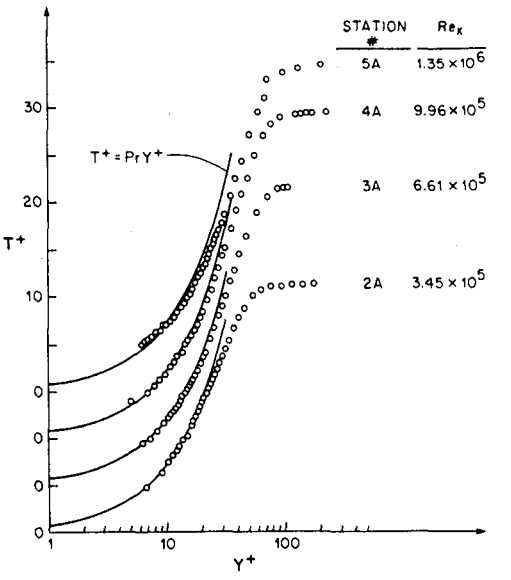

FIG. 7 MEAN TEMPERATURE PROFILES FOR CASE A

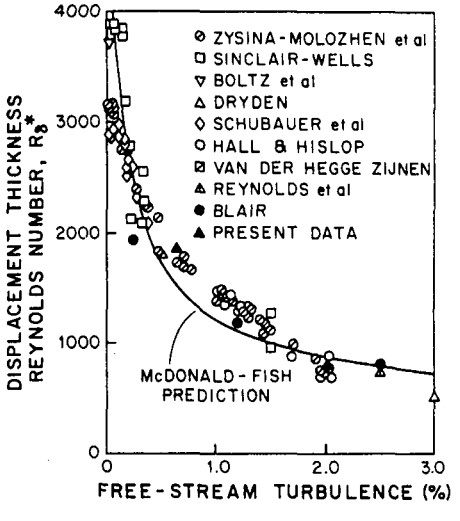

FIG. 8 EFFECT OF FREE-STREAM TURBULENCE ON TRANSITION REYNOLDS NUMBER FOR ZERO PRESSURE GRADIENT FLOW (FROM REF. 22)

This poor closure is believed to be due to the sparcity and inaccuracy of the skin friction coefficients deduced from velocity profiles, the inability to measure time-average skin friction coefficients (as was done with the Stanton number data for the energy balance), and the inability to measure momentum thicknesses with low uncertainty. Note that because of the sparce skin friction data, a momentum balance from only the first profile station to the last could be taken. This required taking precise measurements of the momentum thickness in the very thin laminar boundary layer at the first station. Such a problem did not exist with the thermal energy balance which was taken from the leading edge to the last station.

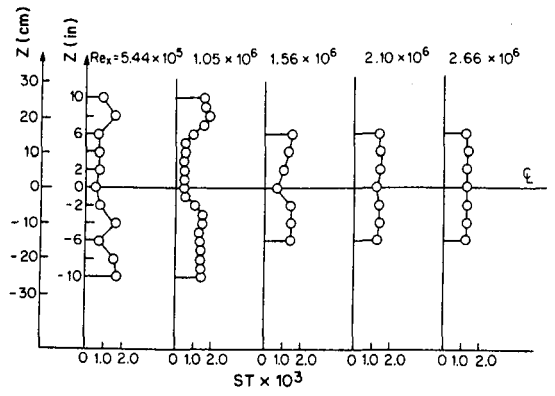

FIG. 9 SPANWISE DISTRIBUTION OF LOCAL STANTON NUMBER FOR CASE B

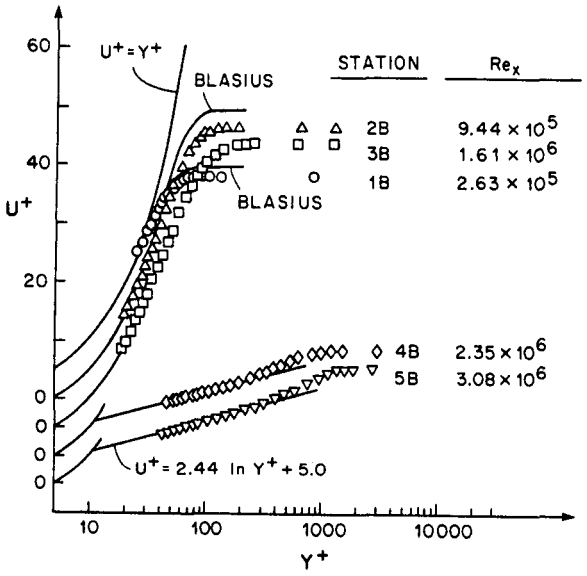

FIG. 10 MEAN VELOCITY PROFILES FOR CASE B

B. The Lower Free-Stream Turbulence Intensity Case - Case B

In the second case, the free-stream velocity was increased to nominally 35 m/s which moved the location of the beginning of transition to about one-third of the test length. The resulting free-stream turbulence intensity became 0.68%. Stanton number and skin friction coefficient data for this case are shown on Fig. 3. Transition, taken to be the beginning of the dramatic increase in heat transfer coefficient and shear stress, is shown to be at an x-Reynolds number of about 1.2×10^6. At this location the displacement thickness Reynolds number is 1890. Transition at this location is consistent with the van Driest and Blumer (4) model or the McDonald and Fish (32) model (shown on Fig. 8). The skin friction coefficient and Stanton number data follow the laminar correlation well. No significant change in the laminar data due to the increase in free-stream turbulence from that of case A is observable. Stanton number values have been previously shown to exceed $C_f/2$ values in a mature turbulent boundary layer (33, 34). Spalding (33) showed that the value of the "Reynolds Analogy Factor", $2\ St/C_f$, for air is 1.2. The Reynolds analogy factor for the early-turbulent region of case B is about 0.75, however. This indicates a slower response of the heat transfer data in transition than that of the hydrodynamic data, as was observed by Blair (22). It will subsequently be shown that the turbulent Prandtl number in the low-Reynolds-number turbulent flow for case B is considerably larger than 0.9, the value measured for mature turbulent boundary layers. Skin friction values for the laminar flow were calculated as discussed previously in case A. Two $C_f/2$ values, $Re_x = 1.4 \times 10^6$ and 1.6×10^6 (Fig. 3), were calculated assuming a laminar boundary layer though the profiles clearly indicate a beginning of transition (as will be discussed). The values shown, therefore, represent lower-bound values. $C_f/2$ values for turbulent flows were deduced from the law-of-the wall using the Clauser technique (35). No direct measurements of wall shear stress were made.

Spanwise distributions of local Stanton number are shown on Fig. 9. At the first station, the boundary layer momentum thickness Reynolds number, 300, exceeded the stability limit of $Re_\theta = 200$, and is clearly showing signs of transition. These are observable as streaks of high local heat transfer coefficient off the center-span. Downstream, these regions of early transition grow to effect transition on the centerline. A notable difference from the profiles shown for case A is the lack of symmetry. Transition at the center-span location is underway by the second profile and is complete by the fourth (Figs. 3 and 9). At the last station, effective turbulent cross-stream transport has restored two-dimensionality.

The local heat transfer data for this run were repeatable to within 1% over a six-hour test period, beginning after the standard ten-hour equilibrium period. In a similar case they were repeatable to within 3% over a period of one month.

Mean velocity profiles are shown in Fig. 10. The two upstream profiles (Stations 1 & 2B) follow the $U^+ = Y^+$ correlation to $Y^+ = 20$, indicating laminar-like behavior even though there are signs of the beginning of transition at these locations as discussed above. The two downstream profiles (Stations 4B & 5B) follow the law-of-the wall relationship over a sufficient range of Y^+ that using the Clauser technique was deemed appropriate. The third profile (Station 3B), though reduced with a skin friction coefficient calculated from the near-wall velocity gradient, as done with the laminar profiles, is clearly not laminar-like. This profile also does not display the turbulent log-linear behavior with an appropriate choice of $C_f/2$--it is clearly transitional. One method for finding the transition region $C_f/2$ is to force closure of the two-dimensional momentum integral equation through the transition region (22). This method was tried and found to give values which appear unreasonably high for this case. This is believed to be attributable to the influence of the lack of two-dimensionality in the transition region for this low free-stream turbulence case.

Mean temperature profiles are shown on Fig. 11. The first profile (Station 2A), taken in the laminar-like flow, follows the near-wall correlation, $T^+ = PrY^+$, well. The two downstream profiles (Stations 4A and 5A), taken in the turbulent flow, display thermal-log-law behavior. In fitting the log regions, the turbulent Prandtl number, Pr_t, and the conduction layer thickness, $Y^+_{c\ell}$, were considered free parameters. Best-fits were found with $Y^+_{c\ell} = 20$ and $Pr_t = 1.20$ and 1.15 for $Re_x = 2.1 \times 10^6$ and 2.9×10^6, respectively. These values of Pr_t are consistent with the trend in $2\ St/C_f$

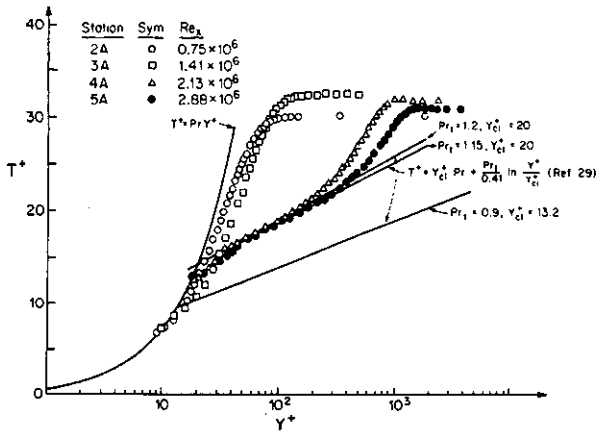

FIG. 11 MEAN TEMPERATURE PROFILES FOR CASE B

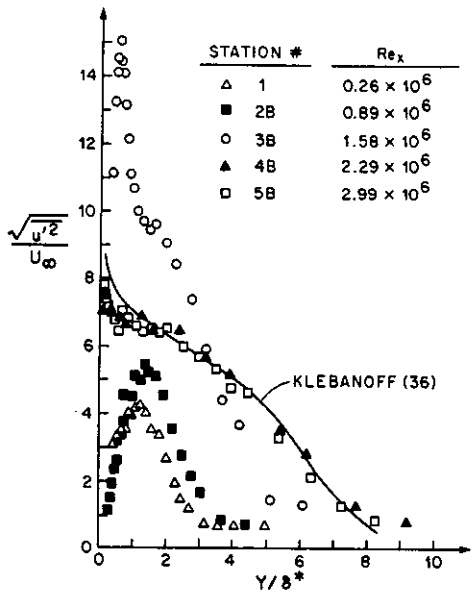

FIG. 12 REYNOLDS STREAMWISE-NORMAL STRESS PROFILES FOR CASE B

observed in Fig. 3 and the conclusion, also made by Blair (22), that Reynolds analogy is violated in the low-Reynolds number turbulent boundary layer. Figure 11 also shows that the conduction layer thickness is larger in the low-Reynolds-number turbulent flow than that observed in higher Reynolds number flows (29).

Profiles of Reynolds normal stresses, $\sqrt{u'^2}/U_\infty$, are shown in Fig. 12. The two upstream profiles (Stations 1B & 2B) have some turbulence-like characteristics although the mean velocity and temperature profiles and the Stanton numbers at this streamwise position appear laminar-like. The anemometer output signals were viewed on a storage oscilloscope. At the peak value, i.e. $y/\delta^* = 1.3$ for the first station, the waveform was turbulent-like indicating a distribution of energy over a large range of frequencies. No intermittent non-turbulent behavior was observable. At the innermost y-position of station 1 data ($Re_x = 2.63 \times 10^5$, $y/\delta^* = 0.3$), some intermittency was observed where a quiet signal was present about 5% of the time. These findings are consistent with the results of Dyban (13) et. al. They termed such a boundary layer "pseudo-laminar". It is believed that this turbulence is produced by non-linear amplification of the free-stream disturbances. This process gives rise to streamwise vortices which concentrate in a thin layer termed that "shear layer" by Klebanoff et. al. (8). This "shear layer" is characterized by high-frequency disturbances and turbulence intensities similar to the peaks of streamwise turbulence intensity shown in Fig. 12. The near-wall decay of turbulence intensity is presumed to be due to stabilizing viscous forces. The effect of these turbulent-like fluctuations on the transition process is presently unknown. Schubauer and Skramstad (7) observed weak oscillations preceding transition in a flow where disturbances were very small. Klebanoff, Tidstrom, and Sargent (8) observed that, in a laminar boundary layer disturbed by a vibrating ribbon, an initially two-dimensional wave develops into a three-dimensional pattern which is terminated by a sudden increase of wave amplitude. Profiles of rms values of these waves are similar (including a peak at $y/\delta^* = 1.3$) to those profiles of Fig. 12, which precede transition.

Transition is observable in the normal stress profiles as a very large increase in peak turbulence intensity concentrated near the wall where it is believed that turbulent bursts are agitating the flow (Station 3B profile of Fig. 12). The residue of the laminar profile peaks remain in the downstream profiles but soon becomes overshadowed by the intense near-wall peak (Stations 4B & 5B). The outer half of the transitional boundary layer profile (Station 3B) has a low turbulence intensity compared to fully-turbulent profiles (i. e., Stations 4B & 5B). Though the two downstream stations (4B and 5B) are in a low-Reynolds-number turbulent flow, they appear to have reached an equilibrium shape. This is evidence that the turbulence characteristics are established almost immediately after transition. The last two profiles appear similar to one measured in a mature turbulent boundary layer by Klebanoff (36). Note that the Station 3B profile is different than either the laminar or turbulent profile and therefore cannot be reproduced from the two by way of an intermittency factor, as is often done in transitional flow modeling.

Reynolds shear stress profiles for the two downstream stations are shown on Fig. 13 (37). The probe was too large to take similar profiles in the laminar and transitional boundary layers. This data and the Klebanoff (36) data, also shown, support the earlier conclusion that the turbulence characteristics rapidly assume those of a fully-turbulent flow. The reduced

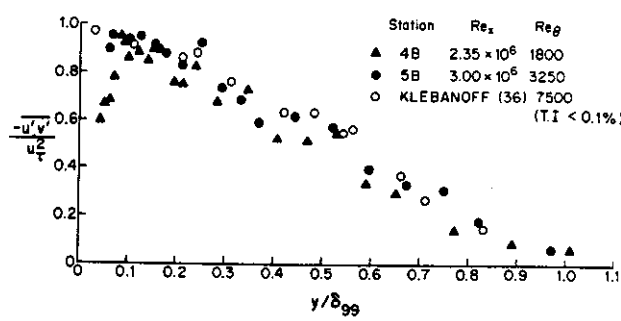

FIG. 13 REYNOLDS SHEAR STRESS PROFILES FOR CASE B

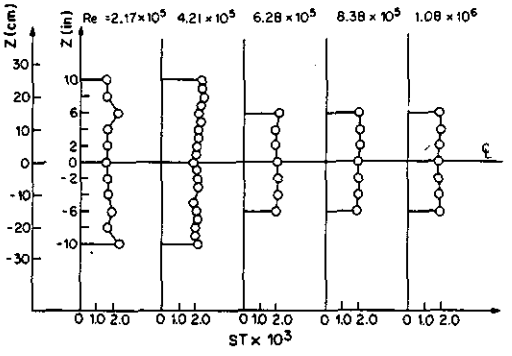

FIG. 14 SPANWISE DISTRIBUTIONS OF LOCAL STANTON NUMBER FOR CASE C

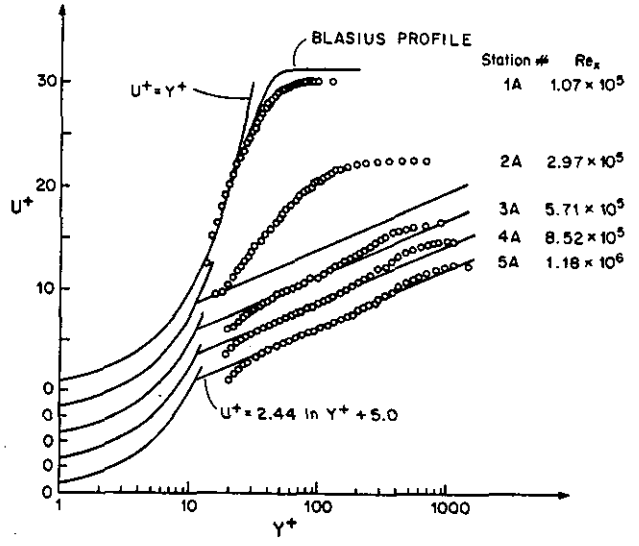

FIG. 15 MEAN VELOCITY PROFILES FOR CASE C

shear-stress values near the wall in the $Re_x = 2.35 \times 10^6$ profile are probably due to averaging by the probe over the length of the wire. This was not observable in the last station profile where the boundary layer was considerably thicker.

C. The Higher Free-Stream Turbulence Intensity Case Case C

To set up the third case, a square grid constructed of 5 cm wide metal strips on a 10 cm pitch, was inserted between the screen pack and the nozzle. The free-stream velocity was then reduced to approximately 13 m/s to place the onset of transition onto the first one-third of the test length. This gave free-stream turbulence intensities which decay from 2.1% to 1.9% over the test length; 2.0% was recorded in the transition region. Larger values of free-stream turbulence intensity, though more representative of the gas turbine environment, decay rapidly and are difficult to characterize and reproduce. This case is considered representative of cases with higher free-stream disturbance (TI < 5%)†.

The Stanton number and skin friction coefficient data, Fig. 3, show that the onset of transition has been moved to approximately $Re_x = 2.1 \times 10^5$ ($Re_{\delta^*} = 788$). This is consistent with earlier data shown on Fig. 8 for 2% free-stream turbulence intensity. There also is some indication of a higher heat transfer coefficient in the late laminar flow due to the higher free-stream turbulence intensity although the data for $Re_x < 10^5$ seems to be insensitive to turbulence intensity. The two skin friction coefficient values at $Re_x \approx 3 \times 10^5$ were found by forcing closure of the integral momentum equation over the transition region as previously done by Blair (22). In contrast to case B this technique was found to give values that appear reasonable on Fig. 3. It is believed that this model was successful in case C and not in case B because case C was shown to be more two-dimensional. The data indicate that the x-Reynolds number at the end of transition is about twice that of the onset of transition for both cases B and C. This is consistent with the transition length model presented by Abu-Ghannam and Shaw (12). The turbulent data ($Re_x > 4 \times 10^5$) indicate a lower value of $2\,St/C_f$ than 1.2, the accepted value for fully-mature turbulent flow (33, 34), but a higher value than observed in case B. Also, it will be shown that turbulent Prandtl numbers are reduced somewhat from those of case B. A thermal energy balance yielded closure to within 5% over the full test length for this case and a momentum balance closed to within 4% from the first profile ($Re_x \approx 10^5$) to the last ($Re_x \approx 1.3 \times 10^6$). It should be noted, however, that the two $C_f/2$ values within the transition region ($Re_x \approx 3.5 \times 10^5$) were chosen to force momentum balance closure over the transition region, $2.1 \times 10^5 < Re_x < 5 \times 10^5$.

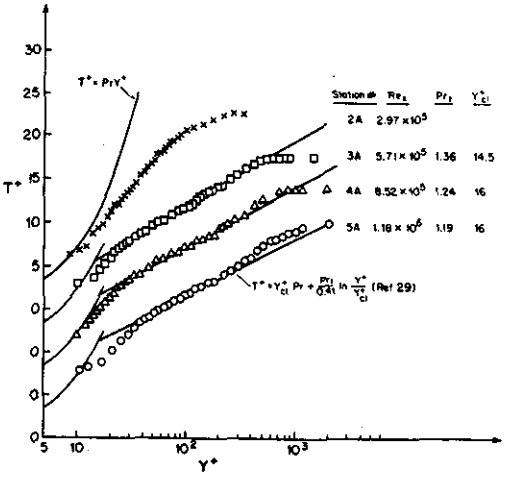

FIG. 16 MEAN TEMPERATURE PROFILES FOR CASE C

† The upper limit of 5% was imposed based upon the findings of Dyban et. al. (13) that the characteristics of "pseudo-laminar" flows for TI > 5% are different than those for TI < 5% .

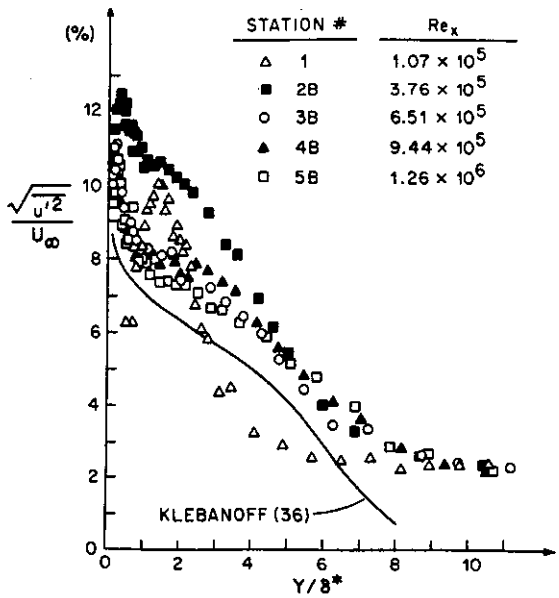

FIG. 17 REYNOLDS STREAMWISE-NORMAL STRESS PROFILES FOR CASE C

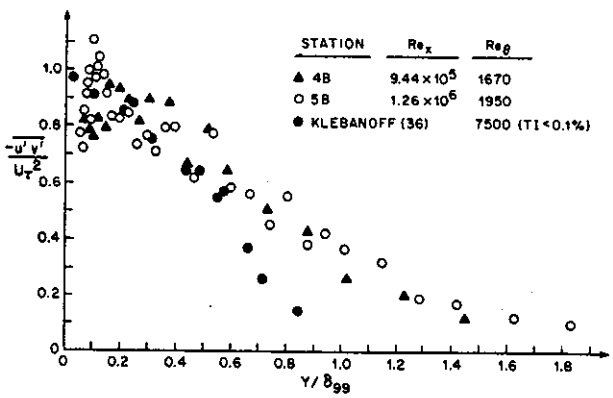

FIG. 18 REYNOLDS SHEAR STRESS PROFILES FOR CASE C

Spanwise distributions of Stanton number are shown in Fig. 14. The first distribution is in late-laminar flow. Transitional streaks are beginning to form off center-span as was observed in case B. The second distribution is in late-transitional flow. It appears that transition near the center-span is spanwise-uniform and that the flow remains two-dimensional throughout, for this high turbulence case.

Mean velocity profiles, Fig. 15, show behavior similar to that of case B. The upstream station (Station 1) is laminar-like, the next (Station 2B) is in transition and the three downstream stations (3A, 4A and 5A) are clearly turbulent -- each with a longer log-linear region and a decreased wake strength than the last. A comparison of the Station 1 profile with the Blasius profile (Fig. 15) shows a lack of agreement at the edge of the boundary layer. This may be due to the nearness of the flow to transiton (Fig. 3) or due to the higher free-stream turbulence level of Case C. Mean temperature profiles of case C, Fig. 16, show behavior similar to that of the case C velocity profiles. Note that the upstream profile (Station 2A) is in transition. The turbulent profiles (Stations 3A, 4A and 5A) show log-linear behavior. As in case B, the log regions were fit by assuming the turbulent Prandtl number, Pr_t, and the conduction layer thickness, $Y^+_{c\ell}$, to be free parameters. Best fits were achieved with $Y^+_{c\ell}$ = 14.5, 16 and 16, and Pr_t = 1.36, 1.24 and 1.19 for Stations 3A, 4A and 5A, respectively. Note that the conduction layers for the last two profiles are thinner than those of case B, but thicker than those of a mature turbulent boundary layer ($Y^+_{c\ell}$ = 13.2 (29)). Note also that the turbulent Prandtl number are higher than 0.9, the fully turbulent value, and less than those observed just after transition in case B.

Reynolds normal stress profiles, plotted in Fig. 17, continue to show a peak at y/δ^* = 1.3 in the laminar flow (Station 1) as was observed in case B. The peaks and values throughout the profile are larger than the case B counterparts, however. The residue of the peak in the laminar profiles remains in the downstream profiles but soon becomes overshadowed by the near-wall peak. The three downstream profiles (3B, 4B and 5B) are nearly the same, supporting the earlier conclusion that the turbulence quantities are rapidly established. Due to the higher free-stream turbulence, the values throughout the profile are higher than the case B values and those of Klebanoff (36), however.

Reynolds shear stress profiles are shown on Fig. 18. Though the scatter is large, the figure shows that the downstream profiles (Stations 4B and 5B) are essentially the same. Fig. 18 also shows that the near-wall shear stress is approximately the same, in these coordinates, as that in the Klebanoff profile (36). The shear stress near the edge of the boundary layer is considerably larger than Klebanoff's values, however -- the free-stream turbulence for the Klebanoff data was very low (TI < 0.1%). Figure 19 compares the shear stress profiles from the last station for cases B and C. Although the near-wall values are essentially the same in these coordinates, the case C values near the edge of the boundary layer are considerably higher.

CONCLUSIONS AND RECOMMENDATIONS

1. An unstable laminar flow is described as a separate flow from that of laminar or transitional flow. In this flow, turbulence intensities significantly higher than the free-stream turbulence intensity are observable in the boundary layer. Heat transfer rates appear to be somewhat sensitive to free-

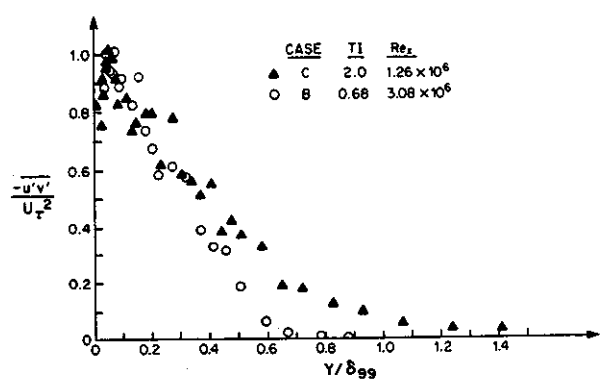

FIG. 19 COMPARISON OF REYNOLDS SHEAR STRESS PROFILES AT STATION 5B (FIG. 2) FOR CASES B AND C

stream turbulence in this flow -- a contrast to the lack of sensitivity to free-stream turbulence intensity in the early laminar flow. More investigation into the role of this boundary layer turbulence intensity on the process of transition is needed.

2. Increased free-stream turbulence intensity decreases the transition onset Reynolds number and the length of transition. The locations of the onset and end of transition in the present cases were consistent with results of earlier experiments. Onset of transition is taken to be the location where Stanton number data begin to rise sharply with increasing streamwise distance; the end of transition is the peak of the Stanton number curve.
3. Turbulent Prandtl number values in the early turbulent flow, just downstream of transition, are significantly higher than the 0.9 value known to apply to fully-mature turbulent flows. These values decrease, somewhat, with higher free-stream disturbance levels. Temperature profiles in the early turbulent flow indicate a thicker conduction layer than observed in fully-turbulent flows. This thicknesss decreases with increased free-stream disturbance levels.
4. Values of the Reynolds analogy factor, $2\ St/C_f$, in the early turbulent flow are significantly smaller than 1.2, the fully-turbulent value.
5. Profiles of turbulent streamwise-normal and shear stresses develop rapidly to fully-turbulent shapes immediately after transition.
6. Transition is characterized by a very large spike in streamwise turbulence intensity near the wall. This spike is considerably larger than the maximum value observed in turbulent normal stress profiles.
7. The effect of higher free-stream turbulence intensity is seen to penetrate to very near the wall in profiles of streamwise-normal stresses. The effect of higher free-stream disturbance on the shear stress profiles in the fully turbulent flow is seen predominately in the outer portion of the boundary layer.
8. Long-period unsteadiness was observed in a low free-stream-disturbance (TI = 0.3%) laminar flow downstream of the theoretical instability limit. Similar unsteadiness was not observed just before transition in higher-disturbance flows (TI = 0.68% and 2%).

ACKNOWLEDGMENTS

This study was supported by the NASA-Lewis Research Center grant number NAG 3-286. The grant monitor is Dr. Raymond Gaugler. Additional support was provided by the Graduate School of the University of Minnesota.

REFERENCES

1. Turner, A. B., "Local Heat Transfer Measurements on a Gas Turbine Blade," J. of Mech. Engr. Sci, Vol. 13, No. 1, 1971, pp. 1-12.
2. Taylor, G. I., "Statistical Theory of Turbulence, Part V", Proc. Roy. Soc. (London) A156, 1936, pp. 307-317.
3. Hall, A. and Hislop, G. S., "Experiments on the Transition of the Laminar Boundary Layer on a Flat Plate," British Aeronautical Research Committee, R & M 1843, 1938.
4. van Driest, E. R. and Blumer, C. B., "Boundary Layer Transition: Free-stream Turbulence and Pressure Gradient Effects," AIAA J., Vol. 1, No. 6, June 1963, pp. 1303-1306.
5. Hylton, L. D., Mihelc, M. S., Turner, E. R., Nealy, D. A., and York, R. E., "Analytical and Experimental Evaluation of the Heat Transfer Distribution Over the Surfaces of Turbine Vanes," NASA CR-168015, May 1983.
6. Wells, C. S., Jr., "Effects of Freestream Turbulence on Boundary Layer Transition," AIAA J., Vol. 5, No. 1, 1967, pp. 172-174.
7. Schubauer, G. B. and Skramstad, H. K., "Laminar Boundary Layer Oscillations on a Flat Plate," NACA Report, No. 909, 1948.
8. Klebanoff, P. S., Tidstrom, K. D., and Sargent, L. H., "The Three-Dimensional Nature of Boundary Layer Instability," J. Fluid Mech., 12, Part I, 1962, pp. 1-34.
9. Spangler, J. G. and Wells, C. S., Jr. "Effects of Freestream Disturbances on Boundary Layer Transition," AIAA J., Vol. 6, No. 3, 1968, pp. 543-545.
10. Tani, I., "Boundary Layer Transition," Annual Rev. of Fluid Mech., Vol. I, 1969, W. R. Sears, Editor, pp. 169-196.
11. Hall, D. J. and Gibbings, J. C., "Influence of Stream Turbulence and Pressure Gradient Upon Boundary Layer Transition," J. of Mech. Engr. Div. Vol. 14, No. 2, 1972, pp. 134-146.
12. Abu-Ghannam, B. J., and Shaw, R., "Natural Transition of Boundary Layers -- The Effects of Turbulence, Pressure Gradient, and Flow History," J. of Mech. Engr. Sci., Vol. 22, No. 5, 1980, pp. 213-228.
13. Dyban, YE. P., Epik, E. YA., and Suprun, T. T., "Characteristics of the Laminar Boundary Layer in the Presence of Elevated Free-Stream Turbulence," Fluid Mech.-Soviet Research, Vol. 5, No. 4, 1976, pp. 31-36.
14. Clauser, M. and Clauser, F., "The Effect of Curvature on the Transition from Laminar to Turbulent Boundary Layer," NACA Tech. Note No. 613, 1937.
15. Liepmann, H. W., "Investigations on Laminar Boundary-Layer Stability and Transition on Curved Boundaries, NASA Wartime Advanced Confidential Rept. 3H3D, Aug. 1943.
16. Morkoven, M. W., "Instability, Transition to Turbulence and Predictability, AGARDograph, 236, 1978.
17. Reshotko, E., "Boundary Layer Stability and Transition," Annual Rev. of Fluid Mech., Vol. 8, 1976, pp. 311-350.
18. Tani, I., "Three-Dimensional Aspects of Boundary Layer Transition," Proc. Indian Acad. Sci., Vol. 4, Part 2, August 1981, pp. 219-238.
19. "Laminar-Turbulent Transition," AGARD-CP224, May, 1977.
20. Junkhan, G. H. and Serovy, G. K., "Effects of Free-Stream Turbulence and Pressure Gradient on Flat-Plate Boundary Layer Velocity Profiles and on Heat Transfer," Trans. of ASME, J. of Heat Transfer, May, 1967, pp. 169-176.
21. Simon, T. W. and Moffat, R. J., "Turbulent Boundary Layer Heat Transfer Experiments: A Separate Effects Study on a Convexly Curved Wall," J. of Heat Transfer, Vol. 105, November 1983, pp. 835-840.
22. Blair, M. F., "Influence of Free-Stream Turbulence on Boundary Layer Transition in Favorable Pressure Gradients," Trans. of ASME, J. of Engr. for Power, Vol. 104, October 1982, pp. 743-750.
23. Blair, M. F., "Influence of Free-Stream Turbulence on Turbulent Boundary-Layer Heat Transfer and Mean Profile Development, Part I -- Experimental Data," Trans. of ASME, J. of Heat Transfer, Vol. 105, February 1983, pp. 33-40.

24. Perry, A. E., "Hot-Wire Anemometry," Claredon Press, Oxford, 1982.
25. Kline, S. J. and McClintock, F. A., "Describing Uncertainties in Single-Sample Experiments," J. of Mech. Eng. Sci., Vol. 75, 1953, pp. 3-8.
26. Moffat, R. J., "Contributions to the Theory of Single-Sample Uncertainty Analysis," J. of Fluids Engr., Vol. 104, 1982, pp. 250-260.
27. Wang, T. and Simon, T. W., "Using Uncertainty Analysis to Guide Test Program Development: A Case Study," Internal Report, Heat Transfer Lab., Dept. of Mech. Engr., University of Minnesota, January 1984.
28. Wang, T., "An Experimental Investigation of Curvature and Free-Stream Turbulence Effects on Heat Transfer and Fluid Mechanics in Transitional Boundary Layers," Ph.D. Thesis, Dept. of Mech. Engr., University of Minnesota, December 1984.
29. Kays, W. M. and Crawford, M. E., Convective Heat and Mass Transfer, McGraw-Hill, 2nd Ed., 1980.
30. Schlichting, H., Boundary Layer Theory, McGraw-Hill, NY, 7th Ed., 1979, Chap. XVI.
31. Kachanov, Yu. S. and Levchenko, V. Ya., "The Resonant Interaction of Disturbances at Laminar-turbulent Transition in a Boundary Layer," J. of Fluid Mech., Vol. 138, 1984, pp. 209-247.
32. McDonald, H. and Fish, R. W., "Practical Calculations of Transitional Boundary Layers," Int. J. Heat Mass Transfer, Vol. 16, 1973, pp. 1729-1744.
33. Spalding, D. B., "Contribution to the Theory of Heat Transfer Across a Turbulent Boundary Layer," Int. J. Heat Mass Transfer, Vol. 17, No. 7, July, 1964, pp. 743-761.
34. Simonich, J. C. and Bradshaw, P., "Effect of Free-Stream Turbulence on Heat Transfer through a Turbulent Boundary Layer," J. of Heat Transfer, Trans. of ASME, Vol. 100, Nov. 1978, pp. 671-677.
35. Clauser, F. H., "The Turbulent Boundary Layer," Advances in Applied Mechanics, Vol. IV, 1956, Academic Press, New York, pp. 1-51.
36. Klebanoff, P. S., "Characteristics of Turbulence in a Boundary Layer with Zero Pressure Gradient," NACA Report, 1247, 1955.
37. Buddhavarapu, J., "An Experimental Study of Transitional Boundary Layers on a Flat Plate". M. S. Thesis, Dept. of Mech. Engr., University of Minnesota, Sept. 1984.

A REVIEW AND ANALYSIS OF BOUNDARY LAYER TRANSITION DATA FOR TURBINE APPLICATION†

Raymond E. Gaugler*
National Aeronautics and Space Administration
Lewis Research Center
Cleveland, Ohio 44135

A number of data sets from the open literature that include heat transfer data in apparently transitional boundary layers, with particular application to the turbine environment, were reviewed and analyzed to extract transition information. The data were analyzed by using a version of the STAN5 two-dimensional boundary layer code. The transition starting and ending points were determined by adjusting parameters in STAN5 until the calculations matched the data. The results are presented as a table of the deduced transition location and length as functions of the test parameters. The data sets reviewed cover a wide range of flow conditions, from low-speed, flat-plate tests to full-scale turbine airfoils operating at simulated turbine engine conditions. The results indicate that free-stream turbulence and pressure gradient have strong, and opposite, effects on the location of the start of transition and on the length of the transition zone.

INTRODUCTION

Designing efficient cooling configurations for the airfoils in a gas turbine engine requires a detailed knowledge of the variations of the heat transfer coefficient on the hot-gas side. However, in many cases, there is a region on the blade surface where the heat transfer coefficient experiences a dramatic rise in magnitude. This is the region where the boundary layer transition from laminar to turbulent flow occurs. The location of the start of this transition and the length of the transition zone depend strongly on a number of flow parameters, such as the Reynolds number, the free-stream turbulence level, and the pressure gradient.

Computing the heat transfer coefficient in the transition region requires that a mathematical model be used to smoothly turn on the turbulent calculations. At present no model is available that adequately accounts for the effects of these parameters in the turbine environment. One of the reasons for this is a lack of good experimental data on boundary layer transition under the severe conditions encountered in a gas turbine engine. However, a number of heat transfer data sets do exist that include transitional boundary layers. In this study these data sets were analyzed by using the STAN5 two-dimensional boundary layer computer code in order to extract transition information. The code was run against the data with different transition parameters assumed until a match between data and calculations was found. The transition data were then tabulated in a form useful to the researcher attempting to model the transition process in the turbine environment.

---

†Also published as NASA Technical Memorandum 86880.
*Member, ASME.

METHOD OF ANALYSIS

An iterative method was used to derive transition data from the selected heat transfer data sets. The general procedure was to assume a transition starting point and a transition length, to do a numerical boundary layer analysis to compute heat transfer parameters, and finally to compare the computed results with the data. If the agreement was poor, new transition points were assumed, and the process was repeated until reasonable agreement was found between computed and measured results. The final values of transition starting point and transition zone length are reported herein, in terms of location as well as of momentum thickness Reynolds number.

The boundary layer analysis used was the widely accepted STAN5 two-dimensional boundary layer code, developed at Stanford University by Crawford and Kays (ref. 1) and based on the scheme of Patankar and Spalding (ref. 2). The version of STAN5 used has been modified at the NASA Lewis Research Center as described in reference 3. In this version the user has the option of supplying the program with a specific location where transition is to start and with a specific length of the transition region. Within the transition zone the turbulent eddy viscosity is gradually turned on by using an intermittency factor variation taken from the work of Abu-Ghannam and Shaw (ref. 4). The intermittency factor varies smoothly from zero at the transition starting point to 1 at the end of the specified transition length. No attempt was made to account for local effects such as pressure gradient or free-stream turbulence in computing intermittency. The Prandtl mixing length model was used to compute the turbulent eddy diffusivity.

SELECTION OF DATA SETS

A number of heat transfer data sets were reviewed for their applicability to this report. From these, six data sets were selected for analysis. The prime criterion used in the selection process was that the data show evidence of boundary layer transition. When this was met, the completeness of the documentation of the experimental conditions became the prime criterion. As a minimum, to do the boundary layer analysis, the aerodynamic and thermal boundary conditions must be known, including the specification of free-stream turbulence parameters.

Each of the selected data sets is described here and summarized in table I.

(1) The first data set was extracted from a report by Blair and Werle (ref. 5). Their tests concerned incompressible flow over a heated, smooth flat plate for different levels of free-stream turbulence. They were primarily looking for the effects of free-stream turbulence level on heat transfer to the fully turbulent boundary layer, but they did allow the boundary layer to undergo a natural transition from laminar to turbulent. Two of their test runs were selected for this analysis, and the conditions are summarized in table I as cases 1(a) and (b). The only difference between the two is the free-stream turbulence level. The inlet Reynolds number is based on the test section length, 2.44 m (8.0 ft).

(2) The second data set used was taken from another report by Blair and Werle (ref. 6) and one by Blair (ref. 7). The tests were similar to the first set but with the addition of a constant flow acceleration. Three of these

test runs, encompassing two pressure gradients and two turbulence levels, were selected for analysis. The pertinent test parameters are summarized in table I as cases 2(a), (b), and (c). Again, the inlet Reynolds number is based on the test section length, 2.44 m (8.0 ft).

(3) The third data set was taken from the work of Han et al. (ref. 8). They measured the heat transfer from three different large-scale turbine airfoils over a range of Reynolds number and free-stream turbulence level. The airfoils had a true chord of 53.3 cm (21 in) and a height of 61 cm (24 in). One of these data sets, for an airfoil suction (convex) surface, was selected for analysis in this study, and the test parameters are summarized in table I as case 3. For this case, and those remaining, the inlet Reynolds number is based on airfoil true chord. The data set from reference 8 is for incompressible flow, as the test used ambient air flowing over an electrically heated airfoil.

(4) The fourth data set considered was extracted from the report by Consigny and Richards (ref. 9). They used the isentropic light-piston tunnel at the Von Karman Institute to closely simulate actual turbine engine conditions and measured the heat transfer rates to the model airfoil. The airfoil had a true chord of 8.0 cm (3.15 in) and a height of 10 cm (3.94 in). Information from two of their runs was used for this report, and the conditions are tabulated in table I as cases 4(a) and (b). The runs selected differed only in the initial free-stream turbulence level. Again, only the suction surface data were considered herein. For these cases the air was hotter than the surface.

(5) The fifth data set was taken from the report of Schultz et al. (ref. 10), and from additional information reported by Daniels and Browne (ref. 11). They used the free-piston tunnel at Oxford University and techniques similar to those in case 4 to measure heat transfer rates to a turbine airfoil. The airfoil had a true chord of 5.0 cm (1.96 in) and a height of 7.5 cm (2.96 in). The two cases described in references 10 and 11 were both used herein, and the conditions are tabulated in table I as cases 5(a) and (b). As in the previous cases only suction surface data were considered for this analysis. The only difference between cases 5(a) and (b) was the inlet Reynolds number.

(6) The final data set considered for this report was taken from the suction surface data reported by Lander (ref. 12) and Lander et al. (ref. 13). These data were generated in a transient test by using hot combustion gases to heat a cascade of turbine airfoils that was quickly shuttled into the hot stream. The airfoils had a true chord of 6.0 cm (2.36 in) and a height of 5.8 cm (2.3 in). The reported tests were characterized by extremely high free-stream turbulence levels. The conditions of the case used herein are tabulated in table I as case 6.

RESULTS AND DISCUSSION

The results of this analysis are presented in figures 1 to 6, and important parameters are tabulated in table II. The figures show either Stanton number or heat transfer coefficient as functions of the surface distance from the stagnation point. The two parameters most frequently found in the literature to govern the boundary layer transition are free-stream pressure gradient and turbulence level: the favorable pressure gradient associated with streamwise acceleration has a stabilizing effect, and free-stream turbulence triggers

instabilities. These two parameters are tabulated in table II for the cases studied herein and are included on the figures. The turbulence level is defined as the ratio of the root mean square of the streamwise fluctuating velocity u to the free-stream velocity U. The pressure gradient is characterized by the acceleration parameter K, defined as the product of the kinematic viscosity ν and the streamwise velocity gradient dU/dx divided by the square of the free-stream velocity.

$$K = \frac{\nu}{U^2} \frac{dU}{dx}$$

Included in table II are the derived values of momentum thickness Reynolds number at the start and at the end of transition. The momentum thickness Reynolds number at the start of transition is the parameter calculated in most attempts to model the start of transition.

In all cases the figures include curves for two additional STAN5 calculations: one where the boundary layer was assumed to remain laminar, and one where it was assumed to be fully turbulent from the start. These two cases form the limits between which the transitional calculations fall. In general the laminar calculations matched the laminar data quite well, and the fully turbulent calculations acceptably matched the turbulent data. For the turbulent case the Prandtl mixing length model was used to compute the turbulent eddy diffusivity.

Case 1

The data for case 1 (fig. 1; table II) differed only in the inlet free-stream turbulence level. As expected, higher free-stream turbulence resulted in an earlier transition as well as a shorter transition length. The best fit occurred when transition was assumed to start close to the point of minimum measured heat transfer. This was not true for the cases that include pressure gradient effects.

Case 2

The data for case 2 (fig. 2; table II) had the added complication of an accelerating free-stream flow. For reference the free-stream velocity distribution is included on figure 2 and all subsequent figures. An interesting feature of the calculations is that, in order to match the data, the transition starting point must be located considerably ahead of the minimum heat transfer point. The largest effect of acceleration is seen in comparing figures 2(a) and (b), which are for about the same turbulence level. The higher acceleration of case 2(b) resulted in a considerably longer transition zone than that for case 2(a). Comparing figures 2(b) and (c) shows that for a constant free-stream acceleration parameter free-stream turbulence had a strong effect on the length of the transition zone, with the more turbulent case 2(c) having a short transition region.

Case 3

Case 3 (fig. 3; table II) represents flow over an actual airfoil, so flow accelerations are not constant and surface curvature effects are present. However, the free-stream turbulence level is relatively low. The transition had to be forced in the calculations to start in a region where the flow

acceleration was high, well ahead of the minimum heat transfer point, in order to match the behavior of the data.

Case 4

Case 4 (fig. 4; table II) was for a turbine vane suction surface. Essentially the only difference between the two cases was the free-stream turbulence level. The distribution of the flow acceleration parameter K over the airfoil surface was the same for both. In both cases it was necessary in the calculations to force transition to begin very close to the leading-edge stagnation point, but the length of the transition zone was markedly different in each case. For lower turbulence (fig. 4(a)) the calculated boundary layer never reached a fully turbulent state. The agreement between the STAN5 laminar and turbulent calculations and the data was significantly worse for the higher turbulence case.

Case 5

The data for case 5 (fig. 5; table II) differed only in the Reynolds number. Since the velocity distributions were the same, this resulted in a different level of acceleration parameter. For an inlet Reynolds number of 1.26 million (case 5(b)), three times the value for case 5(a), major differences are apparent in the heat transfer data for the transitional boundary layer. The most obvious reason for this is the effect of K which, for a constant velocity, varies inversely with Reynolds number. Thus the transition zone was longer for the low-Reynolds-number case since the stabilizing parameter, K, was higher.

Case 6

The distinguishing feature of case 6 (fig. 6; table II) is the high inlet turbulence level. However, the effect of the free-stream turbulence was offset by a strongly accelerating flow for about the first 15 percent of the vane surface. Once the flow acceleration diminished, the transition progressed rapidly.

CONCLUDING REMARKS

A number of heat transfer data sets were analyzed to determine the location of the start of the boundary layer transition from laminar to turbulent flow and the length of the transition zone. The analysis used was the STAN5 two-dimensional boundary layer program. The transition starting point and the length of the transition zone were adjusted in the program input until the calculated heat transfer distribution satisfactorily matched the measured distribution. From this analysis the momentum thickness Reynolds numbers at the start and end of transition were determined, and the results were tabulated as a function of experimental conditions. The location of the start of the boundary layer transition exhibited a strong dependence on both free-stream pressure gradient and turbulence level. A favorable pressure gradient tended to delay the onset of turbulent flow, but the effect of free-stream turbulence was to hasten the transition. The length of the transition zone appeared to depend strongly on free-stream parameters within the zone rather than just on the conditions at the start of transition, as is frequently assumed.

REFERENCES

1. Crawford, M.E., and Kays, W.M., "STAN5 - A Program for Numerical Computation of Two-Dimensional Internal and External Boundary Layer Flows," NASA CR-2742, 1976.

2. Patankar, S.V., and Spalding, D.B., Heat and Mass Transfer in Boundary Layers, 2nd ed., International Textbook Company, Ltd., London, 1970.

3. Gaugler, R.E., "Some Modifications to, and Operational Experience with, the Two-Dimensional, Finite-Difference, Boundary Layer Code, STAN5," ASME Paper 81-GT-89, Mar. 1981.

4. Abu-Ghannam, B.J., and Shaw, R., "Natural Transition of Boundary Layers - The Effects of Turbulence, Pressure Gradient, and Flow History," Journal of Mechanical Engineering Science, Vol. 22, No. 5, Oct. 1980, pp. 213-228.

5. Blair, M.F., and Werle, M.J., "The Influence of Free Stream Turbulence on the Zero Pressure Gradient Fully Turbulent Boundary Layer," UTRC/R80-914388-12, Sept. 1980. (AD-A101094.)

6. Blair, M.F., and Werle, M.J., "Combined Influence of Free-Stream Turbulence and Favorable Pressure Gradients on Boundary Layer Transition and Heat Transfer," UTRC/R81-914388-17, Mar. 1981. (AD-A101089.)

7. Blair, M.F., "Influence of Free-Stream Turbulence on Boundary Layer Transition in Favorable Pressure Gradients," Journal of Engineering for Power, Vol. 104, No. 4, Oct. 1982, pp. 743-750.

8. Han, L.S., Chait, A., Boyee, W.F., and Rapp, J.R., "Heat Transfer on Three Turbine Airfoils," AFWAL TR-82-2124, 1983. (AD-A128762.)

9. Consigny, H., and Richards, B.E., "Short Duration Measurements of Heat-Transfer Rate to a Gas Turbine Rotor Blade," Journal of Engineering for Power, Vol. 104, No. 2, July 1982, pp. 542-551.

10. Schultz, D.L., Jones, T.V., Oldfield, M.L.G., and Daniels, L.C., "A New Transient Cascade Facility for the Measurement of Heat Transfer Rates," High Temperature Problems in Gas Turbine Engines, AGARD CP-229, 1977, pp. 31-1 to 31-27.

11. Daniels, L.D., and Browne, W.B., "Calculation of Heat Transfer Rates to Gas Turbine Blades," International Journal of Heat and Mass Transfer, Vol. 24, No. 5, May 1981, pp. 871-879.

12. Lander, R.D., "Evaluation of the Effect of Free Stream Turbulence on the Heat Transfer to Turbine Airfoils," AFAPL-TR-69-70, Sept. 1969. (AD-857303.)

13. Lander, R.D., Fish, R.W., and Suo, M., "External Heat-Transfer Distribution on Film Cooled Turbine Vanes," Journal of Aircraft, Vol. 9, No. 10, Oct. 1972, pp. 707-714.

TABLE I. - EXPERIMENTAL CONDITIONS FOR SELECTED DATA SETS

Case and figure	Reference	Test conditions	Inlet				Exit Mach number
			Ratio of wall to gas temperature	Reynolds number	Streamwise turbulence intensity	Pressure, atm	
1(a)	Blair and Werle (5)	Heated flat plate, no acceleration, low speed	1.02	47.3×10^5	0.012	1.0	0.09
1(b)	Blair and Werle (5)			47.3	.025		.09
2(a)	Blair and Werle (6) and Blair (7)	Heated flat plate, constant acceleration, low speed		24.1	.021		.07
2(b)				15.1	.023		.12
2(c)				15.1	.053		.12
3	Han et al. (8)	Heated large-scale airfoil, low speed	1.09	2.33	.008		.04
4(a)	Consigny and Richards (9)	Short test, high speed	.76	7.23	.030	2.33	.92
4(b)			.76		.052	2.33	.92
5(a)	Shultz et al. (10) and Daniels and Brown (11)	Short test, high speed	.68	4.2	.040	1.88	.94
5(b)			.68	12.6	.040	5.75	.94
6	Lander (12)	Transient test, combustion heated	.53	3.75	.187	2.7	.85

TABLE II. - DERIVED LOCAL TRANSITION PARAMETERS

Case and figure	Start of transition					End of transition		
	Assumed transition starting point		Acceleration parameter, K	Streamwise turbulence intensity	Momentum thickness Reynolds number	Assumed length of transition zone		Momentum thickness Reynolds number
	m	ft				m	ft	
1(a)	0.213	0.70	0	0.012	400	0.262	0.86	985
1(b)	.076	.25	0	.025	260	.183	.60	730
2(a)	.061	.20	$.20 \times 10^6$	.021	165	.564	1.85	895
2(b)	.043	.14	.75	.023	92	1.524	5.00	975
2(c)	.030	.10	.75	.053	92	.244	.80	330
3	.098	.32	3.9	.005	150	.363	1.19	1355
4(a)	.003	.01	11.0	.030	74	(a)	(a)	(a)
4(b)	.003	.01	11.0	.052	74	.061	.20	1440
5(a)	.009	.03	2.1	.030	192	.038	.125	1325
5(b)	.001	.005	.88	.035	114	.020	.065	1620
6	.001	.005	120	.187	28	.030	.10	688

[a]Transition not complete at end of vane surface.

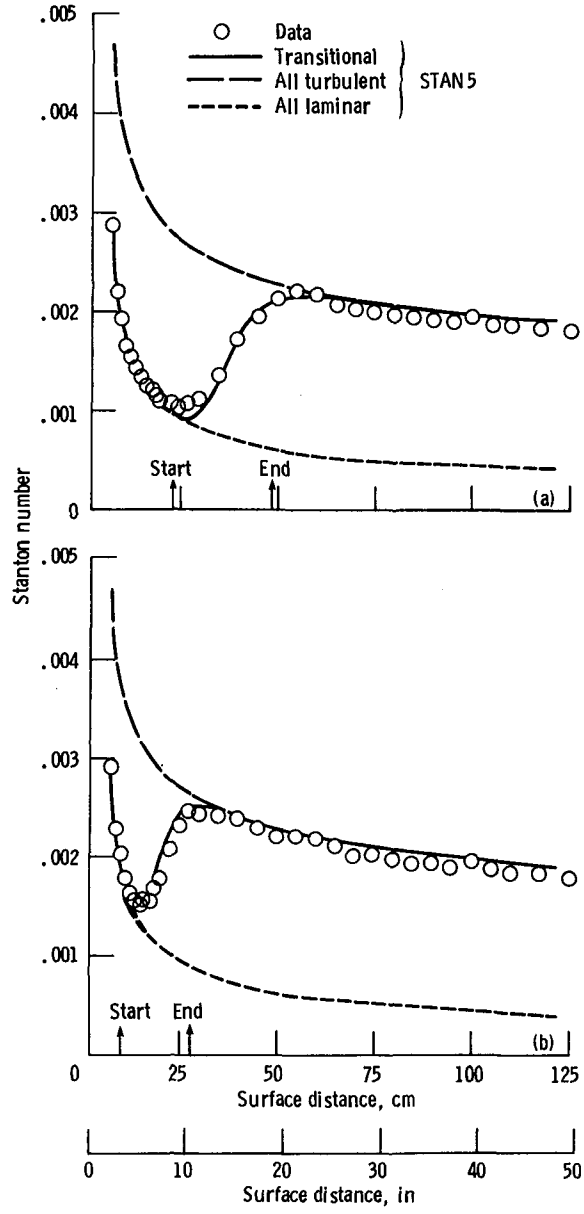

(a) Inlet turbulence level, 0.012.
(b) Inlet turbulence level, 0.025.

Figure 1. - Stanton number as a function of surface distance. Flate plate; free-steam velocity, 30.5 m/sec (100 ft/sec). (Data from ref. 5).

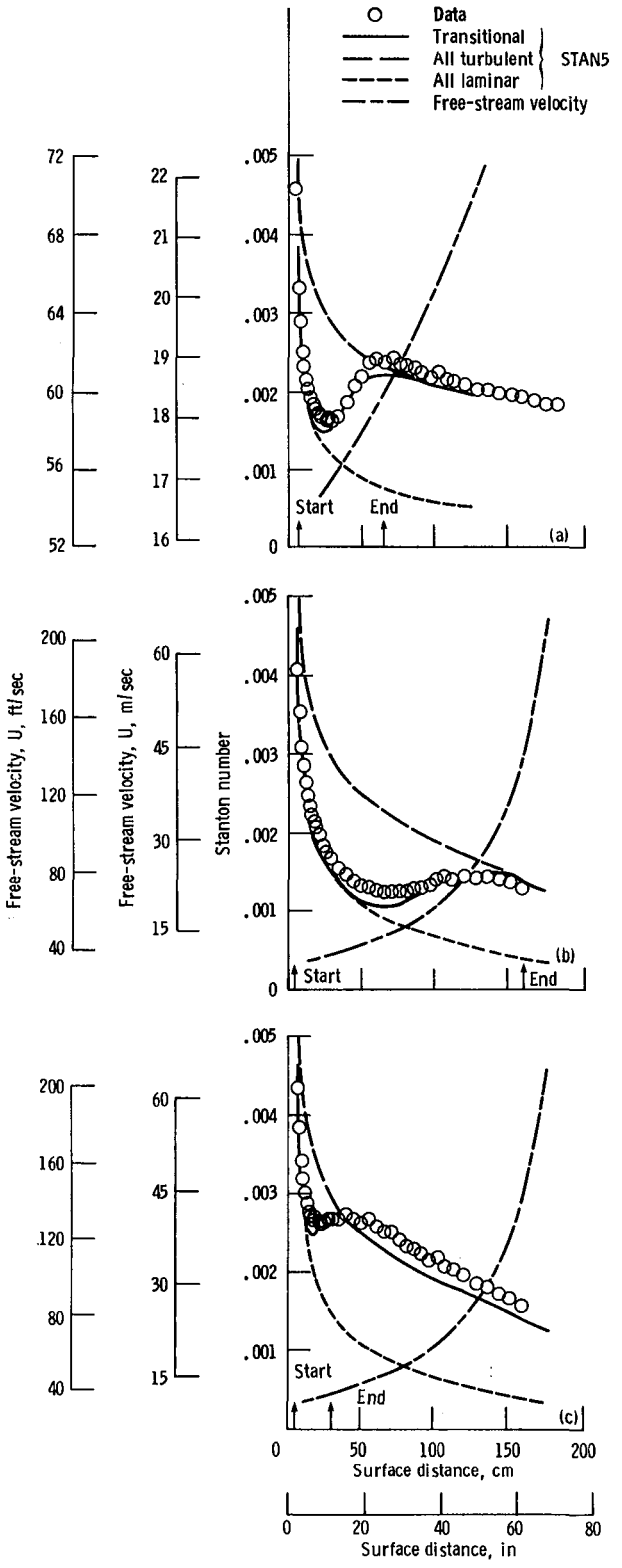

(a) Inlet turbulence level, 0.021; local acceleration parameter, K, 0.2×10^{-6}.
(b) Inlet turbulence level, 0.023; local acceleration parameter, K, 0.75×10^{-6}.
(c) Inlet turbulence level, 0.053; local acceleration parameter, K, 0.75×10^{-6}.

Figure 2. - Stanton number as a function of surface distance. Flat plate; constant acceleration. (Data from ref. 6).

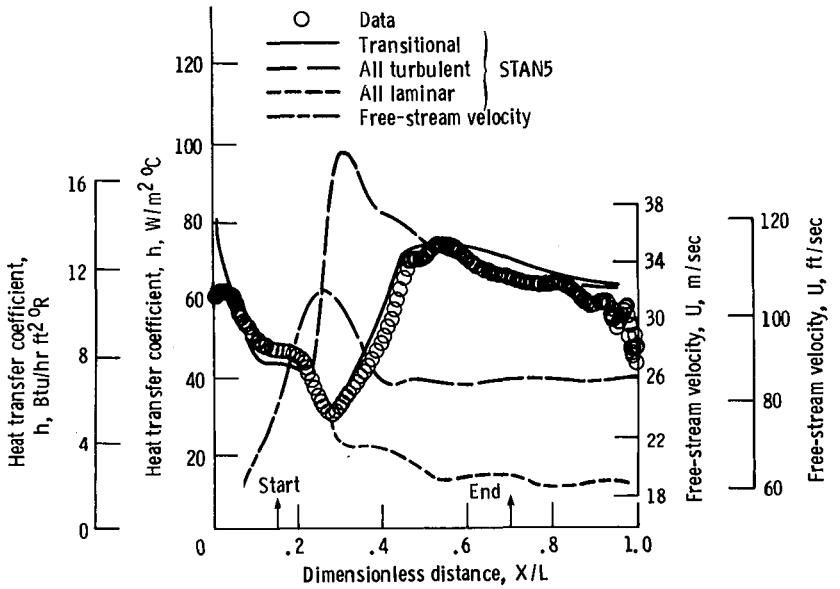

Figure 3. - Heat transfer coefficient as a function of surface distance. Large-scale turbine vane; suction surface; inlet turbulence level, 0.008; local acceleration parameter K at transition start, 0.39×10^{-5}. (Data from Han et al. (ref. 8).)

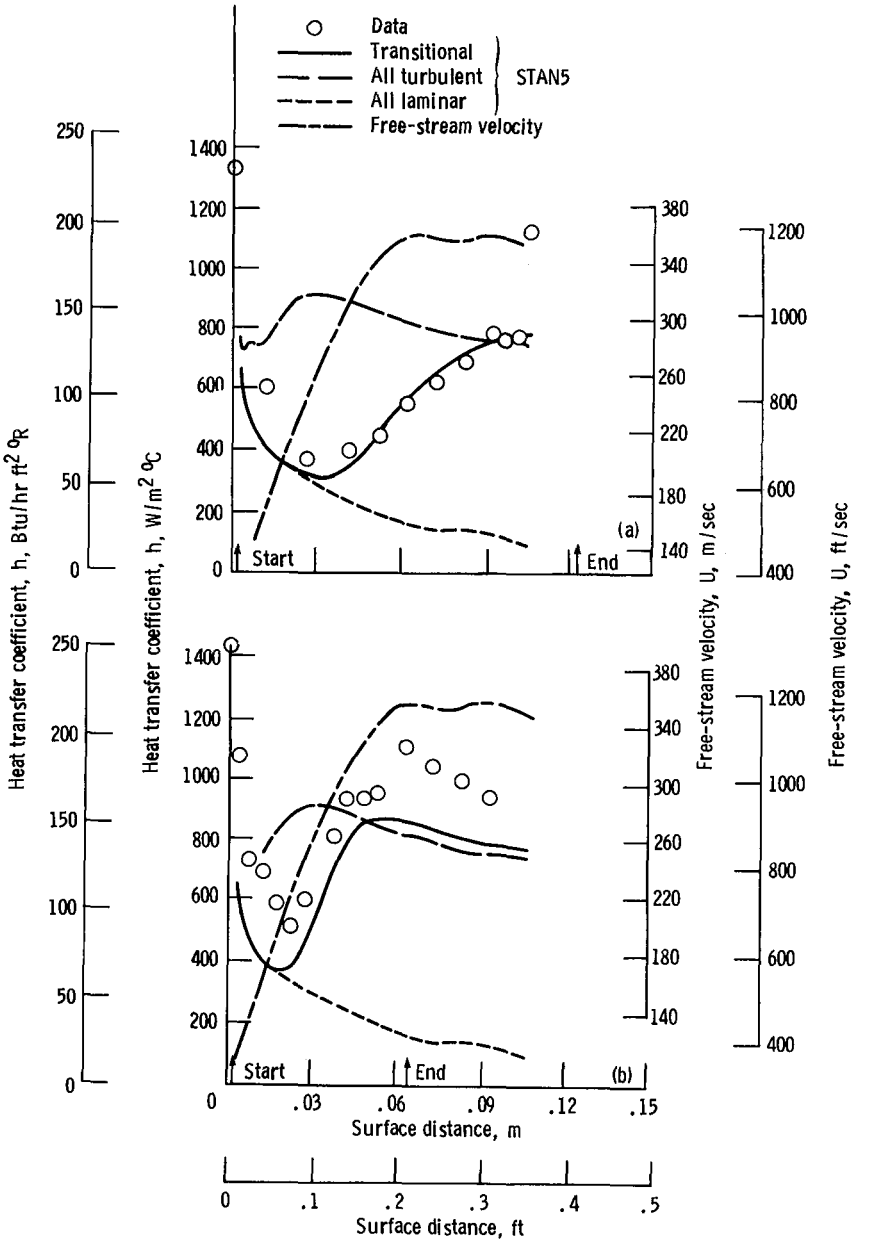

(a) Inlet turbulence level, 0.030.
(b) Inlet turbulence level, 0.052.

Figure 4. - Heat transfer coefficient as a function of surface distance. Turbine vane suction surface; simulated engine conditions; local acceleration parameter K at transition start, 0.11×10^{-4}. (Data from ref. 9.)

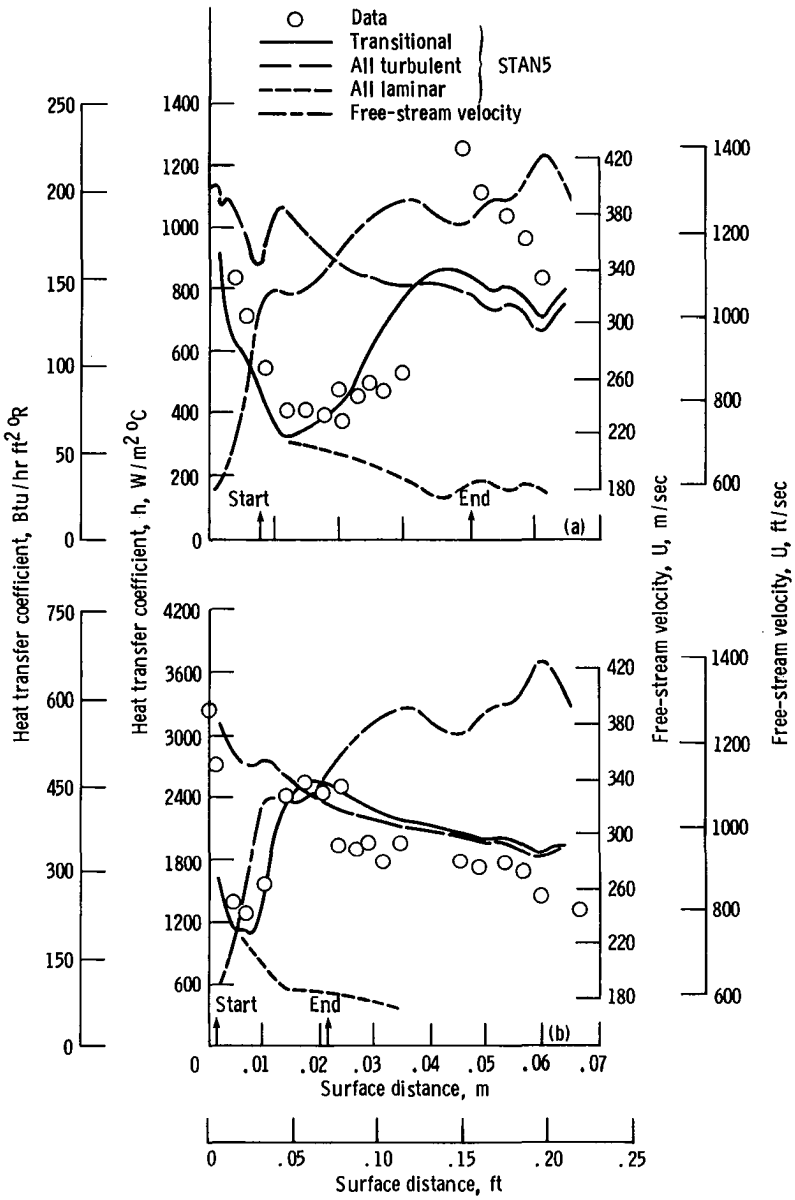

(a) Local acceleration parameter K at transition start, 0.21×10^{-5}; Reynolds number, Re, 4.2×10^{5}.

(b) Local acceleration parameter K at transition start, 0.88×10^{-6}; Reynolds number, Re, 12.6×10^{5}.

Figure 5. - Heat transfer coefficient as a function of surface distance. Turbine vane suction surface; simulated engine conditions; inlet turbulence level, 0.040. (Data from ref. 10.)

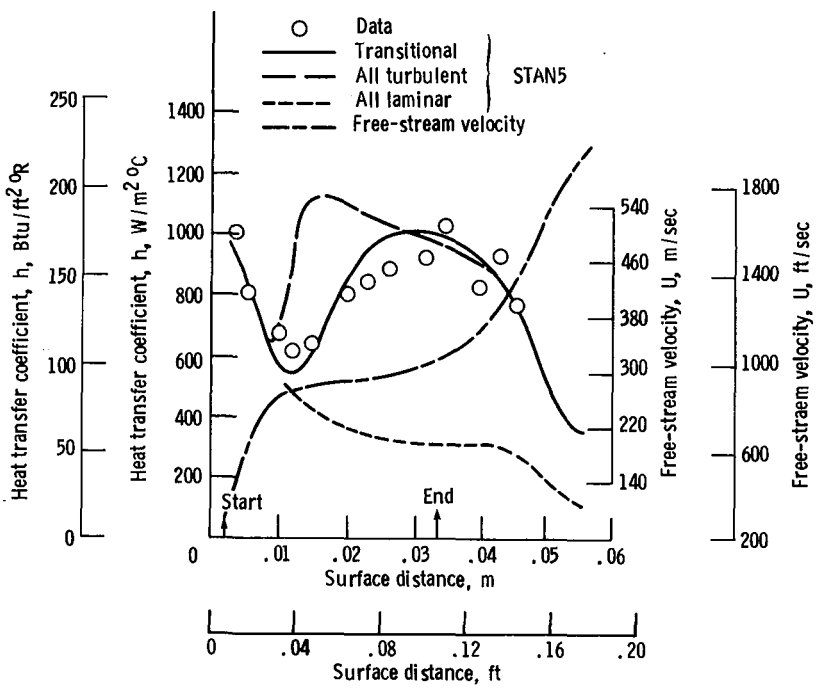

Figure 6. - Heat transfer coefficient as a function of surface distance. Turbine vane suction surface; simulated engine conditions; inlet turbulence level, 0.187; local acceleration parameter K at transition start, 0.12×10^{-3}. (Data from ref. 12 for very high turbulence.)

TURBULENT SOLUTIONS OF EQUATIONS OF FLUID MOTION*

Robert G. Deissler
National Aeronautics and Space Administration
Lewis Research Center
Cleveland, Ohio 44135

Some turbulent solutions of the unaveraged Navier-Stokes equations (equations of fluid motion) are reviewed. Those equations are solved numerically in order to study the nonlinear physics of incompressible turbulent flow. Initial three-dimensional cosine velocity fluctuations and periodic boundary conditions are used in most of the work considered. The three components of the mean-square velocity fluctuations are initially equal for the conditions chosen. The resulting solutions show characteristics of turbulence, such as the linear and nonlinear excitation of small-scale fluctuations. For the stronger fluctuations the initially nonrandom flow develops into an apparently random turbulence. Thus randomness or turbulence can arise as a consequence of the structure of the Navier-Stokes equations. The cases considered include turbulence that is statistically homogeneous or inhomogeneous and isotropic or anisotropic. A mean shear is present in some cases. A statistically steady-state turbulence is obtained by using a spatially periodic body force. Various turbulence processes, including the transfer of energy between eddy sizes and between directional components and the production, dissipation, and spatial diffusion of turbulence, are considered. It is concluded that the physical processes occurring in turbulence can be profitably studied numerically.

I. INTRODUCTION

Nearly all of the flows occurring in nature, as well as those that are manmade, are turbulent. For instance, the boundary between a column of rising smoke and the surrounding atmosphere is generally irregular and contains a range of scales of motion, indicating the presence of turbulence. The atmosphere itself is usually turbulent, as shown by the irregular appearance of many of the clouds present in it. Jets, wakes, astrophysical flows, and flows over surfaces are commonly turbulent, as is the region downstream of a grid in a wind tunnel or downstream of a waterfall. In general, turbulent flows are the rule and laminar flows the exception.

Because of the importance and challenge of the turbulence problem a great deal of research has been done over the past century. Basic ideas have been set forth, for instance, in papers by Reynolds (1883, 1895), Taylor (1921, 1935), von Karman (1937a, 1937b), and Heisenberg (1948). That work, together with more recent research, is discussed in books by Batchelor (1953), Hinze (1975), Frost and Moulden (1977), and others.

In spite of considerable research activity there is no general deductive theory of high-Reynolds-number (strong) turbulence. (Reynolds number is defined as the product of a velocity and a length divided by the kinematic viscosity of the fluid. It is a measure of the ratio of inertial to viscous effects.) Most of the analytical theories depend on a closure assumption for

*Also published in Reviews of Modern Physics, vol. 56, no. 1, part I, April 1984.

a hierarchy of averaged equations.[1] This immediately calls into question the appropriateness of referring to the analytical theories as deductive, except at low Reynolds numbers or in the final stage of decay, where nonlinear effects are small (Batchelor, 1953; Deissler, 1977).

One way in which a closure assumption can be avoided is by closure by specification of sufficient random initial conditions (Deissler, 1979). That method can successfully predict turbulence decay, and in the sense that the evolution of all initially specified quantities can be calculated, gives a complete solution. To use it, however, the initial conditions must be fully turbulent, and a large amount of initial data is required to satisfactorily specify the initial turbulence. The method does not seem capable of extension to some cases of turbulence maintained by mean gradients, where the effect of initial conditions may eventually become negligible (e.g., in fully developed turbulent pipe flow).

In view of the foregoing comments it seems desirable to consider numerical solutions of the unaveraged Navier-Stokes equations that display features of turbulence. Numerical methods and computers can be considered as tools for the solution of equations, just as can Fourier transforms and series expansions. It might be pointed out that it is more appropriate to refer to a numerical solution of the unaveraged equations as deductive than it is to so refer to most of the analytical theories, which are based on averaged equations and require closure assumptions. Moreover, most of the analytical theories are so complicated that a large amount of numerical work is required to obtain results from them. Attempts to obtain analytical solutions of the unaveraged equations have not been successful, mostly because of the nonlinearity of those equations. Herring (1973) mentions that the simplest turbulence theory is just the Navier-Stokes equations. Since most turbulence calculations are numerical anyway, no insight is lost by considering direct integration of the Navier-Stokes equations forward in time, starting from some suitable initial data.

Numerical solution (or numerical simulation) has sometimes been called experiment. It seems, at least to this writer, that there is an important difference between numerical solution and experiment as generally practiced. The former uses directly, and attempts to solve, a given set of constitutive equations, in this case the Navier-Stokes equations. The latter ordinarily does not, although both methods may arrive at the same result if the constitutive equations are congruous with the portion of nature to which they are applied. In general, it appears that experiment works directly with nature, whereas numerical solution works with a set of constitutive equations that should represent at least a portion of nature.

Several numerical solutions of the unaveraged equations have appeared that use a spectrum of random initial fluctuations (e.g., Orszag and Patterson, 1972; Clark et al., 1979; Rogallo, 1981; and Feiereisen et al., 1982). These studies, which appear to demonstrate the feasibility of carrying out turbulent solutions with present-day computing equipment, represent major advances.

---

[1]The hierarchy of correlation (averaged) equations obtained from the unaveraged Navier-Stokes equations is unclosed because of the nonlinearity of the latter. That is, there are more unknowns than equations, so that a closure assumption is required to obtain a solution.

Because of the difficulty of specifying realistic turbulent initial conditions (experimentally or analytically), it may be more appropriate to initially specify a simple regular fluctuation with a single length scale (as actually occurs downstream of a grid in a wind tunnel). This should be better for studying the development of small-scale fluctuations (and of turbulence in general) than would a spectrum of initial fluctuations, since for the latter, small-scale fluctuations are already present in the initial flow. Moreover, much higher Reynolds number flows can be calculated with a given numerical grid when a single length scale is initially present, at least for early and moderate times. Taylor and Green (1937) and others (e.g., Deissler, 1970a; Van Dyke, 1975; Corrsin and Kollman, 1977; and Deissler and Rosenbaum, 1973) have used a perturbation series to calculate the nonlinear development of higher harmonics from lower ones, but the calculations could not be carried very far in time. In these analyses the directional components of the initial fluctuation intensity were not equal. Orszag and Fateman (Orszag, 1977a) have recently used Taylor and Green's initial conditions and obtained a numerical solution for higher Reynolds numbers and longer times. The inviscid (infinite Reynolds number) case was investigated in some detail by Betchov and Szewczyk (1978).

The present review considers the nonlinear physics of turbulence numerically. Although the initial conditions used herein are nonrandom, the flow at higher Reynolds numbers breaks up into an apparently random turbulence. Unlike the problem of Taylor and Green all three of the directional components of the mean-square velocity fluctuations are equal at the initial time. In the absence of mean shear they are also equal at later times. Taylor and Green's directional components, on the other hand, do not approach equality, even at long times (Orszag, 1977a).

To study the processes in turbulence, first some background on the basic fluid flow and turbulence equations is given in section II and on numerical methods and solutions in section III. Four cases of turbulence are then considered, starting in section IV with the simplest one, in which mean gradients are absent (Deissler, 1981a). In this case no energy sources are present and the turbulence decays freely. (By contrast the presence of mean gradients would imply energy sources in the flow.) Here (in section IV) one can study viscous dissipation and the nonlinear transfer of energy between wave numbers or eddy sizes, as well as the randomization of the flow. Next, in section V a uniform mean shear is applied to study turbulence production and maintenance, and the linear and nonlinear transfer of energy between wave numbers and between directional components (Deissler, 1981c). The transfer of energy between wave numbers (both linear and nonlinear) is manifested by the creation of small-scale structure in the turbulence. Then, in section VI, the spatial diffusion of the inhomogeneous turbulence in a developing shear layer is considered (Deissler, 1982). Finally, by using a spatially periodic body force a turbulence that is statistically steady state at long times is studied in section VII. The first three of these cases have also been studied, but with a spectrum of random initial fluctuations and in some cases with an assumption for the small eddies, in Orszag and Patterson (1972), Clark et al. (1979), Rogallo (1981), Shannan et al. (1975), and Cain et al. (1981). Here we will confine ourselves to the development of turbulence from nonrandom initial conditions with a single length scale.

One of the problems in the numerical study of turbulence is that of accuracy, because of the small scale of some of the turbulent eddies. As the

Reynolds number (strength) of the turbulence or the time increases, smaller eddies are generated. No matter how small the numerical mesh size, one can always pick a Reynolds number or time large enough that the results will be quantitatively inaccurate. One way of improving the accuracy is by extrapolation to zero mesh size, as will be done here. The effectiveness of that procedure depends to some extent on the accuracy of the unextrapolated solution. If the solution has to be extrapolated too far, the results may not be accurate. Another popular method (not used here) is to model eddies smaller than the grid spacing (subgrid modeling) (e.g., Smagorinsky, et al., 1963; Deardorff, 1970; Clark et al., 1979; and Ferziger, 1977). This method requires an empirical input, although not as great a one as that for full modeling of the averaged equations. One might think of subgrid modeling as a useful crutch that can be phased out as numerical resolution improves. However, when it is used, it is sometimes difficult to tell which effects come from the equations of motion and which result from the subgrid modeling. Siggia (1981) has recently considered the converse problem; he made a numerical study of the small-scale eddies in which he modeled the larger ones.

Here we are mainly concerned with physical processes and trends, rather than with highly accurate numerical results (possibly unattainable at very high Reynolds numbers). Of course some degree of accuracy is necessary; otherwise we will not even be able to calculate trends. As the numerical mesh size decreases, quantitative differences in the results might be obtained. It is to be hoped, however, that the results will not be qualitatively different. Results to date indicate that to be the case.[2]

Other relevant review articles are given by Orszag (1977b), Schumann, et al. (1980), Eckman (1981), and Ott (1981).

II. BASIC EQUATIONS AND CONCEPTS

A. The Unaveraged Equations

Turbulent flows of a great many liquids and gases obey the Navier-Stokes equations. Those equations assume that the fluid is Newtonian (stress proportional to strain rate) and that it can be considered a continuum. The latter

---

[2]The attainment of accurate quantitative results appears to be a question of improvement of computers and of numerical methods. If state-of-the-art numerical methods and computers are used, good quantitative as well as qualitative results can already be obtained, at least for low and moderate Reynolds numbers. Orszag and Patera (1981) (as well as Moin and Kim (1982) using subgrid modeling) made significant numerical calculations of the velocity profile in the wall region of fully developed turbulent channel flow. The results agreed reasonably well with experiment, showing a wall transition region and a fully turbulent region in which the velocity varies as the logarithm of distance from the wall. The advent of high-speed computers and efficient numerical algorithms may be making possible for the first time the use of the Navier-Stokes equations in the solution of a wide range of realistic (turbulent) fluid-flow problems.

is usually a good assumption because in most cases intermolecular lengths are much smaller than the smallest significant turbulent eddies.

1. Equations in terms of instantaneous quantities

The Navier-Stokes and continuity equations for constant fluid properties (including incompressibility)[3,4] can be written as (e.g., Batchelor, 1967; or Deissler, 1976)

$$\frac{\partial \tilde{u}_i}{\partial t} = - \frac{\partial(\tilde{u}_i \tilde{u}_k)}{\partial x_k} - \frac{1}{\rho} \frac{\partial \tilde{p}}{\partial x_i} + \nu \frac{\partial^2 \tilde{u}_i}{\partial x_k \partial x_k} \tag{1}$$

and

$$\frac{\partial \tilde{u}_k}{\partial x_k} = 0 \tag{2}$$

The subscripts can take on the values 1, 2, and 3, and a repeated subscript in a term indicates a summation, with the subscript successively taking on the values 1, 2, and 3. The quantity $\tilde{u}_i$ is an instantaneous velocity component, x_i is a space coordinate, t is the time, ρ is the density, ν the kinematic viscosity, and $\tilde{p}$ is the instantaneous pressure. Equations (1) and (2) are, respectively, statements of the conservation of momentum and of mass. In order to obtain an explicit equation for the pressure, we take the divergence of equation (1) and apply the continuity equation (2) to get

$$\frac{1}{\rho} \frac{\partial^2 \tilde{p}}{\partial x_\ell \partial x_\ell} = - \frac{\partial^2 (\tilde{u}_\ell \tilde{u}_k)}{\partial x_\ell \partial x_k} \tag{3}$$

In the remainder of the paper it will usually be convenient to use equations (1) and (3) rather than (1) and (2). Equations (1) ($i = 1, 2, 3$) and (3) constitute a set of four equations in the four unknowns u_i and p. Since they are for instantaneous velocities and pressures, they should apply to turbulent as well as to laminar flows, subject to the restrictions mentioned at the beginning of this section. The Navier-Stokes equations have been known for more than a century, but their use in turbulent flows, other than in a schematic sense, has been restricted by a lack of ability to obtain solutions. Now, with advances in computers and numerical methods the situation appears somewhat brighter.

---

[3]The continuity equation is sometimes included in the Navier-Stokes equations.

[4]Most turbulence studies have been carried out for constant properties, for simplicity. That flow is realistic if the turbulence velocities are reasonably low compared with the velocity of sound, and if temperature gradients are not large.

The fundamental turbulence problem is an initial-value problem. That is, given initial values for the u_i as functions of position, a value for ν, and suitable boundary conditions, equations (1) and (3) should be sufficient for calculating the u_i and p/ρ as functions of time and position. The initial and boundary conditions used herein are specified in section III.

To interpret the terms in equation (1), it is convenient to multiply it through by ρ and by the stationary volume element $dx_1\, dx_2\, dx_3$. Then the term on the left side of the equation is the time rate of change of momentum in the element $\rho u_i\, dx_1\, dx_2\, dx_3$. This rate of change is contributed to by the terms on the right side of the equation. The first term on the right side, a nonlinear inertia term, is the net rate of flow of momentum into the element through its faces. The next term, also nonlinear, is a pressure-force term and gives the net force acting on the element by virtue of the pressure gradient in the x_i direction. It is nonlinear because of the nonlinear source term on the right side of the Poisson equation for the pressure (eq. (3)). Finally, the last term in equation (1), a linear viscous-force term, gives the net force acting on the element in the x_i direction by virtue of the viscosity.

2. Equations in terms of mean and fluctuating components

Following Reynolds (1895) one can break the instantaneous velocities and pressure in equations (1) to (3) into mean and fluctuating (or turbulent) components; that is, set

$$\tilde{u}_i = U_i + u_i \tag{4}$$

and

$$\tilde{p} = P + p \tag{5}$$

where

$$\overline{u}_i = \overline{p} = 0 \tag{6}$$

$$U_i = \overline{\tilde{u}}_i \tag{7}$$

and

$$P = \overline{\tilde{p}} \tag{8}$$

The overbars designate averaged values.[5] Equation (2) becomes, on using equations (4), (6), and (7),

$$\frac{\partial u_k}{\partial x_k} = \frac{\partial U_k}{\partial x_k} = 0 \tag{9}$$

which shows that both the fluctuating and mean velocity components obey continuity. Equations (1) and (3) become, on using equations (4) to (9), taking averages, and subtracting the averaged equations from the unaveraged ones,

$$\frac{\partial u_i}{\partial t} = -\frac{\partial}{\partial x_k}(u_i u_k) - \frac{1}{\rho}\frac{\partial p}{\partial x_i} + \nu\frac{\partial^2 u_i}{\partial x_k \partial x_k} - u_k\frac{\partial U_i}{\partial x_k} - U_k\frac{\partial u_i}{\partial x_k} + \frac{\partial}{\partial x_k}\overline{u_i u_k} \qquad (10)$$

$$\frac{1}{\rho}\frac{\partial^2 p}{\partial x_\ell \partial x_\ell} = -\frac{\partial^2 (u_k u_\ell)}{\partial x_k \partial x_\ell} - 2\frac{\partial u_k}{\partial x_\ell}\frac{\partial U_\ell}{\partial x_k} + \frac{\partial^2 \overline{u_k u_\ell}}{\partial x_k \partial x_\ell} \qquad (11)$$

Equations (10) and (11) will be used to study the processes in turbulence, but not for computational purposes (except in linearized cases). The first four terms of equation (10) and the first two of equation (11) look like the terms in equations (1) and (3), although their meanings are exactly the same only if $U_i = P = 0$ (eqs. (4) and (5)). The first three terms on the right side of equation (10), which contribute to $\partial u_i/\partial t$, can still be interpreted as an inertia-force (or turbulence self-interaction) term, a pressure-force term, and a viscous-force term. The remaining terms are, respectively, a turbulence production term, a mean-flow convection term, and a mean-turbulent-stress term, which appears when the turbulence is statistically inhomogeneous (when mean turbulence quantities such as $\overline{u_i u_k}$ are functions of position). (The reasons calling the production and convection terms as such will perhaps become clearer when the equivalent terms in the averaged equations (eqs. (14) and (15)) are discussed.) It will be seen that when the mean velocity gradient is not zero, the term $-U_k\,\partial u_i/\partial x_k$ generates a small-scale structure in the turbulence by vortex stretching. The nonlinear self-interaction term $-\partial(u_i u_k)/\partial x_k$ also produces a small-scale structure and in addition produces randomization of the flow. These effects will be considered in sections IV to VI. The Poisson equation for the pressure fluctuation (eq. (11)) has three source terms: a nonlinear term, a mean-gradient term, and a mean-turbulent-stress term, which appears when the turbulence is inhomogeneous.

We have defined an inhomogeneous turbulence as one in which averaged turbulence quantities are functions of position. Thus, a homogeneous turbulence is one in which averaged turbulence quantities are not functions of position. For instance, in homogenous turbulence

---

[5]For the most general flows the average is usually an ensemble average over a large number of macroscopically identical flows (i.e., mean quantities, but not fluctuating quantities, are the same in all the flows). In most cases, however, statistical uniformity or stationarity with respect to one or more coordinates, or with respect to time, obtains. Then, the average is taken with respect to the one or more coordinates or with respect to time. According to the ergodic theorem those averages are the same as the ensemble average if the flow is turbulent. In section V (uniform mean shear) three-dimensional spatial averages are used, even when the periodic boundary conditions introduce some local inhomogeneity into the fluctuations. Those averages still have meaning since their values are independent of the position of the boundaries of the cycle over which the averages are taken.

$$\overline{u_i u_j} \neq \overline{u_i u_j}\,(x_\ell)$$

$$\overline{u_i u_j u_k} \neq \overline{u_i u_j u_k}\,(x_\ell)$$

and

$$\overline{p\ \partial u_i/\partial x_j} \neq \overline{p\ \partial u_i/\partial x_j}\,(x_\ell)$$

Similar statements apply to other averaged turbulence quantities in a homogenous turbulence.

B. Averaged Equations

Although the averaged equations will not be solved numerically because they do not form a closed set, they are useful for studying the processes in turbulence.

1. Equations for mean flow

First consider the equations obtained by averaging each term of equations (1) and (3) and using equations (4) to (9).[5] This gives

$$\rho\frac{\partial U_i}{\partial t} = -\rho U_k \frac{\partial U_i}{\partial x_k} - \frac{\partial P}{\partial x_i} + \frac{\partial}{\partial x_k}\left(\rho\nu\frac{\partial U_i}{\partial x_k} - \rho\overline{u_i u_k}\right) \tag{12}$$

and

$$\frac{\partial^2 P}{\partial x_\ell\ \partial x_\ell} = -\rho\frac{\partial}{\partial x_\ell}\left(U_k\frac{\partial U_\ell}{\partial x_k}\right) - \rho\frac{\partial^2\ \overline{u_\ell u_k}}{\partial x_\ell\ \partial x_k} \tag{13}$$

These equations look like equations (1) and (3) with instantaneous values replaced by average values, but with the important difference that an extra term involving the quantity $\overline{u_i u_j}$ now appears in each of the equations. These terms arise from the nonlinear velocity terms in equations (1) and (3) and are a manifestation of the closure problem of turbulence[1]. If those terms were absent, equations (12) and (13) could be solved, and turbulent flows would be no more difficult to calculate than laminar ones. Note that terms in equations (12) and (13) that contain lower-case letters (other than x's) are turbulent terms.

The form of equation (12) suggests that the quantity $-\rho\overline{u_i u_k}$ augments the viscous stress $\rho\nu\partial U_i/\partial x_k$. Since it involves the fluctuating or turbulent velocity components u_i and u_k, we interpret it as a turbulent or Reynolds stress. For instance $-\rho\overline{u_1 u_2}$ will, in the presence of a mean-velocity gradient $\partial U_1/\partial x_2$, act like a shear stress on an x_1-x_3 plane. In the presence of $\partial U_1/\partial x_2$, u_1 will more likely be negative than positive when u_2

is positive, so that $\overline{u_1 u_2}$ will have a nonzero negative value. The quantity $-\rho\overline{u_1 u_2}$ can be compared with a viscous shear stress obtained in the kinetic theory of gases, where u_1 and u_2 are now molecular, rather than macroscopic velocity components. Similarly $\rho\overline{u_1^2}$ will act like a normal stress on an x_2-x_3 plane (similar to a normal stress or pressure obtained in kinetic theory, where u_1 is again taken to be a molecular velocity component).

2. One-point correlation equations

a. Construction of equations

We can construct equations for the undetermined quantities $\overline{u_i u_j}$ in equations (12) and (13) from the evolution equation for u_i (eq. (10)) and a similar equation for the component u_j:

$$\frac{\partial u_j}{\partial t} = -\frac{\partial}{\partial x_k}(u_j u_k) - \frac{1}{\rho}\frac{\partial p}{\partial x_j} + \nu\frac{\partial^2 u_j}{\partial x_k \partial x_k} - U_k\frac{\partial U_j}{\partial x_k} - U_k\frac{\partial u_j}{\partial x_k} + \frac{\partial}{\partial x_k}\overline{u_j u_k}$$

Multiply equation (10) by u_j and the preceding equation for u_j by u_i, add the two equations, and average.[5] This gives, using continuity (eq. (9)),

$$\frac{\partial}{\partial t}\overline{u_i u_j} = -\left(\overline{u_j u_k}\frac{\partial U_i}{\partial x_k} + \overline{u_i u_k}\frac{\partial U_j}{\partial x_k}\right) - U_k\frac{\partial}{\partial x_k}\overline{u_i u_j}$$

$$- \frac{\partial}{\partial x_k}\overline{u_i u_j u_k} - \frac{1}{\rho}\left(\frac{\partial}{\partial x_i}\overline{pu_j} + \frac{\partial}{\partial x_j}\overline{pu_i}\right) + \nu\frac{\partial^2\overline{u_i u_j}}{\partial x_\ell \partial x_\ell}$$

$$+ \frac{1}{\rho}\left(\overline{p\frac{\partial u_j}{\partial x_i}} + \overline{p\frac{\partial u_i}{\partial x_j}}\right) - 2\nu\overline{\frac{\partial u_i}{\partial x_\ell}\frac{\partial u_j}{\partial x_\ell}} \qquad (14)$$

Setting $i = j$ and using continuity, we get, for the rate of change of the kinetic energy per unit mass,

$$\frac{\partial}{\partial t}\left(\frac{\overline{u_i u_i}}{2}\right) = -\overline{u_i u_k}\frac{\partial U_i}{\partial x_k} - U_k\frac{\partial}{\partial x_k}\left(\frac{\overline{u_i u_i}}{2}\right) - \frac{\partial}{\partial x_k}\left(\frac{\overline{u_i u_i}}{2}u_k\right)$$

$$- \frac{1}{\rho}\frac{\partial}{\partial x_k}\left(\overline{pu_k}\right) + \nu\frac{\partial^2(\overline{u_i u_i}/2)}{\partial x_\ell \partial x_\ell} - \nu\overline{\frac{\partial u_i}{\partial x_\ell}\frac{\partial u_i}{\partial x_\ell}} \qquad (15)$$

As in equations (12) and (13), quantities in equations (14) and (15) that contain lower-case letters (other than x's) are turbulent quantities.

The one-point correlation equation (eq. (14)) gives an expression for the rate of change of $\overline{u_i u_j}$ that might be used in conjunction with equations (12) and (13). But the situation with respect to closure is now worse than it was before. Whereas without equation (14) we only had to determine $\overline{u_i u_j}$, with it we have to determine quantities like $\overline{u_i u_j u_k}$, $\overline{p u_j}$, $\overline{p\, \partial u_j/\partial x_i}$, and $\overline{(\partial u_i/\partial x_\ell)(\partial u_j/\partial x_\ell)}$. We might use equation (11) to obtain the pressure correlations, but that would only introduce more unknowns. However, equations (14) and (15) are useful for studying the processes in turbulence in that most of the terms have clear physical meanings. Moreover, we will be able to calculate terms in those equations from our numerical solutions.

b. Physical interpretation of terms

As in the case of equation (1) it is helpful, for purposes of interpretation, to multiply the terms in equations (14) and (15) through by ρ and by a volume element $dx_1\, dx_2\, dx_3$. Then the term on the left side of equation (14) or (15) gives the time rate of change of $\rho\overline{u_i u_j}$, or of the kinetic energy $\rho\overline{u_i u_i}/2$, within the element. This rate of change is contributed to by the terms on the right side of the equations. The first of those terms is equal to the net work done on the element by turbulent stresses acting in conjunction with mean-velocity gradients. It is therefore called a turbulence production term; it equals the rate of production of $\rho\overline{u_i u_j}$ or of $\rho\overline{u_i u_i}/2$ within the volume element by work done on the element. A somewhat abbreviated interpretation suggested by the form of the term, which is often given, is that it represents work done on the turbulent stress $\rho\overline{u_i u_i}$ by the mean-velocity gradient.

The next term in each of the equations describes the convection or net flow of turbulence or turbulent energy into a volume element by the mean velocity U_k. It moves the turbulence bodily, rather than doing work on it by deforming it, as in the case of the production term. It vanishes when either U_k is zero (no mean flow) or when the turbulence is homogenous ($\overline{u_i u_j} \neq \overline{u_i u_j}\,(x_k)$). In the latter case there is no accumulation of turbulence within a volume element, even with a mean flow.

The next three terms in equation (14) and in equation (15) also vanish for homogeneous turbulence. Since they do not contain the mean velocity, they do not convect or move the turbulence bodily. Therefore we interpret them as diffusion terms, which diffuse net turbulence from one part of the turbulent field to another by virtue of its inhomogeneity. The pressure-velocity-gradient terms in equation (14) drop out of the contracted equation (15) because of continuity (eq. (9)). Therefore, they contribute nothing to the rate of change of the total energy $\overline{u_i u_i}/2$, but they can distribute the energy energy among the three directional components $\overline{u_{(i)}^2}/2$ (no sum on i). The last term in equations (14) and (15) is the viscous dissipation term, which dissipates turbulence by the presence of fluctuating velocity gradients.

3. Two-point correlation and spectral equations

To consider the transfer of turbulence between eddy sizes or wave numbers (spectral transfer), we must obtain two-point correlation equations. Terms related to that process do not appear in the single-point equations ((14) and (15)). To obtain two-point equations, we use in addition to equations (10) and (11), written at the point P, the following equations written at the point P':

$$\frac{\partial u_j'}{\partial t} = -\frac{\partial}{\partial x_k'}(u_j'u_k') - \frac{1}{\rho}\frac{\partial p'}{\partial x_j'} + \nu\frac{\partial^2 u_j'}{\partial x_k' \partial x_k'} - u_k'\frac{\partial U_j'}{\partial x_k'} - U_k'\frac{\partial u_j'}{\partial x_k'} + \frac{\partial}{\partial x_k'}\overline{u_j'u_k'} \tag{16}$$

and

$$\frac{1}{\rho}\frac{\partial^2 p'}{\partial x_\ell' \partial x_\ell'} = -\frac{\partial^2(u_k'u_\ell')}{\partial x_k' \partial x_\ell'} - 2\frac{\partial u_k'}{\partial x_\ell'}\frac{\partial U_\ell'}{\partial x_k'} + \frac{\partial^2 \overline{u_k'u_\ell'}}{\partial x_k' \partial x_\ell'} \tag{17}$$

Multiplying equation (10) by u_j' and equation (16) by u_i, adding, taking averages,[5] and using equation (16) and the fact that quantities at one point are independent of the position of the other point result in

$$\frac{\partial}{\partial t}\overline{u_iu_j'} = -\overline{u_ku_j'}\frac{\partial U_i}{\partial x_k} - \overline{u_iu_k'}\frac{\partial U_j'}{\partial x_k'} - U_k\frac{\partial}{\partial x_k}\overline{u_iu_j'} - U_k'\frac{\partial}{\partial x_k'}\overline{u_iu_j'} - \frac{\partial}{\partial x_k}\overline{u_iu_ku_j'}$$

$$- \frac{\partial}{\partial x_k'}\overline{u_iu_j'u_k'} - \frac{1}{\rho}\left(\frac{\partial}{\partial x_i}\overline{pu_j'} + \frac{\partial}{\partial x_j'}\overline{u_ip'}\right) + \nu\left(\frac{\partial^2 \overline{u_iu_j'}}{\partial x_k \partial x_k} + \frac{\partial^2 \overline{u_iu_j'}}{\partial x_k' \partial x_k'}\right) \tag{18}$$

To simplify the equations, the turbulence will be considered homogeneous (correlations independent of x_i). (See Hinze (1975) or Deissler (1961) for inhomogeneous equations.) Then the two-point correlations (e.g., $\overline{u_iu_j'}$) will be functions only of $r_i \equiv x_i' - x_i$, so that $\partial/\partial x_i = -\partial/\partial r_i$ and $\partial/\partial x_i' = \partial/\partial r_i$. In addition, homogeneity requires that $\partial U_i/\partial x_j'$ be a constant, so that $\partial U_i/\partial x_j' = \partial U_i/\partial x_j$ and $U_k' - U_k = r_\ell\,\partial U_i/\partial x_j$. (If $\partial U_i/\partial x_j$ were a function of x_i', we could not remove all x_i' dependency from eq. (18).) Equation (18) becomes

$$\frac{\partial}{\partial t}\overline{u_iu_j'} = -\overline{u_ku_j'}\frac{\partial U_i}{\partial x_k} - \overline{u_iu_k'}\frac{\partial U_j}{\partial x_k} - \frac{1}{\rho}\left(\frac{\partial}{\partial r_j}\overline{u_ip'} - \frac{\partial}{\partial r_i}\overline{pu_j'}\right)$$

$$+ 2\nu\frac{\partial^2 \overline{u_iu_j'}}{\partial r_k \partial r_k} - \frac{\partial U_k}{\partial x_\ell} r_\ell \frac{\partial \overline{u_iu_j'}}{\partial r_k} - \frac{\partial}{\partial r_k}\left(\overline{u_iu_j'u_k'} - \overline{u_iu_ku_j'}\right) \tag{19}$$

The equations for the pressure-velocity correlations obtained from equations (11) and (17) are, for homogeneous turbulence,

$$\frac{1}{\rho}\frac{\partial^2 \overline{u_i p'}}{\partial r_\ell \partial r_\ell} = -2\frac{\partial \overline{u_i u_k'}}{\partial r_\ell}\frac{\partial U_\ell}{\partial x_k} - \frac{\partial^2 \overline{u_i u_\ell' u_k'}}{\partial r_\ell \partial r_k} \tag{20}$$

$$\frac{1}{\rho}\frac{\partial^2 \overline{pu_j'}}{\partial r_\ell \partial r_\ell} = 2\frac{\partial \overline{u_\ell u_j'}}{\partial r_k}\frac{\partial U_k}{\partial x_\ell} - \frac{\partial^2 \overline{u_\ell u_k u_j'}}{\partial r_\ell \partial r_k} \tag{21}$$

a. Interpretation of terms

The terms on the right side of the Poisson equations (eqs. (20) and (21)) are source terms associated with the mean velocity and with triple correlations arising from the nonlinear velocity terms in equations (11) and (17). The right side of the two-point equation (eq. (19)) contains, as in the case of the single-point equation (eq. (14)), turbulence production, directional distribution (pressure-velocity), and viscous terms. There are no diffusion terms in equation (19) since the turbulence is homogeneous. The last two terms in that equation are new terms that do not have counterparts in the single-point equations. To interpret them, we convert equation (19) to spectral form by taking its Fourier transform. Thus, define the following three-dimensional Fourier transforms:

$$\overline{u_i u_j'}(\vec{r}) = \int_{-\infty}^{\infty} \varphi_{ij}(\vec{\kappa}) e^{i\vec{\kappa}\cdot\vec{r}}\, d\vec{\kappa} \tag{22}$$

$$-\frac{\partial}{\partial r_j}\overline{u_i p'} + \frac{\partial}{\partial r_i}\overline{pu_j'} = \int_{-\infty}^{\infty} \Pi_{ij}(\vec{\kappa}) e^{i\vec{\kappa}\cdot\vec{r}} d\vec{\kappa} \tag{23}$$

$$-\frac{\partial U_k}{\partial x_\ell} r_\ell \frac{\partial \overline{u_i u_j'}}{\partial r_k} = \int_{-\infty}^{\infty} T_{ij}'(\vec{\kappa}) e^{i\vec{\kappa}\cdot\vec{r}}\, d\vec{\kappa} \tag{24}$$

and

$$-\frac{\partial}{\partial r_k}\overline{u_i u_j' u_k'} - \overline{u_i u_k u_j'} = \int_{-\infty}^{\infty} T_{ij}(\vec{\kappa}) e^{i\vec{\kappa}\cdot\vec{r}}\, d\vec{\kappa} \tag{25}$$

where φ_{ij}, Π_{ij}, T_{ij}', and T_{ij} are, respectively, Fourier transforms of the quantities on the left sides of the defining equations (eqs. (22) to (25)), $\vec{\kappa}$ is a wave-number vector, and $d\vec{\kappa} = d\kappa_1\, d\kappa_2\, d\kappa_3$. Physical interpretations of the Fourier transforms defined by equations (22) to (25) follow. Equation (19) becomes, on taking its Fourier transform,

$$\frac{\partial}{\partial t}\varphi_{ij} = -\varphi_{kj}\frac{\partial U_i}{\partial x_k} - \varphi_{ik}\frac{\partial U_j}{\partial x_k} + \frac{1}{\rho}\Pi_{ij}(\vec{\kappa}) - 2\nu\vec{\kappa}^2\varphi_{ij} + T_{ij}' + T_{ij} \tag{26}$$

If we let $\vec{r} = 0$ in equation (22), we have

$$\overline{u_i u_j} = \int_{-\infty}^{\infty} \varphi_{ij} \, d\vec{\kappa} \tag{27}$$

so that we can interpret φ_{ij} as a spectral component of $\overline{u_i u_j}$. As in equation (19), terms on the right side of equation (26) can be interpreted as production, directional distribution, and viscous dissipation terms. They contribute to the rate of change of a spectral component φ_{ij} of $\overline{u_i u_j}$.

To interpret the term T'_{ij} in equation (26), we let $\vec{r} = 0$ in equation (24). This gives

$$0 = \int_{-\infty}^{\infty} T'_{ij} \, d\vec{\kappa} \tag{28}$$

Thus, T'_{ij} gives zero total contribution to the rate of change of $\overline{u_i u_j}$. But it can distribute, or transfer between wave numbers or eddy sizes, spectral contributions φ_{ij} to $\overline{u_i u_j}$. So T'_{ij}, which is proportional to $\partial U_k / \partial x_\ell$, is interpreted as a mean-gradient spectral transfer term (Deissler, 1961). The term $-r_\ell (\partial \overline{u_i u'_j} / \partial r_k) \, \partial U_k / \partial x_\ell$ in equation (19) is therefore the Fourier transform of a mean-gradient spectral transfer term.

To interpret the last term in equation (26), we use equation (25), where we note that $\partial/\partial r_k = \partial/\partial x'_k = -\partial/\partial x_k$, that quantities at one point are independent of the position of the other point, and that continuity (eq. (9)) holds. Equation (25) becomes

$$\int_{-\infty}^{\infty} T_{ij} \, e^{i\vec{\kappa}\cdot\vec{r}} \, d\vec{\kappa} = -\overline{\frac{\partial}{\partial x'_k} u_i u'_j u'_k} - \overline{\frac{\partial}{\partial x_k} u_i u_k u'_j}$$

$$= -\overline{u_i u'_k \frac{\partial u'_j}{\partial x'_k}} - \overline{u'_j \frac{\partial u_i u_k}{\partial x_k}} \tag{29}$$

If we let $\vec{r} = 0$, equation (29) becomes

$$\int_{-\infty}^{\infty} T_{ij} \, d\vec{\kappa} = -\frac{\partial}{\partial x_k} \overline{u_i u_j u_k} = 0 \tag{30}$$

since we have assumed homogeneity of the turbulence. Thus, as in the case of T'_{ij}, T_{ij} contributes nothing to the rate of change of $\overline{u_i u_j}$. It can, however, transfer spectral components of $\overline{u_i u_j}$ from one part of wave-number space to another. So we interpret T_{ij} as a spectral transfer term associated with turbulence self-interaction (as opposed to interaction between

turbulence and mean gradients). The term $-(\partial/\partial r_k)(\overline{u_i u_j' u_k'} - \overline{u_i u_k u_j'})$ in equation (19) is therefore the Fourier transform of a self-interaction spectral transfer term. Although the turbulence has been assumed to be homogeneous for interpreting T_{ij} and T'_{ij} as transfer terms, it has been shown that similar interpretations apply when the turbulence is inhomogeneous (Deissler, 1981b).[6]

The transfer of turbulence from one part of wave-number space to another, or from one eddy size to another, produces a wide range of scales of motion in most turbulent flows as illustrated by the numerical solutions in sections IV and V (e.g., figs. 2(c), 8, and 24). The state of affairs is neatly summarized in a nonmathematical way by a poem written long before equations (26), (28), or (30) was known (Richardson, 1922):

> Big whirls have little whirls,
> Which feed on their velocity;
> And little whirls have lesser whirls,
> And so on to viscosity.

4. Vorticity and dissipation

For homogeneous turbulence one can obtain a relation between the viscous dissipation term in equation (15) or (19) ($i = j$) and the vorticity or swirl in the turbulence. The dimensionless vorticity $\vec{\omega}$ is defined as the curl of $\vec{u}$:

$$\vec{\omega}(\vec{x}) = \vec{\nabla} \times \vec{u}(\vec{x}) \tag{31}$$

or

$$\omega_i = \varepsilon_{ijk} \frac{\partial u_k}{\partial x_j} \tag{32}$$

where ε_{ijk} is the alternating tensor.[7] Then

$$\overline{\omega_k \omega_k} = \varepsilon_{ijk}\varepsilon_{pmk} \overline{\frac{\partial u_i}{\partial x_j} \frac{\partial u_\ell}{\partial x_m}} = (\delta_{ip}\delta_{jm} - \delta_{im}\delta_{jp}) \overline{\frac{\partial u_i}{\partial x_j} \frac{\partial u_\ell}{\partial x_m}} = \overline{\frac{\partial u_i}{\partial x_j} \frac{\partial u_i}{\partial x_j}} - \overline{\frac{\partial u_i}{\partial x_j} \frac{\partial u_j}{\partial x_i}} \tag{33}$$

But, because

$$\frac{\partial u_j}{\partial x_j} = 0 \tag{34}$$

---

[6] The fact that terms related to T_{ij} or T'_{ij} do not appear in the one-point eq. (14) for inhomogeneous turbulence indicates that T_{ij} and T'_{ij} do not contribute to $\partial \overline{u_i u_i}/\partial t$. Thus, even for inhomogeneous turbulence they can only transfer turbulence from one part of wave-number space to another.

$$\overline{\frac{\partial u_i}{\partial x_j}\frac{\partial u_j}{\partial x_i}} = \frac{\partial^2 \overline{u_i u_j}}{\partial x_i \partial x_j} = 0 \tag{35}$$

for homogeneous turbulence. Equation (33) then becomes

$$\overline{\omega_k \omega_k} \equiv \overline{\omega^2} = \overline{\frac{\partial u_i}{\partial x_j}\frac{\partial u_i}{\partial x_j}} \equiv \frac{\varepsilon}{\nu} \tag{36}$$

Thus, for homogeneous turbulence the mean-square vorticity is just the rate of viscous dissipation ε of turbulent energy divided by the kinematic viscosity (eq. (15)). So the more intense the swirl in the turbulence, the faster it dissipates.

From a closure standpoint we are somewhat better off with the two-point equations (eqs. (19) to (21)) than we were with the single-point equation (eq. (14)), since we no longer have to model terms like $\overline{p\, \partial u_j/\partial x_i}$ and $\overline{(\partial u_i/\partial x_\ell)(\partial u_j/\partial x_\ell)}$. However, we still have to evaluate triple-correlation terms unless the turbulence is very weak or unless the interaction between the turbulence and the mean flow is large compared with the turbulence self-interaction.

5. Remarks

We shall not discuss here the many schemes that have been proposed for closing the averaged equations considered in this section. Instead, we will avoid the closure problem by obtaining numerical solutions of the unaveraged equations (eqs. (1) and (3)). The importance of the averaged equations is enhanced by these numerical solutions; by using the solutions of the unaveraged equations, terms in the averaged equations that represent various physical processes in the turbulence can be calculated. Thus, the averaged equations appear to be necessary, or at the least very convenient, for the physical interpretation of the numerical results.

III. NUMERICAL SOLUTIONS AND METHODS

A. Initial conditions

For most of the numerical solutions considered here, the initial velocity fluctuation is assumed to be given by

$$u_i = \sum_{n=1}^{3} a_i^n \cos \vec{q}^n \cdot \vec{x} \tag{37}$$

Then, from equation (4)

---

[7] $\varepsilon_{ijk} = 0$ when i, j, and k are not all different. When the subscripts are all different, $\varepsilon_{ijk} = +1$ when they are in cyclic order and -1 when they are in acyclic order.

$$\tilde{u}_i = \sum_{n=1}^{3} a_i^n \cos \vec{q}^n \cdot \vec{x} + U_i \tag{38}$$

The quantity a_i^n is an initial velocity amplitude or Fourier coefficient of the velocity fluctuation, $q^{\rightarrow n}$ is an initial wave-number vector, and U_i is an initial mean-velocity component. To satisfy the continuity conditions (eqs. (2) and (9)), we set

$$a_i^n q_i^n = 0 \tag{39}$$

For the present work let

$$a_i^1 = k(2, \pm 1, 1),\ a_i^2 = k(1, \pm 2, 1),\ a_i^3 = k(1, \pm 1, 2)$$

$$q_i^1 = (-1, \pm 1, 1)/x_0,\ q_i^2 = (1, \mp 1, 1)/x_0,\ q_i^3 = (1, \pm 1, -1)/x_0 \tag{40}$$

where k has the dimensions of a velocity and determines the intensity of the initial velocity fluctuation. The quantity x_0 is the length scale of the initial velocity fluctuation. The quantities k and x_0, together with the kinematic viscosity ν and equation (40) then determine the initial Reynolds number $\overline{u_0^2}^{1/2} x_0/\nu$, since the square of equation (37), averaged over a period, gives $\overline{u_0^2}$. In addition to satisfying the continuity equation (eq. (39)), equations (37) and (40) give

$$\overline{u_1^2} = \overline{u_2^2} = \overline{u_3^2} = \overline{u_0^2} \tag{41}$$

at the initial time.[8] Thus, equations (37) or (38) and (40) give a particularly simple initial condition in that we need specify only one component of the mean-square velocity fluctuation. Moreover, for no mean shear they give an isotropic turbulence at later times, as will be seen. Note that it is necessary to have at least three terms in the summation in equation (37) or (38) to satisfy equation (41). We do not specify an initial condition for the pressure because it is determined by equation (3) and the initial velocities.

B. Numerical grid and boundary conditions

To carry out numerical solutions subject to the initial condition given by equations (37) or (38) and (40), we use a stationary cubical grid with a maximum of 32^3 points and with faces at $x_i^* = x_i/x_0 = 0$ and 2π. For boundary conditions we assume periodicity for the fluctuating quantities. That is, let

$$(u_i)_{x_j^*=2\pi+b_j^*} = (u_i)_{x_j^*=b_j^*} \tag{42}$$

and

$$P_{x_j^*=2\pi+b_j^*} = P_{x_j^*=b_j^*} \tag{43}$$

for $b_j^* \ll 2\pi$, where $b_j^* = b_j/x_0$, $x_j^* = x_j/x_0$, and b_j is a variable length.

By using equations (4) and (5) these become

$$(\tilde{u}_i)_{x_j^*=2\pi+b_j^*} = (\tilde{u}_i)_{x_j^*=b_j^*} + (U_i)_{x_j^*=2\pi+b_j^*} - (U_i)_{x_j^*=b_j^*} \tag{44}$$

and

$$\tilde{p}_{x_j^*=2\pi+b_j^*} = \tilde{p}_{x_j^*=b_j^*} + P_{x_j^*=2\pi+b_j^*} - P_{x_j^*=b_j^*} \tag{45}$$

In the present work we assume also that P, given by equation (13), is periodic, so that

$$P_{x_j^*=2\pi+b_j^*} = P_{x_j^*=b_j^*} \tag{46}$$

and equation (45) becomes

$$\tilde{p}_{x_j^*=2\pi+b_j^*} = \tilde{p}_{x_j^*=b_j^*} \tag{47}$$

These equations are used to calculate numerical derivatives at the boundaries of the computational grid.

C. Numerical solutions

In carrying out the numerical solutions, we have a choice of solving a set of equations containing u_i, p, U_i, and P (eqs. (10) to (13)), or one containing $\tilde{u}_i$ and $\tilde{p}$ (eqs. (1) and (3)). The latter set, which is much simpler, is generally used here.[9] That is, we solve equations (1) and (3) subject to initial condition (38) and boundary conditions (44) and (47).

The spatial- and time-differencing schemes (which numerically conserve momentum and energy) are essentially those used by Clark et al. (1979). For the spatial derivatives in equations (1) and (3) we use centered fourth-order difference expressions (e.g., McCormick and Salvadore, 1964). For instance, the fourth-order difference expression used for $\partial\tilde{u}_i/\partial x_k$ is

---

[8]The first three terms of eq. (41) apply at all times when there are no mean gradients in the flow.

$$\left(\frac{\partial \tilde{u}_i}{\partial x_k}\right)_n = \frac{1}{12\,\Delta x_k}\left[(\tilde{u}_i)_{n-2} - 8(\tilde{u}_i)_{n-1} + 8(\tilde{u}_i)_{n+1} - (\tilde{u}_i)_{n+2}\right]$$

where Δx_k is the grid-point spacing, and the subscripts n, $n + 1$, etc. refer to grid points in the x_k direction. Fourth-order difference expressions are often considered more efficient than the usual second-order ones (Orszag and Israeli, 1974). (Spectral methods devised by Orszag and associates are still more efficient but may be somewhat trickier to use.) Centered expressions (same number of points on both sides of n, see preceding expression) can be used both at interior grid points and at the boundaries of the grid; when n refers to a point on a boundary, values for $\tilde{u}_i$ outside of the grid, which are required for calculating the numerical derivatives at the boundary, are obtained from boundary condition (44).

For time differencing we use a predictor-corrector method with a second-order (leapfrog) predictor and a third-order (Adams-Moulton) corrector (Ceschino and Kuntzman, 1966). If m represents a time step, and $(R_i)_m$ the right side of equation (1), then at each grid point in space the second-order leapfrog predictor for $\tilde{u}_i$ at time step $m + 1$ is

$$(\tilde{u}_i)^{(1)}_{m+1} = (\tilde{u}_i)_{m-1} + 2\,\Delta t(R_i)_m$$

and the third-order Adams-Moulton corrector is

$$(\tilde{u}_i)^{(2)}_{m+1} = (\tilde{u}_i)_m + \frac{\Delta t}{12}\left[5(R_i)^{(1)}_{m+1} + 8(R_i)_m - (R_i)_{m-1}\right]$$

where Δt is the time increment. The quantity $(R_i)^{(1)}_{m+1}$ in the preceding corrector is calculated by using $(\tilde{u}_i)^{(1)}_{m+1}$ in the right side of equation (1), where $(\tilde{u}_i)^{(1)}_{m+1}$ is calculated from the leapfrog predictor. Note that the leapfrog method (so-called because it leaps over the time step m), although unstable for all Δt when used by itself for Navier-Stokes equations, is stable when used as a predictor.

The Poisson equation for the pressure (eq. (3)) is solved directly by a fast Fourier transform method. This method of solution was found to preserve continuity quite well ($\nabla.\vec{u} \approx 0$) except near the ends of some of the runs for no mean gradients, where the solutions began to deteriorate. (Another indication of incipient solution deterioration near the ends of some of the runs for no mean gradients was that equation (41) was no longer accurately satisfied.[8])

---

[9]Dividing the velocities and pressures into mean and fluctuating components is evidently not advantageous from a computational standpoint except, possibly, in linearized cases.

Two known types of numerical instabilities can occur in the present solutions: a viscous instability connected with the first and last terms in equation (1), which occurs if $\nu\,\Delta t/(\Delta x_k)^2$ is too large; and a convective instability connected with the first and second terms (or the first and third terms through eq. (3)), which occurs if $u_i\,\Delta t/\Delta x_k$ is too large. In these criteria Δt, Δx_k, and u_i are, respectively, a time step, distance step, and velocity. Thus, a particular solution should be numerically stable if, for a given Δx_k, the time step is sufficiently small. Numerical stability is typically obtained when the solution varies smoothly from time step to time step, with no significant breaks in the slope from one step to the next. This is the case for all of the results given here.

For the present solution very good temporal resolution is obtained automatically when Δt is sufficiently small to give numerical stability. That temporal resolution is much better than the three-dimensional spatial resolution, which is more severely limited by the storage and power of the computer. However, as will be seen (fig. 19), sufficient spatial resolution is obtained to give reasonably accurate averaged results for times not excessively large. Some of the averaged results are extrapolated to zero spatial mesh size in an effort to obtain more accuracy. The fourth-order method of extrapolation (consistent with the fourth-order differencing used here) is given in Deissler (1981a, 1981c).

IV. HOMOGENEOUS FLUCTUATIONS AND TURBULENCE, NO MEAN FLOW

For this case ($U_i = \partial\,\overline{u_i u_k}/\partial x_k = 0$), equations (10) and (11) reduce to (1) and (3) without the ~'s over instantaneous quantities. We thus solve numerically

$$\frac{\partial u_i}{\partial t} = -\frac{\partial(u_i u_k)}{\partial x_k} - \frac{1}{\rho}\frac{\partial p}{\partial x_i} + \nu\frac{\partial^2 u_i}{\partial x_k x_k} \tag{48}$$

and

$$\frac{1}{\rho}\frac{\partial^2 p}{\partial x_\ell\,\partial x_\ell} = -\frac{\partial^2(u_\ell u_k)}{\partial x_\ell x_k} \tag{49}$$

subject to initial conditions (37) and (40) and boundary conditions (42) and (43). In equation (40) for the coefficients in the initial conditions, we choose the first set of signs.

A. Dimensionless form of equations

For carrying out the numerical solutions and presenting the results in as general and compact a form as possible, we nondimensionalize equations (48) and (49) as

$$\frac{\partial u_i^*}{\partial t^*} = -\frac{\partial(u_i^* u_k^*)}{\partial x_k^*} - \frac{\partial p^*}{\partial x_i^*} + \frac{\partial^2 u_i^*}{\partial x_k^*\partial x_k^*} \tag{48a}$$

and

$$\frac{\partial^2 p^*}{\partial x_\ell^* \, \partial x_\ell^*} = - \frac{\partial^2 (u_\ell^* u_k^*)}{\partial x_\ell^* \, \partial x_k^*} \tag{49a}$$

where

$$u_i^* = \frac{x_0}{\nu} u_i, \quad t^* = \frac{\nu}{x_0^2} t$$

$$x_i^* = \frac{x_i}{x_0}, \quad p^* = \frac{x_0^2}{\rho \nu^2} p$$

and x_0 is the initial fluctuation length, which first appeared in equation (40). Note that all of the quantities have been nondimensionalized by x_0 and the kinematic viscosity ν.

The initial and boundary conditions in equations (37), (40), (42), and (43) become in dimensionless form

$$u_i^* = \sum_{n=1}^{3} a_i^{n*} \cos \vec{q}^{n*} \cdot \vec{x}^* \tag{37a}$$

$$\left.\begin{aligned} a_i^{1*} &= k^*(2,\pm 1,1), \quad a_i^{2*} = k^*(1,\pm 2,1), \quad a_i^{3*} = k^*(1,\pm 1,2) \\ q_i^{1*} &= (-1,\pm 1,1), \quad q_i^{2*} = (1,\mp 1,1), \quad q_i^{3*} = (1,\pm 1,-1) \end{aligned}\right\} \tag{40a}$$

$$(u_i^*)_{x_j^* = 2\pi + b_j^*} = (u_i^*)_{x_j^* = b_j^*} \tag{42a}$$

and

$$p^*_{x_j^* = 2\pi + b_j^*} = p^*_{x_j^* = b_j^*} \tag{43a}$$

where, in addition to the dimensionless quantities defined above,

$$a_i^{n*} = \frac{x_0}{\nu} a_i^n, \quad q_i^{n*} = x_0 q_i^n, \text{ and } k^* = \frac{x_0}{\nu} k.$$

Note that k^* has the form of a Reynolds number, where x_0 is the length and k is the velocity. The initial Reynolds number appearing in the figures of this paper, $\left(\overline{u_0^2}\right)^{1/2} x_0/\nu$, where $\left(\overline{u_0^2}\right)^{1/2}$ is an initial root-mean-square velocity component, is obtained by choosing a value for k^* in equations (40a) and

space averaging u_1^{*2} over a period, by using equation (37a). The value of $\left(\overline{u_0^{*2}}\right)^{1/2} = \left(\overline{u_0^2}\right)^{1/2} x_0/\nu$ so obtained is also used in the ordinates of figures 1 and 2, where $u_1/\left(\overline{u_0^{*2}}\right)^{1/2} = u_1^*/\left(\overline{u_0^{*2}}\right)^{1/2}$, and u_1^* is calculated from equations (48a) and (49a) (starting with initial values from eq. (37a)).

B. Development of random fluctuations

Figure 1 shows the calculated evolution of velocity fluctuations (normalized by the initial root-mean-square velocity) at two fixed points in space for the initial Reynolds number shown in the figure (no correction for discretization error). Since there is no input of energy, the fluctuating motion eventually decays to a state of rest. In spite of the nonrandom initial condition (eq. (37) or (37a)), the velocity fluctuations have the appearance of those for a random turbulence. It is important to point out that the fluctuations are not due to numerical instability since a large number of time steps (typically about 20) lie between changes of sign of du_1/dt. In connection with the high Reynolds number in figure 1 it might be pointed out that Betchov and Szewczyk (1978) obtained reasonable turbulent-like numerical results even for infinite Reynolds number for times not excessively large (see also Schumann et al., 1980).

1. Randomness as sensitivity to initial conditions

The dashed curves of $u_1/\left(\overline{u_0^2}\right)^{1/2}$ are for initial conditions perturbed approximately 0.1 percent. (The coefficients a_1^n and q_1^n given by eq. (40) are changed by 0.1 percent of their values.) The perturbed curves follow the unperturbed ones for a short time and then depart sharply. Thus, a very small perturbation of initial conditions causes a large change in the values of u_1 (except near $t = 0$). On the other hand, the root-mean-square values of the velocities (spatially averaged) decrease smoothly and are unaffected by the perturbation of the initial conditions. All of these features are characteristic of turbulence. (The observed sensitivity of the instantaneous flow to small changes in initial conditions may have unfavorable implications for detailed long-term weather predictions (Lorenz, 1963).)

We note that the spatially averaged values in figure 1 follow approximately the decay law $\overline{u^2} \sim t^{-n}$, where $n \sim 2.5$. This lies between the value for n of 3.3 observed for turbulence downstream of a waterfall (Ling and Saad, 1977), and the value of 1.2 generally observed for turbulence generated by flow through a grid in a wind tunnel (Uberoi, 1963). The decay law is evidently very much dependent on the initial condition for the turbulence.

2. Effect of numerical mesh size on randomness

To get an idea of the effect of mesh size in the numerical grid on the apparent randomness of the velocity fluctuations, values of $u_1/\left(\overline{u_0^2}\right)^{1/2}$ at the center of the grid are plotted against t^* in figure 2 for three mesh sizes. All three of the curves have a random appearance. However, as the number of mesh points increases (as the mesh becomes finer), smaller scale

fluctuations are resolved and the randomness appears to be greater. This trend indicates that the observed randomness is not due to the use of too coarse a grid.

C. Further evidence for randomness and indications of isotropic turbulence

For turbulence the correlation between velocities at two times $\overline{u_1(t)u_1(t_0)}$ should go to zero as the separation of the times t and t_0 increases. Figure 3 shows that this occurs for the present high-Reynolds-number calculations. For true turbulence the correlation should probably decrease smoothly with time. This is nearly the case for the larger t_0 (fig. 3(b)). (t_0 is the time in the correlation coefficient in fig. 3 that remains fixed as the other (variable) time t increases.) At early times there is probably some nonrandom structure in the turbulence caused by the nonrandom initial conditions (fig. 3(a)).

As a further indication that the high-Reynolds-number flow breaks up into turbulence, we calculate the evolution of the cross correlation $\overline{u_1u_2}$. Although $\overline{u_1^2} = \overline{u_2^2} = \overline{u_3^2}$ at all times,[8] the initial $\overline{u_1u_2}$ given by equations (37) and (40) is not zero. However, figure 4 shows that because of the apparent randomization of the flow $\overline{u_1u_2}$ goes to zero as time increases. The fluctuations in the curve at early times (as also in the curve of fig. 3(a)) are probably caused by nonrandom structure in the flow at early times.[10]

Figures 1 to 4, together with the fact that the three components $\overline{u_{(i)}^2}$ are equal, show that at later times we appear to get a reasonable approximation to isotropic turbulence, although the initial conditions are nonrandom. One of the consequences of isotropy is that the cross correlations, say $\overline{u_1u_2}$, are zero, as in figure 4 at later times. These calculations differ from others where turbulence was obtained by using random initial conditions.

Because the initial conditions for the present calculations are nonrandom, the turbulence must arise as a result of the structure of the Navier-Stokes equations. In particular the nonlinear terms play a crucial role. It is easy to verify that if nonlinear terms are neglected for the present case, equations (48), (49), (37), and (40) give

$$u_i = (u_i)_0 \, e^{-3t^*} \tag{50}$$

So if the equations are linear, the flow given by the nonrandom initial condition (37) remains nonrandom. The nonlinear terms must be present in equations (48) and (49) if the development of turbulence is to take place.

---

[10] All averaged values would be expected to vary smoothly only for highly random fluctuations.

Our calculations at lower Reynolds numbers give results that are less like turbulence. Thus, the fluctuations develop apparent randomness only at the higher Reynolds numbers.

Calculated values of velocity-derivative skewness factor for a high Reynolds number (fig. 5) also appear to be of reasonable magnitude when compared with experimental values for isotropic turbulence. Values of that quantity of the order of 0.4 have been obtained experimentally and have long been considered an indication of true moderately strong or strong isotropic turbulence. The falloff near the end of the curve may be due to a more laminar flow there, where fluctuation levels are lower. A longer period of agreement with experimental values is obtained by Clark et al. (1979), apparently because they used turbulent initial conditions, so that the turbulence was already partially developed at $t = 0$.

D. Origin of the randomness (strange behavior)

A question remains as to how the nonlinear terms in equations (48) and (49) produce the randomness observed in figures 1 to 4. Until recently, it was generally assumed that randomness in a turbulent flow is due to randomness in the initial conditions, to random external fluctuations, or to the presence of so many eddies or harmonic components (or of so many degrees of freedom) that the identity of the individual eddies is lost (Monin, 1978; Rabinovich, 1978). In the present results the first of these is absent. Concerning the second, roundoff errors might be considered a form of external fluctuations. However, when the calculations were repeated using double precision, so that roundoff errors were reduced by a factor of about 10^6, the mean-square velocities were practically unchanged. The instantaneous velocities were different, although still as random as before. Thus, the effect of a large decrease in roundoff errors is similar to the effect of a small perturbation of the initial conditions (fig. 1). Since roundoff errors do not affect the turbulence level or the randomness, they cannot be considered a major sustaining cause of the turbulence or randomness observed here, although they may in some cases affect the initial transition. In the present case the transition is so rapid that the effect appears to be small.

This leaves only the proliferation of eddies or harmonic components as a source of apparent randomness. That might well produce the randomness observed in figure 1, since the nonlinear production of harmonics tends to be explosive, particularly at high Reynolds numbers (each harmonic component interacts with every other one) (Deissler, 1970a). However, the randomness may be produced, at least partially, by strange attractors or, more properly, by analogous strange behavior (Eckmann, 1981; Ott, 1981). (We talk about analogous strange behavior here, rather than strange attractors, since, strictly speaking, strange attractors exist only for steady-state turbulence (section VII-A). Here, analogous strange behavior refers mainly to apparent randomness in flows where a large number of degrees of freedom or harmonic components are not a necessary ingredient and randomness occurs by a loss of hydrodynamic stability.) Lorenz (1963) and others (Monin, 1978; Rabinovich, 1978; Ruelle, 1976; Lanford, 1982) have shown that a system of nonlinear ordinary differential equations similar to the spatially differenced form of the Navier-Stokes equations used here, or to the spectral form of those equations (Orszag, 1977b), can develop an apparently random behavior in time as a result of the loss of

stability of the solutions.[11] In conjunction with this, regions appear in the phase space of the system to which solutions are attracted. Randomness arises in those regions, which are known as strange attractors, from a haphazard movement of the phase point among the neighborhoods of various critical points in the phase space (steady-state points of unstable equilibrium where $\partial u_i/\partial t = 0$). (The presence of critical (or fixed) points is not always considered a necessary ingredient of strange attractors, but randomness or sensitivity to initial conditions is essential. However, the spatially differenced and spectral forms of the Navier-Stokes equations do appear to have critical points, as do the Lorenz equations.) Unlike randomization by proliferation of harmonic components, randomization by strange behavior can occur either with a few or with many degrees of freedom. In the present case both processes may be important. At any rate, as mentioned earlier, the results show that the structure of the Navier-Stokes equations is such that apparently random or turbulent solutions can arise from nonrandom initial conditions. With the results from the low-order models, in which apparent randomness appears with as few as three degrees of freedom (e.g., in the Lorenz equations), the turbulence observed to be manufactured by the Navier-Stokes equations should perhaps not come as a surprise.

The presence of strange behavior may be fortunate from a numerical standpoint in that it should enable turbulent solutions that are qualitatively correct (at least insofar as they appear random in time) to be obtained with a relatively coarse grid. The use of a fine three-dimensional grid, of course, requires the use of a large amount of computer time.

Figure 6 shows a dimensionless velocity component u_1 plotted against component u_2 (forming a plane in phase space) for one point in physical space. Although the behavior here is much more complicated than that observed for the low-order models that are usually used to observe strange attractors or strange behavior (here there are not well-defined orbits around fixed critical points, possibly because there may be an almost infinite number of critical points), there are similarities. Both the present turbulent results and those for the low-order models show trajectories consisting of loops and cusps, with frequent changes in the sign of the curvature of the trajectory (e.g., Franceschini, 1983). (Note that the present turbulent results ultimately decay, whereas the low-order models usually do not, since they contain forcing terms.) Although there are large changes in the direction of the trajectory, particularly in the regions of the cusps, the density of calculated points in those regions is very high, so that the numerical results should be reasonably accurate. Curves for u_i versus t (the numerical integrations are with respect to t) are, in fact, smooth. Note that u_1 and u_2 start out equal (on a 45° line) but that their equality is quickly destroyed when randomness sets in.

---

[11]Results from the differenced or spectral forms of the Navier-Stokes equations become arbitrarily close to those from the original equations as the number of grid points or Fourier components increases (assuming convergence of the numerical method). Theoretically, the Navier-Stokes equations correspond to an infinite number of ordinary differential equations or to an infinite number of degrees of freedom.

Randomization by strange behavior, or by a loss of hydrodynamic stability, almost certainly occurs in the present high-order turbulent results (high order here meaning many numerical grid points and thus many equations and degrees of freedom). This follows, first, from the fact that such randomness has been demonstrated to occur in low-order models (few equations and few degrees of freedom), such as that of Lorenz (1963) or Franceschini (1983), and second, from the fact that with the many more degrees of freedom present here than in the low-order models, many more critical points exist, and thus many more opportunities for randomization or loss of stability occur. Of course, because of the many degrees of freedom here, there will also be randomization by proliferation of harmonic components (so many harmonic components or eddies present that the identity of the individual eddies is lost and the flow appears random). The present large number of degrees of freedom encourages both types of randomness, and both very likely occur.

E. Evolution of mean quantities

In the results given so far, no correction for discretization error due to the finite numerical mesh size was applied. The primary purpose of the present work, of course, is to study the physics of turbulence rather than to obtain highly accurate results (possibly unattainable at very high Reynolds numbers). For low Reynolds numbers surprisingly good results for the decay can be obtained even with coarse grids (fig. 7). At higher Reynolds numbers the results, although less accurate, should still be qualitatively correct. Their accuracy can be improved by applying fourth-order extrapolations to zero numerical grid spacing (in consistency with the fourth-order numerical differencing used in the calculations (Deissler, 1981a)). This is done in lieu of subgrid modeling (making an assumption for the eddies smaller than the numerical grid spacing), e.g., Clark, et al., 1979. The method is related to subgrid modeling in that it assumes that the subgrid eddies are closely related to the calculated eddies but does not require the introduction of a subgrid eddy viscosity (which is, in effect, a kind of closure assumption). In all of the remaining results in this section the fourth-order discretization corrections are applied by extrapolating results for three mesh sizes to zero mesh size. However, the corrections are negligibly small except at the highest Reynolds number.

1. Mean-square velocity fluctuations

Figure 8 shows the calculated evolution of mean-square velocity fluctuations (spatially averaged) for a series of initial Reynolds numbers. As the Reynolds number increases (ν and initial length scale x_0 held constant), the rate of decay of $\overline{u^2}$ increases sharply, as in experimental turbulent flows (Deissler, 1979). This can be attributed to the nonlinear excitation of small-scale turbulence-like fluctuations at the higher Reynolds numbers. The high shear stresses between the small eddies cause a rapid decay.

2. Microscales and nonlinear transfer of turbulence to smaller eddies

The development of the small-scale eddies is seen more clearly in figure 9, where the microscale λ, normalized by its initial value, is plotted against dimensionless time. The microscale is defined by

$$\overline{\frac{\partial u_i}{\partial x_\ell}\frac{\partial u_i}{\partial x_\ell}} \propto -\frac{\overline{u_i u_i}}{\lambda^2} \tag{51}$$

For homogeneous turbulence and $U_i = 0$, λ can be calculated from equation (15) as

$$\lambda^2 \propto -\nu \frac{\overline{u_i u_i}}{d\overline{u_i u_i}/dt} \tag{52}$$

As the Reynolds number increases, the small-scale structure becomes finer. The microscale decreases until the fluctuation level (inertial effect) is low enough so that viscous forces prevent a further decrease. After λ decreases to a minimum, it begins to grow. (Results for coarser grids were not qualitatively different from these, but the minimums were somewhat higher.) The increase of λ at later times is due to the selective annihilation of eddies by viscosity, the small eddies being the first to decay. Thus, at large times only the big eddies remain. It is this period of increasing λ that is generally observed experimentally in grid-generated turbulence (turbulence observed downstream of a grid of wires or bars whose plane is normal to the flow in a wind tunnel). The increases of λ with time observed experimentally (Batchelor, 1953, fig. 7.2) are generally of the same order as those in figure 9 (doubling the time increases λ by a factor of about 1.5). The early period, in which λ decreases with time, is of interest as illustrative of inter-wave-number energy transfer. To generate the small-scale structure, turbulent energy must be transferred from big eddies to small ones.

For homogeneous turbulence the equation for the rate of change of turbulent kinetic energy (eq. (15)) reduces to

$$\frac{\partial}{\partial t}\left(\frac{\overline{u_i u_i}}{2}\right) = -\nu \overline{\frac{\partial u_i}{\partial x_\ell}\frac{\partial u_i}{\partial x_\ell}} \tag{53}$$

That is, only viscous dissipation contributes to the rate of change of kinetic energy, there being no indication that nonlinear transfer of energy between scales of motion is taking place. There may seem to be a paradox here in view of the large transfer of energy to smaller eddies indicated in figure 9. This is as it should be, however, since energy transfer between wave numbers or scales of motion should not contribute to the rate of change of total energy. To consider inter-wave-number energy transfer, two-point equations must be used. Thus, equation (30) shows that the self-interaction transfer term $T_{ij}(\vec{\kappa})$ in the two-point spectral equation (eq. (26)) has the property that

$$\int_{-\infty}^{\infty} T_{ij}(\vec{\kappa})\, d\vec{\kappa} = 0$$

as a spectral transfer term should. The quantity $\vec{\kappa}$ is the wave-number vector. The spectral transfer term $T_{ij}(\vec{\kappa})$, or its Fourier transform $-\partial(\overline{u_i u_j' u_k'} - \overline{u_i u_k u_j'})/\partial r_k$ in equation (19), is responsible for the generation of the small-scale structure in figure 9. Those terms come from the nonlinear term $-\partial(u_i u_k)/\partial x_k$ in the unaveraged equation (48). As mentioned earlier, the term $-\partial(u_i u_k)/\partial x_k$ produces randomization, as well as spectral energy transfer.

Although equation (30) shows that T_{ij} can transfer energy between wave numbers without contributing to the rate of change of total energy $\partial\overline{u_i u_j}/\partial t$, it says nothing about the direction of the transfer or how important it is. For that we need calculations such as those in figure 9, which show that significant energy is transferred to smaller eddies.[12] The energy transfer can be thought of as due to a breakup of big eddies into smaller ones or as a stretching of vortex filaments to smaller diameters. In spite of this transfer to smaller eddies, experimental results generally show a growth of scale (Batchelor, 1953, fig. 7.2). The reason is that those results are usually for the later period shown in figure 9, where, although energy is transferred to smaller eddies, the annihilation of small eddies by viscous action eventually wins out. The early period shown in figure 9, and in figure 2 of Taylor and Green (1937), is of particular interest in that the nonlinear transfer effects are truly dominant there; a sharp decrease in scale actually occurs as energy is transferred to smaller eddies.

3. Dissipation, vorticity generation, and pressure fluctuations

The energy dissipation term, the only term contributing to the rate of change of kinetic energy for homogeneous turbulence without mean gradients (eq. (53)) is plotted in figure 10. That is also the mean-square vorticity (eq. (36)), but the two are distinct physical entities. Although the curve for zero Reynolds number, where nonlinear effects are absent, decreases monotonically to zero, the curves for higher Reynolds numbers increase sharply for a while and then decrease. Thus, the nonlinear terms in the Navier-Stokes equations are very effective vorticity generators and greatly enhance the dissipation at short and moderate times. For long times they appear to have the opposite effect, evidently because the turbulence itself decays rapidly to zero. Nonlinear effects, although they do not appear explicitly in the evolution equation for $\overline{u_i u_i}$ (eq. (53)), thus alter greatly the evolution by altering the dissipation term.

---

[12] A direct numerical calculation of T_{ii} by Clark et al. (1979) for random initial conditions, and corresponding to the region of increasing λ in fig. 8, shows the same thing. Calculated values of T_{ii} are negative at small wave numbers (large eddies) and positive at large wave numbers (small eddies), so that energy is transferred from big eddies to smaller ones.

Figure 11 shows mean-square pressure fluctuations plotted against dimensionless time. The enhancement of the pressure fluctuations, although not as great as that of the vorticity or dissipation, again is due to nonlinear effects: in this case the nonlinear terms on the right side of the Poisson equation for the pressure cause the effect.

4. Further discussion and summary of the processes in isotropic turbulence

Nonlinear velocity and pressure terms do not appear in the evolution equation for $\overline{u_i u_i}$ (eq. (53)). But we can calculate root-mean-square values of the nonlinear terms in the instantaneous evolution equation (eq. (48)), as well as of the linear term. Three measures of the relative importance of inertial (nonlinear) and viscous effects are shown for a moderate Reynolds number in figure 12. The ratio of the nonlinear velocity term to the viscous term and the ratio of the pressure to the viscous term in equation (48), together with the microscale Reynolds number, are plotted against dimensionless time. The terms are space-averaged root-mean-square values. All of those measures show a variation from a rather inertial to a weak fluctuating flow. For instance, R_λ varies from about 90 to 0.7. This is a much greater variation than has been obtained experimentally for a single run. The curves for the term ratios lie somewhat below that for R_λ. They indicate that except at early times the nonlinear inertial effects associated with velocity and with pressure do not differ greatly.

The importance of both nonlinear velocity and pressure effects in figure 12 is somewhat paradoxical in view of equation (53), which says that neither contributes directly to $\partial \overline{u_i u_i}/\partial t$. The nonlinear velocity effects were already discussed in this section; it was pointed out that such effects should not appear in equation (53), since they only distribute energy in wave-number space and so do not directly alter the total energy. Although there is no nonlinear velocity term in equation (53), such a term appears in the two-point equation for $\partial \overline{u_i u_i'}/\partial t$. That equation, for the present case, is obtained from equation (19) as

$$\frac{\partial}{\partial t}\overline{u_i u_i'} = 2\nu \frac{\partial^2 \overline{u_i u_i'}}{\partial r_k \, \partial r_k} - \frac{\partial}{\partial r_k}\left(\overline{u_i u_i' u_k'} - \overline{u_i u_k u_i'}\right) = 3\,\frac{\partial}{\partial t}\overline{u_i u_{(i)}'} \qquad (54)$$

where $\vec{r}$ is again the vector extending from the unprimed to the primed point, and the pressure terms drop out because of continuity. The last term, where the parenthesis indicates no sum on i, is a consequence of the isotropy of the turbulence. The equation for the rate of change of each component of $\overline{u_i u_i'}$ is contributed to by the nonlinear velocity term $-(\partial/\partial r_k)(\overline{u_i u_i' u_k'} - \overline{u_i u_k u_i'})$, but there is no contribution from the pressure. The strong effect of pressure shown in figure 12 must be contained in higher order equations in the hierarchy of averaged equations (moment equations) (Deissler, 1958 and 1960). Thus, although two-point averaged equations contain a nonlinear effect of velocity, we must consider higher order multipoint equations to obtain an effect of pressure. Terms in the unaveraged equations shown in figure 12 (averaged over space after the solution has been obtained) include effects of all orders.

(Effects contained in the numerical results may, however, be limited by the fineness of the numerical grid.)

Although there is a strong effect of pressure in figure 12, the physical significance of that effect is somewhat elusive in contrast to the effects of viscous dissipation and spectral energy transfer. If the turbulence is anisotropic, a clear effect of pressure fluctuations is that they transfer net energy among directional components (eqs. (14) and (15) and the discussion following those equations). That is discussed in the following section. If, in addition, the turbulence is inhomogeneous, pressure can produce a net spatial diffusion of energy (eq. (15)). Those are evidently the only physical effects of pressure fluctuations (at least that we know about). Thus, if the turbulence is homogeneous and isotropic, as it is here, it seems reasonable to attribute the observed pressure effects in the unaveraged equations to those processes. Even though there is no net interdirectional transfer or spatial diffusion of turbulence when the turbulence is isotropic, those processes can still be instantaneously or locally operative. They could, for instance, cause a diffusion of tagged particles. According to figure 12, they have a significant indirect effect on the evolution of the turbulence.

From the findings of the present section we conclude that the following processes occur in isotropic turbulence: nonlinear randomization by proliferation of harmonic components or by strange behavior, nonlinear spectral transfer of turbulence among wave numbers or eddy sizes (mainly to smaller eddies), spatial diffusion and transfer of turbulence among directional components by pressure forces (with zero net diffusion and transfer into each component), generation of vorticity or swirl, and dissipation of turbulence into heat by viscous action.[13] From this description the life of isotropic turbulence appears interesting and includes many aspects.

V. UNIFORMLY SHEARED FLUCTUATIONS AND TURBULENCE

In the preceding section the evolution of nonrandom initial fluctuations into isotropic turbulence was examined numerically. The nonlinear transfer of energy to smaller scales of motion, the zero net (but not zero) spatial diffusion and transfer of energy among directional components, the generation of vorticity or swirl, and viscous dissipation were studied.

Another important process is the production of turbulence by a mean shear. Most turbulent flows, both those occurring in nature and those which are man-made, are in fact shear flows, where the turbulence is produced and maintained by the shear. Because of the added complexity the nonlinear problem of turbulent shear flow is even more difficult than that of isotropic turbulence. So it is not surprising that little progress has been made in obtaining an analytical solution from first principles. An attempt to obtain a numerical solution would seem to be in order.

Conceptually, the simplest turbulent shear flow, although certainly not the simplest to produce experimentally (Champagne, et al., 1970), is one in which the turbulence is uniformly sheared. At least two significant numerical studies of that type of turbulence have recently been made (Rogallo, 1981;

---

[13]According to eq. (36), the vorticity and the dissipation are numerically the same, but they are physically distinct.

Shaanan, et al., 1975). In both of those studies random initial conditions with a range of eddy sizes were used.

In the spirit of the preceding section the present numerical study of uniformly sheared turbulence starts with simple determinate initial conditions that possess a single length scale. As in the preceding section, we can in this way study how the turbulence develops from nonturbulent initial conditions. Again, much higher Reynolds number flows can be calculated with a given numerical grid when a single length scale is initially present, at least for short and moderate times.

Several interesting results that could not be obtained in the previous work on turbulent shear flow are obtained here. One of the significant findings is that the structure of the turbulence produced in the presence of a strong shear is much finer than that produced in its absence.

A. Initial and boundary conditions

In carrying out numerical solutions for uniformly sheared turbulence the instantaneous equations (1) and (3), subject to initial condition (38) and boundary conditions (44) and (47) are used. Since we are considering a uniform shear, we let

$$U_i = \delta_{i1} \frac{dU_1}{dx_2} x_2 \tag{55}$$

in the initial condition (38) and

$$(U_i)_{x_j^*=2\pi+b_j^*} - (U_i)_{x_j^*=b_j^*} = \delta_{i1}\delta_{j2} 2\pi \frac{dU_1}{dx_2} \tag{56}$$

in boundary condition (44). For the coefficients in equation (38) we use equation (40), where we choose the first set of signs. Equations (1) and (3) are written in terms of the total velocity $\tilde{u}_i$, but we can calculate the fluctuating component u_i from equation (4). It should be emphasized that we consider here not a sawtooth type of mean velocity profile, but a continuous profile in which the mean-velocity gradient is uniform at all points. Even with a uniform mean velocity gradient, some local inhomogeneity is introduced into the fluctuations by the periodic boundary conditions. We will not concern ourselves with that inhomogeneity, however, since we can still calculate products of velocities and pressures averaged over a three-dimensional period. Those values are independent of the position of the boundaries of the cycle. Note that for constant uniform mean-velocity gradient and mean pressure the last terms in equations (10) and (11) are zero even though the fluctuations may be inhomogeneous (eqs. (12) and (13)).

The u_2 component of the velocity fluctuation (in the direction of the mean-velocity gradient) is crucial in maintaining the turbulence against the dissipation (Deissler, 1970b and 1972). Therefore, when for brevity only one component of the velocity fluctuation is discussed, that component is chosen as u_2. More will be said about the maintenance of the turbulence later.

B. Development of random fluctuations

Figure 13 shows the evolution of $u_2/\left(\overline{u_0^2}\right)^{1/2}$ at a fixed point in space for a high Reynolds number, as calculated from the full nonlinear equations. As in the preceding section asterisks on quantities indicate that they have been nondimensionalized by using the initial length scale x_0 and the kinematic viscosity ν. Thus $t^* = (\nu/x_0^2)t$, $x_i^* = x_i/x_0$, and $(dU_1/dx_2)^* = (x_0^2/\nu)dU_1/dx_2$. Again the velocity fluctuations have the appearance of those for a random turbulence in spite of the nonrandom initial condition (eq. (37)). The dashed curves for $u_2/\left(\overline{u_0^2}\right)^{1/2}$ are again for initial conditions perturbed approximately 0.1 percent. The perturbed curves at first follow the unperturbed ones but eventually depart sharply. Although the the curves in figures 13(a) and (b) differ considerably in appearance, the perturbed curves in the two figures take about the same length of time to break away from the unperturbed ones. A very small perturbation of initial conditions causes a large change in the values of u_2 except at small times. On the other hand, the root-mean-square values of the velocities change smoothly with time and are unaffected by the perturbation of the initial conditions. These features are characteristic of turbulence. (Although the root-mean-square curve in fig. 13(a) appears almost horizontal, it eventually goes smoothly to zero when extended.)

C. Shear-related small-scale structure

A striking feature of the curves for $u_2/\left(\overline{u_0^2}\right)^{1/2}$ in figure 13 is the small scale structure exhibited for sheared turbulence (fig. 13(b)) when compared with the structure for no shear (fig. 13(a)). This shear-related small-scale structure is produced by the term $-U_k\,\partial u_i/\partial x_k$ in equation (10) which, for uniform shear, is $-(dU_1/dx_2)x_2\,\partial u_i/\partial x_1$. Equation (10) becomes, for a constant uniform mean-velocity gradient and a uniform mean pressure,

$$\frac{\partial u_i}{\partial t} = -\delta_{i1}\frac{dU_1}{dx_2}u_2 - \frac{dU_1}{dx_2}x_2\frac{\partial u_i}{\partial x_1} - \frac{\partial}{\partial x_k}(u_i u_k) - \frac{1}{\rho}\frac{\partial p}{\partial x_i} + \nu\frac{\partial^2 u_i}{\partial x_k\,\partial x_k} \qquad (57)$$

where equation (12) is used. Note that equation (57) is obtained without the assumption of homogeneity. From the term $-(dU_1/dx_2)x_2\,\partial u_i/\partial x_1$ in equation (57), we get the term

$$-\frac{\partial U_k}{\partial x_\ell}r_\ell\frac{\partial\overline{u_i u_j'}}{\partial r_k} = -\frac{dU_1}{dx_2}r_2\frac{\partial\overline{u_i u_j'}}{\partial r_1} \qquad (58)$$

in the two-point correlation equation (19). For periodic boundary conditions x_i dependency is not present in equations (19) and (58) because averages are taken over a three-dimensional period with r_i held constant. This is so even though the periodic boundary conditions may introduce some local inhomogeneities. If we take the Fourier transform of that term, we obtain the mean-gradient transfer term T_{ij}' in the spectral equation (26). Its effect in transferring energy to small-scale components is similar to that of the nonlinear transfer term T_{ij} in equation (26) (the Fourier transform of the

triple correlation term in eq. (19)). The production of small-scale structure by the shear might be thought of as due to stretching of the random vortex lines in the turbulence by the mean gradient or to stretching of mean vortex lines by the turbulence.

Although we first discussed a mean-gradient transfer term more than two decades ago (Deissler, 1961), the present results give the first graphic demonstration of the effectiveness of that term in producing a small-scale structure in turbulence. Since that is a linear effect (when the mean gradient is given), we can study it either by the full nonlinear solutions already considered in figure 13 (which contain linear as well as nonlinear effects) or by linearized solutions.

Equation (11) becomes, for uniform shear and uniform mean pressure,

$$\frac{\partial^2 p}{\partial x_\ell \, \partial x_\ell} = - \frac{\partial^2 (u_k u_\ell)}{\partial x_k \, \partial x_\ell} - 2 \frac{\partial u_2}{\partial x_1} \frac{\partial U_1}{\partial x_2} \tag{59}$$

where equation (13) is used. As in the case of equation (57), equation (59) is obtained without the assumption of homogeneity.

D. Some linearized solutions and comparison with nonlinear solutions

Equations (57) and (59) are linearized by neglecting the terms $-\partial(u_j u_k)/\partial x_k$ and $-\partial^2(u_k u_\ell)/\partial x_k \partial x_\ell$. The numerical solution, with initial and (periodic) boundary conditions given by equations (37), (40), (42), and (43), then proceeds as in the nonlinear case.

We can obtain an analytical solution for unbounded linearized fluctuations by using unbounded three-dimensional Fourier transforms (Deissler, 1961). The solution does not satisfy constant periodic boundary conditions. Instead of working with the averaged equations (Deissler, 1961), it is instructive to work with the unaveraged ones and use the initial condition given by equation (37). In this case the Fourier transforms must be generalized functions (a series of delta functions), but the method of solution is the same as that in the earlier work. Equation (57) for u_2 and equation (59), when linearized, are independent of u_1 and u_3. The solution obtained by using the initial condition (37) is

$$u_2 = \sum_{n=1}^{3} U_2^n \cos\left(\vec{q}^n \cdot \vec{x} - a q_1^n t x_2\right) \tag{60}$$

$$p = \sum_{n=1}^{3} P^n \sin\left(\vec{q}^n \cdot \vec{x} - a q_1^n t x_2\right) \tag{61}$$

where

$$U_2^n = \frac{a_2^n q^{n^2}}{q^{n^2} - 2aq_1^n q_2^n t + a^2 q_1^{n^2} t^2} \exp\left[-\nu t \left(q^{n^2} - aq_1^n q_2^n t + \frac{1}{3} a^2 q_1^{n^2} t^2\right)\right] \tag{62}$$

$$p^n = \frac{-2\rho a a_2^n q_1^n q^{n^2}}{\left(q^{n^2} - 2aq_1^n q_2^n t + a^2 q_1^{n^2} t^2\right)^2} \exp\left[-\nu t \left(q^{n^2} - aq_1^n q_2^n t + \frac{1}{3} a^2 q_1^{n^2} t^2\right)\right] \tag{63}$$

$a = dU_1/dx_2$, $q^{n^2} = q_1^{n^2} + q_2^{n^2} + q_3^{n^2}$, and the a_i^n and q_i^n are given in the initial conditions (eqs. (37) and (40)) (with the first set of signs). Mean values are obtained by integrating over all space. For instance,

$$\overline{pu_2} = \sum_{n=1}^{3} \frac{1}{2} p^n U_2^n \tag{64}$$

It is clear from the form of equations (60) and (61) that the solution does not satisfy constant periodic boundary conditions. By omitting the term $-(dU_1/dx_2)x_2 \partial u_i/\partial x_1$ as well as the nonlinear terms in equations (57) and (59), we can, however, obtain a simple analytical pseudo solution that satisfies those conditions:

$$u_2 = \sum_{n=1}^{3} a_2^n \exp\left[\nu t \left(2a \frac{q_1^n q_2^n}{q^{n^2}} - q^{n^2}\right)\right] \cos \vec{q}^n . \vec{x} \tag{65}$$

$$p = -\sum_{n=1}^{3} \frac{2\rho a q_1^n a_2^n}{q^{n^2}} \exp\left[\nu t \left(2a \frac{q_1^n q_2^n}{q^{n^2}} - q^{n^2}\right)\right] \sin \vec{q}^n . \vec{x} \tag{66}$$

This solution is useful for checking the numerical calculations and for studying the effect of the term $(dU_1/dx_2)x_2 \partial u_2/\partial x_1$ on the fluctuations.

Velocity fluctuations obtained from linearized solutions (numerical and analytical) were plotted (fig. 14). The presence of small-scale structure in the curves for $(dU_1/dx_2)^* = 4434$ and its absence in those for $(dU_1/dx_2)^* = 0$ are apparent. The curve for no shear (eq. (50)) decays monotonically to zero when extended. This is in contrast to the nonlinear case in figure 13(a) for no shear, where at least larger fluctuations are present. The linearized curves for $(dU_1/dx_2)^* = 4434$ in figure 14 follow closely the nonlinear ones in figure 13(b) for short times. Likewise the linearized curves in figure 14 for periodic boundary conditions follow closely those for unbounded conditions for short times. For longer times the fluctuations for unbounded conditions continue to decay, whereas those for constant periodic

boundary conditions grow. Small-scale structure in the curves for unbounded conditions is produced by the term $aq_1^n tx_2$ in the argument of the cosine in equation (60) ($a = dU1/dx2$). This term arises from the term $-ax_2\ \partial u_2/\partial x_1$ in equation (57), as is evident from its absence in equation (65), where the term $-ax_2\ \partial u_2/\partial x_1$ has been neglected.

For discussing the linearized case for constant periodic boundary conditions, it is convenient to convert equations (57) and (59) to a spectral form by taking their three-dimensional Fourier transforms. This gives, for u_2, on neglecting nonlinear terms

$$\frac{\partial \varphi_2^n}{\partial t} = aq_1^n \sum_{\kappa_2'} \frac{1}{\kappa_2'} \varphi_2^n(\kappa_1, \kappa_2 - \kappa_2', \kappa_3) - \nu\left(q_1^{n\,2} + \kappa_2^2 + q_3^{n\,2}\right)\varphi_2^n + \frac{2aq_1^n \kappa_2 \varphi_2^n}{q_1^{n\,2} + \kappa_2^2 + q_3^{n\,2}} \tag{67}$$

where

$$\varphi_2^n(\vec{\kappa}) = \frac{1}{8\pi^3} \int_{-\pi}^{\pi} dx_2 \iint_{-\infty}^{\infty} u_2^n(\vec{x}) e^{-i\vec{\kappa}\cdot\vec{x}}\, dx_1\, dx_3 \tag{68}$$

or

$$u_2^n(\vec{x}) = \sum_{\kappa_2=-\infty}^{\infty} \iint_{-\infty}^{\infty} \varphi_2^n(\vec{\kappa}) e^{i\vec{\kappa}\cdot\vec{x}}\, d\kappa_1\, d\kappa_3 \tag{68a}$$

$$u_2 = \sum_{n=-3}^{3} u_2^n, \quad \varphi_2 = \sum_{n=-3}^{3} \varphi_2^n \tag{69}$$

$\vec{\kappa}$ is the wave-number vector, and φ_2 is the Fourier transform of u_2. Note that a finite transform is used in the x_2 direction in order to satisfy periodic boundary conditions at $x_2/x_0 = -\pi, \pi$.

Strictly speaking, equation (67) is for a sawtooth mean-velocity profile, whereas the numerical results are for a uniform mean-velocity gradient. Equation (67) should still apply, however, at least for the present discussion purposes to points inside, but not outside, the numerical grid.

For constant periodic boundary conditions for u_1, small-scale structure in the fluctuations or the transfer of energy between wave numbers is

produced by the term containing the summation over κ_2' in equation (67). That term is the Fourier transform of $-ax_2\,\partial u_2/\partial x_1$ (eq. 57)). From its form we see that it can produce a complicated inter-wave-number interaction. The quantity φ_2^n at each κ interacts with φ_2^n at every other allowable κ_2. A difference between the solutions for unbounded conditions and those for constant periodic conditions is that only fluctuations at integral κ_2 are possible when periodic conditions are imposed, whereas for unbounded conditions fluctuations are possible at all values of κ_2.

Although the linear term $-ax_2\,\partial u_2/\partial x_1$ is effective in producing oscillations, even in the absence of nonlinear effects (fig. 14), the curves lack the random appearance of those in figure 13(b). Evidently, as in the case of no mean gradients (eq. (50)), the only way we can have a linear turbulent solution is to put the turbulence in the initial conditions (Deissler, 1961). Both $-ax_2\,\partial u_2/\partial x_1$ and the nonlinear terms in equation (57) are necessary to produce the small-scale turbulence in figure 13(b) from nonrandom initial conditions. The former acts like a chopper that chops the flow into small-scale components. Although the latter also do that, their most visible effect here is to produce randomization. As in the preceding section the randomization might occur as a result of the presence of strange attractors (or, more properly, analogous strange behavior) in the flow, by proliferation of eddies or harmonic components (with the loss of identity of the individual eddies) or by both (see section IV for a discussion of these possibilities).

According to the linearized analytical solution given by equation (60), the manufacture of small-scale fluctuations takes place only in the x_2 direction. Figure 15 shows how this has taken place at a moderate time. Figure 16 is a similar plot for the nonlinear case. The randomizing effect of the nonlinear terms is evident.

For the nonlinear case, $u_2/\left(\overline{u_0^2}\right)^{1/2}$ was also plotted against x_1 (fig. 17). The curves show some development of small-scale structure in the x_1 direction due to the interaction of the directional components in the nonlinear case. For the linearized flows small-scale structure developed only in the x_2 direction.

E. Evolution of mean quantities with shear

1. Cross-correlation coefficients

Cross-correlation coefficients $\overline{u_i u_j}/\left(\overline{u_i^2}\right)^{1/2}\left(\overline{u_j^2}\right)^{1/2}$ $(i \neq j)$ are plotted against dimensionless time for the nonlinear case in figure 17. Although $\overline{u_1^2} = \overline{u_2^2} = \overline{u_3^2}$ at $t^* = 0$, the initial cross correlations are not zero but are all positive and equal. However, because of the apparent randomization of the flow $\overline{u_2 u_3}$ and $\overline{u_1 u_3}$ approach zero as time increases. On the other hand, the values of the turbulent shear stress $\overline{u_1 u_2}$ change from positive to negative and remain negative because of the dynamics of the imposed mean shear. The presence of the mean-velocity gradient dU_1/dx_2 causes u_1 to be likely

negative when u_2 is positive, so that $\overline{u_1 u_2}$, the correlation between the two, is negative.[2] The waviness in the curves in figure 18, as well as that in some of the curves in later figures (e.g., fig. 21), is probably caused by nonrandom structure in the flow, possibly that produced by the linear term $-(dU_1/dx_2)x_2\ \partial u_1/\partial x_1$ in equation (57) (fig. 14).[10]

2. Growth and anisotropy of the velocity fluctuations

The evolution of the mean-square components of the velocity fluctuations is plotted in figure 19, where $\overline{u_{(i)}^2}^* = (x_0/v)^2\ \overline{u_{(i)}^2}$. After an initial adjustment period all of the components increase with time, in agreement with experiment (Harris, et al. (1977) and the numerical results in Rogallo (1981)). The numerical results in Shaanan, et al. (1975), on the other hand, show $\overline{u_2^2}$ and $\overline{u_3^2}$ decreasing at all times, a difference that remains unexplained. Our u_1^2 component is the largest of the three, $\overline{u_2^2}$ is the smallest, and $\overline{u_3^2}$ lies slightly above $\overline{u_2^2}$, in agreement with experiment Harris, et al. (1977) and previous numerical results.

3. Accuracy of mean and instantaneous quantities

The effect of discretization error on the numerical results for $\overline{u_2^2}$ is shown in figure 20. Curves are plotted for 16^3, 24^3, and 32^3 grid points, together with a fourth-order extrapolation to zero grid-point spacing (an infinite number of grid points) (Deissler, 1981a, 1981c). The differences between the results for 32^3 points and the fourth-order extrapolation are small but increase somewhat at long times. These results appear to indicate that the numerical results given here for averaged values are reasonably accurate. On the other hand the three-dimensional spatial resolution is probably not great enough (except at early times) to give accurate spatial variations of unaveraged quantities, other than that they have a random appearance. However, since the solutions are hydrodynamically unstable, and extremely sensitive to initial conditions, the actual values of the unaveraged quantities are probably not of great significance.

4. Maintenance of the turbulence

For the case considered in this section (uniform velocity gradient dU_1/dx_2) the one-point correlation equation (14) becomes

$$\frac{\partial}{\partial t}\overline{u_i u_j} = -\delta_{i1}\frac{dU_1}{dx_2}\overline{u_j u_2} - \delta_{j1}\frac{dU_1}{dx_2}\overline{u_i u_2} + \frac{1}{\rho}\left(\overline{p\frac{\partial u_j}{\partial x_i}} + \overline{p\frac{\partial u_i}{\partial x_j}}\right) - 2\nu\,\overline{\frac{\partial u_i}{\partial x_\ell}\frac{\partial u_j}{\partial x_\ell}} \qquad (70)$$

where derivatives of averaged values with respect to x_1 do not appear because averages are taken over a three-dimensional period. This is so even though local inhomogeneities may occur when periodic boundary conditions are used, as discussed earlier.[5]

Figure 21 shows the evolution of pressure-velocity-gradient correlations. (Parts of some of the curves are omitted to avoid confusion.) The pressure-velocity-gradient terms in the one-point correlation equation (eq. (70)), together with the production terms, are responsible for maintaining the turbulence against the dissipation (given by the last term in eq. (70)).

There are no production terms in the equations for $\partial\overline{u_2^2}/\partial t$ and $\partial\overline{u_3^2}/\partial t$ ($\delta_{i1}\ \overline{u_j u_2}\ \partial U_1/\partial x_2$ and $\delta_{j1}\ \overline{u_i u_2}\ \partial U_1/\partial x_2$ are zero). Thus $\overline{u_2^2}$ and $\overline{u_3^2}$ generally receive energy only from the $\overline{u_1^2}$ component, whose equation has a nonzero production term. Equation (70) shows that to do that, $\overline{p\ \partial u_j/\partial x_i}$ + $\overline{p\ \partial u_i/\partial x_j}$ must be positive for $i = j = 2, 3$ and negative for $i = j = 1$. Figure 21 shows that is actually the case for constant periodic boundary conditions except for an initial adjustment period, so that the turbulence is maintained (fig. 19). The maintenance of the $\overline{u_2^2}$ or u_2 component is particularly critical because if u_2 goes to zero, the Reynolds shear stress $\overline{u_1 u_2}$ in the production term of the u_1^2 equation (eq. (70)) will go to zero and there will be nothing to keep the turbulence going. All of the components will then eventually decay. That is what happens in the linearized analysis for unbounded turbulence in figure 21 (see also Deissler, 1961).

The nonlinear results for $\overline{u_2^2}$ are compared with various linearized solutions in figure 22. The same initial conditions are used for all of the cases (eqs. (37) or (38), (40), and (55)). For all of the results, except those for the unbounded linearized case (obtained by using unbounded Fourier transforms (eq. (60)), the crucial $\overline{u_2^2}$ component eventually increases so that the turbulence or fluctuations are maintained. In the unbounded linearized case $\overline{u_2^2}$ decreases at all times. That was expected, since the $\overline{u_2^2}$ results for that case in Deissler (1961, 1970b) (for different initial conditions) decreased at all times. Somewhat unexpected are the linearized results for constant periodic boundary conditions, which show that the fluctuations are maintained for those cases. Whereas figure 21 shows that in the unbounded case the pressure-velocity-gradient correlations remove energy from the $\overline{u_2^2}$ component and cause the fluctuations to decay as in Deissler (1961, 1970b) the imposition of constant periodic boundary conditions changes the sign of those correlations and brings energy into $\overline{u_2^2}$, so that the fluctuations are maintained. Equation (65), which satisfies periodic boundary conditions, shows that, at least when the term $-(dU_1/dx_2)x_2\ \partial u_i/\partial x_1$ in equation (57) is neglected, $\overline{u_2^2}$ increases at large times if $2aq_1^n q_2^n > q^{n^4}$ for at least one n.

5. Spectral transfer terms as stabilizing

Comparing the linearized case for periodic boundary conditions in figure 22 with the corresponding nonlinear case shows that the nonlinear terms have a stabilizing influence. That is, the values of $\overline{u_2^2}$ increase more slowly for the nonlinear case. Moreover comparing the curve for the linearized case with periodic boundary conditions and with the term $-(dU_1/dx_2)x_2\ \partial u_2/\partial x_1$ in equation (57) missing (eq. (65)) with the corresponding curve for that term included shows that the presence of that term also has a stabilizing influence. Since neglect of that term is equivalent to neglecting the mean-gradient transfer term T'_{22} in the spectral equation for $\overline{u_2^2}$ (eq. (26)), we can consider the latter term as stabilizing. Thus both the nonlinear spectral transfer term associated with triple correlations T_{22} and the linear mean-gradient transfer term T'_{22} in the spectral equation (26) for $\overline{u_2^2}$ are stabilizing. The reason is that both terms transfer energy to small eddies, where it is dissipated more easily.

It is of interest that the one-point correlation equation for $\partial\overline{u_iu_j}/\partial t$ (eq. (70)) contains neither a term associated with velocity-gradient transfer nor one associated with nonlinear transfer. That is, both of those processes give zero direct contribution to the rate of change of $\overline{u_iu_j}$: they only change the distribution of energy among the various spectral components or eddy sizes. This spectral transfer, of course, still affects the way in which $\overline{u_iu_j}$ evolves (fig. 22). Even though equation (70) contains no transfer terms, the transfer of energy among the various spectral components of the velocity alters the terms that do appear in equation (70), so that $\partial\overline{u_iu_j}/\partial t$ is affected indirectly. That is not a small effect!

The modified linear pseudosolution given by equations (65) and (66) (dash-dot-dot curve in fig. 21) is the simplest solution in which the fluctuations can be maintained against the dissipation. In obtaining it the only mean-gradient term retained in the equations for u_2 (eqs. (57) and (59), $i = 2$) is $-2(dU_1/dx_2)\partial u_2/\partial x_1$, a source term in the Poisson equation for the pressure. If that term is also neglected, u_2 decays and, as discussed earlier, all of the components of the fluctuations decay. Moreover, as shown in figure 22 and already discussed, the term $-(dU_1/dx_2)x_2\ \partial u_i/\partial x_1$ in equation (57) is stabilizing, so it is of no help in maintaining the fluctuations. Thus, at least in the linearized case, the presence of the source term $-2(dU_1/dx_2)\partial u_2/\partial x_1$ in the Poisson equation for the pressure is necessary for maintaining the fluctuations. That term should play a similar important role in the maintenance of nonlinear turbulence, although in that case it is hard to separate the linear effects from the nonlinear ones. In particular, the role of the nonlinear source term in the Poisson equation for the pressure remains unclear, although it may have an effect similar to that of the linear source term.

F. Return to isotropy

Figures 23 and 24 show the approach to isotropy of nonlinear uniformly sheared turbulence when the shear is suddenly removed. Although the shear produces considerable anisotropy, the components $\overline{u_i^2}$ of the mean-square fluctuation approach equality upon removal of the shear and remain accurately equal. The pressure-velocity-gradient correlations in equation (70) are thus successful in transferring energy among the various directional components in such a way that equality of the $\overline{u_i^2}$ is produced. We note that $\overline{u_2^2}$ continues to increase for a short time after the shear is removed, probably because it receives energy from both $\overline{u_1^2}$ and $\overline{u_3^2}$.

In addition to equality of the $\overline{u_i^2}$, zero cross correlations $\overline{u_i u_j}$ $(i \neq j)$ are required for isotropy. Figure 24 shows that $\overline{u_1 u_2}$, which is nonzero when the turbulence is sheared, approaches zero when the shear is removed, and along with the other cross correlations, remains close to zero. The destruction of $\overline{u_1 u_2}$, apparently by nonlinear randomization effects, occurs over a finite time rather than instantaneously on removal of the shear.

Another expected effect of removal of the mean shear is that the small-scale structure produced by the chopping term $-(dU_1/dx_2)x_2\, \partial u_1/\partial x_1$ in equation (57) should die out. According to figure 25, that occurs almost immediately when dU_1/dx_2 goes to zero, evidently because of the large fluctuating shear stresses between the small-scale eddies. Figure 25 shows, in a particularly graphic manner, the effectiveness of the mean-gradient chopping term in equation (57) in producing small-scale turbulent structure.

VI. INHOMOGENEOUS FLUCTUATIONS AND TURBULENCE (DEVELOPING SHEAR LAYER)

Here, the work is extended to an inherently inhomogeneous developing shear layer so that net diffusion, as well as other turbulence processes, can be considered. This case is general enough to include all of the dynamical processes that ordinarily occur in incompressible turbulence.

For the initial conditions we use a three-dimensional cosine velocity fluctuation, as before, and a mean-velocity profile with a step. Thus, in equation (38) we set

$$U_i = \pi\delta_{i1} V[\mathrm{sgn}(x_2^* - \pi) + 1] \tag{71}$$

where V is a constant with the dimensions of a velocity. Equation (71) is plotted against x_2/x_0 in the curve for $t = 0$ in figure 26, where $V^* = Vx_0/\nu$, and x_0 is again the initial length scale of the disturbance. For the coefficients given by equation (40) we choose the second set of signs. With this choice of signs $\overline{u_1 u_2}$ does not have to change sign as a result of the dynamics of the flow, as it did in the last section, and the initial

adjustment period is eliminated or greatly shortened. If the longer adjustment period remained, much of the development of the shear layer would be distorted.

In carrying out the numerical solution of equations (1) and (3) we use boundary conditions (44) and (47), where we let

$$(U_i)_{x_j^*=2\pi+b_j^*} - (U_i)_{x_j^*=b_j^*} = 2\pi\delta_{i1}\delta_{j2}V \tag{72}$$

Equations (1) and (3) are written in terms of the total velocity $\tilde{u}_i$, but we can calculate the fluctuating part from equation (4), which, for the present case, is $u_i = \tilde{u}_i - \delta_{i1}U_1$, where U_i is obtained by averaging $\tilde{u}_i$ over x_1 and x_3 for fixed values of x_2. The fluctuations are inhomogeneous in the x_2 direction, except at $t = 0$.

The calculated evolution of the dimensionless mean velocity $U_1^* = (x_0/\nu)U_1$ (U_2 and U_3 are zero) is plotted against $x_2/x_0 = x_2^*$ for a particular value of $V^* = Vx_0/\nu$ in figure 26. The results in this section may not be as accurate as those in the previous sections because of the presence of the discontinuity in the initial velocity profile, but they should be qualitatively correct. The shear layer grows (from essentially zero initial thickness) because of the presence of the turbulent and viscous shear stresses. The ratio of turbulent to viscous shear stress (averaged over x_1 and x_3 at the central plane $x_2^* = \pi$) is plotted against dimensionless time in figure 27. Except at early times the growth of the shear layer is almost completely dominated by the turbulent shear stress.

Figure 28 shows the evolution of the instantaneous velocity component u_2 and of the root-mean-square value of u_2 (averaged over the central plane $x_2^* = \pi$). Although the initial conditions are nonrandom, the evolution of u_2 has a random appearance, as in the preceding sections. On the other hand, $\left(\overline{u_2^2}\right)^{1/2}$ evolves smoothly. These characteristics are again representative of a turbulent flow. The quantity $\left(\overline{u_2^2}\right)^{1/2}$ increases monotonically at small times in contrast to the corresponding curve in section V, where an initial adjustment period was present. As mentioned earlier, the initial adjustment period has been eliminated here by using the second set of signs in equation (40), so that $\overline{u_1 u_2}$ does not have to change sign as a result of the dynamics of the turbulence. The decrease in $\left(\overline{u_2^2}\right)^{1/2}$ near the end of the curve is caused by a decrease in mean-velocity gradient, and thus of turbulence production, at large times (fig. 26).

As in the case in the preceding section, small-scale fluctuations are generated in the inhomogeneous turbulence in figure 28 by the interaction of the mean velocity with the turbulence. This can be seen by comparing figure 28 with figures 1 and 13(a), where mean-velocity gradients are absent. One might expect this since it has been shown (Deissler, 1981b) that, even for a general inhomogeneous turbulence, a term in the two-point spectral equation for the turbulence can transfer energy between scales of motion as a result of the presence of mean gradients.

A. Inhomogeneous growth of turbulent energy

A dimensionless plot of turbulent kinetic energy as a function of x_2^* and time is given in figure 29, where $\overline{u_k u_k}^* = (x_0/\nu)^2 \, \overline{u_k u_k}$. As for all of the averaged values in this section, $\overline{u_k u_k}/2$ is averaged over x_1 and x_3 for fixed values of x_2. As time increases, an intense concentration of turbulent energy develops near the plane $x_2/x_0 = \pi$, where the mean-velocity gradient is initially infinite. The turbulence is highly inhomogeneous. Inhomogeneity, in fact, seems to be the dominant characteristic of the turbulence generated in the shear layer. The indicated increase in turbulence with time is similar to that obtained experimentally (Brinich, et al., 1975).

B. Turbulence processes in shear layer

Terms in the one-point correlation equation for the rate of change of the turbulent kinetic energy (eq. (15)), which, for the present case, becomes

$$\frac{\partial}{\partial t}\left(\frac{\overline{u_k u_k}}{2}\right) = -\overline{u_1 u_2}\,\frac{dU_1}{dx_2} - \frac{1}{\rho}\,\frac{\partial}{\partial x_2}\,\overline{p u_2} - \frac{\partial}{\partial x_2}\left(\frac{\overline{u_k u_k}}{2}\,u_2\right) + \nu\,\frac{\partial^2}{\partial x_2^2}\left(\frac{\overline{u_k u_k}}{2}\right) - \nu\,\overline{\frac{\partial u_k}{\partial x_\ell}\,\frac{\partial u_k}{\partial x_\ell}} \qquad (73)$$

are plotted for $t^* = 0.000293$ in figure 30. As usual, an asterisk on a quantity indicates that it has been nondimensionalized by using x_0 and ν. For instance $(\overline{u_1 u_2}\; dU_1/dx_2)^* = (x_0^4/\nu^3)\,\overline{u_1 u_2}\; dU_1/dx_2$. The terms that contribute most to the rate of change of $\overline{u_k u_k}/2$ are the production term $-\overline{u_1 u_2}\; dU_1/dx_2$, the pressure diffusion term $(-\overline{\partial p u_2}/\partial x_2)/\rho$ and the kinetic energy diffusion term $-(1/2)\partial\overline{u_k u_k u_2}/\partial x_2$. The viscous diffusion term $\nu\partial^2(\overline{u_k u_k}/2)/\partial x_2^2$ and the dissipation term $-\nu\overline{\partial u_k/\partial x_\ell \; \partial u_k/\partial x_\ell}$ are small in figure 30. At early times, however, when the mean-velocity gradient is large, the dissipation term is appreciable.

The production term, whose form shows that turbulent energy is produced by work done on the Reynolds shear stress by the mean-velocity gradient, is largest near the plane $x_2^* = \pi$, where the velocity gradient is initially infinite. The plots of the pressure and kinetic energy diffusion terms show that those terms are negative near $x_2 = \pi$ and positive away from that plane. Thus, they remove turbulent energy from the maximum-energy region and deposit it where the energy is lower. Both diffusion terms therefore tend to make the turbulence more homogeneous.

A comparison of the turbulence diffusion processes with the spectral transfer processes and the directional transfer processes arising from the

pressure-velocity correlations (sections IV and V) is instructive. The spectral transfer processes remove energy from wave-number (or eddy size) regions, where the energy is high, and deposit it in regions of lower energy. The directional transfer processes remove energy from high-energy directional components and deposit it in a directional component (or components) where the energy is lower. The turbulence diffusion processes, as shown here, remove energy from regions of space where the energy is high and deposit it in regions of lower energy. The spectral transfer, directional transfer, and turbulence diffusion processes tend, respectively, to make the turbulence more uniform in wave-number space and more isotropic and homogeneous in physical space.

Although one might suppose that turbulence diffusion terms would always tend to make the turbulence more homogeneous, that supposition is not supported by all of the experimental data. For instance, measurements of wall-bounded turbulence (Laufer, 1954) indicate that the pressure diffusion and the kinetic energy diffusion terms transfer energy in opposite directions, although the total diffusion is from regions of high to regions of lower energy. On the other hand, measurements of turbulence in a free jet (Wygnanski and Fiedler, 1969) and in a wake (Townsend, 1949), which are closer to the case considered here, seem to support the present findings.

VII. A STEADY-STATE HOMOGENEOUS TURBULENCE WITH A SPATIALLY PERIODIC BODY FORCE

In all of the cases considered so far the turbulence either ultimately died out or increased in intensity with time. However, there are many important cases in which the turbulence, after some time, reaches a statistically steady state (e.g., flow in a pipe far from the entrance). Moreover, a discussion of strange attractors (e.g., Eckmann, 1981, and Ott, 1981) should, strictly speaking, be based on a steady-state turbulence; a strange attractor is, roughly, the region of phase space inhabited by the phase point of a system after the initial transients have died out, where the phase point moves in an apparently chaotic fashion. For the decaying turbulence of section IV the attractor would then be only a point in phase space. Of course, we could still talk about analogous strange behavior, even in an unsteady-state case, as we did in section IV-D.

One way of obtaining a statistically steady-state turbulence is by adding a spatially periodic body-force term (forcing term) F_i to the right side of equation (41). A convenient term for that purpose is

$$F_i = - c \left(- \frac{\partial(\tilde{u}_i \tilde{u}_k)}{\partial x_k} - \frac{1}{\rho} \frac{\partial \tilde{p}}{\partial x_i} + \nu \frac{\partial^2 \tilde{u}_i}{\partial x_k \partial x_k} \right)_0 \tag{74}$$

where the subscript 0 signifies initial values, the $\tilde{u}_i$ are given by equations (38) and (40) with $U_i = 0$ and $\tilde{p}$ by equation (3), and c is a constant. The first set of signs is used in equation (40). Equation (74), which is time independent, is used for F_i at all times. For $c = 1$, the the quantities $\tilde{u}_i$ and $\tilde{p}$, as calculated from equation (1) (with F_i added to the right side) and equation (3), do not change from their initial equation (3), do not change from their initial values. To introduce some initial time

dependence, we set $c = 1.05$. The boundary conditions are taken to be periodic, as in section IV.

Calculated results for this case are plotted in figures 31 and 32, where t^* is again equal to $(\nu/x_0^2)t$ and x_0 is the initial length scale. Figure 31 shows the time evolution of $\tilde{u}_1$ and $\left(\overline{\tilde{u}_1^2}\right)^{1/2}$ at a point away from the center of the numerical grid, where as before, overbars indicate space averages. The values are normalized by dividing them by $\left(\overline{u_0^2}\right)^{1/2}$, the initial value of $\left(\overline{\tilde{u}_1^2}\right)^{1/2} = \left(\overline{\tilde{u}_2^2}\right)^{1/2} = \left(\overline{\tilde{u}_3^2}\right)^{1/2}$. Since we are interested in steady-state solutions at long times it is necessary, to obtain reasonably accurate results, to use a lower Reynolds number than in the preceding cases, where shorter-time transient flows were considered.

Figure 30 shows that, for $0 < t^* < 0.17$, the flow is essentially laminar with small fluctuations of u_1. Then for $0.17 < t^* < 0.18$ there is a rather sharp transition from laminar to turbulent flow, as $\left(\overline{\tilde{u}_1^2}\right)^{1/2}$ increases. For $t^* > 0.18$ the turbulence is statistically steady state, as indicated by the nearly constant value of $\left(\overline{\tilde{u}_1^2}\right)^{1/2}$. Curves for $\tilde{u}_2$ and $\tilde{u}_3$ are similar to those for $\tilde{u}_1$, including the same location of the transition region and nearly the same values for $\left(\overline{\tilde{u}_2^2}\right)^{1/2}$ and $\left(\overline{\tilde{u}_3^2}\right)^{1/2}$ as for $\left(\overline{\tilde{u}_1^2}\right)^{1/2}$.

After the transition region ($t^* > 0.18$) the flow appears to lie on a strange attractor, since it has the following characteristics:[14] first, a volume in the phase space of our system decreases with time, since the Navier-Stokes equations describe a dissipative system and phase-volume shrinkage can be shown to occur for the Navier-Stokes equations.[14] This implies that an attractor exists for our system. Second, the chaotic appearance of the velocity components (figs. 31 and 32) indicates that the attractor is strange. Finally, the fact that transients have died out for $t^* > 0.18$, leaving a statistically steady state (fig. 31), indicates that beyond the transition region the phase point is on the strange attractor.

Figure 32 shows the projection on the $\tilde{u}_2$-$\tilde{u}_3$ plane (at the center of the numerical grid) of the trajectory of the phase point as it moves on the strange attractor. As in figure 6 the trajectory consists of loops and cusps with frequent changes in the sign of the curvature, but unlike figure 6 the trajectory does not, of course, tend toward a point. The cusps might be considered as loops with very small or zero radii. Also, as in figure 6, randomization is very likely associated with the large number of harmonics (eddy sizes) present, as well as with the strange attractor or strange behavior.

---

[14]These characteristics, as well as the possibility of obtaining a steady-state turbulence with periodic boundary conditions by slightly modifying the existing program, were pointed out to the author by R.J. Deissler.

VIII. CONCLUSIONS

From the present review it is concluded that the nonlinear and linear processes in turbulence can be profitably studied numerically. The results show that, at least at higher Reynolds numbers, an apparently random turbulence can develop from nonrandom initial conditions. The numerically calculated turbulence is not numerical hash, since a large number of time steps correspond to each fluctuation. For both sheared and unsheared fluctuations the structure of the Navier-Stokes equations is such that turbulence can develop even when the/initial flow is nonturbulent. This is indicated by the appearance of the instantaneous velocity fluctuations and by the sensitivity of those fluctuations (and the insensitivity of average values) to small perturbations in the instantaneous initial conditions. The randomness appears to increase as the numerical mesh size decreases. Moreover, the two-time velocity correlation becomes small as the time between the occurrence of the two velocities increases. In addition, for no mean shear the correlation between any two components of the velocity becomes small as the time increases, as a result of the randomization. This correlation is not small initially, even though the three components of the mean-square velocity fluctuation are equal at early as well as at late times for the initial conditions chosen. Also, calculated velocity-derivative skewness factors for no mean shear appear to be of reasonable magnitude when compared with those for isotropic turbulence. Thus, except in the initial period the results for no mean shear evidently give a reasonably good approximation to isotropic turbulence.

The source of the observed randomness may lie in the presence of strange attractors or, more properly, of analogous strange behavior (Monin, 1978) in the phase space of the system, as well as in the occurrence of a large number of eddies or harmonic components (large number of degrees of freedom). It appears that no conclusions can be drawn as to the relative importance of the two processes, but both probably occur. (A strange attractor is a region in the phase space of the system to which solutions are attracted and in which the phase point moves in an apparently chaotic fashion. It can occur even with a small number of degrees of freedom.) Roundoff errors appear not to be a sustaining cause of the randomness; a large decrease in roundoff errors did not appreciably affect the turbulence level or the randomness of the fluctuations, although the instantaneous values were different. Thus, the affect of a large decrease in roundoff errors is similar to that of a small perturbation of the initial conditions. Roundoff errors may in some cases affect the transition to turbulence. The present turbulent solutions bear some similarity to those for low-order models in that both have trajectories in phase space that consist of loops and cusps, with frequent changes in the sign of the curvature of the trajectory (fig. 6). Moreover, with the results from the low-order models in which apparent randomness appears with as few as three degrees of freedom (e.g., in the Lorenz equations), the turbulence observed to be manufactured by the Navier-Stokes equations should perhaps not come as a surprise.

At early times the calculated nonlinear transfer of energy from big eddies to small ones is almost completely dominant and causes a sharp decrease in the size of the microscale. This has not been generally observed experimentally or analytically because the period usually studied is for later times, where the annihilation of small eddies by viscous action causes the scale to grow, even though energy is being transferred to smaller eddies. This later period of scale growth is also observed in the present results.

The nonlinear terms in the equations of motion, besides transferring energy among eddy sizes and producing randomization, are very effective vorticity generators and increase the dissipation and the rate of decay. The increased rate of decay is a result of the nonlinear transfer of energy to smaller eddies; the small eddies decay faster than the big ones because of the higher shear stresses between the small eddies. Calculation of (averaged) terms from unaveraged equations of motion shows, as might be expected, that the flow is dominated by nonlinear inertial effects at early times and by viscous effects at later times (fig. 12). The nonlinear effects are associated with both velocity and pressure terms in the unaveraged equations of motion, even for isotropic turbulence. Since the one- and two-point averaged or correlation equations for isotropic turbulence do not contain pressure terms, the effects of pressure observed for the unaveraged equations must be contained in higher order averaged equations. The infinite hierarchy of averaged equations should contain all effects, as do the unaveraged equations. The only physical processes associated with pressure (that we know about) are interdirectional transfer and spatial diffusion of turbulence (eq. (14)). It thus seems reasonable to attribute the observed pressure effects in the unaveraged equations to those processes. Even though there is no net interdirectional transfer or spatial diffusion in isotropic turbulence, those processes can still be locally operative.

The processes occurring in isotropic turbulence thus include the following: nonlinear randomization, nonlinear spectral transfer (mainly to smaller scales of motion), zero net (but not zero) spatial diffusion and transfer of turbulence among directional components, generation of vorticity or swirl, and viscous dissipation.

If a uniform shear is present in the flow, we have, in addition to these processes, production of turbulence by the mean-velocity gradient, net transfer of turbulence among directional components by pressure forces, and linear spectral transfer among scales of motion by the mean gradient. The last of these processes results in the production of small-scale fluctuations in the flow. This can be attributed to a mean-gradient transfer term in the spectral equation for the velocity fluctuations (eq. (26)). Although we first discussed that term over two decades ago, the recent numerical results considered herein give the first graphic demonstration of the effectiveness of that term in generating a small-scale structure in the turbulence. However, the small-scale fluctuations produced by that term alone (linear solution) are essentially nonrandom. Evidently, the only way we can have a turbulent linear solution, either with or without mean gradients, is to put the turbulence in the initial conditions. To produce the small-scale turbulence from nonrandom initial conditions observed herein for shear flow, the presence of both the linear mean-gradient transfer term and the nonlinear terms in the equations is necessary. The former term, or its equivalent in the unaveraged equation (57), acts like a chopper that chops the flow into small-scale components. The latter terms, while they also produce small-scale components, act most visibly here as randomizers.

In all of the uniform-shear cases calculated with constant periodic boundary conditions, including both linear and nonlinear flows, the pressure-velocity-gradient correlations are successful in distributing energy among the directional components, so that the turbulence or the fluctuations are maintained. This is in spite of the presence of a production term in the equation for only one of the components. Both the linear mean-gradient transfer term

and the nonlinear terms mentioned in the preceding paragraph have a stabilizing effect. That is, they cause the fluctuations to increase at a slower rate. The reason is that both terms transfer energy to small eddies, where it is dissipated more easily. It is shown that, at least for the linearized solution with constant periodic boundary conditions, a mean-gradient source term in the Poisson equation for the pressure is necessary for maintaining the fluctuations against the dissipation. That term should play a similar important role in the maintenance of nonlinear turbulence, although in that case it is hard to separate the linear effects from the nonlinear ones. For the linearized unbounded solution (obtained by using unbounded Fourier transforms) the fluctuations decay, as expected from earlier results.

When the mean-velocity gradient is suddenly removed, the turbulent shear stress goes to zero in a finite time, and the velocity-pressure-gradient correlations cause the turbulence to attain the isotropic state. The intensities of the directional components become and remain equal. In addition, the small-scale structure produced by the mean-gradient transfer term quickly vanishes (fig. 25). Figure 25 shows, in a particularly graphic manner, the effectiveness of the mean-gradient chopping term in equation (57) in producing small-scale turbulent structure.

For a developing shear layer the turbulence is inhomogeneous and, in addition to the processes considered so far, a net spatial diffusion of turbulence occurs. The thickness of the shear layer, which is initially zero, increases with time because of the presence of turbulent and viscous shear stresses. Except at very early times the growth of the shear layer is almost completely dominated by the turbulent shear stress. As time increases, an intense concentration of turbulent energy develops near the plane where the mean-velocity gradient is initially infinite. The turbulence is highly inhomogeneous. The calculated turbulence production is always positive, and is largest near the plane where the velocity gradient is initially infinite. The pressure and the kinetic energy diffusion are negative near that plane and positive away from it. Thus, they remove turbulent energy from the high-energy region and deposit it where the energy is lower. Both diffusion processes therefore tend to make the turbulence more homogeneous.

A comparison of the various transfer and diffusion processes occurring in turbulence is of interest. The spectral transfer processes remove energy from wave-number (or eddy size) regions where the energy is high and deposit it in regions of lower energy. The directional transfer processes remove energy from high-energy directional components and deposit it in a directional component (or components) where the energy is lower. The turbulence diffusion processes remove energy from regions of space where the energy is high and deposit it in regions of lower energy. The spectral transfer, directional transfer, and turbulence diffusion processes tend, respectively, to make the turbulence more uniform in wave-number space and more isotropic and homogeneous in physical space.

By adding a spatially periodic body-force term to the Navier-Stokes equations, a solution is obtained in which the flow first passes through laminar and transition-to-turbulence stages. The turbulence then quickly settles down to a statistically steady state. In this last stage the flow appears to have characteristics corresponding to those of a strange attractor.

REFERENCES

Batchelor, G.K., 1953, Homogeneous Turbulence (Cambridge, New York), pp. 100, 137, 88, 86.

Batchelor, G.K., 1967, An Introduction to Fluid Dynamics (Cambridge, New York), p. 131.

Betchov, R., and A.A. Szewczyk, 1978, Phys. Fluids 21, 871.

Brinich, P.F.; D.R. Boldman, and M.E. Goldstein, 1975, NASA TN D-8034.

Cain, A.B., W.C. Reynolds, and J.H. Ferziger, 1981, Rept. No. SU-TF-14, Stanford Univ.

Ceschino, F., and J. Kuntzmann, 1966, Numerical Solution of Initial Value Problems (Prentice-Hall, Englewood Cliffs, New Jersey), p. 141, example 2, and p. 143.

Champagne, F.H., V.G. Harris, and S. Corrsin, 1970, J. Fluid Mech. 41, 81.

Clark, R.A., J.H. Ferziger, and W.C. Reynolds, 1979, J. Fluid Mech. 91, 1.

Corrsin, S., and W. Kollman, 1977, in Turbulence in Internal Flows, edited by S.N.B. Murthy (Hemisphere, Washington), p. 11.

Deardorff, J.W., 1970, Geophys. Fluid Dyn. 1, 377.

Deissler, R.G., 1958, Phys. Fluids 1, 111.

Deissler, R.G., 1960, Phys. Fluids 3, 176.

Deissler, R.G., 1961, Phys. Fluids 4, 1187.

Deissler, R.G., 1970a, Appl. Sci. Res. 21, 393.

Deissler, R.G., 1970b, Phys. Fluids 13, 1868.

Deissler, R.G., 1972, Phys. Fluids 15, 1918.

Deissler, R.G., 1976, Am. J. Phys. 44, 1128.

Deissler, R.G., 1977, in Handbook of Turbulence, vol. 1, edited by W. Frost and T.H. Moulden (Plenum, New York), p. 165.

Deissler, R.G., 1979, Phys. Fluids 22, 1852.

Deissler, R.G., 1981a, Phys. Fluids 24, 1595.

Deissler, R.G., 1981b, Phys. Fluids 24, 1911.

Deissler, R.G., 1981c, NASA TM-82925.

Deissler, R.G., 1982, NASA TM-82969.

Deissler, R.G.; and B.M. Rosenbaum, 1973, NASA TN D-7284.

Eckmann, J.P., 1981, Rev. Mod. Phys. 53, 643.

Feiereisen, W.J., E. Shirani, J.H. Ferziger, and W.C. Reynolds, 1982, in Turbulent Shear Flows 3, edited by L.J.S. Bradbury, F. Durst, B.E. Launder, F.W. Schmidt, and J.H. Whitelaw (Springer-Verlag, New York), p. 309.

Ferziger, J.H., 1977, AIAA J. 15, 1261.

Franceschini, V., 1983, Phys. Fluids 26, 433.

Frost, W., and T.H. Moulden, 1977, Handbook of Turbulence (Plenum, New York).

Harris, V.G., J.A.H. Graham, and S. Corrsin, 1977, J. Fluid Mech. 81, 657.

Heisenberg, W., 1948, Proc. Roy. Soc. A 195, 402.

Herring, J.R., 1973, in Free Turbulent Shear Flows, Vol. 1 - Conference Proceedings, NASA SP-321, p. 41.

Hinze, J.O., 1975, Turbulence (McGraw-Hill, New York).

von Karman, T., 1937a, R. Aeronaut. Soc. J. 41, 1109.

von Karman, T., 1937b, J. Aero. Sci. 4, 131.

Lanford, O.E., 1982, in Annual Review of Fluid Mechanics, vol. 14, edited by M. VanDyke, J.V. Wehausen, and J.L. Lumley (Annual Reviews, Palo Alto, CA), p. 347.

Laufer, J., 1954, NACA TR-1174.

Ling, S.C., and A. Saad, 1977, Phys. Fluids 20, 1796.

Lorenz, E.N., 1963, J. Atmos. Sci. 20, 130.

McCormick, J.M., and M.G. Salvadore, 1964, Numerical Methods in Fortran

(Prentice-Hall, Englewood Cliffs, NJ), p. 38.

Moin, P., and J. Kim, 1982, J. Fluid Mech. 118, 341.

Monin, A.S., 1978, Usp. Fiz. Nauk [Sov., Phys. - Usp. 21, 429.

Orszag, S.A., 1977a, in Fluid Dynamics, edited by R. Balian and J.L. Peube (Gordon and Breach, New York), pp. 273, 261.

Orszag, S.A., 1977b, in Handbook of Turbulence, edited by W. Frost and T.H. Moulden (Plenum, New York), p. 281.

Orszag, S.A., and M. Israeli, 1974, in Annual Review of Fluid Mechanics, edited by M. Van Dyke, W.G. Vincenti, and J.V. Wehausen (Annual Reviews Inc., Palo Alto, CA), pp. 282-288.

Orszag, S.A., and A.T. Patera, 1981, Phys. Rev. Lett. 47, 832.

Orszag, S.A., and G.S. Patterson, Jr., 1972, Phys. Rev. Lett. 28, 76.

Ott, E., 1981, Rev. Mod. Phys. 53, 655.

Rabinovich, M.I., 1978, Usp. Fiz. Nauk [Sov. Phys. - Usp. 21, 443.

Reynolds, O., 1883, Phil. Trans. Roy. Soc. London 174, 935.

Reynolds, O., 1895, Phil. Trans. Roy. Soc. London 186, 123.

Richardson, L.F., 1922, Weather Prediction by Numerical Process (Cambridge, New York).

Rogallo, R.S., 1981, NASA TM 81315.

Ruelle, D., 1976, in Turbulence and Navier-Stokes Equations, edited by R. Temam (Springer-Verlag, New York), p. 146.

Schumann, U., G. Groetzbach, and L. Kleiser, 1980, in Prediction Methods for Turbulent Flows edited by W. Kollmann (Hemisphere Publishing Comp., Washington, D.C.), p. 123.

Shaanan, S., J.H. Ferziger, and W.C. Reynolds, 1975, Rept. No. SU-TF-6, Stanford Univ.

Siggia, E.D., 1981, J. Fluid Mech. 107, 375.

Smagorinsky, J., 1963, Mon. Weath. Rev. 93, 99.

Taylor, G.I., 1921, Proc. Lond. Math. Soc. 20, 196.

Taylor, G.I., 1935, Proc. Roy. Soc. A, 151, 421.

Taylor, G.I.; and A. E. Green, 1937, Proc. Roy. Soc. A, 158, 499.

Townsend, A.A., 1949, Proc. Roy. Soc. London, 197A, 124.

Uberoi, M.S., 1963, Phys. Fluids 6, 1048.

Van Dyke, M., 1975, SIAM J. Appl. Math. 28, 720.

Wygnanski, I., and H. Fiedler, 1969, J. Fluid Mech. 38, 577.

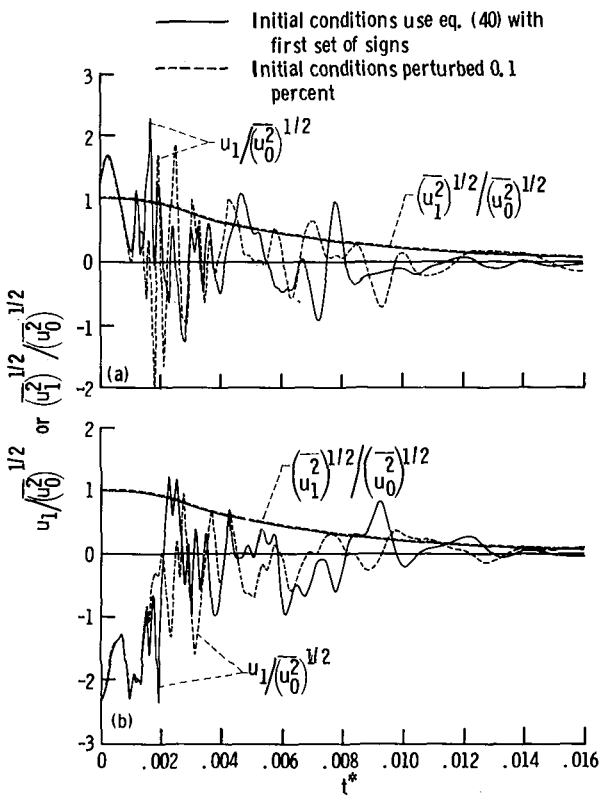

(a) $x_1^* = x_2^* = 9\pi/8$, $x_3^* = 3\pi/8$, for unaveraged fluctuations.

(b) $x_1^* = x_2^* = x_3^* = \pi$, for unaveraged fluctuations.

Figure 1. - Calculated evolution of turbulent velocity fluctuations (normalized by initial condition) for a high Reynolds number $\left(\overline{u_0^2}\right)^{1/2} x_0/\nu = 2217$. No mean shear; root-mean-square fluctuations spatially averaged; 32^3 grid points.

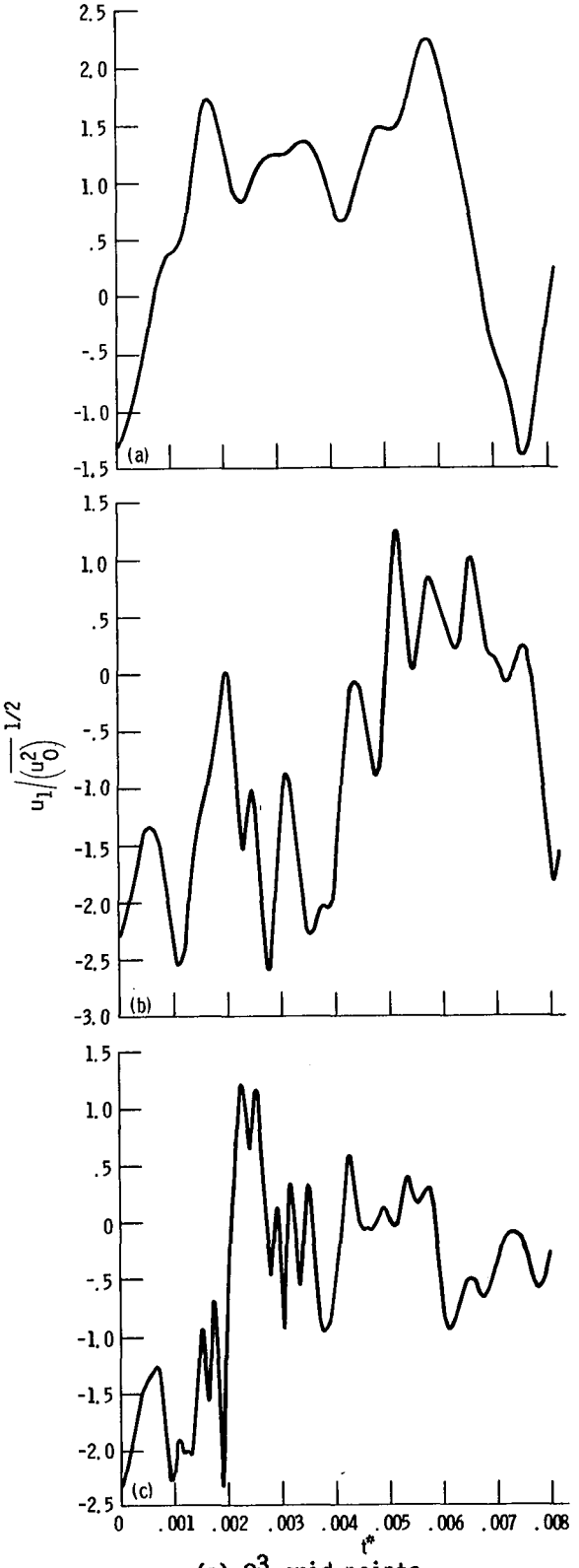

(a) 8^3 grid points.
(b) 16^3 grid points.
(c) 32^3 grid points.

Figure 2. - Effect of numerical mesh size on calculated evolution of velocity fluctuations. No mean shear; $\left(\overline{u_0^2}\right)^{1/2} x_0/\nu = 2217$; $x_i^* = \pi$ (at grid center).

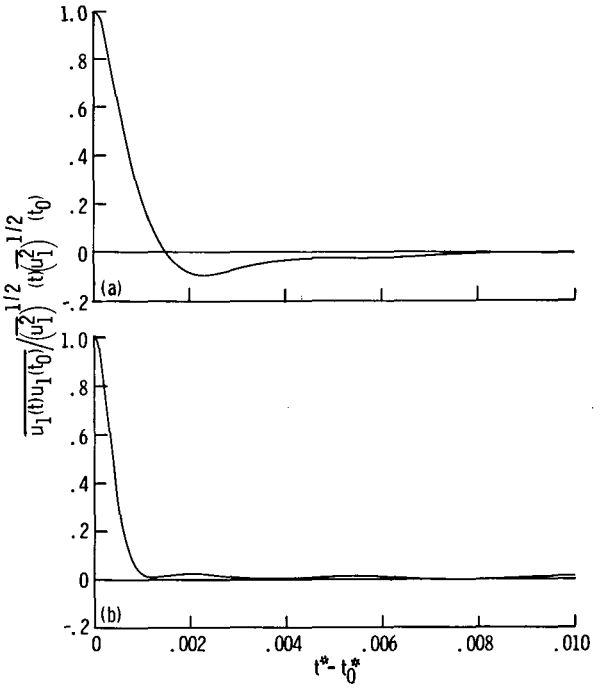

(a) $t_0 = 0.$
(b) $t_0 = 0.00813.$

Figure 3. - Calculated correlation coefficient for velocities at dimensionless times t_0^* and t_0^* plotted against $t^* - t^*$. No mean shear; $\left(\overline{u_0^2}\right)^{1/2} x_0/\nu = 2217$; 32^3 grid points.

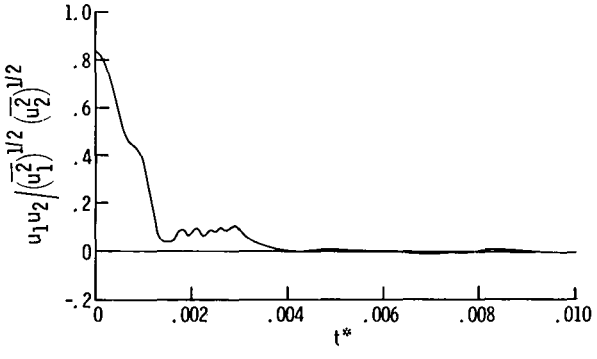

Figure 4. - Calculated correlation coefficient for two velocity components plotted against dimensionless time. No mean shear; $\left(\overline{u_0^2}\right)^{1/2} x_0/\nu = 2217$; 32^3 grid points.

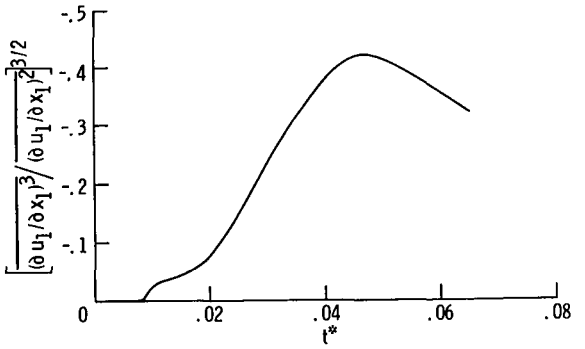

Figure 5. - Calculated evolution of velocity-derivative skewness factor. No mean shear; $\left(\overline{u_0^2}\right)^{1/2} x_0/\nu = 2217$; 32^3 grid points.

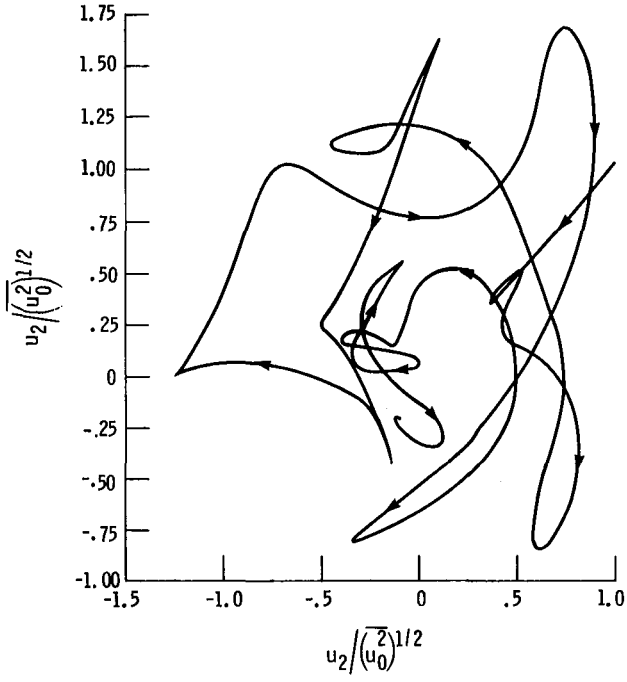

Figure 6. - Calculated trajectory of phase point projected on u_1-u_2 plane $x_1^* = x_2^* = 9\pi/8$, $x_3^* = 3\pi/8$, and $0.00236 < t^* < 0.0108$. Arrows indicate direction of time. No mean shear; 32^3 grid points.

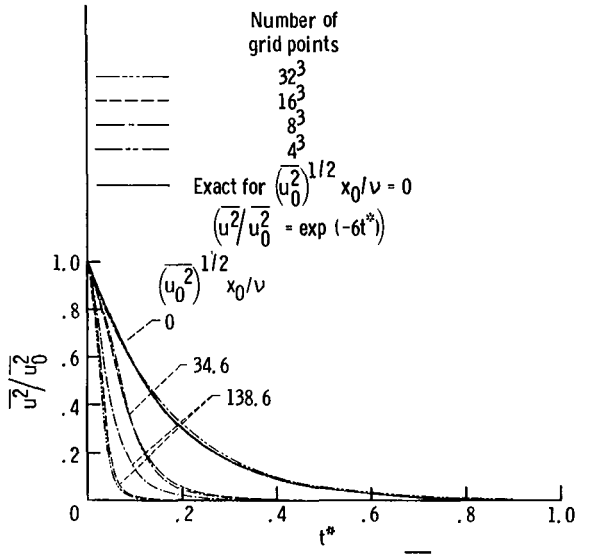

Figure 7. - Effect of numerical mesh size on evolution of $\overline{u^2}$ at low and moderate Reynolds numbers. No mean shear. $\overline{u^2} = \overline{u_1^2} = \overline{u_2^2} = \overline{u_3^2}$.

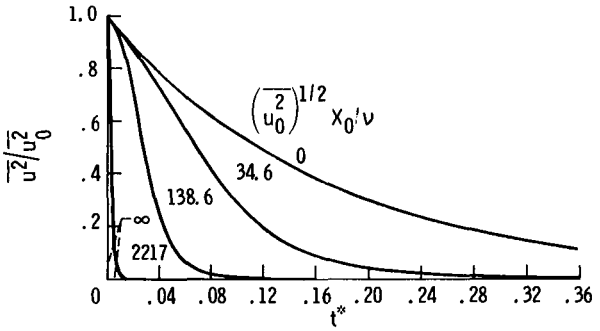

Figure 8. - Calculated evolution of mean-square-velocity fluctuations (normalized by initial value) for various initial Reynolds numbers. No mean shear; $\overline{u^2} = \overline{u_1^2} = \overline{u_2^2} = \overline{u_3^2}$; extrapolated to mesh size.

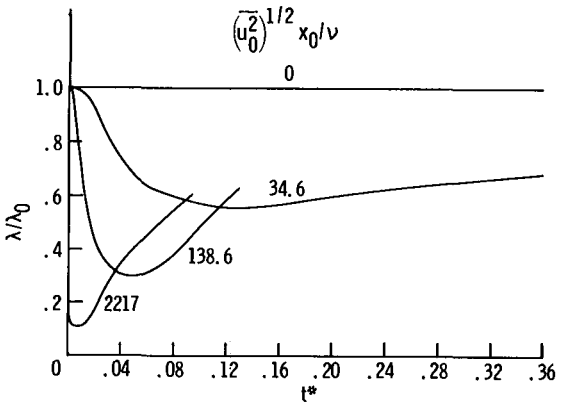

Figure 9. - Calculated evolution of microscale of velocity fluctuations (normalized by initial value) for various initial Reynolds numbers. No mean shear; extrapolated to zero mesh size.

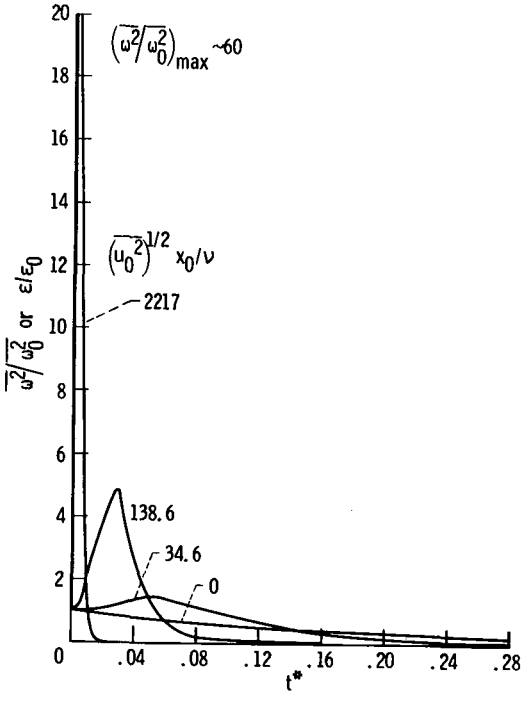

Figure 10. - Calculated development of mean-square-vorticity fluctuations $\overline{\omega^2}$ or dissipation ε (normalized by initial value) for various initial Reynolds numbers. No mean shear; extrapolated to zero mesh size.

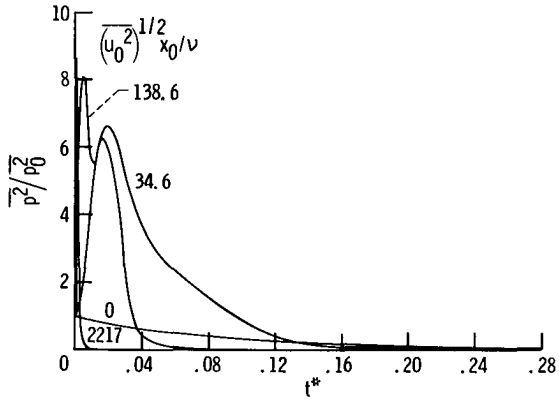

Figure 11. - Calculated evolution of mean-square pressure fluctuation (normalized by initial value) for various initial Reynolds numbers. No mean shear. Extrapolated to zero mesh size.

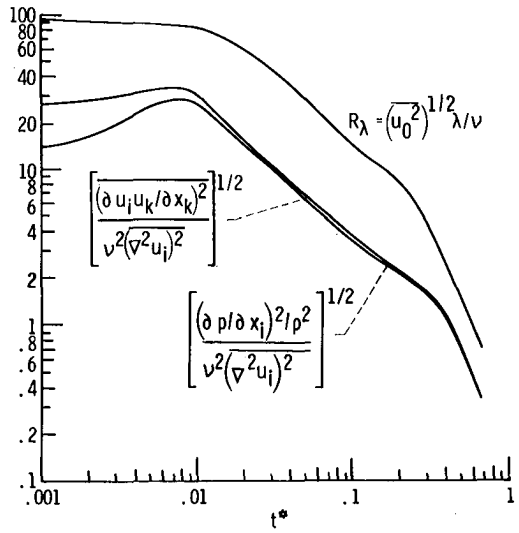

Figure 12. - Three measures of relative importance of inertial and viscous effects plotted against dimensionless time. No mean shear; $\overline{u_0^2}^{1/2} x_0/\nu = 69.3$; i = 1, 2, or 3; extrapolated to zero mesh size.

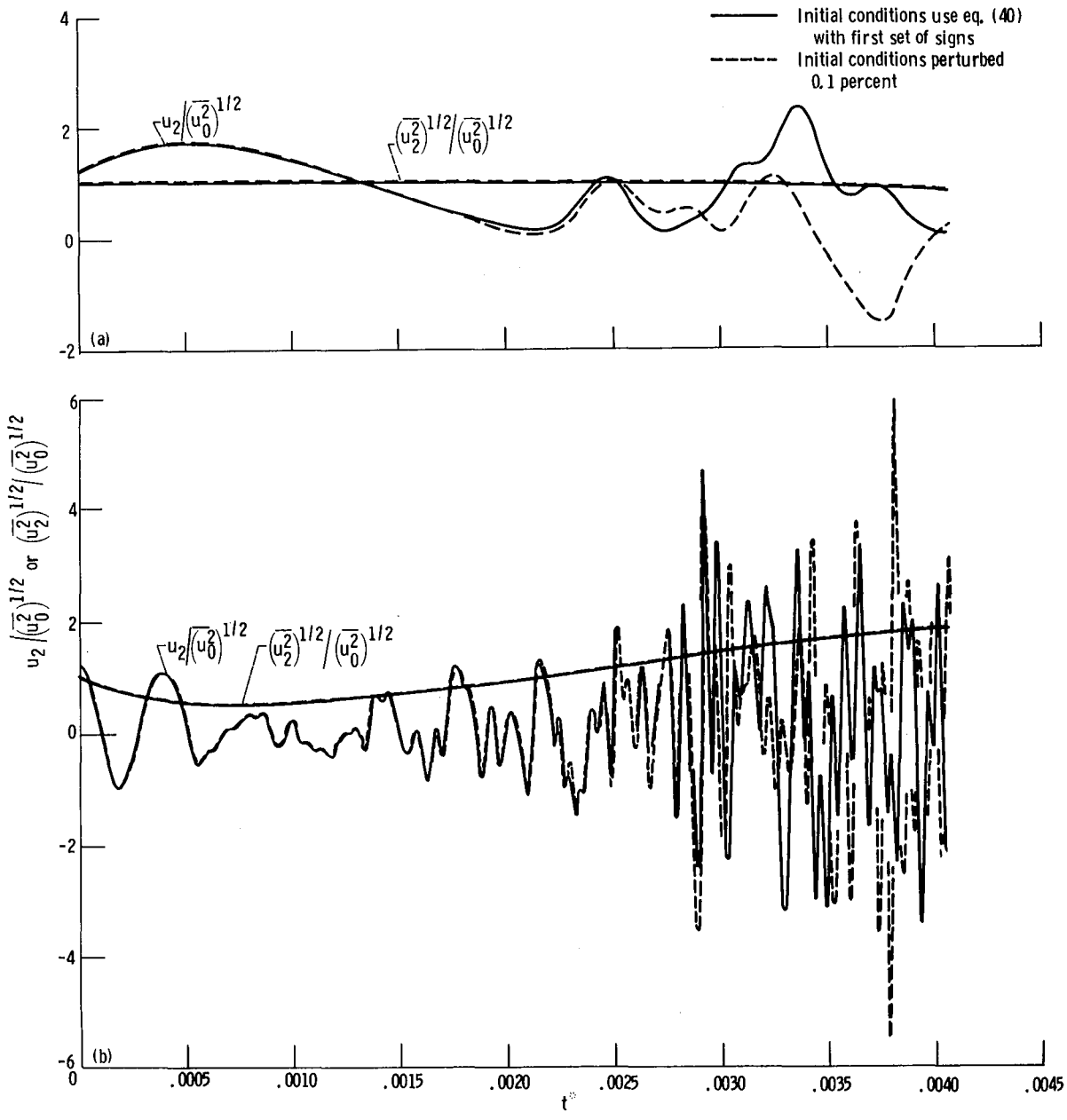

(a) $(dU_1/dx_2)^* = 0.$

(b) $(dU_1/dx_2)^* = 4434.$

Figure 13. - Effect of uniform shear on calculated evolution of nonlinear turbulent velocity fluctuations (normalized by initial value) for a high Reynolds number $\left[\left(\overline{u_0^2}\right)^{1/2} x_0/\nu = 1108\right]$. Root-mean-square fluctuations are spatially averaged; 32^3 grid points; $x_1^* = x_2^* = 9\nu/8$, $x_3^* = 3\pi/8$ for unaveraged fluctuations.

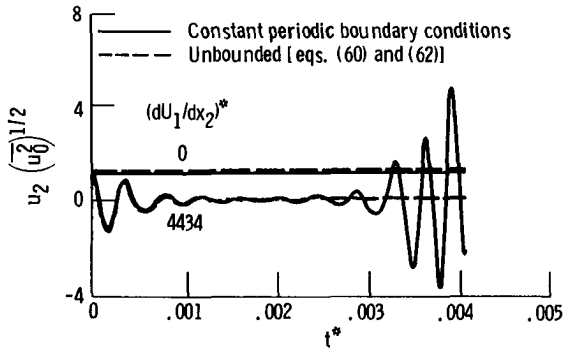

Figure 14. - Calculated evolution of linearized velocity fluctuations (normalized by initial value). $\left(\overline{u_0^2}\right)^{1/2} x_0/\nu = 1108$; $x_1^* = x_2^* = 9\pi/8$; $x_3^* = 3\pi/8$; 32^3 grid points.

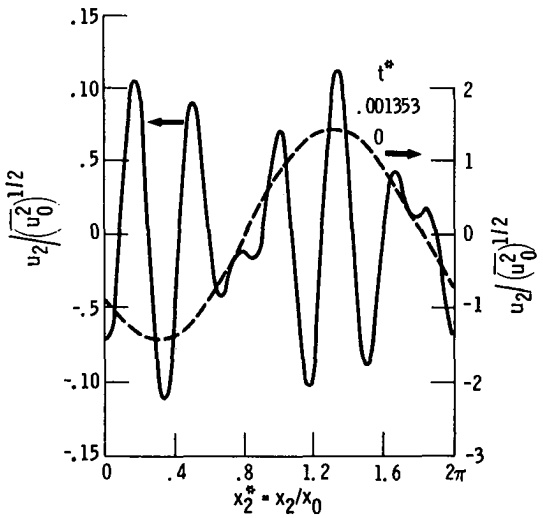

Figure 15. - Linearized analytical solution for $u_2/\left(\overline{u_0^2}\right)^{1/2}$ plotted against x_2^* for unbounded (eq. (60)). $x_1^* = 9\pi/8$; $x_3^* = 3\pi/8$; $(dU_1/dx_2)^* = 4434$; $\left(\overline{u_0^2}\right)^{1/2} x_0/\nu = 1108$.

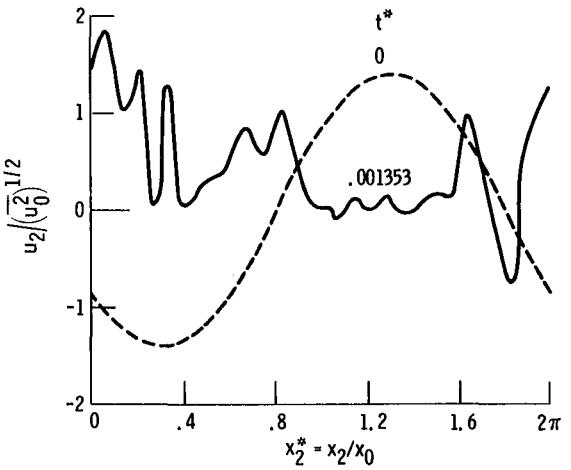

Figure 16. - Nonlinear solution for $u_2/\left(\overline{u_0^2}\right)^{1/2}$ plotted against x_2^*. $x_1^* = 9\pi/8$; $x_3^* = 3\pi/8$; $(dU_1/dx_2)^* = 4434$; $\left(\overline{u_0^2}\right)^{1/2} x_0/\nu = 1108$; 32^3 grid points.

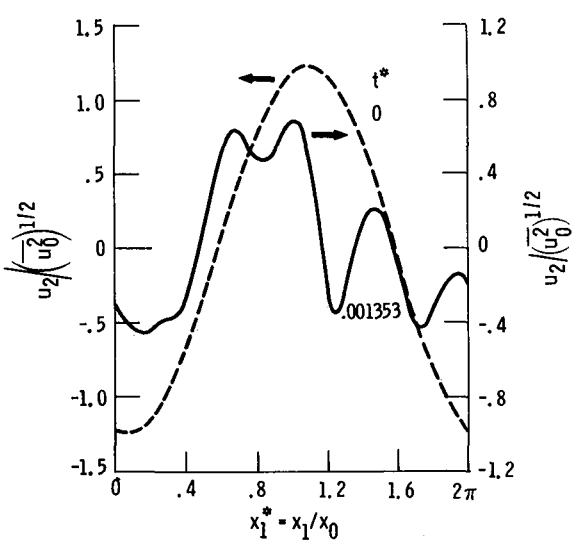

Figure 17. Nonlinear solution for $u_2/\left(\overline{u_0^2}\right)^{1/2}$ plotted against x_1^*. $x_2^* = 9\pi/8$; $x_3^* = 3\pi/8$; $(dU_1/dx_2)^* = 4434$; $\left(\overline{u_0^2}\right)^{1/2} x_0/\nu = 1108$; 32^3 grid points.

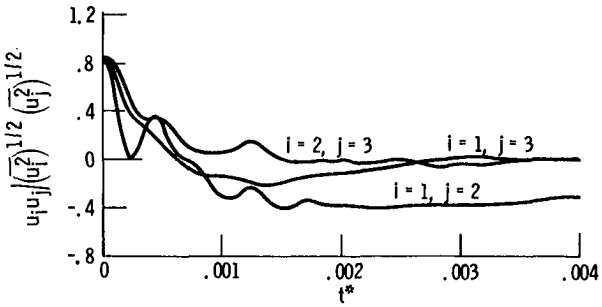

Figure 18. - Calculated cross-correlation coefficients ($i \neq j$) plotted against dimensionless time. $(dU_1/dx_2)^* = 4434$; $\overline{u_0^2}^{1/2}\, x_0/\nu = 1108$; 32^3 grid points.

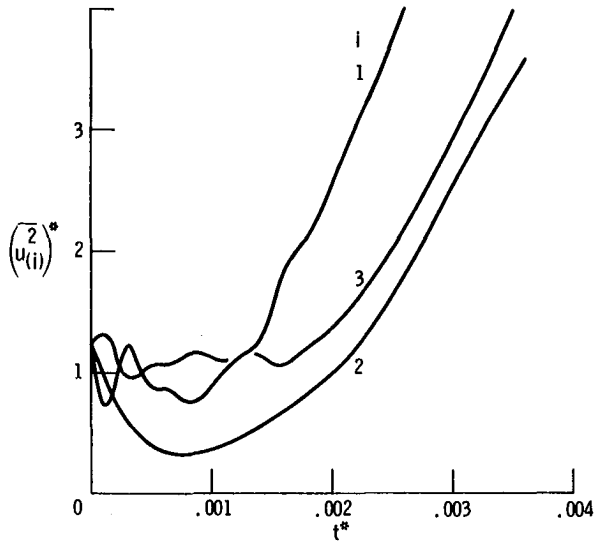

Figure 19. - Calculated evolution of mean-square velocity components. $(dU_1/dx_2)^* = 4434$; $\left(\overline{u_0^{*2}}\right)^{1/2} x_0/\nu = 1108$; 32^3 grid points.

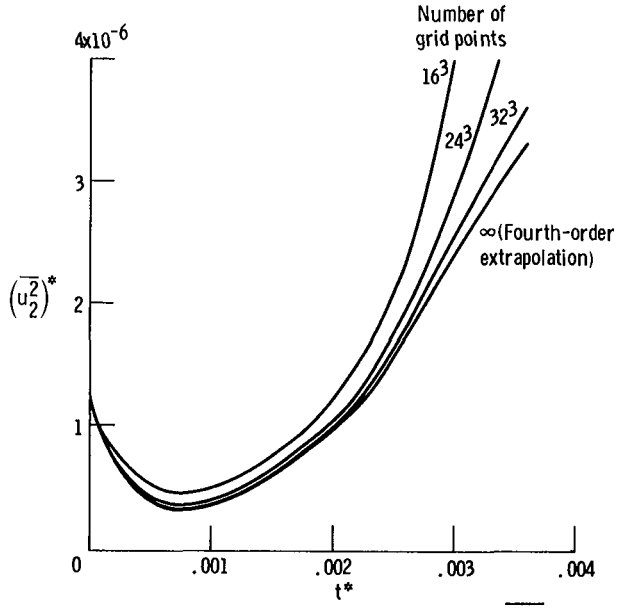

Figure 20. Effect of numerical mesh size on evolution of $\overline{u_2^{2*}}$. $(dU_1/dx_2)^* = 4434$; $\left(\overline{u_0^2}\right)^{1/2} x_0/\nu = 1108$.

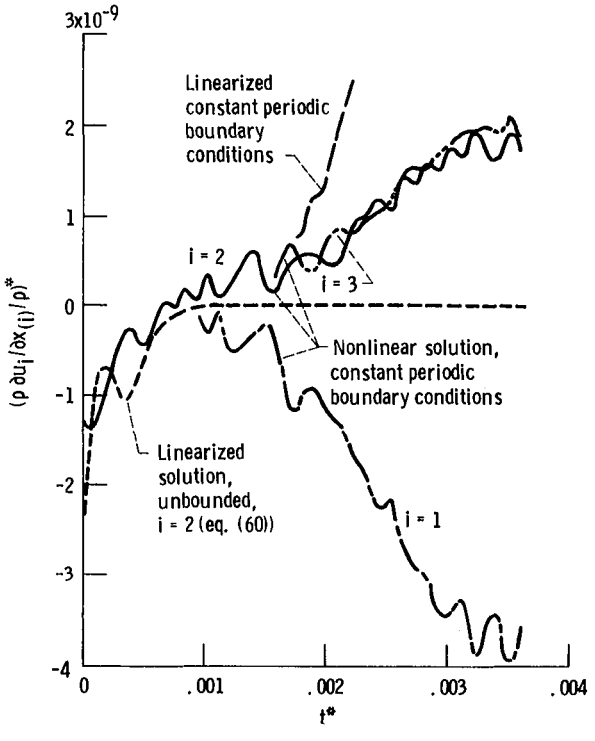

Figure 21. - Calculated evolution of pressure-velocity-gradient correlations. $(dU_1/dx_2)^* = 4434$; $\left(\overline{u_0^2}\right)^{1/2} x_0/\nu = 1108$; 32^3 grid points.

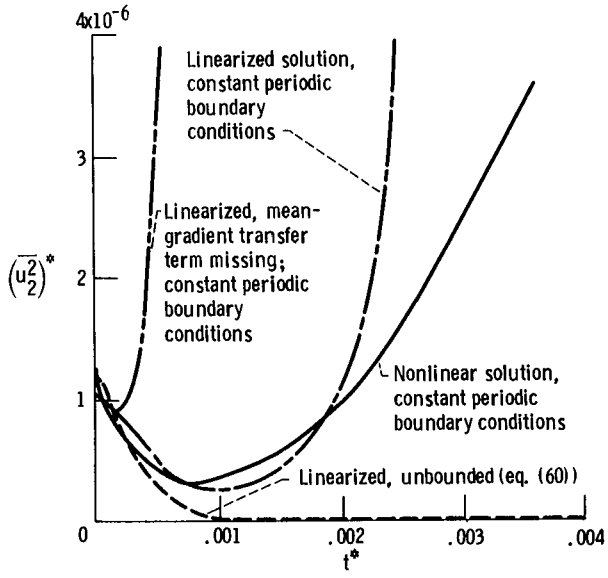

Figure 22. - Evolution of $\overline{u_2^2}$ for various linear and nonlinear solutions. $(dU_1/dx_2)^* = 4434$; $\left(\overline{u_0^2}\right)^{1/2} x_0/\nu = 1108$.

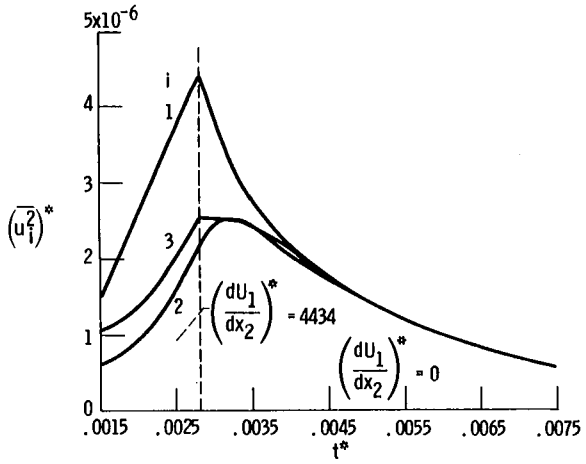

Figure 23. - Calculated approach to isotropy of uniformly sheared turbulence upon sudden removal of the shear. $\left(\overline{u_0^{*2}}\right)^{1/2} x_0/\nu = 1108$; 32^3 grid points.

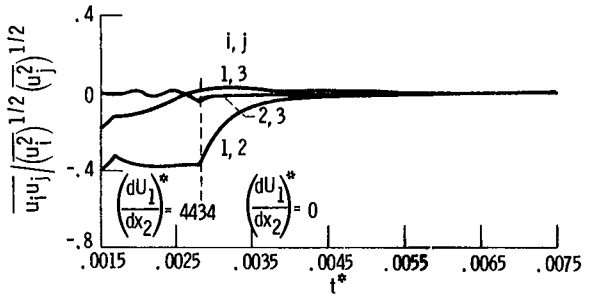

Figure 24. - Calculated evolution of cross-correlation coefficients upon sudden removal of uniform shear. $\left(\overline{u_0^2}\right)^{1/2} x_0/\nu = 1108$; 32^3 grid points.

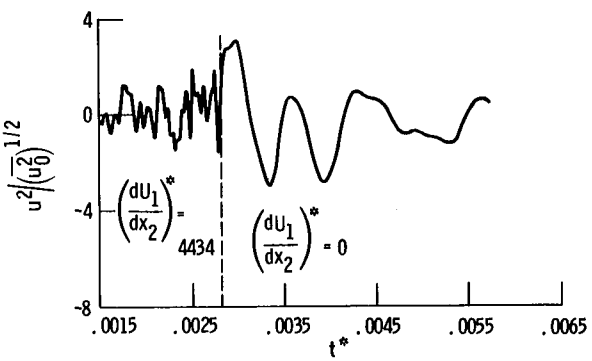

Figure 25. - Effect of removal of uniform shear on structure of turbulence. $\left(\overline{u_0^2}\right)^{1/2} x_0/\pi = 1108$; 32^3 grid points.

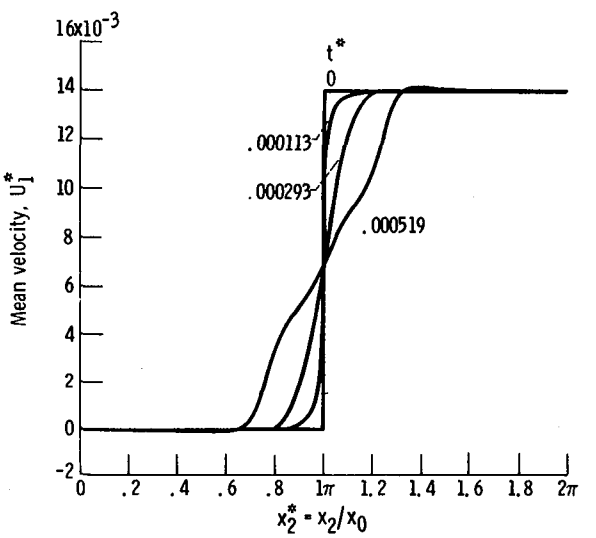

Figure 26. - Calculated development of shear layer mean-velocity profile with dimensionless time. $\left(\overline{u_0^2}\right)^{1/2} x_0/\nu = 554$; V* = 2216 in eq. (71); 32^3 grid points.

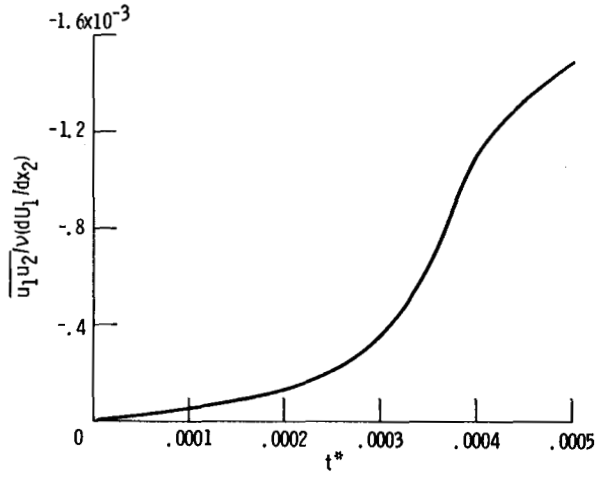

Figure 27. - Calculated time variation of ratio of turbulent-to-viscous shear stress for developing shear layer at $x_2^* = \pi \cdot \left(\overline{u_0^2}\right)^{1/2} x_0/\nu = 554$; $V^* = 2216$ in eq. (71); 32^3 grid points.

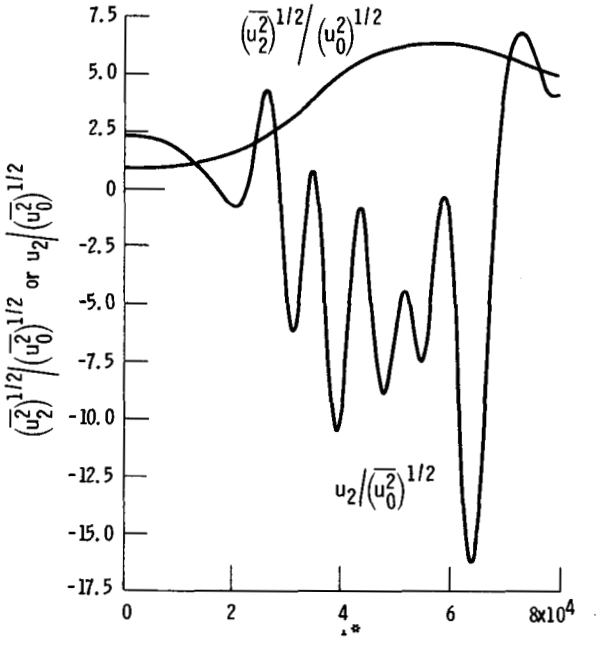

Figure 28. - Calculated evolution of turbulent velocity fluctuations (normalized by initial value) for developing shear layer. Unaveraged fluctuations are calculated at center of numerical grid ($x_1^* = \pi$). Root-mean-square fluctuations are averaged over x_1^* and x_3^* at central plane $x_2^* = \pi \cdot \left(\overline{u_0^2}\right)^{1/2} x_0/\nu = 554$; $V^* = 2216$ in eq. (71); 32^3 grid points.

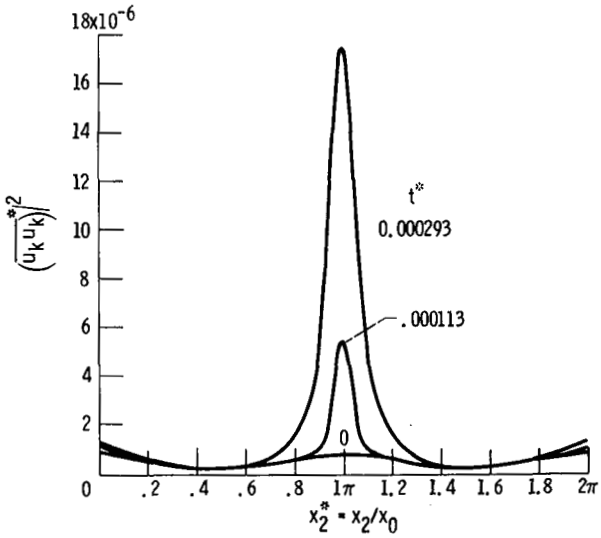

Figure 29. - Development of dimensionless kinetic energy profile with dimensionless time for developing shear layer. $\left(\overline{u_0^2}\right)^{1/2}$ x_0/ν = 554; V* = 2216 in eq. (71); 32^3 grid points.

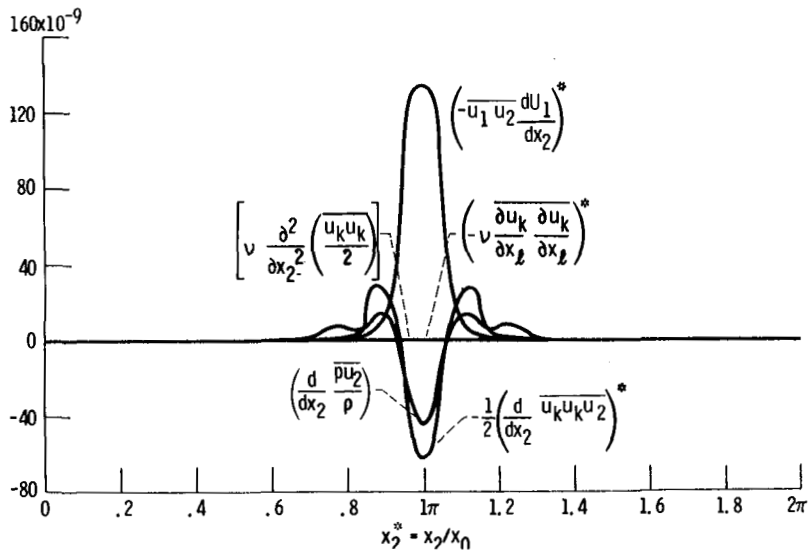

Figure 30. - Plot of terms in one-point correlation equation for kinetic energy (eq. (73)) for developing shear layer. $\left(\overline{u_0^2}\right)^{1/2}$ x_0/ν = 554; V* = 2216 in eq. (71); t* = 0.000293; 32^3 grid points.

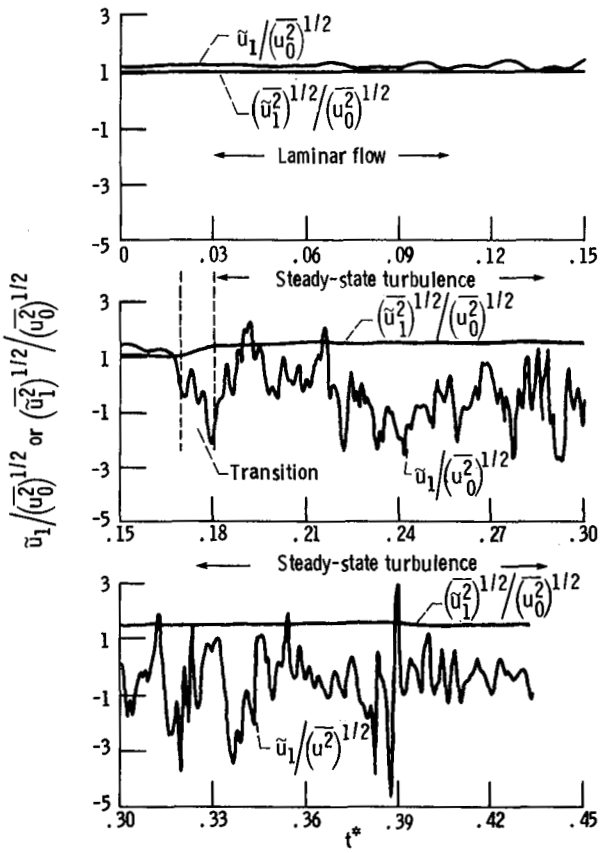

Figure 31. - Calculated evolution of turbulent velocity fluctuations (normalized by initial condition) with a spatially periodic body force. $\left(\overline{u_0^2}\right)^{1/2} x_0/\nu = 138.6$; $x_1^* = x_2^* = 9\pi/8$; $x_3 = 3\pi/8$ for unaveraged fluctuations. Root-mean-square fluctuations spatially averaged; 32^3 grid points.

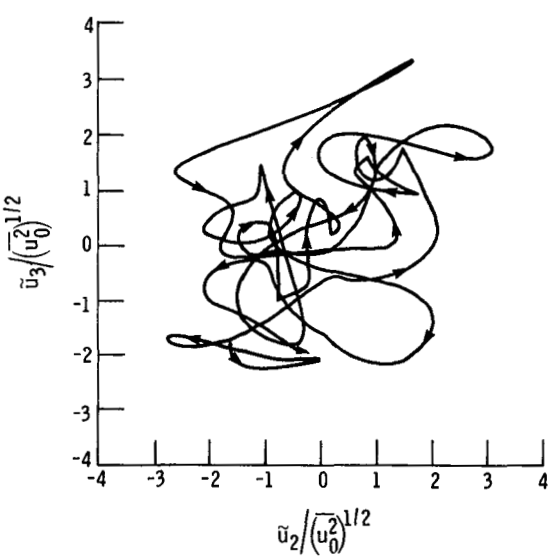

Figure 32. - Calculated trajectory of phase point projected on u_2-u_3 plane at numerical grid center with a spatially periodic body force. $0.26 < t^* < 0.32$; $\left(\overline{u_0^2}\right)^{1/2} x_0/\nu = 138.6$; 323 grid points. Arrows indicate direction of time.

BYPASS TRANSITION TO TURBULENCE AND RESEARCH DESIDERATA

Mark V. Morkovin
Illinois Institute of Technology
Chicago, Illinois 60616

Bypass transitions are seldom mentioned in texts or meetings on instability and transition to wall turbulence. Like poor relations, they are untidy; they spoil the beautiful orderly structure of instability theories and devalue our rational tools for improved understanding of the onset of turbulence in boundary layers, pipes, and ducts. I shall first try to illustrate the nature of a number of bypass transitions by examples. Like a Sunday preacher, I will use visualizations of concrete phenomena to have something to preach about and to convey a physical feeling for the associated mechanisms whenever possible.

HISTORIC BYPASS - THE BLUNT-BODY PARADOX

Turbulent wedges on blunt noses (fig. 1) was the first class of bypass identified (ref. 1). The fact that transition occurred very early on many spherical noses was a shock to designers of reentry vehicles in 1957. All theories said that the accelerated cooled boundary layer was stable, and yet flight tests (ref. 2) showed transition on the nose for laminar Reynolds numbers based on the momentum thickness Re_θ of the order of 100 to 200. Two multimillion dollar contracts based on copper heat sinks "melted away" with this finding of high turbulent heat transfer. Tens of millions of dollars were lost because the path to turbulence bypassed all known theories. Ten years later I coined the word "bypass" to describe this "blunt-body paradox" and to drive home to designers that we cannot trust stability theory alone. Predicting transition, without allowing for bypasses, remains risky. To this day, the mechanism of the early transition on blunt bodies remains unexplained. Many classes of bypass, as Bob Graham described in the Introduction, are due to large disturbances, but there are no clearly large disturbances evident in the blunt-body paradox. I found wall roughness to be the most likely contributor to the phenomenon (ref. 3, sections III-6 and III-9). When the mirror finish on NASA Lewis test vehicles (protected by plastic sheets up to the test altitudes) did not keep the roughness below 5 ?in rms, a bypass occurred. Even 10-?in roughness is very small (not truly measurable by most mechanical profilometers); yet it was in some sense excessive for the thin boundary layers in the given flight disturbance environment. Until we truly understand why this is so, predicting transition on the basis of theory or statistically inadequate correlations (as they all are) entails risks that should be considered in justifying any design involving transition.

CONCEPT OF MINIMUM REYNOLDS NUMBER FOR SELF-SUSTAINING WALL TURBULENCE AND LATERAL CONTAMINATION

Figure 1 also illustrates the concept of the turbulent $Re_{\theta,min}$. To me, a most important concept is that at certain low Reynolds numbers a temporarily turbulent boundary layer cannot sustain itself. If made turbulent through forced local separation, it relaminarizes. Relaminarization in accelerating boundary layers on smooth spheres or cylinders is known to occur within 15° to 20° from the stagnation point, at least for the Reynolds number based

on the diameter of the sphere or cylinder Re_D in the range $3x10^4$ to $3x10^5$. Sustenance of turbulent "bursting" processes near the wall is the crucial feature. A vehicle returning from a Mars mission must remain below $Re_{\theta,min}$ or carry extra weight in retrorockets and their fuel so as not to burn up in Earth's atmosphere. One of the most important results that should come out of any bypass transition research is consistent identification of $Re_{\theta,min}$ for the different boundary-layer classes.

In flat-plate boundary layers (fig. 1) disturbances were introduced (refs. 4 and 5) through large isolated roughnesses or sparks. One of the primary effects of such large disturbances is local boundary-layer separation, which brings about highly unstable inflectional profiles. An early transition on an inflectional profile may or may not grow. It may relaminarize after reattachment as already mentioned. The non-Blasius boundary layer may sustain turbulence in the narrow wake (fig. 1). The wake diverges slowly and parabolically, as a turbulent diffusing wake will do when the boundary layer next to it remains completely laminar and stable. At some stage the neighboring Blasius layer, the boundary layer in which we are interested, suddenly "allows" the turbulence to spread along a turbulent wedge-front, making an angle of 8° to 11° with the streamwise direction. The beginning of the wider spreading locates $Re_{\theta,min}$ empirically. The spreading is called transition by transverse or lateral contamination. Note that there is nontrivial uncertainty in pinpointing this location - a matter of subjective judgment. For the flat plate this location coincides very nearly with that of the Tollmien-Schlichting-Schubauer (TS) critical Reynolds number Re_{cr} for the growth of infinitesimal disturbances. This was noticed by Dr. H.L. Dryden some 9 years before he became head of NASA. We then have a large disturbance and yet its initiation of turbulence in a Blasius layer coincides with the infinitesimal instability criterion. We now know that this happens to be a coincidence, though it is still not understood.

FLOWS WITH KNOWN $Re_{\theta,min}$ AND Re_{cr}

On spheres and circular cylinders Re_{cr} and $Re_{\theta,min}$ have a completely different relationship: $Re_{\theta,min}$ can be substantially below Re_{cr}. Because of the pressure gradient my conjecture is that $Re_{\theta,min}$ depends on Re_D - all unexplored research territory. For pipe flows Re_{cr} is infinite, whereas Re_D for self-sustained wall bursting in so-called turbulent slugs (ref. 6) is about 2700. (The flow confinement in pipes makes possible a different mode of steady self-sustenance of turbulence at an Re_D of about 2200, the puff turbulence (ref. 6); this turbulence is presumably sustained by self-perpetuating inflectional instability taking place away from the wall.) In two-dimensional Poiseuille duct flows Re_{cr} based on half of the distance between the parallel plates is approximately 5770; growing and convecting turbulent patches, however, arise spontaneously (ref. 7) at the low Re of about 1500, the effective minimum Reynolds number. The nature of this transition remains unknown - another bypass. The physical confinement enhances the role of unsteady pressure fluctuations, which spread elliptically in all directions at large effective rates.

One unconfined boundary layer also maintains constant thickness and therefore constant Re_θ all along its length: the boundary layer along the attachment lines on a swept wing of constant chord or on an inclined long cylinder. For such attachment layers $Re_{\theta,min}$ is approximately 100 (ref. 8), whereas the critical Re_θ is 236 (ref. 9). Forced turbulent

spots at Re_θ below 100 relaminarize as they travel along the blunt leading edge; clearly this information is relevant in turbomachinery.

The information in the preceding paragraph essentially exhausts our knowledge concerning $Re_{\theta,min}$. Before we go on to other types of bypass, we should comment on an assumption that is often hidden in the experimental accounts. Since we are dealing with self-sustenance of turbulence, the momentum thickness θ should refer to the nonintermittent, turbulent boundary layer at the given location x. We can often measure or at least compute with some degree of assurance the laminar velocity profile, and hence θ_{lam}, as a function of x but not the new turbulent profile. If a laminar profile were to turn turbulent "instantaneously" at the given x, without the intervention of a drag-producing element, θ_{turb} would equal θ_{lam}. All of the $Re_{\theta,min}$ values quoted above are understood in this sense. A useful discussion of the relation between contiguous laminar and turbulent boundary layers and of transition tripping devices is due to Preston (ref. 10). Finally, we should observe that the mechanism of lateral contamination is distinct from the mechanism that originally caused the turbulence. Lateral contamination by turbulent wedges or intermittent turbulent spots in boundary layers therefore represents a separate bypass mode that can be present anywhere downstream of $Re_{\theta,min}$. There is no theory nor even a crude model for, say, the angle of lateral contamination as a function of pressure gradient and Mach number. At supersonic speeds it can be as low as 5°.

BROAD CLASSIFICATION OF LARGE DISTURBANCES

Large "disturbances" that can cause bypass transition in otherwise smoothly developing boundary layers can be steady or unsteady and can originate in the oncoming stream or at the body surface. One way to look for the potential causes of bypasses of all established stability theories is to ask what features make possible the analysis of the instability mechanisms besides the presence of small disturbances. Invariably the base flows that are perturbed to study the instabilities are characterized by dependence on a minimum of independent variables (x, y, z, and t) and other parameters such as wall curvature and sweepback. The smoothly distributed vorticity $\vec{\omega}$ of the base flow is generally oriented along a single coordinate, spanwise or azimuthal (in axisymmetric shear layers). The perturbations of the nonlinear vorticity-rotating and -stretching source term $\vec{\omega} \cdot \text{grad}(\vec{V})$ in the vorticity equation is then absent from the linearized perturbation equations. The associated powerful inviscid vorticity-generating mechanism thus remains inoperative in the first (primary) instability. If, however, there is a sufficiently large steady deformation of the wall or if a sufficiently large steady secondary flow or shear layer in the stream such as a wake from an upstream stator interacts with the boundary layer, the base flow possesses a three-dimensional $\vec{\omega}$ to start with. When we perturb these flows, the extra vorticity-generating mechanism is then present in the primary instability and is likely to lead to an earlier transition. The steady large disturbances would cause a bypass of the known, analyzed instability patterns.

Similarly a large unsteady disturbance can make the base flow temporarily highly unstable. If the instability is very fast, it may be completed before the original large disturbance runs its course and thus generate a bypass. Inflectional instabilities and the rotate-stretch mechanism in particular can be very rapid in many practical situations.

The distributed vorticity in the base flow may be likened to an amplifier system. Steady and unsteady large disturbances can redistribute the vorticity enough to make the amplifier act more powerfully and in new modes not excitable in the original amplifier system. In the examples given, the large disturbances did just that. Besides acting in this role of a modifier of the amplifier system, large disturbances invariably provide direct input into the amplified signal, higher in intensity and richer in spatiotemporal spectral content. This is also the role assigned to the "environment" in small-disturbance theory. Unsteady potential pressure gradients (including sound), entropy, and vorticity fluctuations and nonhomogenities in the stream can all induce unstable vorticity eigenfunctions in boundary layers through many mechanisms broadly called receptivity. Linearized quantitative theories of receptivities to the different stream disturbances are currently under development.

The increased intensity of the disturbances should make the same primary instabilities develop faster and farther upstream. This is important even though not strictly a bypass behavior. However, finite amplitudes should open up additional threshold-dependent instabilities in the "enlarged amplifier system." Many interactive instabilities (ref. 11), which are relegated to secondary instabilities in small-disturbance environments, may emerge as primary instabilities and alter the path to turbulence. Admittedly, many of these possibilities are speculative, simply because no reliable studies have been reported on the instability characteristics in boundary layers forced by large three-dimensional disturbances, in which at least two of the three rms fluctuation levels u', v', and w' exceed 3 percent of the mean free-stream velocity U_e. If we compare these 3-percent magnitudes to those present at the onset of turbulence in a Blasius layer at the Herbert breakdown (ref. 11), we can appreciate better the possibilities of interactive instabilities. These latter disturbances correspond roughly to a u'_{max} of the fundamental TS wave of the order of $0.01\ U_e$ and to similar amplitudes of the resonant skew subharmonic and of the rest of the broadband spectrum. Since rms fluctuations add in the square, the forcing large disturbances with nonresonant $u' \approx 0.03\ U_e$ exceed the disturbances in observed cases of incipient turbulence. Herbert's interaction can begin at levels of the fundamental $u' \approx 0.006\ U_e$ and the subharmonic at $u' \approx 0.0006\ U_e$. In view of such indirect information the likelihood of interactive instabilities becoming primary appears quite plausible. Mentioning such possibilities is intended primarily to stimulate the imagination of those embarking on research into large disturbances, and not as a prediction.

LARGE WALL DISTORTIONS AND HORSESHOE VORTICES

We have established that large disturbances, steady or unsteady, at the body surface or in the stream, enhance and modify the vorticity-amplifying system and in addition supply more intense and spectrally richer fluctuations, which are amplified. Let us go back to the visual evidence of concrete examples; we start with strong disturbances due to wall deformation - a more detailed elaboration of the phenomena leading gradually to the top pattern of figure 1 - and continue with even stronger disturbances. The motivation for the choice of this example is multiple. First, the fixity of wall deformations makes evident many modes of vorticity behavior that cannot be easily photographed and analyzed when the strong disturbances are convected with the stream. Second, a very damaging disturbance in turbomachinery is associated with a horseshoe vortex formed at the intersection of the blades or vanes with the hub or casing wall. Our example deals with a circular cylinder that

protrudes to an increasing height k into and ultimately through the laminar boundary layer of thickness δ. Since smoke tracers do not penetrate into all of the regions of interest, we shall precede the photographs with two complementary sketches of the flows of interest (figs. 2 and 3) due to Gregory and Walker (ref. 12) and to Charles R. Smith of Lehigh University. These sketches are based on numerous observations, with different tracers introduced at different locations, and represent a consensus of most observers.

To my knowledge the Gregory-Walker sketch is historic; it gave the first three-dimensional topography of separated flow around a three-dimensional protuberance. Also, as a result, our intuitive concept of separation, nurtured by quasi-two-dimensional textbook examples, requires revision to allow for throughflow and partial openness of the "local pockets of separation": the separation surface has "inlets" and "exits." A central-plane streamline, just above that shown approaching the protuberance in figure 2(b), comes to a stagnation point S', where the highest pressure is experienced on the surface of the obstacle. Pressure gradients on the obstacle from S' toward the wall propel the rollup of the open slice of the vortical boundary layer from the wall to the dividing stream surface, which has S' as its high point. The resultant horseshoe vortex H diverts the initial ω_z vorticity into the two spiraling vorticity tubes oriented in the x direction. The slice of the oncoming boundary layer above the dividing stream surface through S' forms the side and top shear layers, which are stable at the low Reynolds number portrayed here. In steady flow these shear layers effect an incomplete closure of the near wake along a higher pressure dashed line through S at the wall, a very complex rear singularity. The top rear surface of this steady three-dimensional separation pocket is pierced by a steady outflow in the form of two weak spiral vortices (evident in all three projections). The inflow into the slowly recirculating rear "separated" region comes partly from the inner segments of the side and top shear layers and partly through two symmetric back openings in the wall (figs. 2(a) and (b)). The two arms of the horseshoe vortex tube lift off the wall as they are forced to rotate around the obstacle and open two symmetrically located "inlets."

The Reynolds number Re_k that governs the flow around obstacles is defined as $(U_k k)/\nu$, where U_k is the boundary-layer velocity at the obstacle height k in the absence of the obstacle and ν is the dynamic viscosity. The complicated flow described above and depicted in figure 2 is stable at Re_k of 300 to 450, depending on the shape of the obstacle and the pressure gradient along the wall. As far as we know, all symmetric protuberances at low Reynolds numbers have flow fields topologically similar to that depicted in figure 2. These flows are the base flows that would have to be perturbed if we were to study their stability analytically. At present not even advanced computers can resolve such details of the base flows as the spiral vortices and the wall inlets. The resulting instabilities will have to be specified empirically. Because of the complex flow geometry they bypass previously analyzed patterns. Here we are following the visual evidence to obtain a "feel" for what can happen in fields generated by large disturbances.

TRANSITION CAUSED BY ISOLATED THREE-DIMENSIONAL EXCRESCENCES

As Re_k grows past 300 to 450 (depending on obstacle shape) the weak top spiral vortices strengthen and begin to weave closer and closer to the rear separating surface. With rising Re_k the separating surface becomes unsteady and soon sheds periodic intertwined hairpin vortices (fig. 3). Lift is exerted

on the hairpin loops by the boundary layer, and the loops move toward the edge of the boundary layer as they are convected downstream. Norman (ref. 13) measured local u'/U_e as high as 0.04 at distances 30k to 40k (k = height length) downstream of the protuberance without any subsequent instability that would render this complex periodic flow turbulent. Under these conditions the pattern decays and transition occurs far downstream, usually through primary TS and subsequent secondary and tertiary instabilities. There is, however, some evidence that the far wake of the large disturbance caused by the protuberance contributes to a somewhat earlier growth of the TS and secondary instabilities.

As Re_k reaches 550 to 650, depending on the shape of the obstacle, with x_k past Re_{cr}, the transition starts moving upstream very rapidly. An increment of 20 in Re_k may halve the $x_{tr,0} - x_k$ distance to transition. This rate decreases as x_{tr} approaches x_k asymptotically. As we shall see shortly, transition will remain near the obstacle although new instabilities will appear as Re_k increases. The nature of the instability that brings on the rapid forward movement of x_{tr} is currently being investigated by P. Klebanoff. It bears resemblance to the final instability in the transitions commencing with TS waves as the primary instability. The final "burst" takes place near the wall, probably as an interaction of the horseshoe vortex and the intertwined legs of the hairpin vortices; stretching of these legs by convection and lifting of the loops (fig. 3) should provide extra intensification.

In figure 4(a), due to Norman (ref. 13), x_{tr} is far downstream of the protruding cylinder. Any smoke that may have penetrated the wake was diffused by the motions of the hairpin loops of figure 3. The horseshoe vortex is clearly upstream of the cylinder; downstream, along the inner edge of the arms of the horseshoe vortex, weak periodic undulations indicate the influence of the unseen loops. In figure 4(b), the interaction with the moving hairpin vortices is clearly visible at the inner boundary of the horseshoe vortex tubes. The wake spreading is still parabolic, but x_{tr} must be approaching the downstream end of the photograph. In figure 4(c), turbulence starts near the end of the separation and spreads along a nearly straight turbulent wedge front, as discussed in connection with figure 1(a).

In figure 4, Re_k was changed by increasing U_e and keeping the height constant and equal to the diameter of the cylinder. Except for figure 4(c), Re_{cr} was downstream of x_k. In figure 5, the height k and the cylinder diameter were increased in a constant boundary layer, keeping k/D equal to unity. In figure 5(a), the larger disturbance of the cylinder protruding through the boundary layer is seen to generate two additional horseshoe vortices upstream of the cylinder. Simultaneously, we witness the appearance of a new type of instability on the inner horseshoe. This spiral instability now governs the transition to turbulence as its dominant factor. But the horseshoe vortices begin to oscillate as Re_k is increased. Configurations of four horseshoe vortices collapsed periodically, as if the inner one broke and convected away, while the others moved up by one, an occurrence labeled "burping." Three-vortex configurations burped occasionally, presumably because of larger random modulation of free-stream disturbances, which must introduce the unsteadiness into fixed-obstacle instabilities. This behavior is probably present in the horseshoe vortices formed at the intersection of the blades or vanes with the hub or casing wall in turbomachinery. If the configuration burped, letting loose some fluid that was next to the wall and replacing it with fresh fluid, a condition of high heat transfer would be created. Unsteady motion at the

equivalent of the stagnation point S' in figure 2(b) also generates high local heat transfer. This is compounded by intersecting shock waves at supersonic and hypersonic speeds; special tailoring of local geometry is needed to protect the roots of control fins on high-speed vehicles operating at lower altitudes.

In figure 5(c), the disturbance is so strong that transition actually occurs on the horseshoe vortices as they form in front of the obstacle. There is little probability that such instability and transition can be handled with confidence computationally for decades. All of the preceding illustrations of bypass transition were for relatively low Reynolds numbers for two reasons. First, bypasses are expected to occur at the lower Reynolds numbers between Re_{cr} and $Re_{\theta,min}$ (if these can be estimated). Second, we are able to observe the otherwise undescribable complexity of the motions and the multiplicity of instabilities and thus acquire some "feel" for what may be in store.

At higher body Reynolds numbers these events will move toward the leading edge and be lost to the resolution of our visualization techniques. Nevertheless, to the extent that we have accounted for the dominant characteristic length and velocity scales, we can extrapolate the present lessons to practical situations, at least qualitatively, through the appreciation for the mechanisms that may be involved. Such appreciation is a prerequisite for designing of meaningful experiments in the realm of large disturbances.

We may ask what would happen in these cases of large wall disturbances if we added stronger free-stream turbulence. It depends on whether the local flows in figure 4 can sustain turbulence once it is triggered; in other words are the flows in the horseshoe vortex and at the separation surface above their own Re_{min}? Since these flows already have three-dimensional vorticity and locally inflectional profiles, the turbulence might be sustainable in figures 4(a) and (b) without propagating into the neighboring laminar layer by lateral contamination as occurred upstream of Re_{cr} in figure 1(a). The local heat transfer at the obstacle would then rise substantially. If in the case of figure 4(a), say, Re_{min} were not reached, the heat transfer in the presence of higher free-stream disturbances would rise much less because it would remain governed by laminar conduction scales. The additional unsteadiness imposed by the external free-stream turbulence is then likely to bring about a second-order effect.

EFFECT OF A WAKE IMPINGING ON A BLUNT BODY

Let us now consider what lessons we can draw from a few experiments with moderate disturbances coming from the free stream toward a body without the disturbing wall deformation just discussed. For larger stream disturbances the region of concern is usually the leading edge, especially when the oncoming fluid is hot, whether in propulsive and cooling devices or downstream of a strong shock in supersonic flight. Figure 6, due to Hodson and Nagib (ref. 14), shows schematically how a low-Re wake from an upstream cylinder of diameter d causes a pair of horseshoe vortices in the stagnation region of a circular or rectangular cylinder of breadth D. In 1973 it occurred to me that a momentum defect in a stream impinging at right angles to the stagnation line S_ℓ-S of a two-dimensional body should generate horseshoe vortices just like the momentum defect in a boundary layer does as the high-pressure region of the protruding cylinder is approached in figure 4. The next day Nagib and Hodson produced visual evidence of the phenomenon and later went on to document its

nonlinear onset and its implication for heat transfer. The stagnation pressure along S_ℓ, on the sides of the wake, induces flow down the pressure gradient toward the full stagnation point at S. When the pressure at S exceeds sufficiently the stagnation pressure associated with the streamline of least momentum, such as that leading to S_f, there is counterflow and horseshoe vortex formation. (See also Morkovin (ref. 15) for a detailed discussion of theoretical and experimental evidence of instabilities in stagnation regions and the empirical threshold curve for the vortex formation of Hodson and Nagib.)

One of the Hodson-Nagib dye visualizations in water of the vortex pair in front of the flat face (dark vertical line on left) is shown at the top of figure 7. The horizontal dye line marks the center of the steady laminar wake of a rod at $Re_d = 30$; the body Reynolds number $Re_D = 1040$ has only secondary influence. Heat can be carried to and from the body on a large nonmolecular scale, and its transfer has local spanwise maximums and minimums. These can be quite high and could cause local damage. In steady flow the spatially averaged heat transfer along the leading edge appears to be of second order, according to Hodson and Nagib (ref. 14).

UNSTEADY EFFECTS AND HEAT TRANSFER

The average heat transfer increases with unsteadiness. In the lower half of figure 7 where $Re_d = 365$ and the wake is weakly turbulent, horseshoe vortices are still forming but they dance back and forth. The blue dye (B) and the yellow dye (Y) originate far upstream and pass just below and above the wake-generating rod. Despite the turbulence and slight three-dimensionality of the wake, both dyes are drawn into the two-dimensional "mushroom" from the region of high stagnation pressure, as suggested in the lower half of figure 6.

Figure 8 features frames from a Hodson-Nagib film. At $Re_d = 90$ the wake, 111 diameters downstream from the rod, has decayed considerably to u'/U_e of the order of 0.02 to 0.03. The condition of a regular formation of Karman vortex street at approximately 40 Hz was chosen so that the contrast caused by a sudden additional disturbance would be readily perceptible. The sudden disturbance was caused by a single water drop falling on the surface of the water half a channel height above the rod. The effect of the disturbance consists primarily of a sudden change in the phase rather than in the amplitude of the oscillatory wake; the phase change is marked by the letter P in figure 8. We can follow it as it progresses toward the flat face of the rectangular cylinder at the dark vertical line on the left side of the frames. The heads of the oscillating pair of vortices begin to be affected at $t = 0.24$ sec. The evidently forceful ejection of a single horseshoe vortex at $t = 0.44$ sec and further strong vorticity interactions leading to two smaller horseshoe vortices at $t = 0.55$ sec were not previously observed and are initially surprising. They testify to the strength of possible vortical interactions when distributed vorticity is allowed to concentrate locally through instability rollups. The wall gradients associated with such unsteady developments especially in the last two frames of figure 8 are bound to produce high heat transfer rates. Yet the flow is in no sense turbulent. This is regular laminar behavior except for the sudden phase change. The phase change alters the ongoing interactions, which follow the Biot-Savart law. We note that a film was necessary to capture effects due to free-stream disturbances. There are few such films. By focusing first on large disturbances due to steady wall deformations new effects could be captured rather easily because of the fixity of the disturbance. There is reason to believe that an equally rich atlas of interactions, beyond

those of figures 7 and 8, awaits researchers into large steady and unsteady free-stream disturbances.

ROLE OF LOCAL SEPARATIONS

This is an opportune occasion to reinforce the earlier statements concerning local separation as an important effect of large disturbances, steady or unsteady. Obviously the formation of separation pockets cannot be linearized. We have seen local separation play important roles in roughness cases (in fact, practically in all roughness phenomena) and in horseshoe vortex formation at three-dimensional obstacles as well as at blunt leading edges. We should add quasi-two-dimensional local separations at locations of rapid changes of curvature, often called leading-edge bubbles or laminar bubbles even though the closure of the bubble is generally turbulent. The effective mechanism here is inflectional instability. Thin blades and airfoils invariably have separation bubbles. In some cases they are most efficient in making the boundary layer turbulent and thus preventing stall losses in turbomachinery, pumps, and fans.

Even for carefully designed blades, free-stream disturbances with larger velocity components perpendicular to the leading edge, steady or unsteady, may generate separation bubbles locally and temporarily. Part of the research on bypass transition should investigate carefully the local behavior when wakes from upstream are "cutting" across sharp and blunt leading edges of surfaces at various angles so as to systematize and generalize the insights of Hodson and Nagib.

Even when transition is not caused just past the leading edge, large steady and unsteady streamwise vorticity, generated there, affects transition downstream. A significant related observation was made by Kendall (ref. 16) in his figure 5. His turbulence-producing grid was made of slender vertical rods placed in the settling chamber some meters upstream of the measuring station above a horizontal flat plate in the test section. At such distance the intensity u'/U_e in the free stream had decayed to 0.11 percent and was uniform across the span. However, inside the boundary layer the intensity varied regularly from 0.15 to 0.23 percent at spanwise intervals set by the 3.2-mm-diameter rods in the settling chamber. Kendall found the horizontal component u' to be out of phase below and above the plate. Somehow, the u' and w' fluctuations in the rod wakes, antisymmetric in the z direction, were converted into motions antisymmetric in the y direction, perhaps at the leading edge or through vorticity stretching by the 9:1 contraction. How the resulting antisymmetric motion of the stagnation point on the 6:0.5 elliptic nose of the plate was related to the spanwise nonuniformity is not clear. We also know that in very low-disturbance environments significant streamwise vorticity somehow forms in boundary layers (ref. 17) and accelerates the Görtler and crossflow primary instabilities and the secondary instabilities initiated by TS waves. The cause must be sought in the imperfect geometry of the leading edge or in its interaction with free-stream disturbances. Any nick in the leading edge creates a pair of streamwise vortices, and possibly a bypass transition.

In two-dimensional bubbles the rolled-up vorticity of the separated shear layer serves as a rapid turbulizer. If the leading edge is swept or otherwise moves at a skew angle with respect to the local stream, the bubble acquires a throughflow velocity component along its axis. Such formations may grow into

concentrated vortices; if they are cast off the solid surface, they represent strong and dynamic large disturbances that can spoil flows downstream.

FREE-STREAM TURBULENCE AND TRANSITION

Let us now return to effects of free-stream disturbances on transition on undeformed bodies, this time on an ogive-cylinder in an axisymmetric wind tunnel as shown on top of figure 9, borrowed from an unpublished study (ref. 18) of D. Arnal and J.C. Juillen of ONERA, Toulouse. Two free-stream conditions are shown, as indicated by the streamwise x variation of u'/U_e, one with a turbulence-producing grid (grille) and the other without the grid (sans grille). The first lesson from this comparison is that anytime we study effects of free-stream turbulence we must monitor the variation in its intensity and spectra throughout the test section. The intensity of the grid turbulence decreased by more than a factor of 2.5 along the body, while the intensity of the old turbulence from the settling chamber upstream of the contraction increased somewhat.

This latter lack of decay was never explained satisfactorily. In the experience of the author and his colleagues, such a behavior means the probable presence of some slow mean gradients or a swirl with production of new turbulence. Neither of the fields behaves like the idealized isotropic turbulence. Note that neither intensity in these experiments represents really large disturbances. Turbulence of high intensity is invariably spatially nonhomogeneous, and its careful mapping would disclose mean lateral and streamwise gradients in intensity. Quotations of grid-produced turbulence with intensity $Tu = u'/U_e > 0.04$ seldom mention that such fields also exhibit mean velocity gradients when measured along continuous traverses. As we have discussed, such mean gradients modify the boundary-layer amplifiers along their paths. Obviously there is no single Tu number that can characterize the turbulent field as a guide to the onset of transition. No wonder that earlier in this symposium, Ray Gaugler reported failure in predicting transition with all techniques and correlations in the cases of large disturbances he had analyzed. There are too many parameters and subtle nonlinearitites (many not even recorded) to make possible any kind of a credible statistical base for such prediction codes to be trustworthy.

The ONERA study at small-to-medium Tu levels illustrates the dilemmas that we often face as we make more measurements: x_{tr} in the absence of the grid was at 0.9 m, which is upstream of the x_{tr} of 1.05 m achieved in the presence of the grid at much higher Tu. These are measurements by professionals that cannot be dismissed as if they were a beginner's masters thesis. Evidently additional factors, more important than u' levels, must be lurking in the experiments. One such factor could be the spectral distribution of the external disturbances conveyed in the insets of figure 9. The authors confirm that the grid actually suppressed the low-frequency end of the spectrum. Could low-frequency fluctuation of higher amplitude more effectively induce TS waves at higher frequencies (between 400 and 550 Hz) in this flow at 29 m/s? This is not altogether out of the question; one important receptivity path (ref. 19) is through unsteady pressure gradients impressed on the inner boundary layer near and past Re_{cr}. We shall return to this issue in connection with figure 10. Another possibility is that the large disturbances caused by the grid rods planted directly into the wall of the tunnel caused a considerably thicker turbulent boundary layer. The growth of the displacement thickness on the wall must have accelerated the flow somewhat and made the boundary layer

on the body more stable than in the absence of the grid. The authors doubt that this effort was significant, but the measurements of $U_e/U_{e,ref}$ in the upper part of figure 9 were not made near the body. Furthermore, Arnal and Juillen's own figure 42 shows that the displacement thickness of the boundary layer grew about 10 percent faster without the grid, indicating a slightly more destabilizing pressure gradient. We are left with speculations. However, that is a frequent predicament of experimenters in transition, when they make more than one experiment, especially when these are separated by unrelated experiments on the different instruments. It is a very useful lesson for researchers embarking upon the much more demanding task of developing understanding of the effects of large disturbances on the multifaceted phenomena of transition.

Unsteady Disturbances in Laminar Boundary Layers and Receptivity

Figure 10 compares hot-wire traces $u(t)$ *at five heights* y/θ *in the* boundary layer as the disturbances inside the layer in the presence of the grid develop with x, where θ is the local momentum thickness at each x. (For approximate estimates we recall that in a Blasius layer $\delta \sim 2.9\delta^* \sim 2.9 \times 2.59\ \theta$.) The first station ($x = 3.7$ cm) is located in the accelerated boundary layer on the nose of the body. Since the time scales in all of the traces are the same, the external high-frequency content (see sample external spectrum in the inset of fig. 9) appears at all the levels of the layer. At the next station, $x = 36$ cm, 10 times as far from the nose, the high frequency has been filtered out or dissipated near the wall. Incidentally, Re_{min} should occur near $x = 15$ cm. The boundary layer on the front of the body is effectively buffeted by the free stream. Upstream of Re_{min} the transport processes across the boundary layer must remain largely laminar (i.e., molecular); the vorticity convected into the parabolic layer and the pressure field of the vorticity remaining outside the layer make it unsteady (i.e., buffet it); see top of figure 14. The small-scale velocity fluctuations carried with the ingested vorticity are effectively damped near the wall. This is evidence against the receptivity path whereby direct free-stream vorticity ingested into the spreading layer would be converted into vertical TS waves. Vorticity entering the layer downstream of Re_{cr} and the vorticity induced by pressure fluctuations across the streamlines remain as possible active agents of receptivity (ref. 19); see top of figure 14.

The small wiggles on the two traces nearest to the wall at x of 66 and 85 cm are in fact the signatures of TS wave packets growing away from the wall. Additional spectral evidence suggests that these TS wave packets keep growing and that after secondary instabilities near $x = 95$ cm and final instabilities near $x = 100$ cm, turbulent intermittency sets in. The important finding is that TS waves first appear near the wall, after all frequencies in the TS range seem to have been filtered out or dissipated upstream. These findings are consistent with the more recent results of Kendall (ref. 16). However, the u' information tells us little about damping of ingested, nearly streamwise vorticity. Such vorticity would produce a zero signal if strictly aligned in the x direction. Since it weaves along its way, all such unsteadiness would be sensed as low-frequency u' signals by the hot wire oriented in the z direction. The low frequencies in the inner y regions at the last two stations are probably partly of this character. However, velocity fields induced by vorticity convected outside the boundary layer should also contribute primarily at lower frequencies: only larger scale formations can influence regions at greater distances (top of fig. 14). Measurements of space-time correlations at two or three points are needed to sort out the complicated

forcing and response fields. Receptivity to free-stream turbulence appears to be very subtle indeed; see Kendall (ref. 16) for additional factual information on the response at a forcing-grid-generated intensity u'/U_e of 0.16 percent.

In the relatively low-intensity experiments of figures 9 and 10, receptivity appears to begin as a linear process seeding linearizable TS wave packets that cumulate and grow to nonlinear levels and lead to higher instabilities. At higher intensities the nonlinear effects described in the section Broad Classification of Large Disturbances should be expected. Important modifications of the oncoming vorticity fields can be anticipated at a sharp leading edge but may be difficult to model.

When a turbulent field approaches a blunt body, the potential field induced by the blunt shape distorts the turbulent field substantially and nonisotropically. It is the distorted field that ultimately interacts with the boundary layer. A serviceable account of the transformed field is obtainable through the so-called "rapid distortion theory" (ref. 20). If applied to ω_z vorticity in figure 6, the theory would indicate that such vorticity is stretched and amplified algebraically as it is convected toward the blunt body. The vorticity lines also deform into a horseshoe shape as they approach the body. Once they penetrate deeply enough into the boundary layer the stretching is counteracted by viscosity and the associated disturbances damp, at least at the linearized level of stability analysis.

A very useful outline of the many phenomena discovered in fields where different turbulent or vortical flows convect into or impinge upon a body is in the recent survey of Bushnell (ref. 21).

LAMINAR BOUNDARY LAYERS BUFFETED BY INTENSE TURBULENCE

What happens in the boundary layers upstream of Re_{min}? As noted in connection with figure 10, there may be a great deal of activity near the wall, much of it dissipated at the low Reynolds number. The dominant mode of transfer remains molecular. However, the ONERA disturbance levels were relatively low. When the stream contains large disturbances, we run into the problem of defining and describing the dominant characteristics of such flows, as discussed earlier in the section on classification. There are many isolated reports on transition, heat transfer, drag, and other overall "outputs" with inadequately defined conditions. Such usually ad hoc tests are often contradictory and leave a great deal of uncertainty in their wake, primarily because the results are not documented in terms of mechanisms or detailed flow behavior. A valid criticism by Dyban, Epik, and Suprun (ref. 22) states, "The observed augmentation of transfer processes (in a layer that remains laminar) is 10 to 80 percent (four quoted references) . . . very little was published on the mechanism of the interaction . . ." The results of Dyban and coworkers, a small sample of which is summarized in figures 11 and 12, deserve attention and an attempt at duplication to see whether turbulent buffeting would act the same way in the United States as it did in Kiev.

Such a suggestion is much more than a joke and deserves clarification. Contradictory and unconfirmed overall "outputs" (such as mean position of transition, average heat transfer over larger areas, drag, etc., labeled "macroscopic measurements" by Lester Lees) were recognized as a major block in the progress of transition research in 1970 by the U.S. Transition Study Group (currently an informal group, chaired by Eli Reshotko). To remedy such

uncertainties and to avoid miscues for further research, USTSG adopted (among others) guideline 4 (ref. 23): "Whenever possible, tests should involve more than one facility; tests should have ranges of overlapping parameters, and whenever possible, experiments should have redundancy in transition measurements." In my function here as a preacher, I would paraphrase Lees: "Go microscopic research (seek detailed mechanisms), young man or woman!" and add, "In transition research, duplicating key measurements is not a Sin, it's a Virtue." In 1977, I broadened (ref. 24) guideline 4 to computer research, whereby by "facility" we understand a theoretical model, however simplified, with its computer program. A case in point is the recent public confusion (ref. 25) concerning supersonic instability, when contradictory numerical results went to print without insistence on rigorous prepublication comparison of the two codes.

Most careful researchers believe that "higher values of free-stream turbulence can be achieved only with increasing inhomogeneous distributions of dynamic head and turbulence across the test section" (ref. 26). On the other hand the Kiev group claims that it is possible to achieve "virtually complete uniformity of the spatial distribution of fluctuating and average velocities at the test section inlet" by the use of high-solidity grids - provided they are placed just ahead of the converging section of the wind tunnel. Hassan Nagib, who was originally skeptical, tells me now that the scheme has possibilities because the immediate acceleration through the contraction may prevent the "anomalous" behavior of high-solidity inserts. (The pressure drop across high-solidity devices is high; in fact they produce multiple jets which have a tendency toward random coalescence, "anomalous" nonhomogeneity, low-frequency intermittency, and spurious intensity growth. This is discussed on page 33 of reference 27, a mechanism oriented text indispensable to researchers into the effects of turbulence.) The Kiev group has approached practical high-turbulence research more systematically than others, and their published results exhibit unexpected consistency.

The abstract in figure 11 describes adequately the six figures in the paper. The graphs in figure 11 convey the development of the mean profiles, including their substantial thickening as compared with the Blasius profile, labeled I. The measurements at the Reynolds numbers noted in figure 11 were achieved with hot-wire anemometers at a free-stream speed of 0.88 m/s at distances x of 105 and 340 mm from the nose of the flat plate sketched in the margin of figure 12. Figure 11 suggests a considerable increase in the slope at the wall at intensities of 8 to 10 percent. In figure 1 of another paper in English, Dyban and Epik (ref. 28) display measured u', v', and w' distribution through evidently the same boundary layer at $Re_x = 20\ 000$. They infer that they also measured the Reynold stress $\overline{uv}$ from Blasius $\eta = 1.5$ outward. Extrapolation to the wall yields an increment of some 45 percent over the laminar value for $Tu \sim 9$ percent in figure 7 of reference 28; see also the three circles (i.e., the three data points in the curve for skin friction C_f in the top graph of our fig. 12). As marked in the margin of that graph, the authors assure us that in the buffeted layers, which they call pseudolaminar, the displacement thickness remains "virtually constant." The shape factor H then decreases from the Blasius value to the 1.9 plateau because the skin friction and momentum thickness (which they denote by δ^{**}) grow as Tu is increased to 14 percent. (In ref. 27, they force-fit the rise in C_f and the Nusselt number Nu with Tu by a second-degree polynomial in Tu and go on to link it with eddy viscosity and other prediction formulas. The quadratic fit would yield a factor of 1.98 for $C_f/C_{f,0}$, which contradicts the top graph

in our figure 12. They arbitrarily limit the predictions to $Tu \sim 14$ percent, the beginning of the plateau in that graph.)

The lower graph in figure 12 displays the intensity distributions u' through the boundary layer as a function of free-stream forcing u'_∞. They focus on the position of the maximum u'_{max} in the boundary layer as a measure of the "penetration of the fluctuations" referred to in the abstract and in their figure 4; they feel it is independent of Reynolds number. However, very pronounced u'_{max} greater than 8 to 10 u'_∞ in laminar layers was observed in the 1950's by A. Favre (personal communication) and P. Klebanoff for low u'_∞; see top of figure 14. This effect, described and referred to as the Klebanoff mode of fluctuations by Kendall (ref. 16), has been explained as a "low-frequency breathing effect"; as the quasi-static Blasius profile shifts with slow thickening and thinning of the layer, the maximum Δu felt by a hot wire at a fixed height is near $\delta/2$. The breathing effect is in no sense dynamic. The dominant contributions to the signal u'_{max} at $\eta = 2.5$ for $u_\infty = 9.69°$ in the lower part of figure 12 are well below 150 Hz; therefore the slow thickening-thinning effect probably has nonnegligible influence on the formation of the u' peak inside the layer even at this high forcing intensity. Some of the authors' interpretations should therefore be accepted temporarily with much caution. Note also that the reader is given no $u'(x)$ decay curve such as was provided by Arnal and Juillen in the lower part of figure 9.

Dyban and Epik (ref. 28) infer that at $Re_x = 60\,000$ the "initial" boundary layer is turbulent. That this would be so for their lowest Tu value of 0.31 percent would be surprising; nevertheless this is as close as they come to the concept of Re_{min}. (Nor is there any discussion of laminar-turbulent intermittency, which would be difficult to identify without a thermal tracer.) They call the initially turbulent layers disturbed by external Tu pseudo-turbulent boundary layers and refer perturbed C^f to the turbulent wall friction at their lowest u'_∞. They measure u', v', w', $\overline{uv}$, C^f, and Nu and interpret the results in terms of a mixing length for prediction purposes. The prediction range once again has to be limited to $Tu < 14$ percent. Their figure 3 for $u'_\infty = 6.85$ percent at $Re_x = 400\,000$ is particularly interesting. First, u'_∞, v'_∞, and w'_∞ are within 6 percent of each other; this achievement of near isotropy at these high turbulence levels lends credibility to their effort. Second, v' has no maximum within the layer, rising monotonically outward to v'_∞; u' and v' on the other hand rise monotonically toward the wall, presumably to maximums at the edge of the sublayer, which remains instrumentally unresolved. Through this account of some of the work of the Kiev group, in the role of an objective reporter I am calling the attention of the researchers starting along this road to this essentially unknown existing systematic information. In my role as a preacher, I am adding the address: Prof. Evgenii Pavlovich Dyban and Dr. Eleanora Yakovlieva Epik, Inst. Techn. Thermophysics, Ukrainian Academy of Sciences, 2a Zhelabova Ul., 252057 Kiev, USSR, in case detente should break out some spring.

LOOKING BACK

Now that we have examined the concepts of Re_{min} and bypasses, identified some of them, classified large disturbances (with special stress on the large mean and quasi-steady distortions of the wall or the free stream as creating bypass amplifiers), acquired some "feel" for their effects via graphic examples of such distortions from protuberances, horseshoe vortices, local separations, and steady and unsteady wake distortions of the stream to more

statistically regular turbulence, large, medium, and small, let us look at a few overview figures. Figures 13 and 14 provide the overall setting for our problem and should make us appreciate why we are up against an especially difficult one. To understand nonunique solutions of nonlinear partial differential equations in four independent variables with very small coefficients of the highest derivatives (viscosity and heat conductivity) is a tall order indeed. Fluid dynamics of generalized Navier-Stokes equations requires us to make sense out of a concatenation of interlaced singular perturbations with multiplicities of solutions. Instabilities represent rapidly crossed moving bridges between subsets of the multiplicity of solutions reachable from physically ill-defined initial conditions at the entry to our open fluid systems. As velocity or x, and hence Re, increase, the effective degrees of freedom increase and so does the large sensitivity to initial conditions. The solutions evolve toward "turbulence."

Actually, it is difficult to define turbulent solutions of the Navier-Stokes equations. As fluid dynamicists we require the presence of the four syndromes in figure 13 to identify turbulent behavior. Syndrome 1, which is used to define "strange attractors," is insufficient for our needs. An examination question: where does a laminar boundary layer buffeted by high external turbulence fit here, and how can we distinguish it empirically from a turbulent boundary layer? The concept is important for design. How can we study it experimentally? In the real world, all laminar boundary layers are buffeted by decaying free-stream turbulence (which remains turbulent as long as there are nonlinear interactions, as intermittent in time and space as these may be). We have little difficulty with that idea as long as transition is downstream of Re_{cr}. The real difficulty faces us near Re_{min}. Of all the syndromes, only syndrome 3, diffusion far in excess of molecular mixing, can guide us. Some of the speculations I offered earlier were based on the assumption that little true turbulent mixing could go on at the scale of local δ below Re_{min}. However, we can imagine a large unsteady turbulent event passing by, say 40δ in length. The temporarily thickened Re_θ may well exceed $Re_{\theta,min}$. Turbulent patches can form in ducts at $Re \approx 1000$, but they decay unless Re exceeds 1500. In response to intermittent large disturbances, intermittent decaying turbulent spots could exist upstream of nominal Re_{min}. If so, the time-average heat or mass transfer would rise much more gradually through the nominal location of Re_{min}. The 1.55 asymptote of the upper graph for skin friction in figure 10 of Dyban et al. (ref. 22) is rather reassuring. The growth curve through Re_{min} may "smear" the contrast in transport behavior, but there should be a practically important upper bound for that transfer rate.

Figure 14 summarizes the processes discussed in connection with figures 9 to 12 as they were driven by free-stream turbulence. A few extra comments are in order: (1) In connection with the ONERA cases we noted that the turbulent vorticity ingested near the leading edge had its finer scales dissipated by viscous wall action; the filtering was so effective that, when the TS waves with wavelengths of 8δ and longer finally grew (fig. 8), they represented higher frequencies and may have been induced across the boundary layer by external turbulent vorticity, as indicated in figure 14 by the label "at distance." (2) TS (or equivalent) waves exist and are induced upstream of the TS Re_{cr}. Forcing motion in linearized system equations induces homogeneous solutions (i.e., decaying or growing eigenfunctions) by the requirement that all boundary conditions be satisfied. Upstream of Re_{cr}, the induced TS response decays shortly after its birth.

The lower sketch in figure 14 adds the effects of an isolated three-dimensional roughness. These we discussed in considerable detail in connection with figures 2 and 5. Finally we noted that in the known systems $Re_{min} < Re_{cr}$, except for the zero-pressure-gradient case, where $Re_{min} \sim Re_{cr}$.

LOOKING FORWARD

The 1984 view of paths to wall turbulence in mildly disturbed environments (fig. 15) can help to organize our thoughts on research into the effects of large disturbances. We need to start with a conceptual framework to project best-bet experiments linked in a systematic way.

Let us review the ingredients along the paths to turbulence and consider how their role is changed because of the higher disturbances. The standard primary linear instabilities (TS, Görtler, and crossflow half-way up in the figure) still can amplify the initially much larger vorticity disturbances (e.g., the visualized nonlinear TS wave packets for $Tu \sim 3.6$ percent in figure 9 of E.M. Gates (ref. 29)). We can expect strong effects of the centrifugal instability (of the Görtler type) in the concave regions of turbine blades, both before and after (!) transition; see Bradshaw (ref. 30) (an important reference for heat transfer estimators).

However, the major upstream movements of transition should come from the quasi-steady, larger scale three-dimensional shear layers carried with the flow, which modify our standard base flows (i.e., our amplifier systems). Because the probably spotty and intermittent regions of largest disturbance bring to the vicinity of the wall three-dimensional vorticity components stronger than those that effect the swift secondary instabilities in the middle of figure 15, we can say - with not much exaggeration - that we essentially begin with a broader class of discretely sprinkled, moving, fast secondary instabilities. (In bypass transitions I expect to see the number in the sequence of instabilities leading to turbulence cut at least by one, in comparison with the standard paths of fig. 15.) But the total number of possible instability paths may be larger. As discussed in the section on classification and illustrated herein (e.g., fig. 8), the larger scales are likely to generate instantaneous three-dimensional profiles (possibly with local separation) subject to inviscid instabilities fast enough to lead all the way to turbulence during the lifetime of these boundary-layer distortions.

Such detailed unsteady behavior is very difficult to document experimentally: instrumental space-time resolution and adequate probe access and traversing with minimal flow interference are major problems. In practical flow configurations, unless we make a heroic effort, the disturbances are likely to be characterized by only one or two averaged parameters and the measured boundary-layer profiles, and "macroscopic" outputs at the wall (even when measured as functions of x) are also severely averaged. Such information is therefore unlikely to lead to better understanding of the particular mechanisms involved in the increased heat transfer. Nor will the smeared information lead to inspired ideas for improvements in design: it does not provide enough linkage between true causes and the measured, averaged output.

Such information will also aid little in modeling and computational code development, for much the same reasons. As I mentioned earlier I am quite pessimistic about Navier-Stokes codes being able to resolve in time and space the clearly important unsteady flows near leading edges such as the sample in

frames 4 to 6 of figure 8 or the transition in the old bypass of the blunt-body paradox, at least for a few decades. So, codes must use grosser modeling. More primitive modeling seldom leads to improved physical insight. For instance, in an earlier talk we heard about the relative success of the Chorin vortex simulation of the flow downstream of a backward-facing step, aimed at one of the simpler cases of combustion. The important simplifications in the model were two-dimensionality of the vortex filaments and neglect of viscosity - for the good physical reasons that the separated shear layers are subject to a quasi-two-dimensional inviscid instability, whether the layer is laminar or turbulent. At least two aspects will have to be added to the model: the presence of the wall below the shear layer and at the termination of the chamber. Actually, the physical effects that those features introduce are three-dimensionality of the vorticity and compressibility. The reason for the first is that the shear layer is three-dimensionally unstable as it approaches the reattachment line on the wall below the layer. From my years at Martin-Marietta Co., I recall an experimental paper, then classified, showing spanwise maximum-minimum variation of heat transfer rates in a ratio of 3 to 1 along the mean reattachment line. The maximums were dangerous for the controls on our maneuverable reentry vehicle, the SV5, and would be undesirable should they occur in the presence of combustion. George Inger refers to it in his linear analysis (ref. 31) of the instability; Anatal Roshko has been interested in this three-dimensionalization of reattachment flows for over two decades and recently has obtained some interesting results (unpublished) that could inspire better local modeling. Adding three-dimensionality of the individual vortices to Chorin's model amounts to more than a slight generalization. Mostly because of the vorticity source term $\vec{\omega} \cdot \text{grad}(\vec{v})$ mentioned in the section on classification, the task is harder than Chorin's developments to the present form of the technique.

FINAL INTERLUDE ON FREE-STREAM DISTURBANCES

The example of the termination of the combustion chamber was chosen mostly to emphasize that free-stream disturbances tend to be overidentified with turbulence (i.e., vorticity and its induced velocity field). It is well known that, when shear flows impinge on a rigid surface, pressure feedback is directed upstream and strongly influences the instability of the separated shear layer and any associated combustion. Incompressibility allows only instantaneous pressure feedback, essentially the near-field acoustic behavior; sound (essentially the far-field behavior) is not allowed and with it many potentially dangerous acoustic resonances common to shear layers separating cleanly from a solid surface. Receptivity to unsteady pressure gradients is one or two orders of magnitude higher at separation lines than it is in unseparated shear layers. (This is the reason why instabilities at isolated three-dimensional excrescences such as seen in fig. 3 are easily pumped up acoustically - forced at distances across streamlines. For x_k past Re_{cr}, transition can thereby be moved substantially upstream.) Realistic prediction codes and diagnostics of free-stream disturbances should allow for such feedback and resonant coupling.

The Chorin model was used only to illustrate the fact that simplified codes quite generally will not be able to simulate satisfactorily this or that mechanism of importance in our transition phenomena. Codes therefore will not be generally able to guide the experiments.

Returning to large free-stream disturbances, the preceding discussion indicates that their theoretical and experimental definition must include unsteady pressure gradients: hydrodynamic (near-field acoustic) and acoustic (far field). The unsteady input disturbances (A.C.) in figure 15 for linearizable amplitudes include entropy disturbances (i.e., density-temperature nonhomogenities (with negligible Δp) convected with the fluid). Such moving entropy nonhomogenities can induce TS waves at supersonic speeds, but the strength of the effect has not been investigated. It has been assumed to be of secondary importance. This is unlikely to be warranted when cooling elements or combustion are present. On the other hand, the unsteady pressure field (sound) generated by turbulent boundary layers on the side walls is known to be so strong and effective at supersonic speeds that it spoils most studies of transition in wind tunnels from Mach 1.5 to 6 or 7; the transition modes that would be present in free flight are bypassed and preempted by the sound forcing.

Ideally, to classify a large free-stream disturbance, we would like to distinguish its steady or moving coherent features from the more homogeneous turbulent background (such as explored by Dyban's Kiev group (refs. 22 and 28)). The first task would then be to identify the stronger, more regular features such as moving shock waves, quasi-two-dimensional wakes from upstream obstacles, free concentrated vortices, and swirl. This requires good understanding of the flow prehistory; such knowledge would then guide subtle diagnostics with two probes, one of which must be traversing within the inlet plane.

The same instrumentation can provide estimates of near-field pressures and far-field acoustic fields. The coherent velocity amplitude of each spectral peak correlated across the inlet plane or test section yields the acoustic field. For nearly plane far-field waves the pressure fluctuation is equal to ρa times the normal velocity fluctuations, where ρ and a are the local mean density and speed of sound, respectively. Few researchers recognize to what extent the low-frequency end of the velocity spectrum measured at the inlet of their test section is actually driven by near-field pressure fluctuations (also called pseudosound). From experience I would guess for instance that more than 50 percent of the very low-frequency contribution to the measured u'/U_e "sans grille" in the inset of figure 9 comes from such pressure fluctuations, which are given very nearly by $\rho U_e u'$. This is a linearized Bernoulli relation for u' fields correlated across the inlet plane. Since the low frequencies correspond to acoustic wavelengths that are far longer than the test section, the sources of the near-field pressure (usually random-like and broadband) can be quite distant. Some of these disturbances come from downstream, as, for example, the low-frequency part of the pressure feedback mentioned earlier (refs. 32 and 33). The role of relatively large, low-frequency pressure fluctuations in the transition process is not clear, but there is some indirect evidence that they contribute to receptivity, especially in the presence of small distributed roughness. They and the acoustic disturbances should be added to the top of figure 14 as additional receptivity paths. Their temporal irregularity evidently modulates the time development of whatever instabilities do arise, forcing random characteristics upon the primary and higher modes long before there is turbulence of the shear layer itself.

Ideally, after identifying the contributions from swirl, shock waves, wakes, and free vortices as well as from the acoustic and near-field fluctuations, we should be able to subtract them in the square from total fluctuation signals and to obtain the residual free-stream turbulences, provided that there

were no significant entropy fluctuations. If there is upstream cooling or combustion, additional probes for measurements of temperature fluctuations will be needed. Should the residual turbulent and entropy fluctuations turn out to be quite uniformly distributed over the inlet section, that would be an indication of the consistency of the decomposition process. When we include spectral and correlation characteristics relevant to the transition process, the number of free-stream parameters will generally exceed 5 and could run past 10 for more complex flows. Also there will be nonnegligible uncertainty concerning each parameter.

It should be fairly clear that after such ideally effective measurements we still would have difficulties relating the input parameters to the output measurements, even if we (still more ideally) could vary the free-stream parameters rather freely in our experiments. We need only to reflect on the lessons from the orders-of-magnitude simpler example of figure 9, where the low-Tu conditions induced an earlier transition. (A third condition with stronger grid-turbulence did not resolve the puzzle.)

REPRISE

From the preceding exercise it appears that a frontal approach to practical flow configurations is likely to run into severe difficulties in defining experimentally the requisite environmental parameters on one hand and in interpreting meaningfully the "output measurements" on the other. Yet, as in all research directed at specific applications, there will be strong pressures to look at the "real thing." A preacher is expected to evoke the path to righteousness, even when he is ignorant of "practical life." So perhaps I may be permitted to give my insufficiently informed views. My experimental bias would be to strive first to establish a qualitative framework of understanding by clarifying individually as many important mechanisms and interaction patterns as can be anticipated. As we have seen, key elements in the interactions are likely to be isolated wakes and vortices coming from different angles toward the leading edges (blunt, slender, and sharp). For strong disturbances the main action of interest should take place from just upstream of the leading edge to past Re_{min}, perhaps to Re_{cr}. Access, transversing of the velocity and thermal fields, and visibility (if possible) in these regions are important. Broadly speaking we could proceed in the spirit of figures 5 and 6 of Hodson and Nagib (ref. 14) to generalize their insight systematically to as many separate geometrical variants as the ingredients in practical configurations would suggest. Each conceptual experiment would have a small number of controlling parameters so that connections between cause and effect could be made with some confidence.

Such simplification and conceptualization is more likely to lead to improvements in codes and design: it more frequently inspires "cures" should particularly detrimental conditions be identified (such as local separation). It was such a simplified wind tunnel test that identified and developed a cure for the dangerous bypass on sweptback aircraft (turbulence contamination from the fuselage juncture to the attachment layer on the leading edge of the wing (ref. 34) - see the section Flows with Known $Re_{\theta,min}$ and Re_{cr}). "Practical" flight tests had failed to improve the poor performance. We note that the experiments of Dyban et al. (refs. 22 and 28) are also simplified in that they strove to make the large turbulence homogeneous and nearly isotropic, so that the relevant parameters were reduced to Tu and the velocity spectrum. (In any recheck of their results attention to the role of the leading edge would

be desirable: measurements just upstream and just downstream, with at least one variant from their sharp edge, to clarify the restructuring of the field and possible local separation in the presence of the large fluctuation normal to the edge.)

From the simpler experiments we could proceed to compound problems, such as combination of wakes approaching bodies with increased free-stream turbulence (homogeneous Tu outside the wakes) to assess the effects of "superposition." The compounding would of course aim at approximating progressively the suspected structure of the environment in key practical configurations. The problem of the "scrubbing" heat transfer at junctures and hubs of blades, where boundary layers (with local separation) on two walls interact, can be approached in a similar conceptual manner. Any time there is a mean velocity component along the leading edge of a blade, a counterpart of the strong contamination bypass encountered on sweptback wings (ref. 34) becomes a potential danger. (Away from the attachment line lateral contamination influences a substantially smaller domain, limited by the spreading angle of the order of 10° from the local potential streamline at the edge of the boundary layer.)

As we commented in connection with the visualization figures, to start with low Reynolds numbers has many experimental and conceptual advantages, in particular space-time resolution and visibility. In experiments at the prototype Reynolds numbers with large disturbances, the transition phenomena that we seek to understand will occur at low Reynolds numbers based on the distance from the leading edge, anyway, but on spatial and temporal scales that are much harder to resolve. I think I am beginning to repeat myself and the obvious as well. In fact, many of the attitudes I am preaching are evident in the papers on NASA Lewis research in progress, in particular those of Jim VanFossen and Barbara Brigham. So I can quit preaching with the sense that the flock knows the way to the Promised Land. Nevertheless, let me remind you in parting to heed the wisdom of the four guidelines for transition research on page 345 of Eli Resotko's review (ref. 23).

REFERENCES

1. Peterson, J.B.; and Horton, E.A.: An Investigation of the Effects of a Highly Favorable Pressure Gradient on Boundary-Layer Transition as Caused by Various Types of Roughnessess on a 10-Foot-Diameter Hemisphere at Subsonic Speeds. NASA Memo 2-8-59L, 1959.

2. Murphy, J.D.; and Rubesin M.W.: A Re-Evaluation of Heat Transfer Data Obtained in Flight Tests of Heat-Sink Shielded Re-Entry Vehicles, J. Spacecraft and Rockets, vol. 3, 1966, p. 53.

3. Morkovin, M.W.: Critical Evaluation of Transition from Laminar to Turbulent Shear Layers with Emphasis on Hypersonically Traveling Bodies. AFFDL TR-68-149, 1969.

4. Schubauer, G.B.; and Klebanoff P.S.: Contributions on the Mechanics of Boundary Layer Transition. NACA Tech. Rept. 1289, 1956.

5. Klebanoff, P.S.; Schubauer, G.B.; and Tidstrom, K.D.: Measurements of the Effect of Two-Dimensional and Three-Dimensional Roughness Elements on Boundary-Layer Transition, J. Aero. Sci., vol. 22, 1955, pp. 803-804.

6. Wygnanski, I.J.; and Champagne F.H.: On Transition in a Pipe. Part 1. The Origin of Puffs and Slugs and the Flow in a Turbulent Slug, J. Fluid Mech., vol. 59, No. 2, 1973, pp. 281-335.

7. Carlson, D.R.; Widnall, S.E.; and Peeters, M.T.: A Flow-Visualization Study of Transition in Place Poiseville Flow, J. Fluid. Mech., vol. 121, 1982, pp. 487-505.

8. Poll, P.J.A.: Transition in the Infinite Swept Attachment Line Boundary Layer, Aero. Quart, vol. 30, 1979, pp. 607-629.

9. Hall, P.; Malik, M.R.; and Poll, D.I.A.: On the Stability of an Infinite Swept Attachment Line Boundary Layer, Proc. Roy. Soc. London A, vol. 395, 1984, pp. 229-245.

10. Preston, J.H.: The Minimum Reynolds Number for a Turbulent Boundary Layer and the Selection of a Transition Device, J. Fluid. Mech., vol. 3, 1958, pp. 373-384. (To be modified in accordance with p. 1418 of D. Coles in Phys. Fluids, vol. 7, pp. 1403-1423.)

11. Herbert, Th.: Secondary Instability of Shear Flow. Nonlinear Effects in Hydrodynamic Stability, Sections 7 and 6 in the Special Course on Stability and Transition of Laminar FLow. AGARD Rept. 709, NATO, Paris, 1984. (Available through National Technical Infomation Services, 5285 Port Royal Road, Springfield, VA 22161.)

12. Gregory, N.; and Walker, W.S.: The Effects of Transition of Isolated Surface Excrescences in the Boundary Layer. British ARC, Res. Memo. 2779, 1956.

13. Norman, R.S.: On Obstacle Generated Secondary Flows in Laminar Boundary Layers and Transition to Turbulence. Ph.D. Thesis, Ill. Inst. Tech., 1972. (Available from University Microfilms International, 300 N. Zeeb Rd., Ann Arbor, MI 48106.)

14. Hodson, P.R.; and Nagib, H.M.: Longitudinal Vortices Induced in a Stagnation Region by Wakes - Their Incipient Formation and Effects on Heat Transfer from Cylinders. NASA CR-152850, 1975. (Condensed in Progress in Astronautics and Aeronautics, vol. 59, 1977, pp. 66-90.)

15. Morkovin, M.V.: On the Question of Instabilities Upstream of Cylindrical Bodies. NASA CR-3231, 1979.

16. Kendall, J.M.: Experiments on the Generation of Tollmien-Schlichting Waves in a Flat-Plate Boundary Layer by Weak Free-Stream Disturbances. AIAA Paper 84-0111, 1984.

17. Anders, J.B.; and Blackwelder, R.F.: Longitudinal Vortices in a Transitioning Boundary Layer, in Laminar - Turbulent Transition, Eppler, R. and Fasel, H., eds., Springer Verlag, 1980, pp. 110-119.

18. Arnal, D.; and Juillen, J.C.: Experimental Contribution to the Study of Receptivity to Turbulence of a Laminar Boundary Layer (in French). ONERA, CERT, DERA Rpt. 1/5018 DY, 31055 Toulouse, 1978.

19. Nishioka, M.; and Morkovin, M.V.: Boundary-Layer Receptivity to Unsteady Pressure Gradients: Experiments and Overview 1984. (Submitted to J. Fluid Mech.)

20. Townsend, A.A.: The Structure of Turbulent Shear Flow, Cambridge Univ. Press, 1976, pp. 71-88.

21. Bushnell, D.M.: Body-Turbulence Interaction, AIAA Paper 84-1527, 1984. (Presented at 17th Fluid Dynamics and Plasmadynamics Conference, Snowmass, CO, June 1984.)

22. Dyban, Ye.P.; Epik, E.Ya.; and Suprun, T.T.: Characteristics of the Laminar Boundary Layer in the Presence of Elevated Free-Stream Turbulence. Fluid Mechanics - Soviet Research, vol. 5, no. 4, 1976, pp. 30-36.

23. Reshotko, E.: Boundary-Layer Stability and Transition. Annual Reviews of Fluid Mechanics, vol. 8, 1976, pp. 311-350 (especially p. 345), Annual Reviews, Palo Alto, CA, 94306.

24. Morkovin, M.V.: Instability, Transition to Turbulence, and Predictability. Keynote address at AGARD Copenhagen Symposium, May 1977. AGARDograph 236, NATO, 1978. (Available through National Technical Information Services, 5285 Port Royal Road, Springfield, VA, 22161.)

25. Mack, L.M.: Remarks on Disputed Numerical Results in Compressible Boundary-Layer Stability Theory, Phys. Fluids, vol. 27, 1984, pp. 342-347.

26. Kiock, R.; Laskowski, G.; and Hoheisel, H.: The Generation of Higher Levels of Turbulence in the Test Section of the High-Speed Cascade Wind Tunnel at Braunschweig for Simulation of Turbomachinery Conditions (in German). DFVLR-Forschungsbericht, 1982, 54 pages.

27. Loehrke, R.I.; and Nagib, H.M.: Experiments on Management on Free-Stream Turbulence, AGARD Rept. 598, NATO, 1972. (Available through National Technical Information Services, 5285 Port Royal Road, Springfield, VA, 22161, as AGARD Rept. or as AD749891.)

28. Dyban, E.P.; and Epik, E.Ya.: Heat Transfer in a Boundary Layer in a Turbulized Air Flow, Vol. 2, Proceedings Sixth International Heat Transfer Conference, Toronto, Canada, Aug. 1978, pp. 507-512.

29. Gates, E.M.: Observations of Transition on Some Axisymmetric Bodies, Laminar-Turbulent Transition, Eppler, R. and Fasel, H., eds., Springer Verlag, 1980, pp. 351-363.

30. Bradshaw, P.: Effects of Streamline Curvature on Turbulent Flow, AGARDograph 169, AGARD, NATO, 1973. (Available through NTIS.)

31. Inger, G.: Three-Dimensional Heat and Mass Transfer Effects Across High-Speed Reattachment Flows, AIAA J., vol. 15, 1977, pp. 383-389.

32. Wills, J.A.B.: Spurious Pressure Fluctuations in Wind Tunnels. J. Acoust. Soc. A., vol. 43, no. 5, May 1968, pp. 1049-1054.

33. Dimotakis, P.E.; and Brown, G.L.: The Mixing Layer at High Reynolds Number: Large-Structure Dynamics and Entrainment. J. Fluid Mech., vol. 78, 1976, pp. 535-560.

34. Gaster, M.: A Simple Device for Preventing Contamination on Swept Leading Edges, J. Roy. Aero, Soc., vol. 69, 1965, p. 788.

BIBLIOGRAPHY

1. Liebert, C.H.; Gaugler, R.E.; and Gladden, H.J.: Measured and Calculated Wall Temperatures on Air-Cooled Turbine Vanes with Boundary Layer Transition. ASME Paper 83-GT-33, 1983.

2. Dillon, R.E.; Watervliet, N.Y.; and Nagamatsu, H.T.: Heat Transfer Rate for Laminar, Transition, and Turbulent Boundary Layer and Transition Phenomenon on Shock Tube Wall. AIAA Paper 82-0032, Jan. 1982.

3. Liepmann, H.W.; and Nosenchuck, D.M.: Active Control of Laminar-Turbulent Transition. J. Fluid Mech., vol. 118, May 1982, pp. 201-204.

4. Priddy, W.J.; and Bayley, F.J.: Heat Transfer to Turbine Blading. Heat and Mass Transfer in Rotating Machinery, D.E. Metzger and N.H. Afgan, eds., Hemisphere Pub. Co., Washington, 1984, pp. 427-438.

5. Wazzan, A.R.; and Taghavi, H.: The Effect of Heat Transfer of Three-Dimensional Spacial Stability and Transition of Flat-Plate Boundary Layer at Mach 3. Int. J. Heat Mass Transfer, vol. 25, no. 9, Sept. 1982, pp. 1321-1331.

6. Brown, A.; and Martin B.W.: Flow Transition Phenomena and Heat Transfer Over the Pressure Surfaces of Gas Turbine Blades. ASME Paper 81-GT-107, Mar. 1981.

7. Daniels, L.D.; and Browne, W.B.: Calculation of Heat Transfer Rates to Gas Turbine Blades. Int. J. Heat Mass Transfer, vol. 24, no. 5, May 1981, pp. 871-879.

8. Tani, I.: Three-Dimensional Aspects of Boundary Layer Transition. Proc. - Indian Acad. Sci., Eng. Sci., vol. 4, Aug. 1981, pp. 219-235, 237, 238.

9. Abu-Ghannam, B.J.; and Shaw, R.: Natural Transition of Boundary Layers - The Effects of Turbulence, Pressure Gradient and Flow History. J. Mech. Eng. Sci., vol. 22, no. 5, Oct. 1980, pp. 213-228.

10. Martin, B.W.; and Brown, A.: Factors Influencing Heat Transfer to the Pressure Surfaces of Gas Turbine Blades. Int. J. Heat Fluid Flow, vol. 1, no. 3, 1979, pp. 107-114.

11. Bippes, H.: Experimental Study of the Laminar-Turbulent Transition of a Concave Wall in a Parallel Flow. NASA TM-75243, 1978.

12. Cebeci, T.; and Brawshaw, P.: Momentum Transfer in Boundary Layers, Hemisphere, 1977.

13. Forest, A.E.: Engineering Predictions of Transitional Boundary Layers. Laminar-Turbulent Transition. AGARD CP-224, 1977, pp. 22-1 to 22-19.

14. Mack, L.M.: Transition Prediction and Linear Stability Theory. Laminar-Turbulent Transition. AGARD CP-224, 1977, pp. 1-1 to 1-22.

15. Reshotko, E.: Boundary Layer Stability and Transition. Annual Review of Fluid Mechanics, Vol. 8, 1976, pp. 311-350.

16. Bushnell, D.M.; Cary, A.M. Jr.; and Holley, B.B.: Mixing Length in Low Reynolds Number Compressible Turbulent Boundary Layers. AIAA J., vol. 13, no. 8, Aug. 1975, pp. 1119-1121.

17. Kaups, K.: Transition Prediction on Bodies of Revolution. MDC-J6530, Douglas Aircraft Co., 1975. (AD-778045.)

18. Merkli, P.; and Thomann, H.: Transition to Turbulence in Oscillating Pipe Flow. J. Fluid Mech., vol. 68, part 3, Apr. 15, 1975, pp. 567-576.

19. Reshotko, Eli: A Program for Transition Research. AIAA J., vol. 13, no. 3, Mar. 1975, pp. 261-265.

20. Cebeci, T.; and Smith, A.M.O.: Analysis of Turbulent Boundary Layers. Academic Press, 1974.

21. McDonald, H.; and Fish, R.W.: Practical Calculations of Transitional Boundary Layers. Int. J. Heat Mass Transfer, vol. 16, no. 9, Sept. 1973, pp. 1729-1744.

22. Dunham, J.: Predictions of Boundary Layer Transition on Turbomachinery Blades. Boundary Layer Effects in Turbomachines. AGARD AG-164, 1972, pp. 55-71.

23. Hall, D.J.; and Gibbings, J.C.: Influence of Stream Turbulence and Pressure Gradient upon Boundary Layer Transition. J. Mech. Eng. Sci., vol. 14, no. 2, Apr. 1972, pp. 134-146.

24. Kobayashi, Ryoji: A Note on the Stability of a Boundary Layer on a Concave Wall with Suction. J. Fluid Mech., vol. 52, part 2, Mar. 28, 1972, pp. 269-272.

25. Seyb, N.J.: The Role of Boundary Layers in Axial Flow Turbomachines and the Predictions of Their Effects. Boundary Layer Effects in Turbomachines. AGARD AG-164, 1972, pp. 241-259.

26. Cebeci, Tuncer: Wall Curvature and Transition, Effects in Turbulent Boundary Layers. AIAA J., vol. 9, no. 9, Sept. 1971, pp. 1868-1870.

27. Turner, A.B.: Local Heat Transfer Measurements on a Gas Turbine Blade. J. Mech. Eng. Sci., vol. 13, no. 1, Feb. 1971, pp. 1-12.

28. Jaffe, N.A.; Okamura, T.T.; and Smith, A.M.O.: Determination of Spatial Amplification Factors and Their Application to Predicting Transition. AIAA J., vol. 8, no. 2, Feb. 1970, pp. 301-308.

29. Radbill, J.R.; and McCue, G.A.: Quasilinearization and Nonlinear Problems in Fluid and Orbital Mechanics. American Elsevier, New York, 1970.

30. Donaldson, Coleman du P.: A Computer Study of an Analytical Model of Boundary-Layer Transition. AIAA J., vol. 7, no. 2, Feb. 1969, pp. 271-278.

31. Tani, I.: Boundary Layer Transition. Annual Review of Fluid Mechanics, Vol. 1, W.R. Sears, ed., Annual Reviews Inc., 1969, pp. 169-196.

32. Knapp, C.F.; and Roache, P.J.: A Combined Visual and Hot-Wire Anemometer Investigation of Boundary Layer Transition. AIAA J., vol. 6, no. 1, Jan. 1968, pp. 29-36.

33. Schlichting, Hermann: The Origin of Turbulence. Boundary Layer Theory, 6th ed., McGraw-Hill, 1968.

34. Spangler, J.G.; and Wells, C.S.: The Effects of Free Stream Disturbances on Boundary Layer Transition. AIAA J., vol. 6, no. 3, Mar. 1968, pp. 543-545.

35. Obremski, H.J.; and Fejer, A.A.: Transition in Oscillating Boundary Layer Flows. J. Fluid Mech., vol. 29, part 1, July 18, 1967, pp. 93-111.

36. Squire, H.B.; and Johnston, W.D.: Measurements of Waviness of Wing Surfaces in Relation to Boundary Layer Transition. BR67826, Royal Aircraft Establishment, 1941.

37. Wells, C. Sinclair, Jr.: Effects of Free Stream Turbulence on Boundary Layer Transition. AIAA J., vol. 5, no. 1, Jan. 1967, pp. 172-174.

38. Bradshaw, P.: The Effect of Wind-Tunnel Screens on Nominally Two-Dimensional Boundary Layers. J. Fluid Mech., vol. 22, part 4, Aug. 1965, pp. 679-687.

39. Coles, Donald: Transition on Circular Couette Flow. J. Fluid Mech., vol. 21, part 3, Mar. 1965, pp. 386-425.

40. Goldstein, S.: Modern Developments in Fluid Dynamics. Dover, New York, 1965.

41. Van Driest, E.R.; and Blumer, C.B.: Boundary Layer Transition: Free-Stream Turbulence and Pressure Gradient Effects. AIAA J., vol. 1, no. 6, June 1963, pp. 1303-1306.

42. Rosenhead, L.: Laminar Boundary Layers. Clarendon Press, Oxford, 1963.

43. Coles, D.: Turbulent Boundary Layer in a Compressible Fluid. R-403-PR, Rand Corp., 1962, Appendix A.

44. Klebanoff, P.S.; Tidstrom, K.D.; and Sargent, L.M.: The Three-Dimensional Nature of Boundary-Layer Instability. J. Fluid Mech., vol. 12, part 1, Jan. 1962, pp. 1-34.

45. Lees, Lester; and Reshotko, Eli: Stability of the Compressible Laminar Boundary Layer. J. Fluid Mech., vol. 12, part 4, Apr. 1962, pp. 555-590.

46. Lin. C.C.; and Benny, D.J.: On the Instability of Shear Flows and Their Transition to Turbulence. Applied Mechanics, Proceedings of the 11th International Congress on Applied Mechanics, Henry Gortler, ed., Springer-Verlag, Berlin, 1966, pp. 797-802.

47. Tani, I.: Some Aspects of Boundary Layer Transition at Subsonic Speeds. Advances in Aeronautical Sciences, Vol. 3, Pergamon Press, New York, London, 1962, pp. 143-160.

48. Benney, D.J.; and Lin, C.C.: On the Secondary Motion Induced by Oscillation in a Shear Flow. Phys. Fluids, vol. 3, no. 4, July-Aug. 1960, pp. 656-657.

49. Elder, J.W.: An Experimental Investigation of Turbulent Spots and Breakdown to Turbulence. J. Fluid Mech., vol. 9, part 2, Oct. 1960, pp. 235-246.

50. Gibbings, J.C.: Aeronautical Research Council Current Paper 462, 1959.

51. Bergh, H.: A Method for Visualizing Periodic Boundary Layer Phenomena. Boundary Layer Research, H. Gortler, ed., Springer-Verlag, Berlin, 1958, pp. 173-178.

52. Dhawan, S.; and Narasimha, R.: Some Properties of Boundary Layer Flow During the Transition from Laminar to Turbulent Motion. J. Fluid Mech., vol. 3, no. 4, Jan. 1958, pp. 418-440.

53. Morkovin, M.V.: Transition from Laminar to Turbulent Shear Flow - A Review of Some Recent Advances in Its Understanding. Trans. ASME, vol. 80, July 1958, pp. 1121-1128.

54. Schubauer, G.B.; and Klebanoff, P.S.: Mechanism of Transition at Subsonic Speeds. Boundary Layer Research, H. Gortler, ed., Berlin, 1958, pp. 84-107.

55. Lin, C.C.: The Theory of Hydrodynamic Stability. Cambridge Univ. Press, 1955.

56. Schubauer, G.B.; and Klebanoff, P.S.: Contributions on the Mechanics of Boundary Layer Transition. NACA TN-3489, 1955.

57. Jedlicka, James R.; Wilkins, Max E.; and Seiff, Alvin: Experimental Determination of Boundary-Layer Transition on a Body of Revolution at M = 3.5. NACA TN-3342, 1954.

58. Stuart, J.T.: On the Stability of Viscous Flow Between Parallel Planes in the Presence of a Co-planar Magnetic Field. Proc. Roy. Soc., London, A, vol. 221, no. 1145, Jan. 21, 1954, pp. 189-206.

59. Granville, P.S.: The Calculations of Viscous Drag of Bodies of Revolution. Navy Dept., The David Taylor Model Basin, Report 849, 1953.

60. Emmons, H.W.: The Laminar-Turbulent Transition in a Boundary Layer - Part I. J. Aeronaut. Sci., vol. 18, no. 7, July 1951, pp. 490-498.

61. Prandtl, L.: Essentials of Fluid Dynamics. Hafner, New York, 1952.

62. Eckert, E.R.G.: Interferometric Studies on the Stability and Transition to Turbulence of a Free-Convection Boundary Layer. Proceedings of the General Discussion on Heat Transfer, Inst. Mech. Eng., London, 1951.

63. Goertler, N.: The Effect on Transition of Isolated Surface Excrescences in the Boundary Layer. R. & M. No. 2779, British A.R.C., 1951.

64. Eckert, Ernst R.G.: Interferometric Studies of Beginning Turbulence in Free and Forced Convection Boundary Layers on a Heated Plate. Heat Transfer and Fluid Mechanics Institute, ASME, 1949, pp. 181-190.

65. Dryden, Hugh L.: Recent Advances in the Mechanics of Boundary Layer FLow. Advances in Applied Mechanics, Vol. 1, Richard von Mises and Theodore Von Karman, eds., Academic Press, New York, 1948, pp. 1-40.

66. Liepmann, Hans W.; and Fila, Gertrude H.: Investigations of Effect of Surface Temperature and Single Roughness Elements on Boundary Layer Transition. NACA TN-1196, 1947.

67. Schubauer, G.B.; and Skramstad, H.K.: Laminar-Boundary-Layer Oscillations and Stability of Laminar Flow. J. Aeronaut. Sci., vol. 14, no. 2, Feb. 1947, pp. 69-78.

68. Liepmann, H.W.: Investigation of Boundary Layer Transition on Concave Walls. NACA Wartime Report W-87, 1945.

69. Liepmann, Hans W.: Investigations on Laminar Boundary-Layer Stability and Transition on Curved Boundaries. NACA Wartime Report W-107, 1943.

70. Dryden, Hugh L.: Turbulence and the Boundary Layer. J. Aeronaut. Sci., vol. 6, no. 3, Jan. 1939, pp. 85-105.

71. Goldstein, S.: On the Stability of Superposed Streams of Fluids of Different Densities. Proc. Roy. Soc., London, A, vol. 132, no. 820, Aug. 1, 1939, pp. 524-547.

72. Hall, A.A.; and Hislop, G.S.: Experiments on the Transition of the Laminar Boundary Layer on a Flat Plate. R. & M. No. 1843, British A.R.C., 1938.

73. Clauser, Milton; and Clauser, Francis: The Effects of Curvature on Transition from Laminar to Turbulent Boundary Layer. NASA TM-79878, 1937.

74. Dryden, Hugh L.: Air Flow in the Boundary Layer Near a Plate. NACA Report 562, 1936.

75. Dryden, H.L.: Boundary Layer Flow near Flat Plates. Proceedings, Fourth International Congress for Applied Mechanics, Cambridge, England, 1934, p. 175.

76. Von Karman, T.: Some Aspects of the Turbulence Problem. Proceedings, Fourth International Congress for Applied Mechanics, Cambridge, England, 1934, p. 54.

77. Taylor, G.I.: Internal Waves and Turbulence in a Fluid of Variable Density. Rapp. Proc. Verb. Cons. Internat. pour l-Exploration de la Mer. LXXVI Copenhagen, 1931, pp. 35-42.

78. Taylor, G.I.: Effects of Variation in Density on the Stability of Superposed Streams of Fluid. Proc. Roy. Soc., London, A, vol. 132, no. 820, Aug. 1, 1931, pp. 499-523.

79. Burgers, J.M.: The Motion of a Fluid in the Boundary Layer along a Plane Smooth Surface. Proceedings, First International Congress for Applied Mechanics, Delft, 1924, p. 113.

80. Rayleigh, Lord: On the Stability of Certain Fluid Motions. Proc. London Math. Soc. 11, 57 (1880) and 19, 67 (1881); Scientific Papers I, 474-487; III, 17: IV, 203 (1895); and VI, 97 (1913).

81. Klebanoff, P.S.; and Tidstrom, K.D.: Evolution of Amplified Waves Leading to Transition in a Boundary Layer with Zero Pressure Gradient. NASA TN D-195, 1959.

82. Crabtree, L.F.: Prediction of Natural Transition in the Boundary Layer on an Aerofoil. J.R. Aeronaut. Soc., vol. 62, no. 571, July 1958, pp. 525-528.

83. Preston, E.J.: Prediction of Transition in the Boundary Layer on an Aerofoil. J.R. Aeronaut. Soc., vol. 62, no. 576, Dec. 1958, p. 901.

84. Smith, A.M.O.; and Giamberoni, N.: Transition, Pressure Gradient and Stability Theory. Proc. Ninth Int. Congr. Appl. Mech., Wiley, 1956.

85. Van Ingen, J.L.: A Suggested Semi-empirical Method for the Calculation of the Boundary Layer Transition Region. Report Nos. V.T.H. 71 and V.T.H. 74, Delft, Holland, 1956.

86. Fage, A.; and Preston J.H.: On Transition from Laminar to Turbulent Flow in the Boundary Layer. Proc. R. Soc., London, A., vol. 178, no. 973, June 12, 1941, pp. 201-227.

87. Dyban, Ye. P.; Epik, E. Ya.; and Suprun, T.T.: Characteristics of the Laminar Boundary Layer in the Presence of Elevated Free-Stream Turbulence. Fluid Mech. - Sov. Res., vol. 5, no. 4, July-Aug. 1976, pp. 30-36.

88. Blair, M.F.: Influence of Free-Stream Turbulence on Boundary Layer Transition in Favorable Pressure Gradients. J. Eng. Power, vol. 104, no. 4, Oct. 1982, pp. 743-750.

89. Blair, M.F.: Influence of Free-Stream Turbulence on Turbulent Boundary Layer Heat Transfer and Mean Profile Development, Part I - Experimental Data, Part II - Analysis of Results. J. Heat Transfer, vol. 105, no. 1, Feb. 1983, pp. 33-47.

90. Kachanov, Yu. S.; and Levchenko, V. Ya.: The Resonant Interaction of Disturbance at Laminar-Turbulent Transition in a Boundary Layer. J. Fluid Mech., vol. 138, Jan. 1984, pp. 209-247.

91. Simon, T.W.; and Moffat, R.J.: Turbulent Boundary Layer Heat Transfer Experiments: A Separate Effects Study on a Convexly Curved Wall. J. Heat Transfer, vol. 105, no. 4, Nov. 1983, pp. 835-840.

92. Chen, Karl, K.; and Thyson, Noel A.: Extension of Emmon's Spot Theory to Flows on Blunt Bodies. AIAA J., vol. 9, no. 5, May 1971, pp. 821-825.

93. Brown, A.; and Burton R.C.: The Effects of Free-Stream Turbulence Intensity and Velocity Distribution on Heat Transfer to Curved Surfaces. ASME Paper 77-GT-48, 1977.

94. Hylton, L.D., et al.: Analytical and Experimental Evaluation of the Heat Transfer Distribution over the Surfaces of Turbine Vanes. (EDR-11209, Detroit Diesel Allison; NASA Contract NAS3-22761.) NASA CR-168015, 1983.

95. Daniels, L.D.; and Browne, W.B.: Calculation of Heat Transfer Rates to Gas Turbine Blades. Int. J. Heat Mass Transfer, vol. 24, no. 5, May 1981, pp. 871-879.

96. Reshotko, Eli: Stability Theory as a Guide to the Evaluation of Transition Data. AIAA J., vol. 7, no. 6, June 1969, pp. 1086-1091.

97. Narasimha, Roddam: On the Distribution of Intermittency in the Transition Region of a Boundary Layer. J. Aeronaut. Sci., vol. 24, no. 9, Sept. 1957, pp. 711-712.

98. Higgins, W. Robert; and Pappas, Constantine C.: An Experimental Investigation of the Effect of Surface Heating on Boundary Layer Transition on a Flat Plate in Supersonic Flow. NACA TN-2351, 1951.

99. Van Driest, E.R.; and Boison, J. Christopher: Experiments in Boundary Layer Transition at Supersonic Speeds. J. Aeronaut. Sci., vol. 24, no. 12, Dec. 1957, pp. 885-899.

100. Mack, L.M.: Notes on the Theory of Instability and Incompressible and Compressible Laminar Boundary Layers. Von Karman Institute for Fluid Dynamics, Brussels, Belgium, 1968.

101. Markovin, M.V.: Critical Evaluation of Transition from Laminar to Turbulent Shear Layers with Emphasis on Hypersonically Traveling Bodies. AFFDL TR-68-149, Martin Marietta Corp., 1983. (AD-686178.)

102. Keltner, G.: Spatial Stability and Transition in Compressible Flat Plate Flows. Ph.D. Thesis, UCLA, 1973.

103. Taghavi, H.: Three-Dimensional Spatial Stability and Transition of Compressible Boundary Layer Flows. Ph.D. Thesis, UCLA, 1977.

104. Deem, R.E.; and Murphy, J.S.: Flat Plate Boundary Layer Transition at Hypersonic Speeds. AIAA Paper 65-128, 1965.

105. Richards, B.E.; and Stollery, J.L.: Transition Reversal on a Flat Plate at Hypersonic Speeds. Recent Developments in Boundary Layer Research, AGARDograph 97, 1965.

106. Shutz, N.W.: Free-Flight Boundary Layer Transition Investigations at Hypersonic Speeds. AIAA Paper 65-127, 1965.

107. Mack, L.M.: On the Application of Linear Stability Theory to the Problem of Supersonic Boundary-Layer Transition. AIAA Paper 74-134, 1974.

108. Dunn, D.W.; and Lin, C.C.: On the Stability of the Laminar Boundary Layer in a Compressible Fluid. J. Aeronaut. Sci., vol. 22, no. 7, July 1955, pp. 455-477.

109. Wazzan, A.R.; and Taghavi, H.: The Effect of Heat Transfer on Three-Dimensional Spatial Stability and Transition of Flat Plate Boundary Layer at Mach 3. Int. J. Heat Mass Transfer, vol. 25, no. 9, Sept. 1982, pp. 1321-1331.

110. Eppler, R.; and Fasel, H.: Laminar-Turbulent Transition. Springer-Verlag, Berlin, 1980.

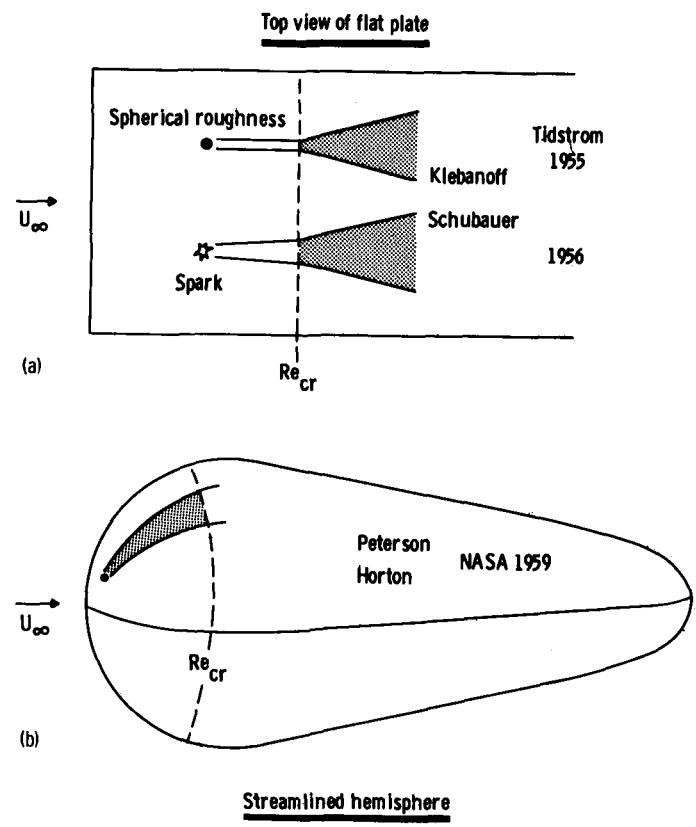

(a) Blasius boundary layer.
(b) Accelerating boundary layer.

Figure 1. - Growth of turbulent wedges in relation to critical Reynolds number Re_{cr} for growth of infinitesimal disturbances in a Blasius and an accelerating boundary layer.

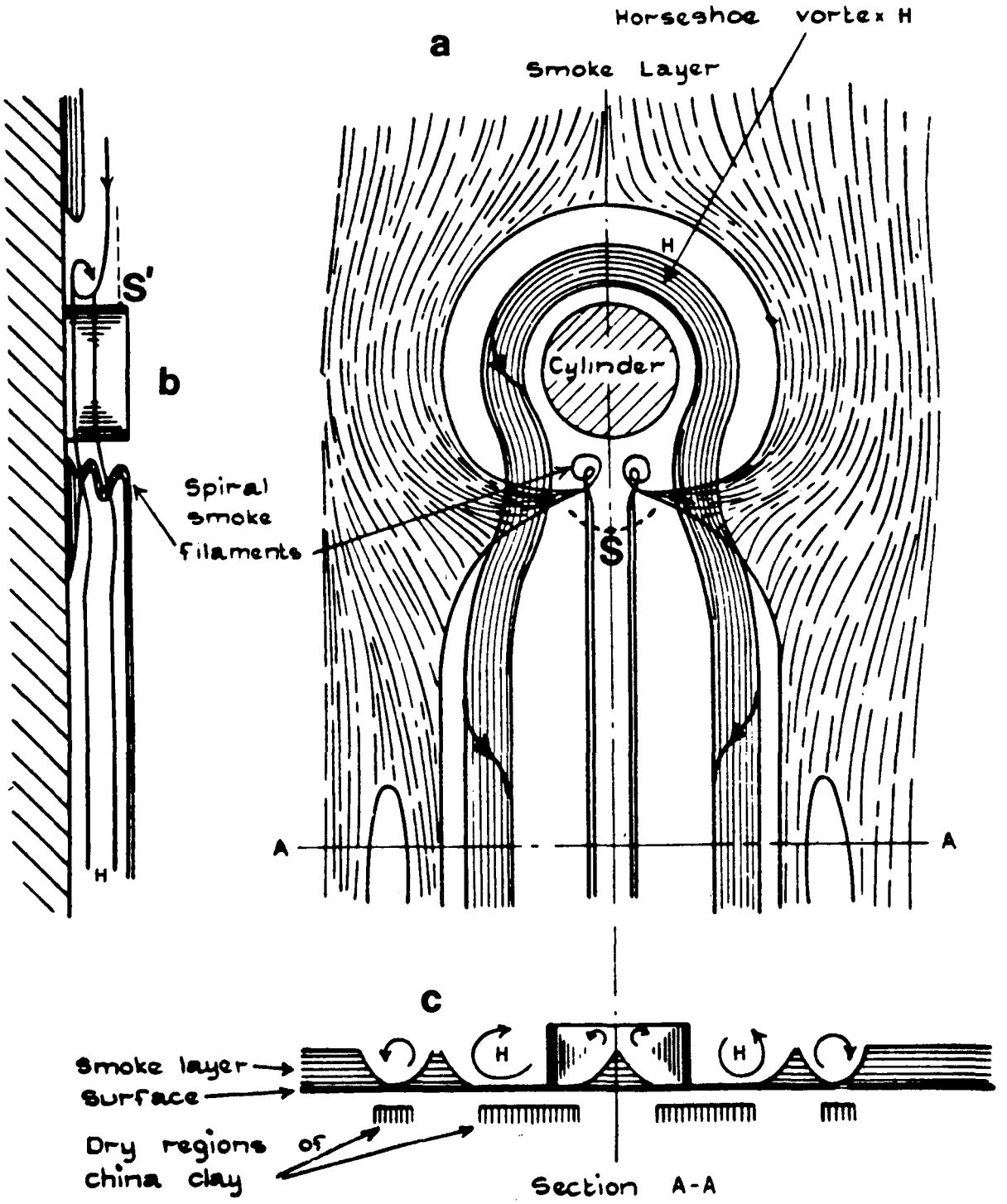

(a) Top view. (b) Side view. (c) Rear view.

Figure 2. - Schematic of features in second steady stage of flows around cylindrical protuberances, as visualized by Gregory and Walker (ref. 12).

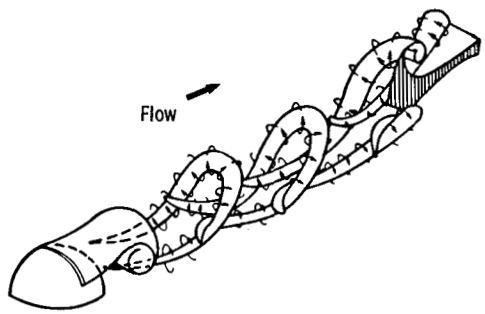

Figure 3. - Schematic of periodic hairpin-vortex formation downstream of hemisphere protuberance, as visualized by C.R. Smith for Re_k in range 450 to 550. At the wake edges these vortices interact with the two arms of a counterrotating horseshoe vortex wrapped around the front of the hemisphere (not shown).

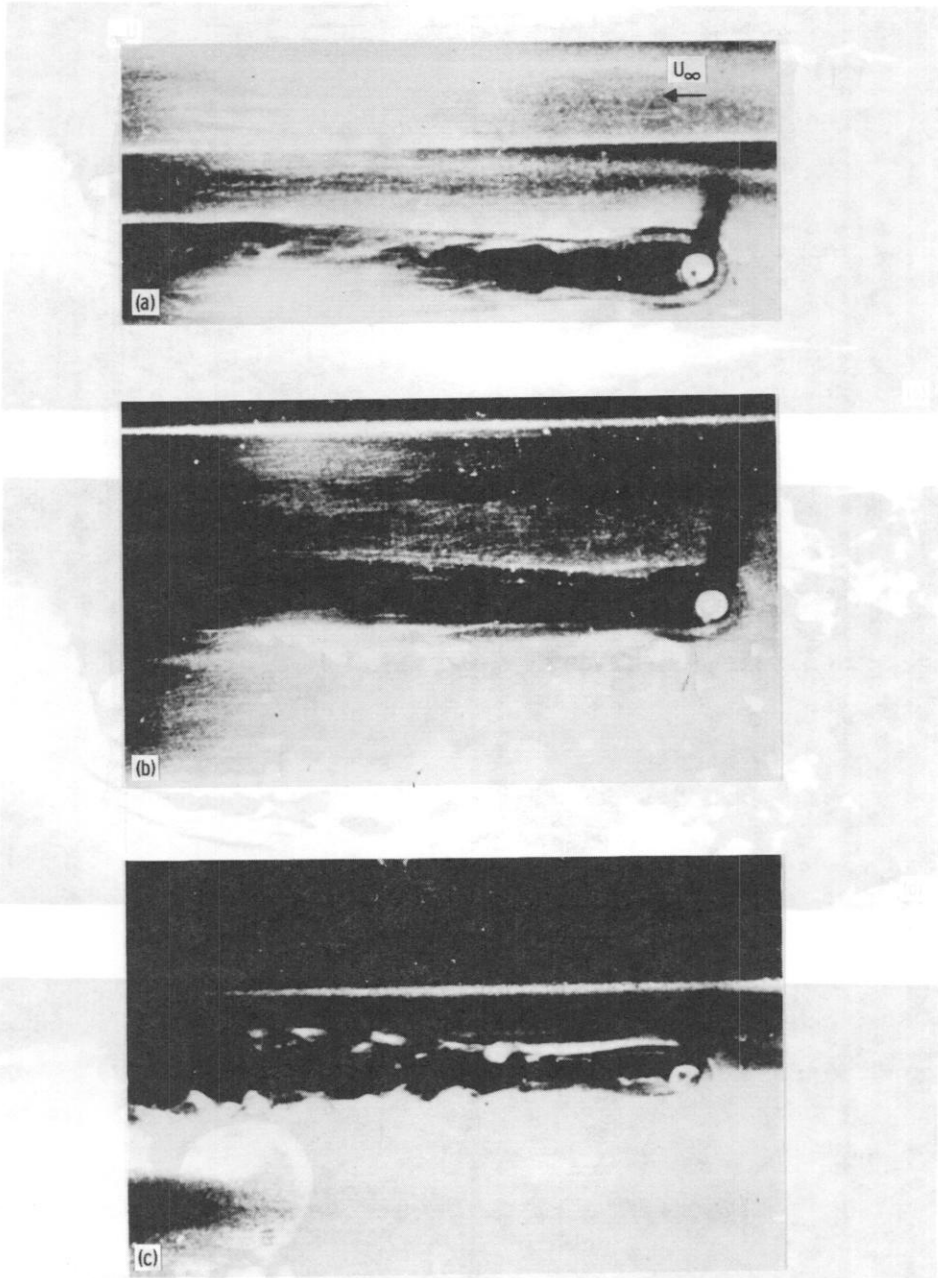

(a) Laminar wake: U_∞ = 7 ft/sec; k = 0.188 in; δ = 0.3 in; Re_k = 610.
(b) Periodic disturbances: U_∞ = 9.5 ft/sec; k = 0.188 in; ∂ = 0.25 in; Re_k = 890.
(c) Turbulent wedge forming near cylinder: U_∞ = 18.3 ft/sec; k = 0.188 in; δ = 0.18 in; Re_k = 1800.

Figure 4. - Smoke visualization of vorticity rearrangement at fixed cylinder that protrudes into thinning boundary layer as external speed increases. (From ref. 13.)

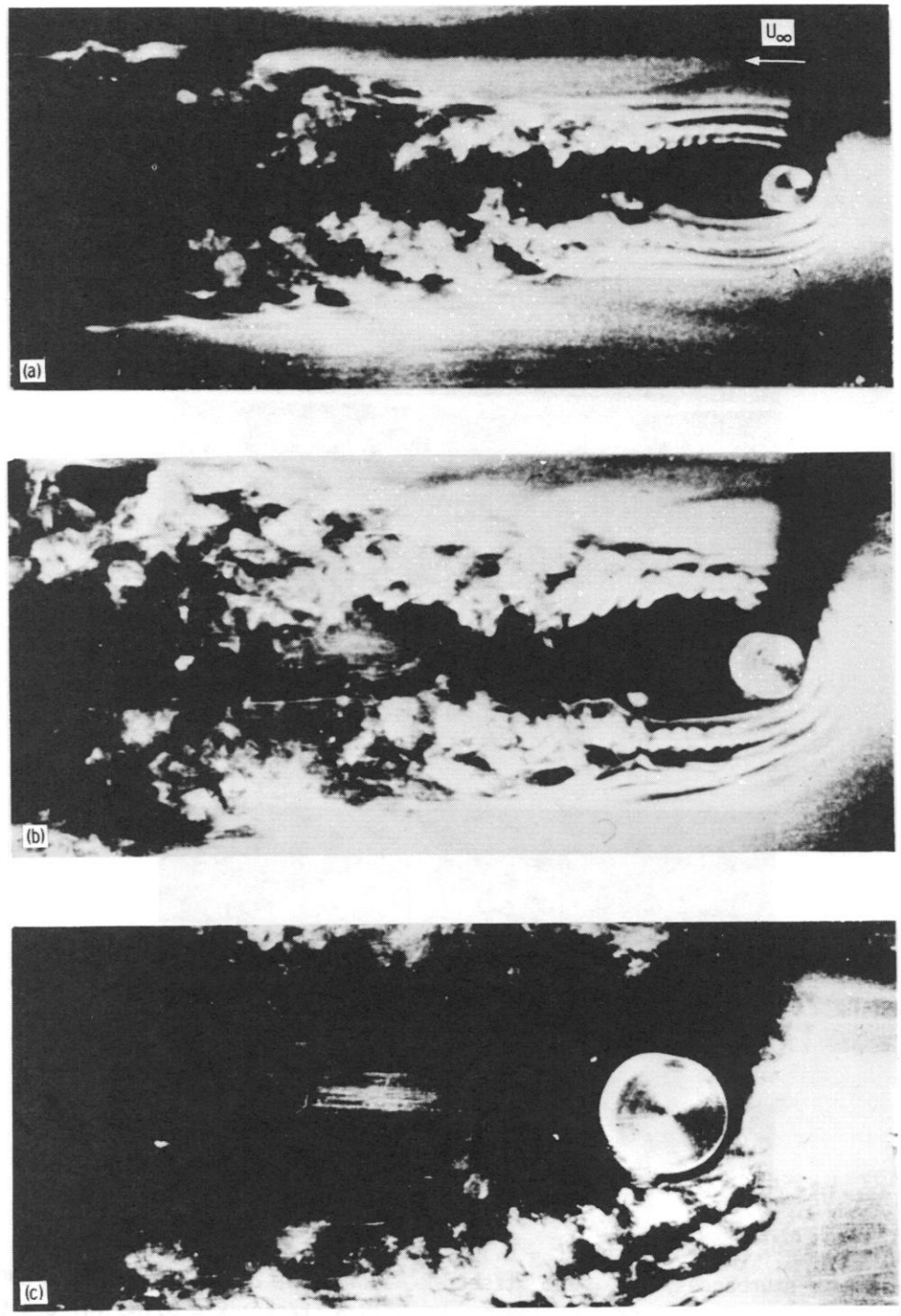

(a) Horseshoe system oscillation beginning: $k = 0.375$ in; $\delta = 0.18$ in; $Re_k = 3600$.
(b) Horseshoe system oscillating strongly: $k = 0.5$ in; $\delta = 0.18$ in; $Re_k = 4800$.
(c) Horseshoe system turbulent upstream of trip: $k = 1.0$ in; $\delta = 0.18$ in; $Re_k = 9600$.

Figure 5. - Smoke visualization (at fixed external speed) of new instabilities in boundary layer distorted by cylinders with $k = D$, as these protrude further outward. $U_\infty = 18.3$ ft/sec. (From ref. 13.)

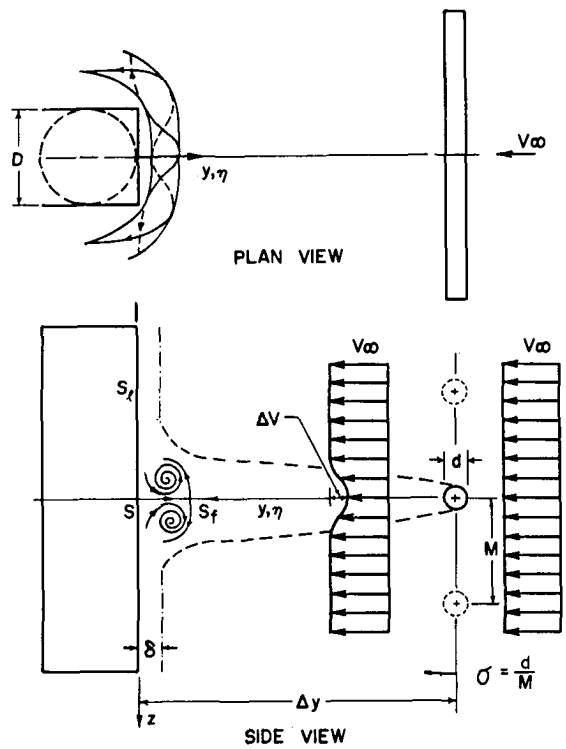

Figure 6. – Schematic of vortex flow module proposed for augmentation of heat transfer from bluff bodies.

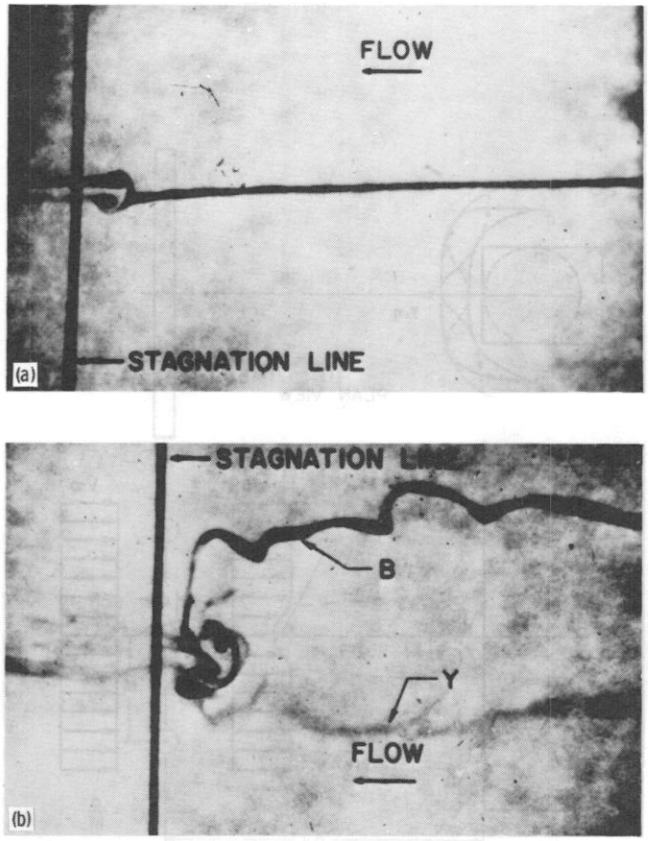

(a) Re_d = 30; Re_D = 1040; $\Delta x/d$ = 111; d = 0.027 in; D = 0.935 in.
(b) Re_d = 365; Re_D = 2730; $\Delta x/d$ = 32; d = 0.125 in; D = 0.935 in.

Figure 7. - Side-view dye visualization of single wake impinging on rectangular cylinder at Re_d of 30 and 365. (From ref. 14.)

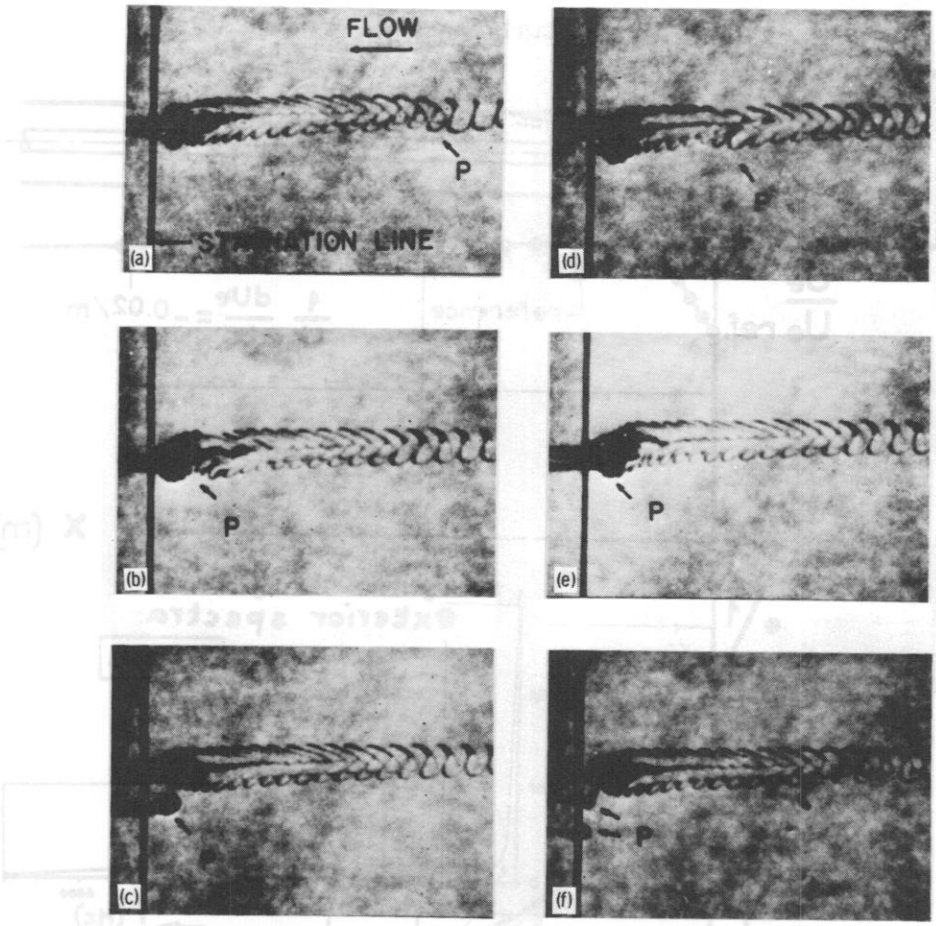

(a) t = 0.
(b) t = 0.14 sec.
(c) t = 0.24 sec.
(d) t = 0.34 sec.
(e) t = 0.44 sec.
(f) t = 0.55 sec.

Figure 8. - Side-view dye visualization showing effect of free-stream perturbation P on vortex flow module at $Re_d = 90$.

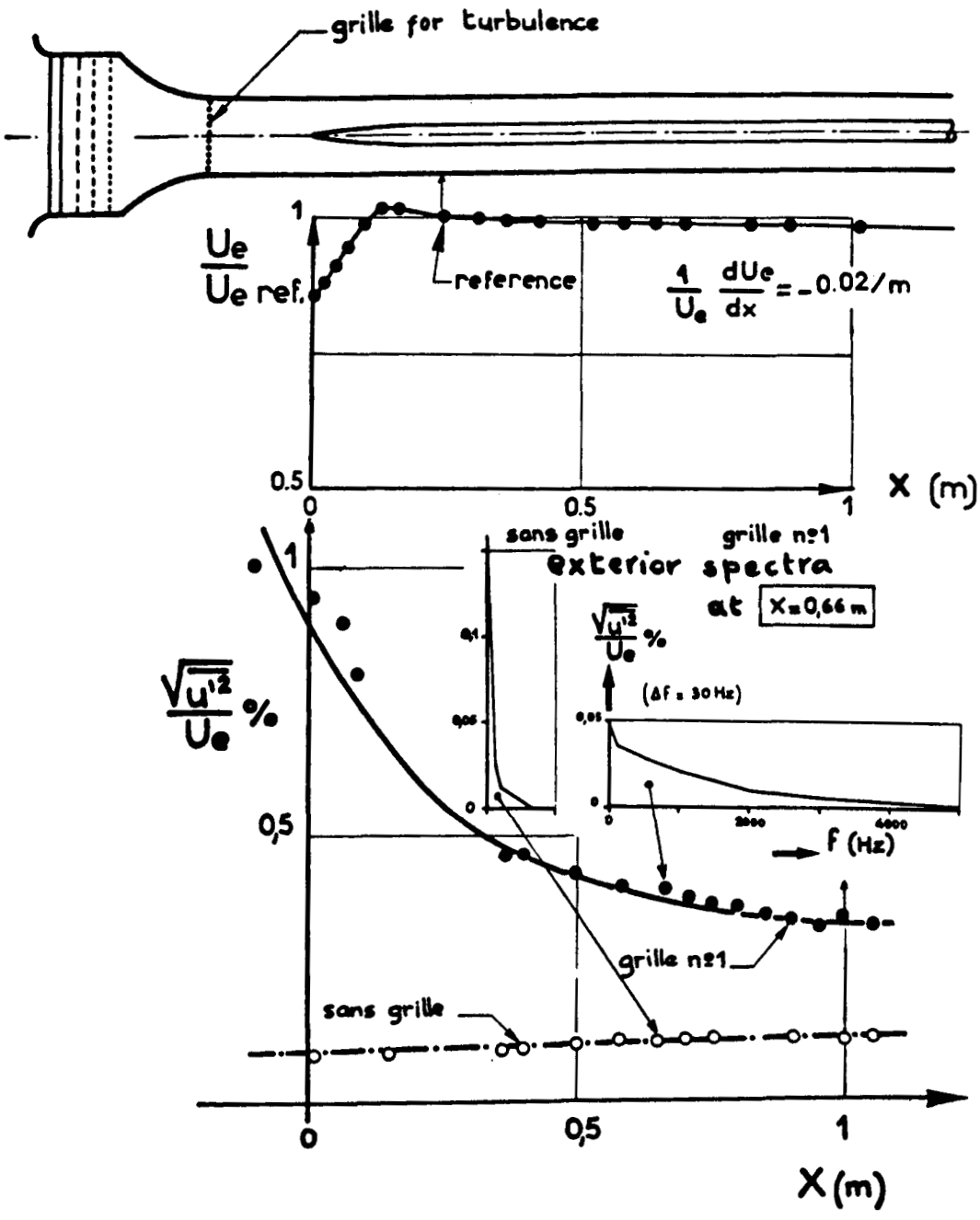

Figure 9. - Turbulence development and sample spectra outside boundary layer along axisymmetric slender body with and without upstream grid. (From ref. 17.)

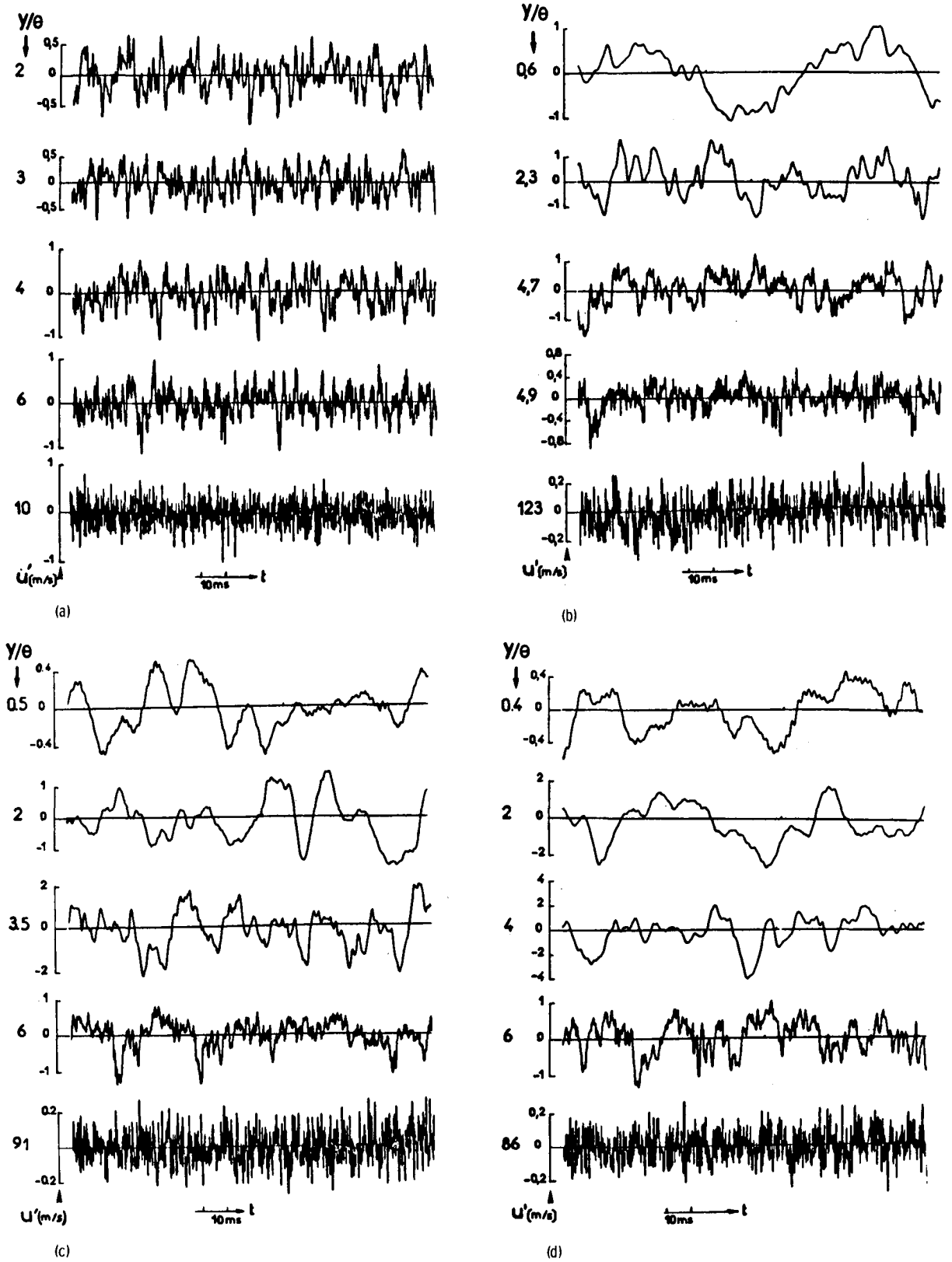

(a) x = 3.7 cm. (b) x = 36 cm.
(c) x = 66 cm. (d) x = 85 cm.

Figure 10. - Samples of fluctuations u(t) at five heights y of laminar boundary layer growing in presence of grid at x of 3.7, 36, 66, and 85 cm. (From ref. 17.)

FLUID MECHANICS–Soviet Research, Vol. 5, No. 4, July-August 1976

Characteristics of the Laminar Boundary Layer in the Presence of Elevated Free-Stream Turbulence

YE. P. DYBAN, E. YA. EPIK AND T. T. SUPRUN

The behavior of the laminar boundary layer was observed at free-stream turbulence of 0.3 to 25.2%. The increases in the boundary layer thickness, in the tangential stress at the wall, and in the momentum thickness with increase in turbulence are estimated. It is shown that the depth to which the fluctuations penetrate into the boundary layer does not depend on the turbulence but only on the Reynolds number. The perturbation peak in the layer are highest at free-stream turbulence of the order of 4.5%. The longitudinal scale of turbulence increases monotonically toward the outer edge of the layer, while its spectral distributions exhibit low (less than 300 Hz) frequencies.

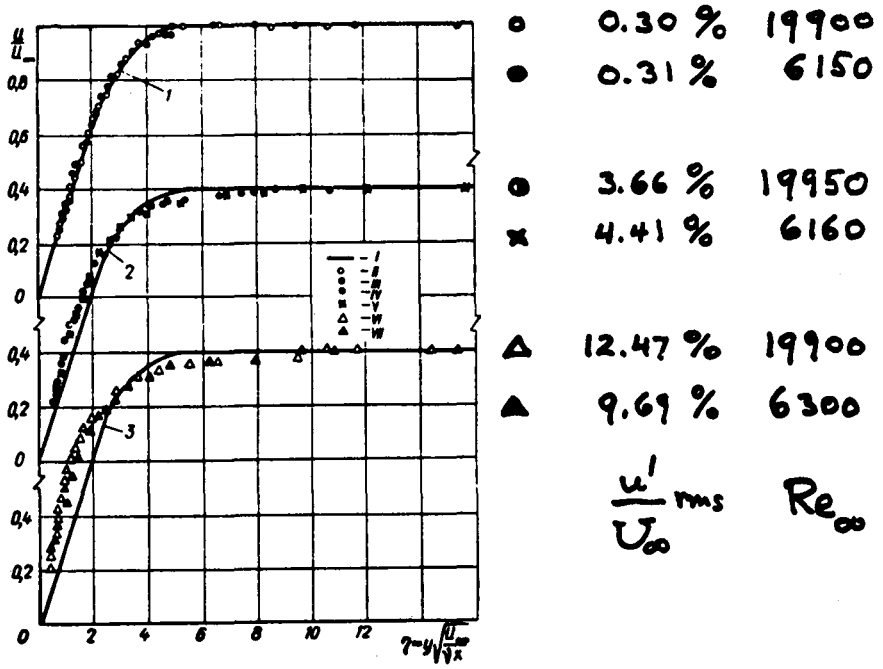

Fig. 1. Velocity distribution in the laminar boundary layer.

Figure 11. – Abstract and mean laminar boundary-layer profiles in presence of increasing free-stream turbulence. (From ref. 22.)

FLUID MECHANICS–Soviet Research. Vol. 5, No. 4, July-August 1976

Characteristics of the Laminar Boundary Layer in the Presence of Elevated Free-Stream Turbulence

Do Q
$\mathcal{L}/\delta^*$

YE. P. DYBAN, E. YA. EPIK AND T. T. SUPRUN

The behavior of the laminar boundary layer was observed at free-stream turbulence of 0.3 to 25.2%. The increases in the boundary layer thickness, in the tangential stress at the wall, and in the momentum thickness with increase in turbulence are estimated. It is shown that the depth to which the fluctuations penetrate into the boundary layer does not depend on the turbulence but only on the Reynolds number. The perturbation peak in the layer are highest at free-stream turbulence of the order of 4.5%. The longitudinal scale of turbulence increases monotonically toward the outer edge of the layer, while its spectral distributions exhibit low (less than 300 Hz) frequencies.

30°

Thickness not given.

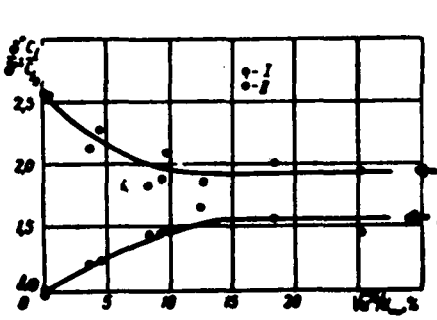

δ^{**} virtually constant
Θ increases with u'/U_∞
H factor δ^*/Θ
C_f/C_{f_0} at no turbulence

Fig. 2. Variation in drag coefficient and form factor in the laminar layer. I) c_f/c_{f_0}; II) δ^*/δ^{**}.

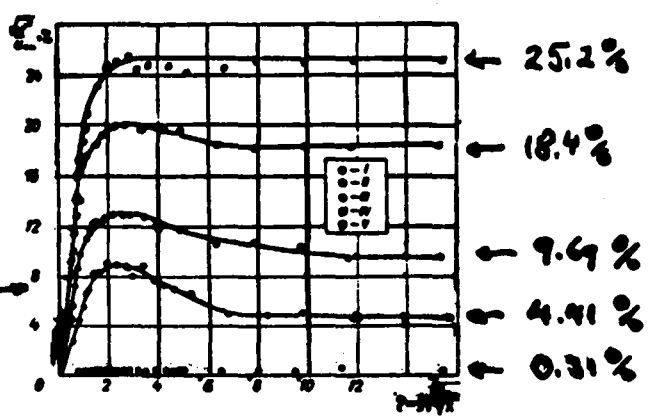

max: Klebanoff breathing effect

Fig. 3. Distribution of fluctuations in the laminar layer at $Re_{\infty} \approx 6.2 \cdot 10^3$. 6200

Figure 12. – Variation of skin friction ratio, shape factor, and u' fluctuation profiles in a laminar boundary layer as free-stream turbulence increases. (From ref. 22.)

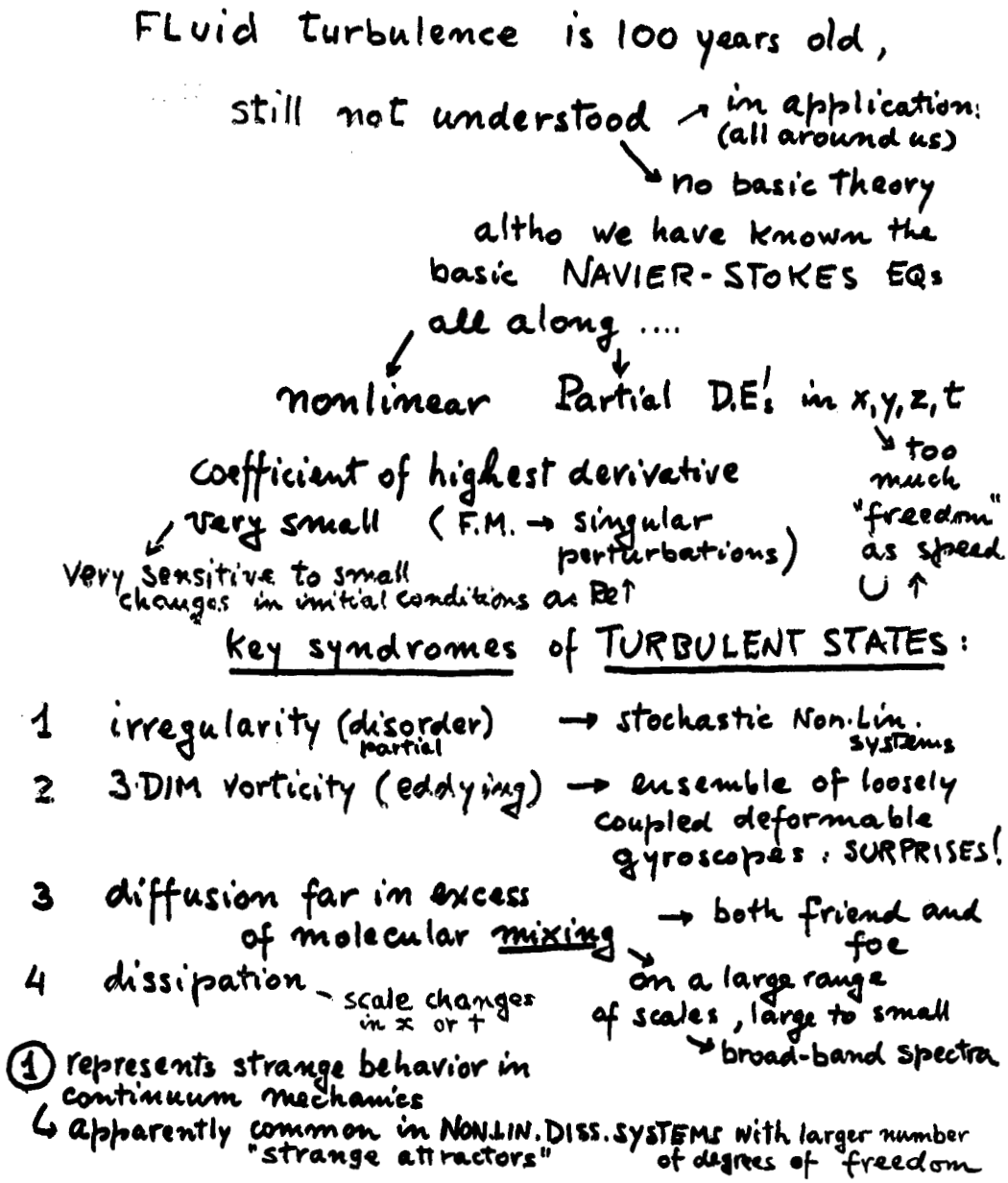

Figure 13. - Salient features of turbulence.

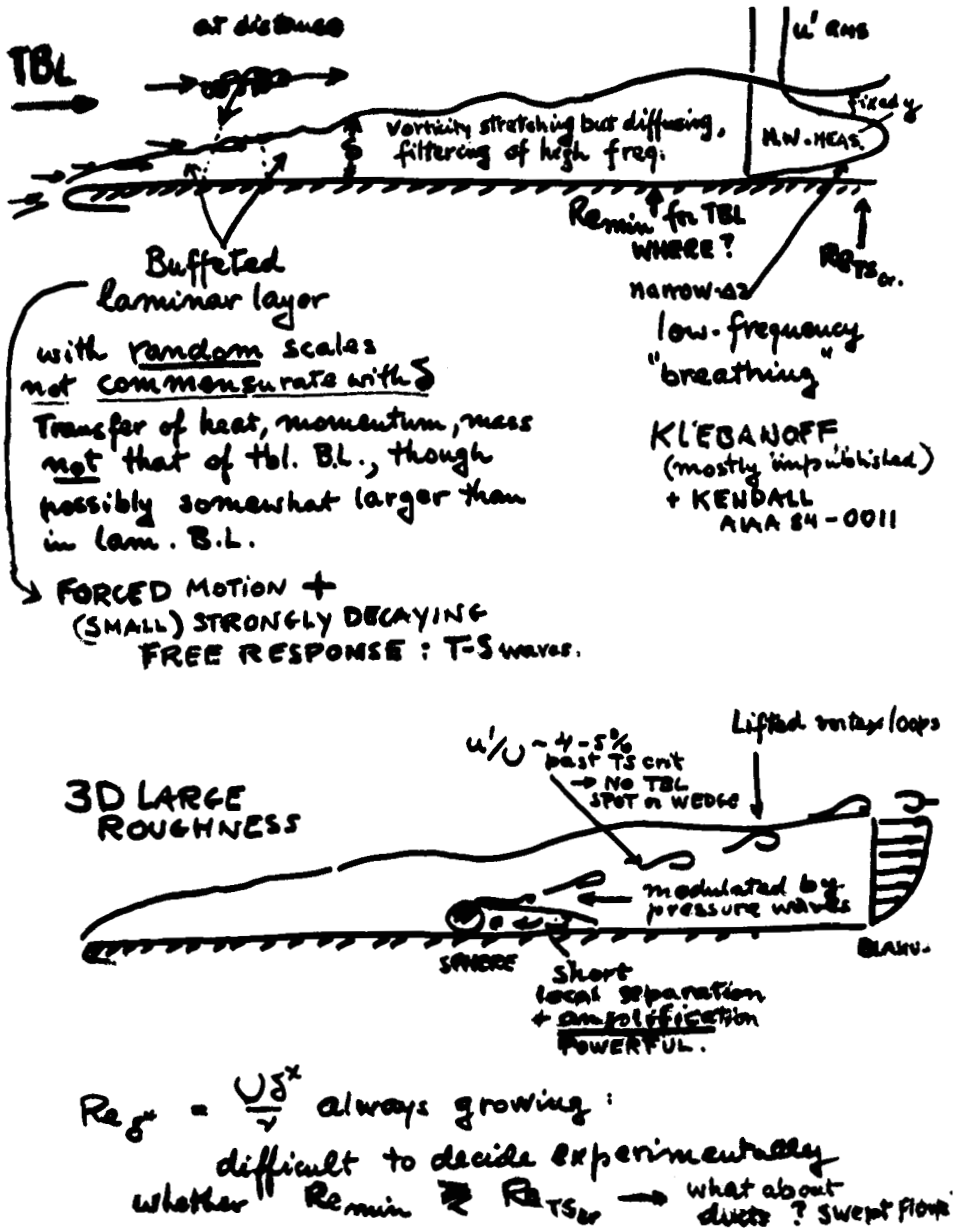

Figure 14. - Schematic of influence on growing laminar boundary layer of external turbulence (top) and a three-dimensional protuberance (bottom).

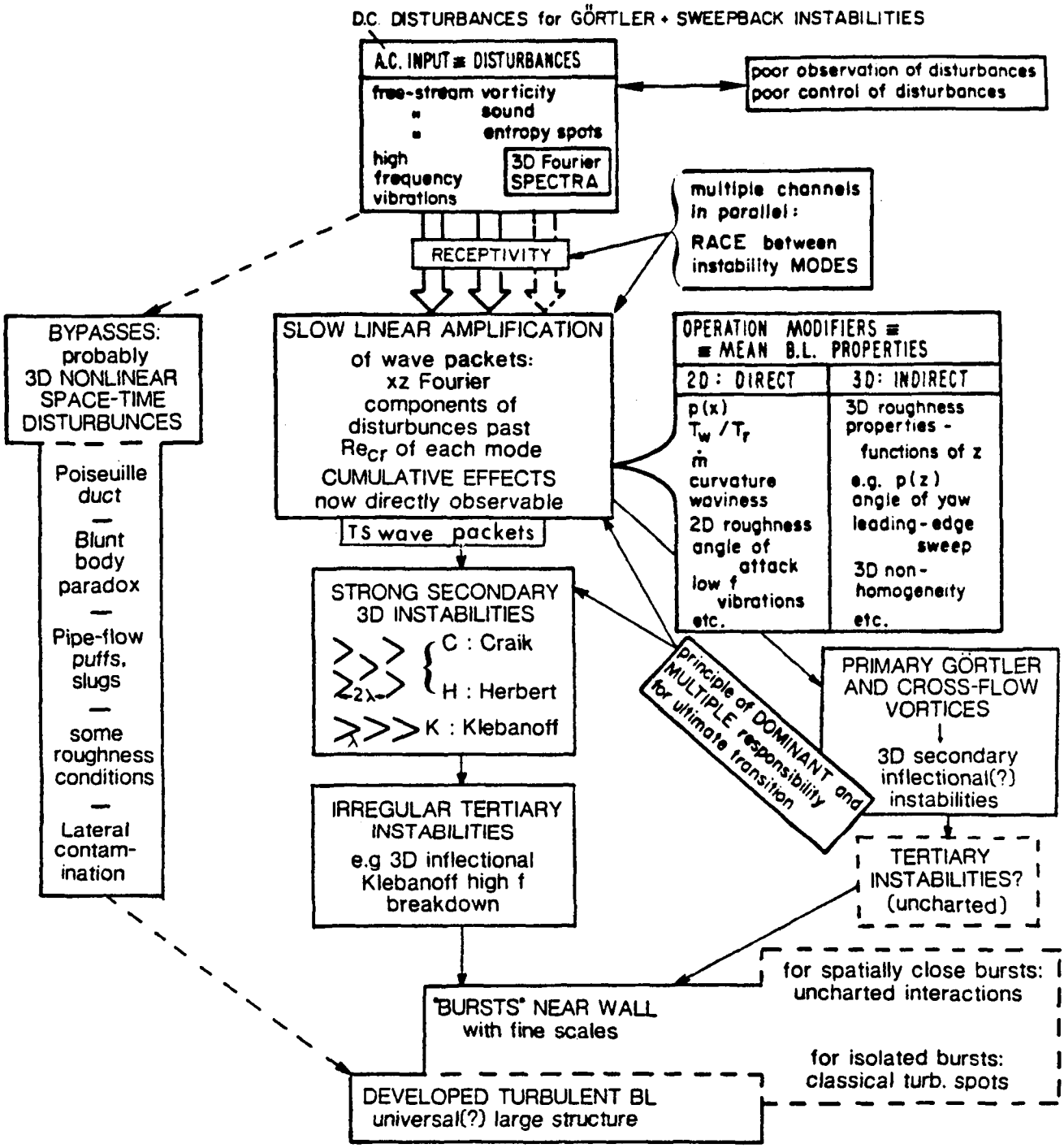

Figure 15. - Evolutionary paths to turbulence in undistorted boundary layers and ducts for mild environmental disturbances - 1984.

REPORT OF GROUP 1

Robert P. Dring
United Technologies Research Corporation
East Hartford, Connecticut 06108

By way of introduction, figure 1 illustrates an important feature of the flow conditions inside turbines: it diagrams the velocity as it leaves the stator and enters the rotor. The absolute flow speed minus the rotor wheel speed gives the rotor incident relative velocity. Group 1 focused primarily on upstream wakes and disturbances and their effect on transition. The wake of the first vane, if we assume that the flow is collateral, which it is not, is in the same direction as the potential flow, but retarded. Subtracting the wheel speed from the wake flow in the rotating frame of reference gives the wake relative velocity. It is obviously not of the same magnitude, and more importantly it is not in the same direction, as the potential flow. Most notably it has a component normal to the potential flow around it, and that component causes the stator wakes in the rotor passage to move preferentially toward the rotor suction surface. These stator wakes pile up on the suction surface in a complex nonlinear pattern. From this introduction to upstream wake disturbances working group 1 put together the following results, conclusions, observations, and suggestions.

We suggest a "building block" approach to the physics. The building block approach is a series of concurrent experiments focused on specific mechanisms, not a series of programs or experiments to be run in series. These concurrent experiments are directed at specific physical phenomena. Each should have some positive effect on our understanding and ultimately on the design process.

Our second suggestion relates to the fact that we are basically talking about unsteady flow: unsteadiness in static pressure, velocity, and turbulence. This unsteadiness can be random or it can be periodic, particularly as it relates to blade passing effects. We need to know in considerable detail about the intensity and scale of these random periodic disturbances because the length scale will vary by orders of magnitude. Much of the periodic disturbance will be at a length scale typical of the airfoil pitch, which is 1000 times the boundary-layer thickness and probably not relevant in terms of a turbulence effect. We need to characterize the inlet conditions to all the airfoil rows. The characterization probably needs to include spatial and temporal details.

Although we were concerned mostly with unsteady effects, the steady flow is not well understood either. So, attention needs to be committed to steady two-dimensional transitional work. Evidence of this is the results presented by Ray Gaugler at this symposium. We believe that both aerodynamic and heat transfer results are needed. Heat transfer results alone are insufficient. We need to understand what is happening in the boundary layers. Boundary-layer measurements require thick boundary layers, which dictates the scale of the experiments. The transition process must be investigated both for the velocity boundary layer and a thermal boundary layer.

Our group suggests that the required facilities be identified. Are there physics that need to be studied that are not compatible with existing facilities? New large-scale facilities are required for the study of unsteady and periodic effects to enable measurements that are useful to the analytical community.

We also recommend "certified experiments" to avoid trying to match data that may not be worth matching. Something similar to the 1968 Stanford boundary-layer conference is needed in which the conditions of the analysis are matched to the experiment. We recommend that a selective set of two-dimensional, steady-flow certified experiments be executed in a parallel schedule. The experiments should probably include what we would generically call flat plates, which includes curved ducts. Certified experiments should also be done on the airfoil. In the first experiments film-cooling conditions should be avoided because of the flow and mass addition complexities. The leading-edge and flow-turning conditions will be sufficiently complex in this set of experiments. Film-cooling interactions will have to be addressed later.

Experiments should be devised to investigate turbine inlet conditions. Combustor exit conditions should be simulated in both hot and cold experiments. The flow simulation should include both spatial and temporal scales and the nonhomogenity and intermittency of the combustor exit. We need a good space-time resolution of what the combustor is producing. The difficulty of making measurements in hot experiments should not preclude doing cold experiments. The simulation of the combustor exit should be reproducible and representative. However, strong feeling were expressed against spending a lot of time trying to make turbulence-generating devices that simulate in great detail what is happening in a combustor downstream of the blade row.

Another category of two-dimensional experiments is unsteady flow, including nonperiodic disturbances such as wake transport and wake accumulation. The transport of wakes across the blade-to-blade passage and their accumulation on the suction surface need to be simulated carefully. The initial effort should be with flat plates, but later the complexities of airfoils should be included in the experiments. It is recognized that several efforts are under way to simulate wake behavior experimentally. The real point here is that the dynamics of these wakes has to be simulated properly. The study of wake migration will require rotating-rig testing, which is by nature three dimensional and involves large-scale, slow-speed facilities or full-scale engines. However, the excessive cost and complexity of engine-scale testing make other approaches more likely, such as transient testing in shock tubes and the blowdown type of engine-scale testing.

Finally, we recommend that experiments be devoted to the effects of mass addition and film cooling, ultimately in a research plan. The group also considered surface roughness, three-dimensional end-wall effects, feedback of downstream disturbances on boundary layers, and free-stream flows. They should receive serious consideration in future planning.

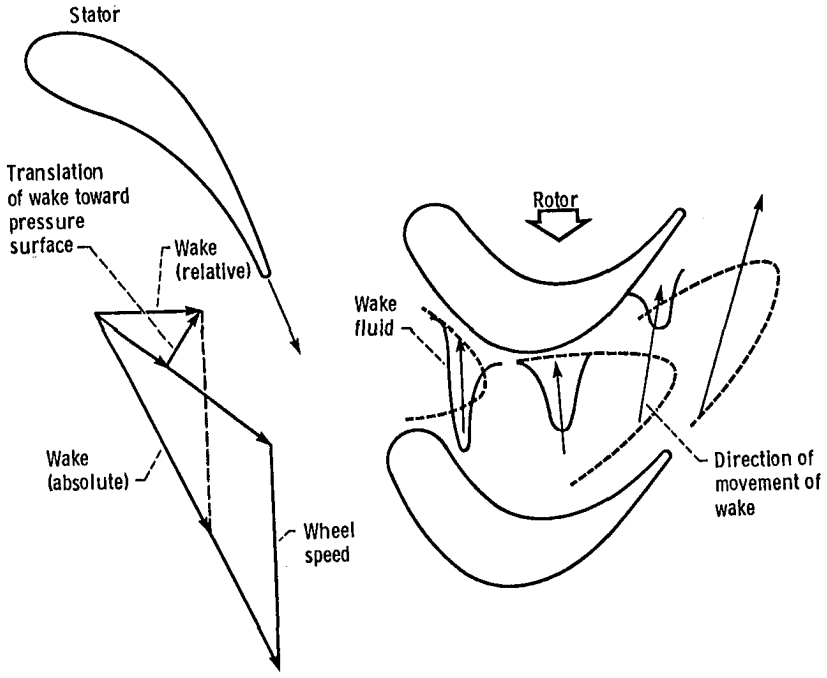

Figure 1. - Stator wake accumulation on rotor suction surface.

REPORT OF GROUP 2

Helen L. Reed
Stanford University
Stanford, California 94305

Group 2 was concerned with transition prediction models and subsequent code development and verification. The objective was to predict the maximum loading and heat transfer rate on turbine blades. It was pointed out at the beginning of the session that the internal flows through a turbine are extremely sensitive to the environment. If you miss predicting heat transfer by as much as 25 percent, you can be off by an order of magnitude on the life of a turbine blade. So it is extremely important to predict turbine metal temperatures accurately.

Although a computational modeler would want to examine flows involving vanes, blades (unsteady effects), end walls (three-dimensional effects), and ducts, we were mainly concerned with identifying which parts of the turbine would be the most interesting to work on. We decided that the vane would be the place to begin the computation because the first vane is somewhat separated from its upstream neighbors. The rotor blade row should be analyzed next. Unsteady flow effects and wake disturbances will have to be considered. Predicting these effects is beyond our current capability, but we hope to be able to do so within 5 years. The flow through vanes or blades can be approximated as two dimensional at the midspan. However, at the tip or root the flow is definitely three dimensional. Thus the three-dimensional effect of the end wall is an important topic.

Duct flows were mentioned as an important category of flows warranting an effort in computational modeling. It was suggested that duct flow might be a logical place to examine methods for including transition prediction. Roughness could be one of the several parameters to be examined in duct flow.

The next topic we identified was the free-stream environment. From earlier presentations most experiments seem to be done at turbulence levels of 1 to 10 percent. In the real engine environment turbulence levels are 10 to 20 percent. Consequently there is a big discrepancy between what happens in real life and the data that seem to be available to use in verification. However, we can still use the lower turbulence results as a guide for code verification and try to extrapolate to the higher turbulence levels. We recommend experiments at the higher turbulence levels.

What transition prediction models are available? Where do we want to go? The only accurate way to predict transition is to do a full Navier-Stokes simulation. The large eddy simulations (LES) are closest to full Navier-Stokes simulations. This type of analysis is being done at NASA Ames, NASA Langley, and Stanford University. It is a very promising technique. Also available are empirical models - the mixing length models. A popular model used in predicting two-dimensional flow and turbulence is the McDonald-Fish model. It was the feeling of the group that no empirical transition method will be general enough to apply to a range of flow conditions. Only the full Navier-Stokes simulation

will be a general method. Chorin's random vortex method was included as a possible analytical approach to representing transition. In this method vorticity is released at a discrete point to simulate turbulence. Group 2 recommends pursuing the Navier-Stokes simulation and the large eddy simulation as the best approaches to predicting transition.

The next recommendation pertains to the difference between the hydrodynamic and thermal boundary layers in the transition process. The thermal boundary layer develops much more slowly than the hydrodynamic boundary layer. If the energy equation contains a model of the $v' - t'$ turbulence terms, the solution to this equation might serve as an interim prediction of transition. It was pointed out that the most success with these simple models has been with those that involve variable Prandtl numbers through the transition region. Such a simplified model would be most applicable to the transition process on the suction side of the blade. The pressure side of a turbine blade has concave curvature and of Görtler vortices, which are complex and therefore difficult to model and analyze. It was suggested that a Görtler vortex model be developed for the concave curvature region of the turbine blade. Such a model would be helpful in predicting heat transfer and transition.

Group 2 has a wish list of effects to be incorporated in transition prediction models. These are not listed in any order since we could not decide which would be the most important. The list includes free-stream turbulence, roughness on the surface of the blade or vane, curvature, pressure gradient, and surface temperature. In developing the computational models we recommend starting with a steady mean-flow model and working toward the unsteady problem. Our group strongly recommends that a research emphasis be put on defining the physics of the transition problem. For example, the large eddy simulation is a promising approach, but it has periodic boundary conditions that makes it extremely difficult to execute the analysis. Appreciable effort has to be devoted to defining the physics realistically and properly.

The next thing we discussed was the numerics themselves. The effort should be directed toward a Navier-Stokes solver. At present, the large eddy simulation and the spectral methods are in common usage. We recommend that subgrid-scale modeling be developed to capture all of the small-length scales in the problem. Currently in a transition calculation the large eddy simulation models break down because the flow loses kinetic energy and the flow structure dissipates into small-scale turbulence. The resolution of the numerics problem of the small scale depends on the size of the computer available and funding support to operate the computer in flow modeling. The group recommends that the Lewis Cray-1S be made available to outside investigators during off-peak hours.

The last issue we discussed was validation of computational codes. In agreement with the group 1 we recommend that all transition boundary-layer data be compiled on magnetic tape and be available in a document listing. The data need to be certified as to validity and accuracy. Certification is a large effort, but we feel it is important in correctly modeling transition. If existing data cannot be certified in the immediate future, we suggest that a list of the data sources be compiled and made available to transition researchers so that they can evaluate it. In designing and executing future verification experiments the free-stream conditions must be totally documented. The intensity of the turbulence in the free stream, the scale, and the frequency spectrum of flow disturbances must be a part of the documentation. Turbulence

profiles should be provided if at all possible. It would be highly desirable if a sampling of data could be taken when the actual transition phenomenon occurs so that an analytical model of transition could be verified. For all operating conditions the mean velocity profiles and heat transfer should be a part of the data set. Skin friction data would also be useful. In predicting transition for external aerodynamics, small-disturbance theory is employed. The so-called e^n theory has been the most successful in predicting this type of transition. The trick seems to lie in predicting the exponent, which is somewhat like throwing dice. Transition depends on so many parameters that it is difficult to prescribe what information should be inserted into the correlation.

REPORT OF GROUP 3

William S. Saric
Arizona State University
Tempe, Arizona 85281

Much of our presentation repeats material from the previous two presentations. Group 3 was concerned with experimental techniques. I will first describe what we interpreted as the experimental base required for predicting transition and then describe existing measurement techniques. Finally, I will comment on new experimental techniques and how to expand present techniques. The reports from groups 1 and 2 have highlighted the complicated flows that we should be aware of. Group 3 concentrated not on the details of those complicated flows but rather on the transition prediction itself, keeping in mind the requirements of the receptivity problem of group 1 and the computational problems of group 2. I think the general consensus of groups 1 and 2 as well is that mean flow measurements by themselves will only produce facility-dependent data. Although these are useful measurements, other information is needed to solve the real problem. The ideal set of data must include the pressure and velocity distributions in the mean flow, the background disturbance level, and boundary-layer information. The background disturbance level must be distinguished from fluid turbulence and from acoustic signals or pressure fluctuations. Acoustic signals can be correlated over the entire geometry. Flow unsteadiness in a blade row may be correlated over a chord but not necessarily over boundary-layer thickness. The transition characteristics will depend a great deal on how upstream disturbances are broken up into turbulence or pressure fluctuations. To distinguish turbulence from pressure fluctuations, the spectra must be carefully measured. Detailed measurements in the boundary layer must also include the phase in addition to the amplitude. Phase-correlated measurements between the background and the boundary layer are highly desirable. A measurement of streamwise vorticity would be a major contributor to understanding the nature of the background. Information on vorticity would lead to an understanding of the scales involved, particularly the spanwise scales of the oncoming turbulent flow. An understanding of scale within the boundary layer is also important - in particular spanwise scale. It has been my experience that spanwise scales are as important or more important than chordwise scales. Multiple hot wires can be employed in making simultaneous measurements of phase and amplitude. Spanwise measurements are essential because simple two-dimensional measurements do not reveal the three-dimensional characteristic of transition. In addition to the boundary-layer measurements, wall measurements incorporating high-frequency surface gauges and skin friction heat transfer gauges are essential. Coupling of the boundary-layer measurements with the wall measurements is needed in determining transition.

Several state-of-the-art types of instrumentation not necessarily used today in transition and turbine research, can be employed in free-stream, boundary-layer, and wall measurements (table I). Laser Doppler systems and hot wires provide the basic state of the free stream. The laser Doppler system coupled to a computer can generate large-scale maps of flow fields in both free-stream and boundary-layer applications. For measurements near a wall, hot

film or heat transfer gauges are commercially available. Miniature skin friction balances have not been developed for use in turbomachinery. Microphones will record small pressure disturbances. For turbine or shock tube experimentation the response range for film gauges must be of the order of megahertz, which is beyond the range of most commercially available film gauges. The gauges are generally small enough to allow spatial resolution of the order of 50 mils. Flow visualization methods such as thermal-sensitive paints and liquid crystals can give local heat transfer information. At low temperature a useful heat transfer measurement method is the sublimation of a material such as naphthalene.

Group 3 suggests a hierarchy of experimental facilities (fig. 1) that would employ these instrumentation and experimental techniques. At the top is the aircraft engine and at the bottom is the basic research facility. In between are cascade and low-speed rotating facilities. The facilities that would be apt to supply transition data are marked with a capital "T." In general, most of these facilities can provide high-turbulence flow conditions, but the same kinds of instrumentation cannot be employed throughout this hierarchy of facilities.

The question arises as to how closely each facility simulates conditions. The degree of approximation is difficult to evaluate. The greater instrumentation capability is associated with tests that do not include the real thermal conditions. Consequently a better documentation of the free-stream environment is a difficult challenge. Group 3 was unable to suggest any new type of facility that could be used to address this issue. However, given the present hierarchy of facilities there appears to be much that can be done with the existing system that would provide important input to the transition problem. Existing experimental facilities should be better utilized to make more detailed measurements. This places a major responsibility on the sponsor of this conference, NASA Lewis, and others to devote more time and resources to the encouragement of researchers throughout the hierarchy to pursue basic measurements that document the nature of turbulence and the unsteady conditions that exist. Spanwise scales are important data that come out of two-point measurements. One of the strongest recommendations offered by group 1 and also by group 2 is the documentation of the free-stream environment. Even with a Navier-Stokes solver, the initial conditions are needed to start the calculation.

The basic recommendation is for a large data base of engine conditions. The generation of such a data base will require widespread participation throughout the industry. There should be a prearranged agreement regarding the content of the data base and how the data are to be obtained in order to "certify" the information. Care must be exercised in specifying the experimental conditions so that the results are not influenced by the test facility. This requirement has been alluded to in previous discussions during this symposium. All experiments in this area should be independent of the facility being employed. With existing instrumentation and facilities much can be done to investigate the boundary layer and the free stream. I mean this also as self-criticism. I have not documented the transition environment as carefully as I should in my own experiments. However, careful documentation is certainly possible, and again this is where the understanding of the sponsor comes in. The sponsor must take the time and have the courage to reject any more trash in the literature. Efforts must be begun to measure three-dimensional compo-

nents in as much detail and spatial resolution as possible with existing techniques. But what about new instrumentation requirements? There is need for a pressure gauge that will operate beyond 5 kHz in high temperatures. It will have to be a cooled probe, 50 mils in diameter, with a liquid-nitrogen channel fed in through it and everything kept under isothermal conditions. This probe will be difficult to build. The streamwise vorticity measurement is also considered important. We need to find out what is happening in the real systems to use as feedback to the transition problem. We still need to establish a large data base for real engine systems.

Different measurements can be made in three categories of facilities without really pushing the state of the art and at the same time contributing basic understanding to the general problem. In turbines there is no reason why one cannot get all of the mean flow measurements that exist as well as the amplitudes of the fluctuating components. Phase information may not be feasible, but at least the amplitudes of fluctuations will give some idea of the spatial nature of these variables. In large, low-speed simulators we can examine the fluctuating components; the amplitude spectra, scales, and heat flux will provide information on transition.

Our group spent some time discussing what information is needed to discern transition. A single-point fluctuating component is not necessarily an indicator of transition. Other gross features such as average heat flux may be more meaningful. Multiple hot wires are being developed to measure average heat flux. Some instrument research is in progress on the use of the laser Doppler for measuring vorticity. With the laser system the major obstacle is the size of the sampling volume. Another possibility in instrumentation is field imagery, which is an image of the entire flow field. Currently friction or heat transfer gauges that have a high dynamic response are used. With small gauges it is possible to place many of them on the flow surfaces. Coupling their outputs and dynamic flow measurements to a computer will provide information that can be used to estimate the scale of phenomena happening at the wall.

A new technique of field imagery is laser speckle velocimetry. Using this technique in conjunction with a large computer makes thousands of data points available from a single measurement. Cinematography is still another technique with potential for field imagery. Motion pictures of schlieren images can yield temporal and spatial scales of some of the behavior taking place in the flow, and this is certainly one area that can be developed. A spanwise scalometer would be a device to ascertain spatial scales in the flow more or less instantaneously.

Our group discussed the required accuracy of the suggested instrumentation. This symposium gave no clues regarding the accuracy needed to specify transition, so accuracy requirements remain an open question. Group 3 also wondered when and if transition will become a higher order element in design practice. Perhaps when we understand more about transition, we will be able to eliminate some of the uncertainty that it poses in design practice. However, at this point it is a major factor. Accuracy requirements for transition measurements should be addressed.

TABLE I. - INSTRUMENTATION FOR FLUCTUATIONS AND DYNAMIC TRANSITIONS

Measurement	Instrument
Free stream	Laser Doppler velocimeter (need high u'; no phase) Hot wire
Boundary layer	Laser Doppler velocimeter Hot wire (limit on number of wires) Smoke wire (low velocity)
Wall	Film gauge (10 kHz - 0.1 MHz) Piezofilm (under development) Pressure (microphone)

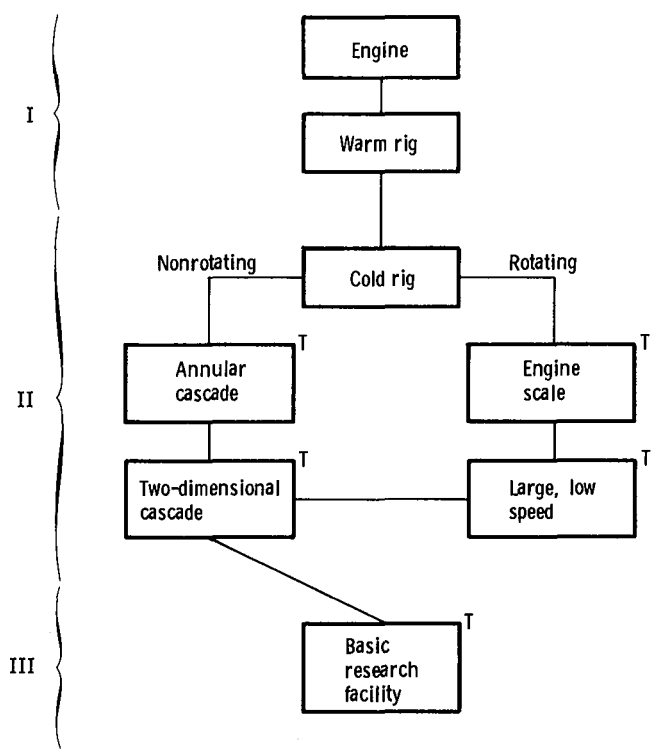

Figure 1. - Hierarchy of experimental facilities, where T denotes the ability to measure transition.

DISCUSSION PERIOD FOLLOWING

GROUP PRESENTATIONS

This session of the symposium was chaired by Eli Reshotko. He reminded the audience that the three groups who reported addressed different issues. The first was concerned with the effects of upstream conditions, wake disturbances, combustion, etc., on turbine entrance conditions. The second addressed analytic and computational techniques to predict turbine flow and heat transfer. The third group examined measurement techniques and discussed the types of measurements that must be made. The moderator asked the audience to address their questions to the appropriate group.

The first comment came from Mark Morkovin, who in commenting on the first group emphasized that the turbine environment is an accumulative result of upstream, large-amplitude disturbances and consequently is quite different from the conditions of low-amplitude disturbances treated in gas dynamics applications.

John Adamczyk of NASA Lewis pointed out the challenge of representing multistage flow effects in a computer code. The computer storage necessary to represent the Reynolds-averaged Navier-Stokes equation far exceeds the capacity of existing computers. The closure problem for a multistage machine that comprehends the variance in the flow from blade row to blade row must be addressed. Data are needed to help formulate such a closure model.

Bryan Roberts concurred with Adamczyk's comments on multistaging. In designing a multistage machine, it is important to match the first blade rows in order to avoid a progression of mismatches that carry through the machine. Robert concluded his commentary by asking for greater definition of the kind of flow experiment needed to test analytical methods.

Helen Reed of Stanford responded by suggesting that the experiment should be designed with a controlled free-stream disturbance that can be easily identified. The initial and boundary conditions must be easily specified.

Ron York of Allison commented that little is known on how to specify transition in an experiment. A time-averaged concept of transition as some average between the laminar and turbulent states is not adequate. Perhaps the emphasis ought to be on a detailed measurement of how turbulence develops and the associated production and dissipation processes.

Henry Nagamatsu supported York's comment about time averaging being inadequate. He advocated use of thin film gauges to obtain instantaneous measurements in the transition zone. Experience in the shock tube has shown their rapid response (1 μsec).

Eli Reshotko injected a call for greater understanding of the laminar or turbulent boundary layers preceding and following the transition zone. They differ from the classical ones described in texts.

Mark Morkovin cautioned that a concept of turbulent spots that is based on a water table visualization may not be a valid model of turbulent production

in a highly disturbed environment. The process of transitioning a buffeted laminar boundary layer to a fully turbulent condition is going to be more complicated in a highly disturbed environment than in the more familiar quiescent environment. The potential interaction of the spots has not been investigated.

Reshotko requested that some discussion be focused more directly on instrumentation and measurement techniques.

Bryan Roberts led off by commenting on the way aircraft turbine engines are maintained in overhaul service. Rather crude methods for reshaping the blades and little apparent effort to regroup the blades on a turbine disk or a compressor wheel are evident. This shocking practice makes one wonder about accuracy in research measurement.

Gordon Pickett of Pratt & Whitney asked Group 3 to comment on the use of LDV methods for making measurements within the boundary layer. Do we need to start with large-scale models to get these data?

Anthony Strazisar of Lewis answered that it may be very difficult to measure the transitional boundary layer with LDV even on large-scale blades (chord of 1 ft). The LDV anemometer has a lower size limit.

Bill Saric of Arizona State added that if the tests could be done in large-scale simulators, LDV techniques in the boundary-layer measurements would probably work. Disturbances of 10 to 20 percent would probably be detectable.

The question was raised as to whether there is a substantial research effort toward accommodating LDV to high-speed conditions and the scale of real engines.

Nagamatsu cited some experience he had in the early 1970's in which LDV was successfully employed in supersonic jet research at modest scales.

Tony Strazisar responded to the question by stating in encouraging terms that the LDV technology for smaller scale measurements is near at hand. Support of instrumentation research is critical at this time. NASA-sponsored research at Penn State is currently able to demonstrate measurements in boundary layers that are about 1/10 in thick. Advancing this technique will require the persistent pushing of those who want it.

Nagamatsu commented that thin film gauges may be the preferred instrumentation for detecting transition, especially transient, intermittent phenomena. Following the trace particles in an LDV system may prove to be very difficult.

Bill Saric pointed out that flow field measurements are needed in addition to wall or boundary-layer measurements. The laser systems are capable of making field measurements. However, it is necessary to correlate the field and wall measurements.

Eli Reshotko asked for comments on the availability of multicomponent laser-measuring systems and two-point measurements.

Strazisar responded that two- and three-dimensional systems do exist. Such systems result in a larger measuring volume. These multidimensional systems have not reached the point of being applicable to boundary-layer investigations. Two-point laser measurements cannot be correlated in the manner of

hot-wire signals. One method would be to generate two probe volumes, but this raises problems of coincidence of measuring the same particle in each volume.

Reshotko introduced the question of scale measurements with LDV systems. The coincidence problem affects the determination of scale especially since scale can be in both the spanwise and longitudinal directions. It is not apparent whether the laser instrumentation can be used to determine scale.

As the discussion grew to a close, David Winstanley commented that the instrumentation group felt it was important to exploit to a greater degree the test rigs and instruments we have before devising new rigs and instruments.

Helen Reed advocated the need to compile and assess all available transition data. Helen also raised the question of a future meeting of this type. Her group strongly favored such an event.

Following these remarks Eli Reshotko expressed his appreciation to the rest of the planning committee and to Mary Lester of Lewis for the effective management of the arrangements.

SUMMARY REMARKS

Robert W. Graham
National Aeronautics and Space Administration
Lewis Research Center
Cleveland, Ohio 44135

I wish to add my thanks to that expressed by Eli Reshotko for the planning and execution of the symposium. I also thank all of you for your participation. It has been, to me, a very exhilarating experience to have such a group of outstanding people who represent a number of areas of interest in this whole problem, including the practical and the theoretical. I will attempt to summarize what I heard from the three groups who reported in the plenary session.

In the area of experiments, we seem to have come to the consensus that we need some kind of certified way of having these data made available to the engineering community. It was agreed that more experiments in steady flow, including two-dimensional flow, are required. Two-dimensional transition data should have priority.

An effort is required in simulating combustion exits wakes and more severe turbulence. In addition to more investigation in steady flow, experiments are required in unsteady flow and wake transport. Such studies would encapsulate much of the three-dimensional flow effects.

All of the groups recommended better use of the existing facilities with focus on measurement techniques in those facilities. For the certification of an experiment a considerable amount of information will be required about the facility, the instrumentation, and the experimental procedure.

In addition to making full use of available facilities and instrumentation, instrument research needs encouragement. This was also recommended in a heat transfer workshop held in 1980. Improved instruments to measure pressure, vorticity, field imagery, and scale are important.

A "hierarchy of facilities" was mentioned several times. A version of this concept that I have used is a structure of building blocks (fig. 1). The base block is basic science. The next higher block is physical modeling. Above that is model verification. The fourth level involves testing the code in as near to real engine conditions as one can get in a facility. Beyond the hierarchy is the application to actual design practice.

In the computational area there is certainly a need for the development of a transition model. Helen Reed's group seemed to think that the Navier-Stokes simulation is the best approach. However, improved empirical models may serve an interim role until the more sophisticated models become available. Vorticity representations are another option that was mentioned in connection with the combustion presentation. We also need Navier-Stokes solvers, LES solvers, and some way of representing the vorticity.

Strong interaction between the computationalists and the experimentalists was also recommended. This kind of interaction is needed to get the physics

into the computational model. It is necessary for the experiments and in the verification of computational codes.

This symposium has been a great experience. I would like to close with a final remark - and I am speaking for NASA. Somebody asked, how important is transition? Well to some of us it is highly important. To the whole of NASA it is hard to answer that question. There is always competition for many things. Although we at Lewis organized this symposium and promoted its importance, support for the program is in competition for NASA funding. I can assure you that those of us on the planning committee will be strong advocates of this program. I cannot promise that, because of this symposium, NASA Headquarters is now going to release some funding and support to this area. I do not want you to go away with that impression. In the last 3 years this area has grown significantly; the reports given yesterday certainly validate that. However, I do make a plea to you to advocate the program. Universities, industries, and private consultants must be heard by those who make the decision on the funding. So, I enlist your support in helping us to continue this kind of work. Basic research, which much of this is, is difficult to justify and maintain support for, as many of you know. We must also realize that the end product of the research must eventually reach the designers and the engine manufacturers. There must be a bridge between basic research and practical application. We must be supportive of one another in advocating these positions. I do not know what the 1985 budget will be, I do not know what the 1986 budget will be, but I can assure you that some of us are going to try our best to keep this program in contention. I hope your support will be there too.

Now, as for the future I do not know when we should reconvene. But, I would like to see this kind of symposium happen again after we report back on what we have done. Perhaps it might be appropriate to try a data certification conference similar to the Stanford computational conferences that have been held. I cannot foresee what the conference or symposium will be like, but I take it that you would like to have another symposium on transition in the not-too-distant future. With that comment I declare the Symposium on Transition in Turbines adjourned.

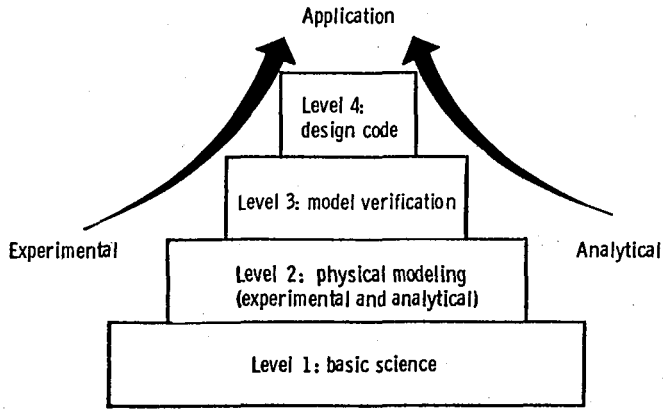

Figure 1. - Hierarchy of facilities.

1. Report No.	2. Government Accession No.	3. Recipient's Catalog No.
NASA CP-2386		

4. Title and Subtitle	5. Report Date
Transition in Turbines	July 1985
	6. Performing Organization Code
7. Author(s)	8. Performing Organization Report No.
	E-2456
	10. Work Unit No.
9. Performing Organization Name and Address	11. Contract or Grant No.
National Aeronautics and Space Administration Lewis Research Center Cleveland, Ohio 44135	13. Type of Report and Period Covered
	Conference Publication
12. Sponsoring Agency Name and Address	14. Sponsoring Agency Code
National Aeronautics and Space Administration Washington, D.C. 20546	

15. *Supplementary Notes*

16. Abstract

A symposium on the transition mechanism in turbine airfoils was held at the NASA Lewis Research Center on May 15-16, 1984. Brief progress reports were presented on a program of in-house and university grant research into the transition problem. This proceedings comprises those reports as well as an invited lecture by Prof. Mark Morkovin on the bypass mechanism and summaries of group discussions on four transition-related subtopics.

17. Key Words (Suggested by Author(s))	18. Distribution Statement
Gas turbines; Transition; Combustion; Bypass transition; Navier-Stokes equations	Unclassified - unlimited STAR Category 34

19. Security Classif. (of this report)	20. Security Classif. (of this page)	21. No. of pages	22. Price
Unclassified	Unclassified	224	A10

For sale by the National Technical Information Service, Springfield, Virginia 22161 — NASA-Langley, 1985

"Dynamics and Computation of Combustor Turbulence"

Motion picture supplement C-315 is available on loan. Requests will be filled in the order received.

The film (16 mm, 5 min, color, sound) shows high-speed color schlieren motion pictures of flow through a nozzle and over a rearward-facing step and flashback into the nozzle for a premixed propane-air combustor. The effect of a downstream contraction step on the flow field is shown to be significant. Computer-generated motion pictures show the turbulent flow field as computed by the numerical technique of Chorin.

Request for film supplement C-315 should be addressed to

Chief, Technical Information Services Division (60-1)
National Aeronautics and Space Administration
Lewis Research Center
21000 Brookpark Rd.
Cleveland, OH 44135

Cut

Date _____

Please send, on loan, copy of film supplement C-315 to NASA CP-2354

_____
Name of Organization

_____
Street Number

_____
City and State Zip Code

Attention: Mr./Ms. _____

Title _____

Place
stamp
here

Chief, Technical Information Services Division (60-1)
National Aeronautics and Space Administration
Lewis Research Center
21000 Brookpark Rd.
Cleveland, OH 44135

DO NOT REMOVE SLIP FROM MATERIAL

Delete your name from this slip when returning material to the library.

NAME	MS
~~Streett~~	~~159~~
~~W. Blackerby~~	~~904~~
K Peters	231

NASA Langley (Rev. May 1988) RIAD N-75